Doctoral Dissertation

Energy Dissipation in Irregular Breaking Waves with Air Bubble Dynamics

MD NUR HOSSAIN

July 2024

International Program of Maritime and Urban Engineering
Division of Global Architecture
Graduate School of Engineering
Osaka University

Statement of Authenticity

The entirety of the research presented in this thesis has been undertaken solely by the author. Any assistance or contributions provided by others have been duly acknowledged through proper referencing.

Abstract

The presence of irregular breaking waves featuring the air bubbles effect is fundamental to the dynamics of shallow water waves, playing a critical role in dispersing wave energy, which is crucial for protecting coastlines and controlling erosion. As waves approach shallow waters, waves interact more intensely with the seabed, increasing turbulence and energy dissipation. Air bubble formation within breaking waves facilitates the conversion of wave energy into turbulent kinetic energy, reducing wave height and intensity. This process mitigates the impact of waves on coastal structures and shorelines. Moreover, breaking waves with air bubble effects significantly impact sediment transport, ecosystem functions, and wave-induced forces in shallow water environments. Accurate modeling of these phenomena is crucial for coastal management and resilient infrastructure design to preserve coastal ecosystems.

This study focused on the role of air bubbles in energy dissipation within irregular waves, aiming to develop a precise model for calculating wave height and set-up during wave breaking. It employed parametric, representative, spectral, and probabilistic approaches to model irregular waves. The research explored the bubble entrainment under spilling and plunging breakers, emphasizing energy dissipation phenomena in unsteady wave dynamics.

Chapter 1 of this study began by presenting the motivation for the research and providing a general background on the dynamics of air bubbles in breaking irregular waves. It then delved into a comprehensive literature review, identifying research gaps that lead to the problem statement, objectives, and research approach.

Chapter 2 provided an experimental overview, detailing the procedures for data collection and data editing. It concluded with a discussion of multiple datasets collected from various sources.

Chapter 3 elaborated on the development of an energy dissipation model for plunging and spilling breakers, integrating the influence of air bubbles using the parametric approach tailored for irregular waves. This model was developed by considering the concept of the fraction of breaking waves.

Chapter 4 explained the adaptation of existing regular wave-breaking models with air bubble effects to irregular waves, resulting in the creation of new models using the representative approach. This method involved the direct transfer of regular wave parameters to characterize irregular wave behavior.

Chapter 5 described the development of the energy dissipation model using the spectral approach, which integrated the concept of fraction of breaking waves with a Weibull distribution.

Chapter 6 discussed the application of a probabilistic approach to formulating a new wave height distribution designed for plunging breaking waves owing to the air bubbles effect. Various wave height parameters were derived from this proposed distribution.

Chapter 7 consolidated the study's findings by addressing the objectives and research questions, while also offering recommendations for future investigations in this field.

Overall, this study focused on computing RMS and significant wave heights using developed models, numerically for irregular bathymetry and analytically for plane-sloping bathymetry. Energy balance equations determined RMS and significant wave height calculations, while the momentum balance equation-controlled wave set-up dynamics. Validation of the models and distributions involved a comprehensive series of experiments, including large-scale, small-scale, and field experiments across various scenarios. Various error analyses indicated that the proposed models, particularly one among them, demonstrated superior performance with lower error indices in comparison to established models and experimental data.

Acknowledgments

First and foremost, I humbly acknowledge the blessings of the Almighty, the Merciful, and the Gracious Allah, whose grace has empowered me to complete this dissertation.

I wish to express my sincere gratitude and utmost respect to my thesis supervisor, **Prof. Dr. Susumu Araki**, for his exceptional guidance, prompt responses, and unwavering encouragement throughout my studies at Osaka University. His invaluable insights and supportive supervision were instrumental in navigating me through the entirety of my research journey. I am truly grateful for his mentorship and expertise, which have been pivotal in shaping my doctoral studies. Additionally, I extend my heartfelt appreciation to Prof. Dr. Masayasu Irie and Assoc. Prof. Dr. Yusuke Nakatani for their thorough review of the thesis.

I am deeply thankful to Prof. Dr. Shin ichi Aoki for his support, invaluable advice, and assistance during my Ph.D. tenure. I also extend my sincere appreciation to Asst. Prof. Yuya Sasaki for his invaluable support throughout my doctoral studies.

I would like to express my gratitude to all the students of the Coastal Engineering Laboratory for their valuable suggestions, cooperation, and assistance during the experimental phase of my research and throughout my Ph.D. journey. Special thanks to Renee, Rajuli, Hisn, Sila, Mew, and Sawada for their unwavering support.

My heartfelt appreciation goes to Prof. Dr. Ashabul Hoque (University of Rajshahi, Bangladesh) for his insightful suggestions, motivation, and contributions during the experimental phase and my Ph.D. tenure.

I am grateful to the Japanese Government (MEXT) for granting me the scholarship, which has been instrumental in supporting my academic endeavors.

Finally, I extend my deepest gratitude to my parents, Md. Joynal Abedin and Most. Kachhiman, my wife, Most. Khadiza Khatun, my daughter, Nusaifa Nur Tanviya, and my siblings, for their unwavering spiritual support, boundless love, nurturing care, invaluable education, philanthropic dedication, and constant encouragement throughout my life journey.

Dedication

I dedicate this dissertation to my parents, wife, and daughter, acknowledging their steadfast love, care, and unwavering support throughout my journey.

List of Publications

Peer-Reviewed Articles

1. **Hossain, M.N.**, Araki, S., 2022. Energy dissipation model for irregular breaking waves owing to air bubbles. Ocean Eng. 266, 112985. https://doi.org/10.1016/j.oceaneng.2022.112985 **[Chapters 2 and 3**
2. **Hossain, M.N.**, Araki, S., 2023. Estimation of air-bubble-induced wave height and set-up using representative wave approach. Coast. Eng. J. 65, 495–513. https://doi.org/10.1080/21664250.2023.2246282 **[Chapters 2 and 4]**
3. **Hossain, M.N.,** Araki, S., 2024. Transformation of significant wave height and set-up due to entrained air bubbles effect in breaking waves. Ocean Model. 190, 102403. https://doi.org/10.1016/j.ocemod.2024.102403 **[Chapters 2 and 5]**
4. **Hossain, M.N.**, Araki, S., Hoque, A., Josiah, N.R., 2024. Wave height distribution for plunging breakers induced by air bubbles. Ocean Eng. 309, 118472. https://doi.org/10.1016/j.oceaneng.2024.118472 **[Chapters 2 and 6]**

Table of contents

List of Figures

List of Tables

List of key symbols and abbreviations

Symbols	Meanings
c	Wave celerity
c_g	Wave group velocity
cm	Centimeter
c_0	Void fraction at still water level
D	Energy dissipation rate e per unit area
$D_{air} = D_a$	Energy dissipation rate per unit area due to air bubbles effect
E	Wave energy
E_f	Wave energy flux
g	Gravitational acceleration
h	Still water depth
h_b	Breaking point still water depth
h_G	Depth of centre of gravity of air bubbles distribution
h_0	Still water depth at offshore point
H	Local individual wave height
$H_{avr} = H_1$	Average wave height
H_b	Wave height at breaking point
H_{max}	Maximum wave height in a wave record
H_{mo}	Spectral significant wave height
$H_{mo,b}$	Spectral significant wave height at breaking point
$H_{mo,0}$	Spectral significant wave height at offshore point
H_0	Wave height at offshore point
H_{rms}	Root-mean-square wave height
$H_{rms,b}$	Root-mean-square wave height at breaking point
$H_{rms,0}$	Root-mean-square wave height at offshore point
$H_s = H_m = H_{\frac{1}{3}}$	Significant wave height
$H_{\frac{1}{10}}$	Average height of the highest one-tenth of waves in a wave record
$\bar{H}$	Mean wave height

k	Wave number
k_0	Empirical coefficient
L	Local wavelength
m	Meter
L_0	Wavelength at the offshore point
N	The total number of waves in a wave record
$P(H)$	Probability of wave height
Q_b	Fraction of all breaking waves
s	Second
S_{xx}	Radiation stress along the *x*-axis
$S_{xx}^{'} = S_{xx}^{''}$	Radiation stress along the *x*-axis due to air bubbles
T	Wave period
T_{rms}	Root-mean-square wave period
$T_{1/3}$	Significant wave period
$\bar{T}$	Mean wave period
t	Time
t_r	Average release time of air bubbles
V	Voltage
V_a	Air volume per unit length and width
w_r	Bubble rise velocity
x	Distance along the flow direction Distance along the still-water surface of the channel
x_{brk}	Distance between wave maker and breaking point
y	Air bubble penetration depth
z	Distance measured perpendicular to the channel bottom Distance measured perpendicular to water level rise
FE	Field Experiment
LS	Large-scale
SS	Small-scale
CDF	Cumulative density function
MWL	Mean water level
PDF	Probability density function
SWL	Still water level

Δh	Water level rise due to entrained air
ΔPE	Potential energy
α	Free parameter
γ	Arbitrary constant
ρ	Density of air-water mixture
ρ_w	Density of water
σ	Surface tension
η	Elevation of water surface
$\bar{\eta}$	Wave set-up/set-down
$\bar{\eta}_b$	Wave set-down at breaking point
$\bar{\eta}'$	Wave set-up/set-down due to air bubble effect

CHAPTER 1

General Introduction

1.1 General

This introductory chapter initiates with the motivation behind the study, followed by an extensive examination of irregular breaking waves. Subsequently, a concise literature review is conducted to identify research gaps, culminating in the delineation of the study's objectives and methodology. Furthermore, the significance of this research is elucidated. Lastly, the abstract concludes with a brief overview of the dissertation structure, summarizing the subsequent chapters.

1.2 Motivation

Located within a low-lying terrain and boasting an extensive coastal stretch (see Fig. 1.01), Bangladesh faces heightened susceptibility to cyclones and storm surges. Annually, the coastal areas of Bangladesh endure numerous cyclonic disturbances, presenting formidable risks to both human lives and essential infrastructure (see Table 1.1).

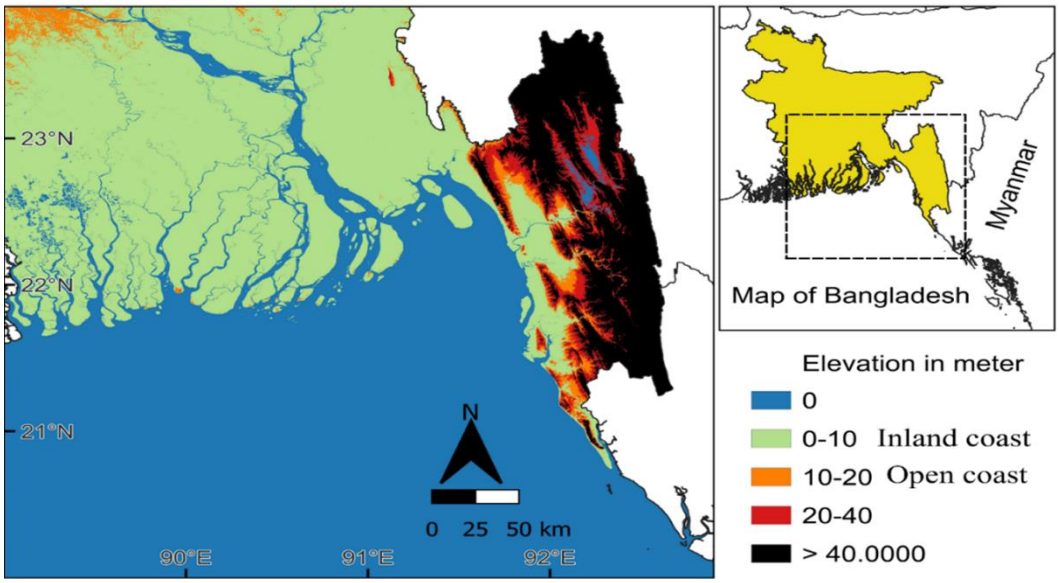

Figure 1.01: Coastal Map of Bangladesh.

The aftermath of these natural calamities often entails substantial loss of life and significant economic damage, encompassing the destruction of vital coastal assets such as residences, transportation networks, and agricultural fields.

Table 1.1: Cyclones with the greatest destructive impact on Bangladesh (Alam, 2023).

Cyclone Name	Year	Wind Speed (km/h)	Loss of Life	Economic Impact (USD)
Bhola	1970	185	300,000+	$86.4 million
Gorky	1991	250	138,866	$1.5 billion
Sidr	2007	240	3,447	$1.7 billion
Aila	2009	120	190	$530 million
Roanu	2016	120	26	$565 million
Amphan	2020	240	118	$13.2 billion
Yaas	2021	155	14	$500 million

It is also noted that the inland coast, located away from the original coastline and often toward the middle of a country, is bordered by other land areas. Unlike coastal regions directly adjacent to the ocean, inland coasts have unique environmental conditions. Residents in these areas may face risks such as flooding during heavy rainfall or riverine flooding, particularly if they are near estuaries or rivers. On the other hand, an open coast refers to a shoreline directly exposed to the open ocean, lacking significant natural barriers like islands or peninsulas. These coasts are characterized by exposure to oceanic elements such as waves, tides, and currents, often experiencing increased wave activity and erosion compared to sheltered or protected coastal areas.

The study of shallow water wave dynamics within the context of Bangladesh is paramount due to a confluence of critical factors. Bangladesh's coastal landscape, characterized by low-lying terrain, underscores its susceptibility to a host of coastal hazards, including cyclones, storm surges, and erosion. With densely populated coastal regions housing a significant portion of the country's populace, comprehending shallow water wave dynamics becomes imperative for not only predicting but also mitigating the adverse impacts of these hazards, thereby safeguarding lives, livelihoods, and essential infrastructure. Furthermore, Bangladesh's coastal zones harbor invaluable ecosystems such as mangroves, wetlands, and fisheries, serving as lifelines for millions

by providing indispensable resources and ecosystem services. The intricate interplay of shallow water wave dynamics profoundly influences sediment transport, water quality,

and the formation of habitats within these ecosystems, underlining the need for a holistic understanding to drive sustainable management and conservation endeavors. In addition, Bangladesh faces heightened vulnerability to climate change, amplifying existing coastal risks through rising sea levels, heightened occurrences of extreme weather events, and shifting precipitation patterns. Shallow water wave dynamics emerge as pivotal factors shaping coastal morphology and responses to climate variability, dictating erosion rates, accretion processes, and the retreat of shorelines. This comprehension forms the bedrock for assessing vulnerability and crafting adaptation strategies aimed at minimizing risks. Lastly, Bangladesh's coastal regions contribute significantly to the nation's economy through key sectors such as fisheries, agriculture, tourism, and port operations. Shallow water wave dynamics exert a tangible influence on navigation, port activities, and the development of coastal infrastructure, thereby directly impacting economic productivity and livelihood opportunities.

Therefore, the study of shallow water wave dynamics in Bangladesh holds immense importance for various aspects of coastal management and ecosystem preservation. By comprehensively understanding these dynamics, coastal hazards can be effectively addressed, adapt to climate change impacts, and foster sustainable development in coastal areas. This holistic approach is crucial for ensuring the safety of coastal communities, conserving vital ecosystems, and enhancing resilience in the face of environmental challenges. So, the research question emerges as outlined in the subsequent subsection.

1.2.1 *Research Question*

How do protect coastal people from natural disasters?

In seeking the answer to this question, potential approaches for safeguarding coastal communities from natural disasters have been identified, including:

1. **Early warning systems:** Implementation of early warning systems to provide timely alerts and evacuation procedures in the event of approaching hazards.

2. **Awareness campaigns:** Conduct awareness campaigns to educate residents about the risks associated with living in coastal areas and the necessary actions to take during emergencies.

3. **Natural defenses:** Utilization of natural defenses, such as mangroves, dunes, and wetlands, to buffer against storm surges, erosion, and flooding.

4. **Land use planning**: Implementation of land use planning measures to regulate development in vulnerable coastal zones, including restrictions on construction in high-risk areas and promoting resilient building practices.

5. **Coastal engineering**: Deployment of coastal engineering solutions, such as seawalls, breakwaters, and beach nourishment, to mitigate the impacts of coastal hazards and stabilize shorelines.

This research highlights **coastal engineering** as the key long-term solution for protecting coastal communities from natural disasters. While early warning systems, awareness campaigns, natural defenses, and land use planning are crucial for short-term preparedness, they may not offer sustainable protection against ongoing coastal threats. Coastal engineering provides durable infrastructure solutions capable of withstanding storms, erosion, and sea-level rise. By focusing on coastal engineering, this research aims to develop effective and sustainable approaches to safeguard coastal areas and enhance resilience to environmental challenges.

1.3 Background

Life on Earth depends entirely on air and water, with our existence intricately intertwined with the surrounding environment. Various environmental challenges profoundly impact societies, encompassing weather patterns and escalating levels of carbon dioxide. Within the realm of coastal dynamics, the phenomenon of air bubble entrainment in irregular breaking waves assumes profound significance and complexity (see Fig. 1.02).

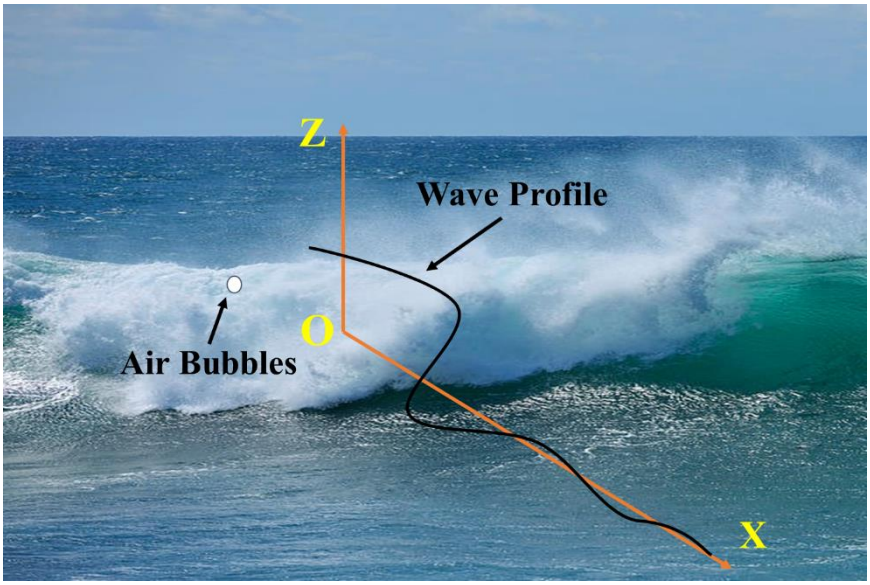

Figure 1.02: A picture of a real ocean wave (irregular wave with breaking) with air bubbles.

When waves approach the coastline, their interaction with diverse bathymetry and coastal terrain leads to irregular breaking, fostering intricate dynamics among air, water, and waves. This process results in the entrainment of air bubbles into the water column, facilitated by turbulent mixing, wave breaking, and the presence of surfactants. The entrapment of air bubbles not only influences the dissipation of wave energy and the attenuation of wave height but also contributes to the formation of whitecaps and foam along coastal regions. Moreover, air bubble entrainment serves a crucial role in mediating gas exchange between the atmosphere and the ocean, thereby impacting fundamental processes like gas transfer and carbon cycling within coastal ecosystems. Hence, unravelling the underlying mechanisms governing air bubble entrainment in irregular breaking waves is imperative for gaining a comprehensive understanding of coastal dynamics and their broader environmental ramifications. In the subsequent subsections, significant topics pertinent to this subject have been thoroughly reviewed.

1.3.1 *Irregular Breaking Waves*

Irregular waves*:* Irregular waves in the ocean lack a consistent or uniform pattern in their shape, size, or timing.

Breaking Waves: Breaking waves are oceanic waves that collapse or rupture upon nearing the shore or encountering shallow water (see Fig. 1.02). This event happens

when the wave crest becomes excessively steep, leading to the wave crest's forward movement surpassing the wave's velocity.

Hence, irregular breaking waves are characterized by their irregular shape and their tendency to meet the conditions for breaking. Irregular breaking waves encompass mainly four types, distinguished by their irregular shapes and breaking behaviour. In Fig. 1.03 below, an overview of these types is provided.

Types	Sketch and Examples	Description
Spilling		Highly steep waves interacting with gentle slopes caus the wave crest to destabilize, spilling water and trapping air bubbles, resulting in foamy water formation.
Plunging		The wave's face steepens, curls, and plunges forward, trapping air. It's common with moderately steep waves on moderate slopes.
Collapsing		The wave crest steepens vertically until its base collapses, reaching the shoreline as a thin layer of water. This occurs at low steepness on steep slopes.
Surging		The wave crest remains intact, and the wave reaches the shoreline with minimal shape changes. This phenomenon occurs with very low steepness on very steep slopes.

Figure 1.03: Various types of breaking waves (Diagrams & Pictures: Hedges, (2003)).

Therefore, depending on the breaking process, another question arises: **What are the primary factors contributing to the dissipation of energy in irregular breaking waves within the surf zone?**

In the pursuit of comprehending wave energy dissipation in the surf zone, several pivotal factors have been pinpointed. These encompass bottom topography, air bubble entrainment within breakers, sediment transport, and turbulence. The intricate interaction of these elements influences how wave energy is transferred and attenuated along coastal areas. This comprehension bears great significance for coastal engineers, researchers, and policymakers tasked with safeguarding against coastal hazards and conserving ecosystems. By delving into the mechanisms governing wave energy

dissipation, the capacity to anticipate and adjust to the dynamic coastal environment can be enhanced. Building upon the preceding discussion, a further inquiry emerges:

How do calculate the energy of irregular breaking waves?

To address this question, delving into a literature review is conducted in the following section.

1.3.2 *Literature Review*

In the realm of wave energy within the surf zone, researchers invest significant efforts in developing energy dissipation models. These models aim to quantify the mechanisms through which wave energy disperses in coastal environments. By scrutinizing factors such as wave-breaking patterns, bottom topography, turbulence, and vegetation presence, researchers construct mathematical models that simulate wave energy dissipation across time and space. In recent years, extensive research and experimentation have sought to enhance these models. Given the intricate nature of the wave-breaking process, all models for calculating energy dissipation rely on empirical or semi-empirical methods validated through experimental data. The majority of these models are grounded in three primary concepts: the bore concept, the stable energy concept, and the air bubble entrainment concept. Bore models, initially proposed by Le Mehaute, (1962), posited that the energy dissipation of broken waves mirrors that of a hydraulic jump. Subsequent versions by Battjes and Janssen, (1978) and Thornton and Guza, (1983) refined this approach. Dally et al., (1985) introduced an energy dissipation model based on stable energy, while Swift, (1993) and Rattanapitikon and Shibayama, (1998) further developed their models by incorporating this concept with modifications. Regarding the air bubbles concept, Hoque, (2002) pioneered an energy dissipation model that accounted for the influence of air bubbles on regular waves. Subsequent research has delved further into this concept, with various studies exploring its implications for regular waves, such as Hossain et al., (2022) proposed a wave distribution model considering the effect of air bubbles. The influence of air bubbles, turbulence, and bottom friction was investigated by Hoque et al., (2021). Additionally, Hoque et al., (2019) theoretically and experimentally explored the characteristics of wave height, wave set-up, and wave energy dissipation due to air bubbles in the surf zone. A concise overview of energy dissipation models is presented in Table 2.

Table 1.2: A short overview of the different energy dissipation models.

Authors	Models	Constraints	Types	Concepts
Battjes and Jenssen, (1978)	$D = 0.47\frac{\rho g H^2}{4T}$	H & $\bar{\eta}$	Regular	Bore
Thornton and Guza, (1983)	$D = 0.67\frac{\rho g H^3}{4Th}$	H	Regular, Irregular	Bore
Dally et al., (1985)	$D = 0.15\frac{\rho g c_g}{8h}\left[H^2 - \frac{4}{25}h^2\right]$	H & $\bar{\eta}$	Regular	Stable energy
Deigaard et al., (1991)	$D = 0.48\frac{\rho g h H^3}{(4h^2 - H^2)T}$	H	Regular	Stable energy
Rattanapitikon, (1998)	$D = 0.15\frac{\rho g c}{8h}\left[H^2 - \left\{he^{\left(-0.36-\frac{1.25h}{\sqrt{LH}}\right)}\right\}^2\right]$	H	Regular, Irregular	Stable energy
Rattanapitikon, (2003)	$D = 0.15\frac{\rho g c_g}{8h}[H^2 - \{0.073Ltanh(kh)\}^2]$	H	Regular, Irregular	Stable energy
Hoque, (2002)	$D = \alpha\rho_w g V_a w_r$	H & $\bar{\eta}$	Regular	Air bubble
Hoque et al., (2019)	$D = \alpha\rho_w g\frac{y}{2}\frac{c_0}{(1-c_0)}w_r$	H & $\bar{\eta}$	Regular	Air bubble

In Table 1.2, the models devised to incorporate the influence of air bubbles in the surf zone were specifically designed for regular breaking waves. However, it's widely recognized that wave breakers in irregular waves present a more complex scenario compared to those in regular waves. Irregular waves lack distinct breakpoints, and their energy dissipates over a broader expanse than regular waves. Consequently, the interaction between irregular waves and air entrainment in shallow water is a significant and intriguing phenomenon. Thus, the following research gap is identified for this study.

1.3.3 *Research Gap*

- ❖ Existing wave models in coastal engineering predominantly rely on bore and stable energy concepts, which are suitable for regular waves but may not be as effective for irregular waves.

- ❖ Many existing models in coastal engineering are inadequate in accurately calculating wave set-up.
- ❖ Currently, there are no existing models that incorporate the air bubble concept to accurately simulate irregular waves.

Now, the inquiry arises: **How can formulate an energy dissipation model for irregular breaking waves that takes into account the influence of air bubbles?** Following this, a succinct summary of the response to this question is presented in the subsequent section.

1.3.4 *Methodology*

In addressing the challenge of developing such a model, researchers have identified four main approaches: parametric, representative, spectral, and probabilistic (see Fig. 1.04). These approaches offer diverse perspectives on modeling the intricate dynamics of wave breaking in irregular conditions and can contribute to enhancing the comprehension of wave behavior in the surf zone. Following this, a brief summary of these methods is presented below:

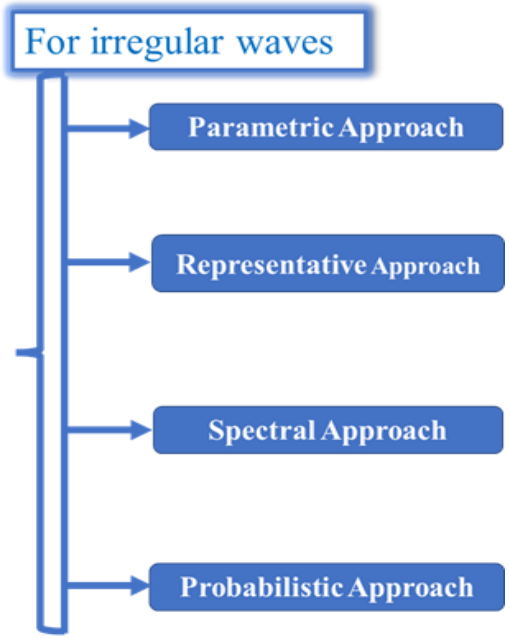

(a)

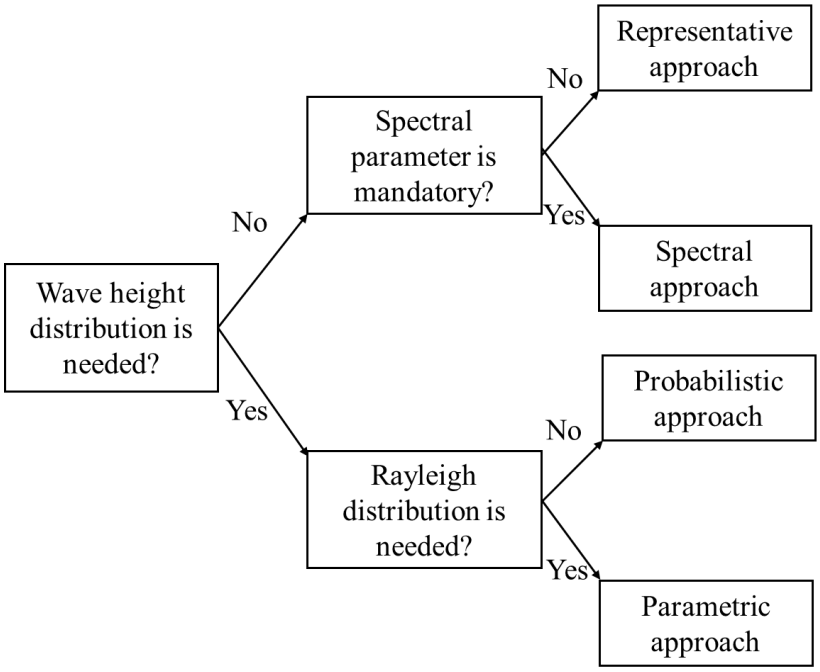

(b)

Figure 1.04: (a) Different approaches for constructing a model to dissipate energy from irregular breaking waves, (b) The fundamental differences among the methods in terms of wave height.

Parametric approach

The parametric approach characterizes the energy dissipation rate through time-averaged parameters, focusing on the macroscopic characteristics of breaking waves and primarily predicting the transformation of the root-mean-square wave height. This method is particularly suitable when a detailed wave height distribution is unnecessary. Research on this approach can be divided into two categories based on assumptions regarding the probability density function (PDF) of wave height in the surf zone. The first category assumes the validity of the Rayleigh pdf in the surf zone, where the average energy dissipation rate is described by integrating the product of the energy dissipation of a single broken wave and the probability of breaking wave occurrence. The second category comprises a semi-analytical model that does not rely on assumptions about the pdf in the surf zone. In this model, the average energy dissipation rate is calculated by summing up the dissipation of each broken wave component and

dividing it by the total number of waves (Larson, 1995; Battjes and Janssen, 1978; Thornton and Guza, 1983; Baldock et al., 1998; Rattanapitikon and Shibayama, 1998).

Representative wave approach

The representative wave approach is a method that entails the direct application of regular wave formulas to examine irregular waves, leveraging representative wave parameters (Rattanapitikon, 2008; Rattanapitikon et al., 2003). This approach is valued for its simplicity and straightforwardness, as it doesn't require making assumptions about the PDF of wave heights. By utilizing representative parameters, this approach provides a practical means of analyzing irregular wave behavior without delving into complex statistical considerations.

Spectral approach

Underlying the spectral approach is the assumption that irregular wave trains encompass a diverse range of wave heights with varying frequencies, constituting what is known as the wave spectrum. This methodology involves decomposing the incident spectrum into multiple component waves. Subsequently, the propagation of each wave component is determined using an appropriate regular wave model. Through linear superposition, the wave spectrum at a specific location is obtained by aggregating the simulation results from all individual wave components (Izumiya and Horikawa, 1987; Isobe, 1987; Panchang et al., 1990; Grassa,1990).

Probabilistic approach

The probabilistic approach primarily focuses on statistical analysis and involves studying the propagation of individual waves in the time domain. Initial individual waves can be obtained from irregular wave records or the PDF of wave height. These waves are subsequently propagated independently towards the shore using an appropriate regular wave model, with no interaction assumed between waves. By combining the simulation results of all individual waves, a new PDF can be constructed at the desired location. This method proves particularly useful when a detailed wave height distribution is required (Dally, 1990; Medez et al., 2004; Jadav and Chen, 2013; Hossain et al., 2022).

After an extensive literature review on energy dissipation calculation in the surf zone and methodologies for developing energy dissipation models, the objective has been defined in the subsequent section.

1.4 Research Objectives

Main Objective: To develop the energy dissipation model considering the influence of air bubbles on irregular breaking waves.

The provided flowchart displays the comprehensive objective of this study:

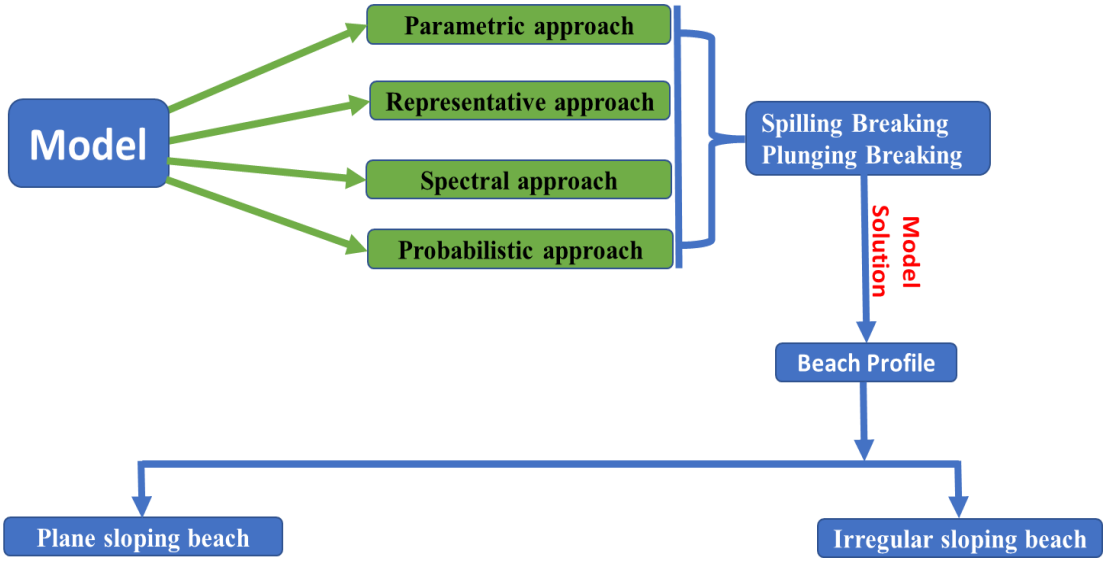

Figure 1.05: Specific aim of the study.

Utilizing the methodology outlined above (refer to Fig. 1.05), this study endeavors to formulate energy dissipation models applicable to both spilling and plunging breaking wave conditions. Subsequently, the developed models will be applied to uniform plane-sloping bathymetry as well as irregular bathymetry. Additionally, a series of experiments has been planned to validate the efficacy of the developed models.

1.5 Research Significance

The entrainment of air bubbles into irregular breaking waves is driven by a combination of turbulent mixing, wave breaking, and the presence of surfactants in the water. As irregular waves approach the coastline and interact with varying bathymetry and coastal features, they undergo breaking, generating turbulent vortices and eddies within the water column. These turbulent motions draw air from the atmosphere downward into the water, where it becomes incorporated into the breaking waves.

Moreover, surfactants present in the water, such as organic matter and dissolved gases, can influence this process by reducing the surface tension of the water. This reduction in surface tension facilitates the formation of air bubbles, which are then entrained into the water column during wave breaking. The entrainment of air bubbles has multifaceted effects, and the air bubble model is crucial in coastal engineering and wave dynamics for several key reasons:

Energy dissipation calculation: The presence of air bubbles within breaking waves significantly impacts the dissipation of wave energy in the surf zone. Understanding the behavior of these bubbles is essential for accurately modeling energy dissipation processes.

Wave dynamics: Air bubbles influence wave-breaking patterns and turbulence in the surf zone, affecting sediment transport, coastal erosion, and wave transformation. Incorporating air bubble dynamics into wave models enhances their predictive accuracy.

Coastal hazard mitigation: Reliable wave models are vital for effective coastal hazard mitigation, including flood forecasting and shoreline protection. Accounting for air bubble effects in these models improves their ability to simulate wave behavior and enhance hazard assessment and management strategies.

Environmental impact: Air bubble entrainment in breaking waves plays a significant role in gas exchange between the ocean and atmosphere, nutrient cycling, and pollutant distribution. Understanding the role of air bubbles in these processes is critical for evaluating and mitigating environmental impacts.

Energy conversion*:* Utilizing the air bubble model can enhance the efficacy of wave energy converters in coastal areas by precisely forecasting the energy dissipation resulting from wave breaking.

Sediment transport estimation*:* Incorporating air bubble effects on wave-induced turbulence, the model can supply more precise evaluations of sediment transport rates along coastlines.

***Deeper insight into surf zone dynamics**:* By accurately predicting wave-breaking patterns and energy dissipation, the air bubble model deepens the understanding of the intricate dynamics within the surf zone.

***Optimized coastal structure design**:* Accurate modeling of wave energy dissipation facilitates the design of coastal structures better equipped to withstand extreme wave conditions, enhancing their resilience and functionality.

Understanding the complexities of air bubble entrainment in irregular breaking waves is pivotal for coastal dynamics, marine ecology, and atmospheric chemistry. It bears significant implications for managing coastal environments and forecasting climate change impacts on coastal regions. In essence, the air bubble model enhances the understanding of coastal wave dynamics, fostering applications in engineering, hazard mitigation, and environmental preservation.

Finally, the chapter concludes by providing a comprehensive overview of this dissertation in the following section.

1.6 Dissertation Structure

This dissertation comprises seven chapters, arranged as follows:

Chapter 1 lays out the motivation, background, and literature review concerning the energy dissipation model, encompassing various methodologies. It identifies research gaps, establishes objectives, and discusses the significance of this research. Additionally, this chapter provides a succinct introduction to the outline of each subsequent chapter.

Chapter 2 examines a series of experimental inquiries concerning both regular and irregular waves. It encompasses detailed discussions on the wave tank specifications, equipment, and setup procedures. Additionally, it elucidates the process of collecting raw data and transforming it into irregular wave data using the zero-up crossing method and irregular waves formula. Furthermore, the chapter addresses the collection of numerous datasets from external sources, providing comprehensive insights into the research methodology employed.

Chapter 3 delves into the parametric wave approach, aiming to devise a novel energy dissipation model considering the influence of air bubbles on plunging and spilling breaking waves. This model incorporates the phenomenon of the ' probability of fraction of breaking wave'. The energy balance equation was utilized to compute the root mean square (RMS) wave height, while wave set-up calculation relied on the momentum balance equation. The FFD technique was utilized to solve the developed model for irregular bathymetry, while analytical solutions were derived for plane-sloping bathymetry. At the end of the chapter, an error analysis was conducted to compare the proposed model with other existing models using experimental data. The validation process involved a comprehensive range of test scenarios, encompassing small-scale, large-scale, and experimental field data.

In **Chapter 4**, the representative wave approach is explored to devise two novel energy dissipation models tailored for calculating RMS wave height (H_{rms}) and set-up, while considering the impact of air bubbles. Firstly, two established regular wave models were studied. Subsequently, in the pursuit to extend these models to irregular waves, two novel energy dissipation models denoted M-I and M-II were developed. While M-I provided an analytical solution applicable to uniformly plane-sloping beaches, the absence of an analytical solution for irregular bathymetry led us to employ the forward finite difference technique for both spilling and plunging breakers. Despite the absence of an analytical solution for M-II, applied the same numerical technique to address this scenario. Finally, a comprehensive error analysis was conducted of the results with existing models, utilizing different experimental data.

Chapter 5, the spectral approach is delved into, aiming to devise two innovative energy dissipation models for computing spectral significant wave height (H_{mo}) and set-up, considering the influence of air bubbles. Initially, two existing regular wave models are scrutinized. Subsequently, leveraging the concept of the fraction of breaking waves, formulated two new energy dissipation models labeled as M-I and M-II. Spectral significant wave height computation relied on energy balance equations, while wave set-up determination employed momentum balance equations. The developed models are solved using the forward finite difference technique for both spilling and plunging breakers. Finally, conducted a comparative error analysis (P20, RMSRE, and BSS) of

the present models with other models using the author's experimental data, and data collected from other sources at the end of this chapter.

Chapter 6 explores the probabilistic approach, commencing with a review of various shallow water wave height distribution models. Subsequently, a novel PDF and corresponding Cumulative Distribution Function (CDF) are introduced for plunging breaking waves, considering the influence of air bubbles. The chapter further elaborates on the derivation of several key statistical parameters from the newly proposed distribution. Additionally, the relationship between the void fraction and the decay coefficient of the distribution is examined, revealing a proportional correlation, while an inverse-proportional relationship is observed between the scale parameter and the decay coefficient. Moreover, the interrelation between the decay coefficient and scale parameter transforms the distribution into a one-parameter distribution. Finally, at the conclusion of the chapter, an error analysis, including RMSRE, P10, and P20, was performed to validate the proposed model against other models using experimental data.

Lastly, **Chapter 7** encapsulates the findings and conclusions drawn from this research endeavor. It also outlines further research needs pertaining to air bubble entrainment into breaking waves and highlights the limitations of this investigation, along with recommendations for addressing them.

CHAPTER 2

Experiment and Data Collection

2.1 Abstract

This chapter presents an overview of the experimental setup, equipment configuration, wave conditions, and data editing procedures employed in the study. Additionally, to enhance the accuracy of the developed models, data from other authors were also collected, and a concise description of these datasets is provided. Through a comprehensive examination of the experimental framework, including the instrumentation and environmental conditions, this chapter lays the foundation for the subsequent analysis and interpretation of results.

2.2 Experiment and Setup

2.2.1 Wave Flume

Between November 2nd and 12th, 2023, experiments were conducted at the wave flume located in the S2 building of the Graduate School of Osaka University, Japan. The primary objective of these experiments was to investigate the dynamics of cross-shore hydrodynamics and air bubble behavior within breaking waves. The experimental setup comprised a compact wave tank measuring 20 meters in length, 0.7 meters in width, and 1.0 meters in depth. The following Table 2.1 provides a concise overview of the flume.

Table 2.1: A short summary of the flume.

Flume structure	Plexiglas and metal frame
Slope Equipment	Wood and Steel
Length	20 m
Width	0.70 m
Height	1 m
Absorber	3 m
Wave Maker	Piston Type
Slope Start	12 m

The flume was positioned horizontally, with glass panels serving as sidewalls along the breaking zone, supported by a metal frame. Additionally, a 5-meter-long sloping beach profile, constructed from wood and steel with a slope ratio of 1/10, was attached to the flume.

2.2.2 Instrument and Wave Generation

Data were collected using capacitance-type wave gauges positioned at 9 cross-shore locations to measure water surface elevation (see Fig. 2.01). These gauges underwent daily calibration by adjusting the water level in the wave flume to establish a linear relationship between wave amplitude and output voltage. Throughout the experiment, the beach remained stationary. Both regular and irregular waves were generated, with the study comprising three key tests, including two under irregular wave conditions.

For the generation of irregular waves, the author employed the JONSWAP spectrum proposed by Hasselmann et al. (1973), with a spectral width parameter set to 3.3. The experimental campaign consisted of 24 cases, with incident spectral wave heights ranging from 6.8 cm to 9.30 cm. Spectral peak periods varied between 1.72 s and 1.19 s. The water depth was consistently set at 30 cm for all cases.

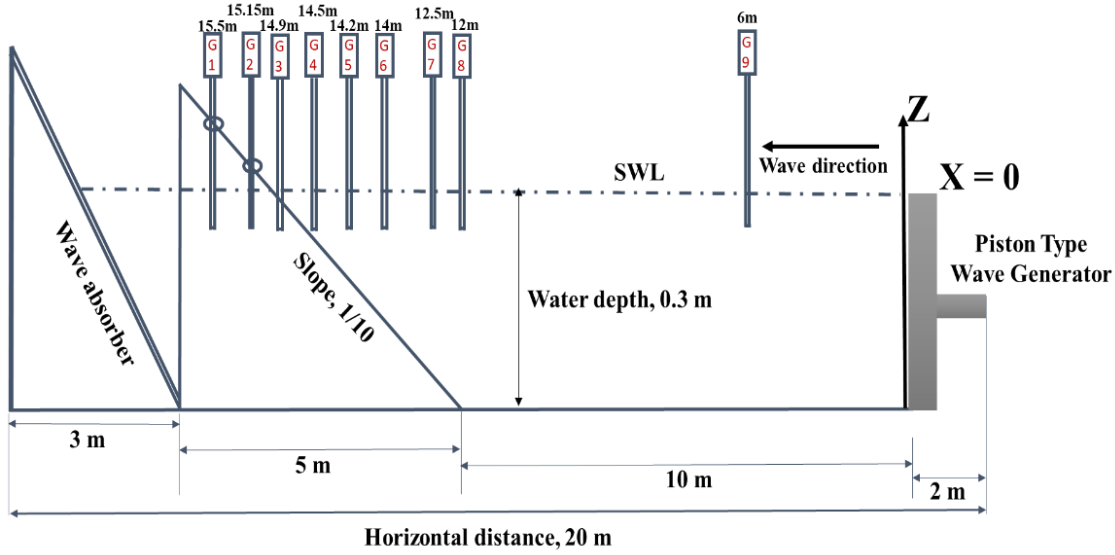

Figure 2.01: A schematic diagram (2-D) of the experiment.

2.3 Data Editing

An abbreviated overview of the data editing process is depicted in Fig. 2.02 (a). Initially, the data was recorded in voltage form, reflecting the measurements obtained from the capacitance-type wave gauges. To facilitate analysis and interpretation, a conversion process was employed, utilizing the calibration coefficient to transform the voltage readings into corresponding measurements in centimeters (cm). Following this conversion, the zero-up crossing method, a commonly used technique in wave analysis, was applied. This method enabled the extraction of individual wave heights and periods from the converted data, thereby providing essential parameters for further analysis (see an example in Fig. 2.02 (b)).

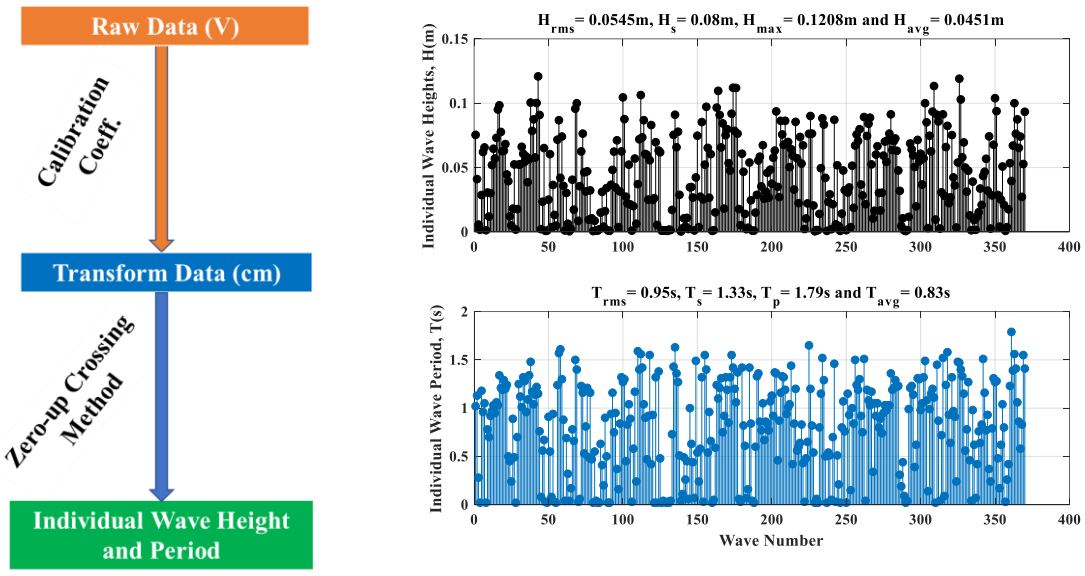

(a) (b)

Figure 2.02: Illustration of the data editing process, comprising two main steps: (a) Converting the recorded data into individual wave heights and periods, and (b) presenting an example of the converted wave heights and periods.

2.3.1 Conversion to Irregular Waves Parameters

Transforming individual wave parameters into irregular wave parameters is a pivotal aspect of wave analysis and comprehension. Individual parameters like wave height, period, and direction provide valuable insights into specific waves within a dataset. However, to accurately characterize the overall wave climate, it's essential to

transform these parameters into irregular wave parameters such as significant wave height and significant wave period. This conversion process is crucial for facilitating a more comprehensive assessment of wave conditions, empowering researchers and engineers to evaluate wave energy, climate trends, and design criteria for marine structures and coastal protection measures. In this study, the following formulas (S. A. Hughes, 1993; Bosboom and Stive, 2023) were applied to convert individual wave parameters into irregular wave parameters, as illustrated in an example at the top of Fig. 2.02 (b).

Mean Wave Height:

$$\bar{H} = \frac{1}{N}\sum_{i=1}^{N} H_i, \tag{2.01}$$

Root-mean-square (RMS) Wave Height:

$$H_{rms} = \sqrt{\frac{1}{N}\sum_{i=1}^{N} H_i^2}, \tag{2.02}$$

Significant Wave Height:

$$H_{1/3} = \textit{average height of the highest 1/3 of the waves} \tag{2.03}$$

Mean Wave Period:

$$\bar{T} = \frac{1}{N}\sum_{i=1}^{N} T_i, \tag{2.04}$$

Root-mean-square (RMS) Wave Period:

$$T_{rms} = \sqrt{\frac{1}{N}\sum_{i=1}^{N} T_i^2}, \tag{2.05}$$

Significant Wave Period:

$$T_{1/3} = \textit{average period of the highest 1/3 of the waves} \tag{2.06}$$

Set-down:

$$\bar{\eta} = -\frac{1}{16}\frac{H^2}{h}, \tag{2.07}$$

Set-down at breaking point:

$$\bar{\eta}_b = -\frac{1}{16}\gamma H_b, \tag{2.08}$$

Set-up:

$$\bar{\eta} = \bar{\eta}_b + \frac{3}{8}\gamma^2(h_b - h), \tag{2.09}$$

Set-down at shore:

$$\bar{\eta}_{shore} = \bar{\eta}_b + \frac{3}{8}\gamma H_b, \tag{2.10}$$

where N is the total number of waves in the record, H is the individual wave height, T is the individual wave period, $\gamma = \frac{H_b}{h_b}$ is the wave-breaking index, H_b is the breaking point wave height, h is the still water depth and h_b is the breaking point still water depth.

2.4 Collected Other Experimental Data

The collected data is classified into three categories: small-scale (SS), large-scale (LS), and field experimental data (FE) which covers a wide range of wave and bottom topography conditions. Table 2.2 provides a summary of the gathered laboratory data. The following section covers a brief description of the collected data sets:

Table 2.2: A concise overview of the wave height data collected from different experimental settings, encompassing SS, LS, and FE.

Data Sources	Acronym	Beach Types	Data Types
Ting, (2001)	Ti-01	Plane	SS
Smith and Seabergh, (2001)	SS-01	Barred and Plane	SS
Grasmeijer and Rijn, (1999)	GR-99	Sandy	SS
Sultan, (1995)	Su-95	Plane	SS
Smith and Kraus, (1990)	SK-90	Barred and Plane	SS
Hurue, (1990)	Hu-90	Plane	SS
Dette et al., (2002)	DPN-02	Sandy	LS
Roelvink and Reniers, (1995)	RR-95	Sandy	LS

Kraus and Smith, (1994)	KS-94	Sandy	LS
Smith et al., (1993)	SLK-93	Sandy	FE
Kraus et al., (1989)	KGR-89	Sandy	FE
Thornton and Guza, (1986)	TG-86	Sandy	FE

2.4.1 Small-Scale Data

A study was conducted by Ting, (2001) to explore wave and turbulence velocities within a broad-banded irregular wave in the surf zone. The research was carried out in a wave flume measuring 37 meters in length, 0.91 meters in width, and 1.22 meters in depth. The flume featured a 1/35 slope, and a false bottom made of marine plywood was used to simulate a plane beach. Irregular waves were generated using the TMA spectrum (Bouws et al., 1985), with a spectral peak period of 2.0 seconds, an RMS wave height of 0.106 meters, and a spectral width parameter of 3.3. Resistance-type wave gauges were deployed to measure water surface elevations at seven cross-shore positions.

Smith and Seabergh, (2001) experimented in the 3D Idealized Inlet Laboratory, employing a steady ebb current to investigate wave breaking on a current through physical-model measurements. The study encompassed both regular and irregular waves. The experimental tank was 99 m in length, 46 m in width, and 0.6 m in depth. Waves were generated using the Texel, Marsen, and Arsloe (TMA) spectral form, as proposed by Bouws et al. (1985), with a gamma value of 3.30. The wave conditions included zero moment wave heights of 3.7 cm and 5.5 cm, and peak spectral periods of 0.7 s and 1.4 s. A total of eleven wave gauges were strategically positioned to measure water surface elevations accurately.

At the Laboratory of Fluid Mechanics at Delft University of Technology, Grasmeijer and Rijn, (1999) experimented using a flume that measured 45 meters in length, 0.8 meters in width, and 1.0 meters in depth. The flume was equipped with a remote-controlled rail-guided transport system. To generate irregular waves, the JONSWAP spectrum (Hasselmann et al., 1973) was used, with a peak spectral period of 2.3 seconds (± 0.2 seconds). Two test series, labeled Series B1 and B2, were carried out, with root-mean-square wave heights of 0.113 meters and 0.1134 meters, respectively.

An experiment was conducted by Sultan, (1995) in a two-dimensional wave tank with a sloping beach attachment on one side. Water surface elevation was measured extensively at 12 cross-shore locations throughout the wave tank using resistance-type wave gauges. Irregular waves were generated based on the Bretschneider–Mitsuyasu spectrum (Bretschneider, 1968; Mitsuyasu, 1970), with an incident root-mean-square wave height of 0.074 meters and a wave period of 1.4 seconds.

Hurue, (1990) experimented to investigate wave as well as undertow celerity on a uniform plane-sloping beach. The experiment was conducted in a small-scale wave flume measuring 17 meters in length and 0.5 meters in width. The beach featured a uniform slope of 1/20 with a smooth bottom. Irregular waves were generated based on the Bretschneider–Mitsuyasu spectrum (Bretschneider, 1968; Mitsuyasu, 1970), with an incident root-mean-square wave height of 0.064 meters and a wave period of 1.26 seconds. Water surface elevations were measured at seven cross-shore locations using a capacitance-style gauge.

An experiment by Smith and Kraus (1990) was conducted in a small wave flume measuring 45.70 meters in length, 0.46 meters in width, and 0.91 meters in depth, to examine the macro-features of breaking waves over bars and artificial reefs. The study employed both regular and irregular waves, with 12 trials dedicated to the irregular waves. For the plane beach and bar configurations, three irregular wave conditions were set up. The JONSWAP spectrum (Hasselmann et al., 1973) was used to generate the irregular waves, featuring a spectral width parameter of 3.3 and peak wave periods of 1.07 seconds, 1.56 seconds, and 1.75 seconds. The incident root-mean-square wave heights were 0.085 meters, 0.106 meters, and 0.099 meters, respectively. Water surface elevations were recorded using resistance-type wave gauges at eight cross-shore locations.

2.4.2 Large-Scale Data

As part of the SAFE project from 1998, Dette et al., (2002) experimented to advance design techniques and assess performance for beach nourishment. This study included four main actions, one of which was performed in a large-scale wave flume. In this experiment, a 250-meter sandy beach was established within a wave tank measuring 300 meters in length, 5 meters in width, and 7 meters in depth. The

experiment was organized into two primary phases, with Phase I (cases A, B, C, and H) focusing on examining beach profile changes with various slope adjustments. Bruun, (1954) technique was tapped to apply the equilibrium beach form $\left(d = 0.12x^{\frac{2}{3}}\right)$. In the second phase of the experiment, the sediment transport behavior of mounds, both with and without structural support, was investigated in cases D, E, F, and G. Irregular waves were generated using the TMA spectrum (Bouws et al., 1985). The experiments were conducted under both normal and storm-wave conditions. Water surface elevations were measured at 27 cross-shore locations using resistance-type wave gauges along a 175-meter stretch of the wave tank barrier, with a slope ranging from 0.010 to 0.018.

Roelvink & Reniers, (1995) experimented to accumulate data to validate the energy dissipation model. In the sandy beach wave flume experiment, a total of 95 cases were completed, resulting in 923 data points. The spectral peak periods varied from 3.0 to 12.0 seconds, with the spectral width parameter around 3.3, and the incident RMS wave height ranged between 0.5 and 0.7 meters. Water surface elevations were recorded at ten cross-shore locations using resistance-type wave gauges.

Between August 5 and 13, 1992, Kraus and Smith, (1994) conducted the SUPERTANK data collection project at Oregon State University to examine cross-shore hydrodynamics and sediment transport processes. The experiment utilized a large wave tank that was 104 meters long, 3.7 meters wide, and 4.6 meters deep, featuring a 76-meter-long sandy beach profile. Both regular and irregular waves were generated during the experiment. A total of 20 primary tests were conducted, with 14 of these tests focusing on irregular wave conditions. The TMA spectrum (Bouws et al., 1985) was used to create the irregular wave conditions. In total, 128 cases involving wave and beach conditions were performed, yielding 2047 wave records. The incident RMS wave heights ranged from 0.14 to 0.71 meters, while the spectral peak periods varied from 3.0 to 10.0 seconds, and the spectral width parameter ranged between 3.3 (broad-banded spectra) and 100 (narrow-banded spectra). Water surface elevations were measured using resistance-type wave gauges at 16 cross-shore locations.

2.4.3 Field Data

The **DELILAH** field data collection project, led by Smith et al., (1993), was conducted on a long sandy barrier island beach at the U.S. Army Engineer Waterways

Experiment Station in Duck, North Carolina, from October 1 to 19, 1990. On October 14, measurements were taken to estimate parameters such as RMS wave height, average longshore velocity, and average wave setup. Data on wave paths and peak wave periods were gathered using an 8-meter array, which captured 8 different instances corresponding to 8 specific periods. The results showed RMS wave heights between 0.65 and 0.94 meters and peak wave periods ranging from 9.7 to 12 seconds.

In September and October 1985, the DUCK85 field data collection project, led by Kraus et al., (1989), focused on gathering data near Duck, North Carolina, on the Outer Banks barrier islands. Measurements were taken for 12 instances associated with 8 specific wave periods at the array. The collected data showed RMS wave heights ranging from 0.23 to 0.86 meters and peak periods between 9 and 15.3 seconds.

Between January 30 and February 23, 1980, an experiment led by Thornton and Guza, (1986) was conducted to collect field data on wave hydrodynamics at Leadbetter Beach in Santa Barbara, California. The study measured the nearshore slope, which varied from 0.03 to 0.06, with RMS wave heights ranging from 0.29 to 0.61 meters and peak wave frequencies from 0.063 to 0.09 per second.

2.4.4 Wave Set-Up Data

For the wave set-up experimental data, Raubenheimer et al., (2001); Stive, (1985); and Battjes and Janssen, (1978) experiments were contemplated. A short explanation of the tests is shown in Table 2.3.

Table 2.3**:** A summary of the wave collected set-up data.

Data Sources	Acronym	Beach Types	Data Types
Raubenheimer et al., (2001)	RGS-01	Sandy	FE
Stive, (1985)	St-85	Plane	SS
Battjes and Janssen, (1978)	BJ-78	Plane	SS

From September to November 1997, Raubenheimer et al. (2001) conducted an experiment to collect field data on a sandy beach along the Atlantic Ocean near Duck, North Carolina, USA. Data were gathered during both high-tide and low-tide conditions. Beach profiles were measured at 11 cross-shore locations using resistance-type wave

gauges. On September 13, they recorded wave heights ranging from 0.27 to 1.1 meters, wave setup from -0.05 to 0.1 meters during low tide, and wave heights from 0.5 to 1.2 meters, wave setup from -0.05 to 0.05 meters during high tide.

An experiment was conducted by Stive, (1985) to validate a random wave-breaking model, using a uniform plane sloping coast with a slope of 1:40. The wave tank used for the experiment measured 55 meters in length, 1.0 meters in width, and 1.0 meters in depth. Random waves were generated by piston-type wavemakers, with initial RMS wave heights of 0.14 meters, a peak period of 1.58 seconds, and a wave steepness of 0.038.

At the Fluid Mechanics Laboratory, Civil Engineering Department, Delft University of Technology, Battjes and Janssen, (1978) conducted an experiment using a wave tank measuring 45 meters in length, 0.8 meters in width, and 1 meter in depth. The setup included a hydraulically focused random-wave maker and featured two beach profiles: one with a slope of 1:20 and another with an ideal bar-trough shape, incorporating two plane slopes (1/20) and a 4.4-meter-long plane slope (1/40) towards the shoreline. The tests conducted in this setup recorded deep water RMS wave heights between 0.113 and 0.157 meters, with frequencies ranging from 0.407 to 0.544 Hz.

2.5 Conclusion

In conclusion, this chapter meticulously outlined the experimental setup, equipment configuration, and data editing procedures utilized in the study, alongside a detailed overview of the wave conditions. Furthermore, the incorporation of additional datasets from other authors was aimed at bolstering the accuracy of the models developed in this study. The thorough examination of the experimental framework, encompassing instrumentation and environmental factors, establishes a robust foundation for the subsequent analysis and interpretation of results.

CHAPTER 3

Parametric modeling of energy dissipation for irregular breaking waves with air bubbles

3.1 Abstract

In this chapter, an irregular energy dissipation model for both plunging and spilling breaker waves has been developed based on the influence of air bubbles. This model applies the probability of wave breaking to its formulation. It has been solved numerically for irregular beaches and analytically for beaches with a plane slope. The root mean square (RMS) wave height and wave setup are determined using energy and momentum balance equations, respectively. Validation of the model involved testing across numerous scenarios, including small-scale, large-scale, and field data experiments. The results demonstrate that this model produces lower normalized RMS errors (NRMSE) in predicting RMS wave height and wave setup compared to other models and various types of experimental data.

3.2 Introduction

To address various coastal engineering challenges, such as the design of coastal structures and the analysis of beach erosion, accurate information on wave characteristics in the surf zone is essential. As waves approach the shore, they increase in height and decrease in wavelength until they break. At the point of breaking, air bubbles are introduced into the water (see Fig. 3.01), converting the wave's energy into turbulence and heat, which leads to a reduction in wave height as it moves toward the shore. Irregular breaking waves are more complex than regular ones; unlike regular waves, irregular waves lack distinct breakpoints. Typically, the largest waves break farther from the shore (Rattanapitikon and Shibayama, 1998). Consequently, irregular waves dissipate energy over a broader area compared to regular waves. This phenomenon, involving both irregular waves and air bubble entrainment in shallow water, is crucial for understanding wave behavior in the surf zone. Accurate assessment of wave loading on coastal structures, sediment transport, wave setup, wave run-up, and wave overtopping requires a focus on the area where waves break.

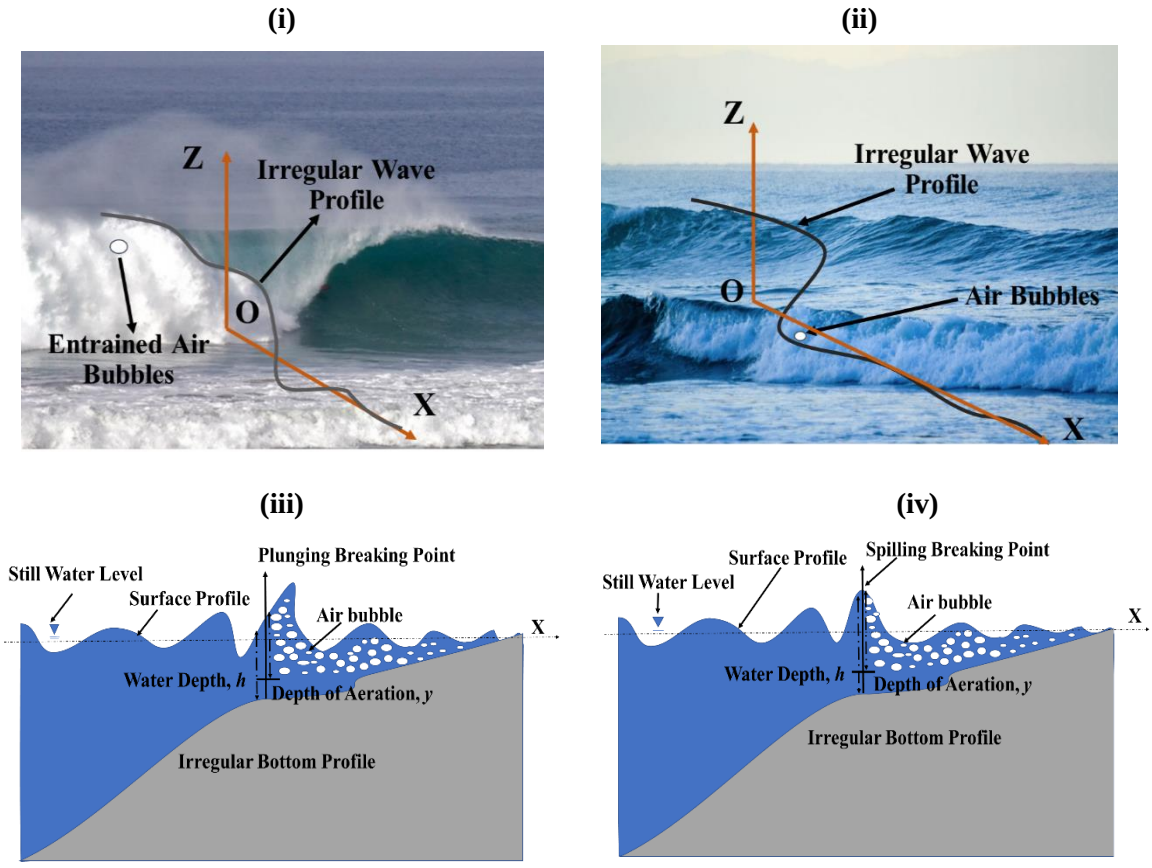

Figure 3.01: (i) Photograph of a real water wave entrained by air bubbles for plunging breakers, (ii) Photograph of a real water wave entrained by air bubbles for spilling breakers, (iii) Surface wave transmission sketch on the irregular beach for plunging breakers, and (iv) A sketch of surface wave transmission on the irregular beach for spilling breakers.

In recent years, significant advancements have been made in improving energy dissipation models for wave-breaking processes. Given the complexity of wave breaking, most models rely on empirical or semi-empirical methods validated by experimental data. These models are generally based on three primary concepts: the bore concept, the stable energy concept, and the air bubbles entrainment concept. The bore concept, initially introduced by Le Mehaute, (1962), posits that the energy dissipation of broken waves is equivalent to that of a hydraulic jump. Battjes and Janssen, (1978) and Thornton and Guza, (1983) developed variations of this model to account for this effect. The stable energy concept was proposed by Dally et al. (1985), and models incorporating this concept were further refined by Swift, (1993) and

Rattanapitikon and Shibayama, (1998), who made additional modifications to include various effects.

In contrast, the air bubble concept focuses on air bubble entrainment and its significant impact on energy dissipation in the surf zone, a topic explored by various researchers (Cox and Shin, 2003; Hwung et al., 1993; Mori et al., 2007). Blenkinsopp and Chaplin (2007) examined the time-varying distribution of air bubbles in different types of breaking waves in the laboratory, finding that void fractions can dissipate up to 14% of wave energy. Hossain et al., (2022) introduced a wave distribution model that incorporates the effects of air bubbles. Hoque et al., (2021) studied the combined effects of air bubbles, turbulence, and bottom friction, while Hoque et al., (2019) conducted both theoretical and experimental investigations into the characteristics of wave height, wave setup, and energy dissipation due to air bubbles in the surf zone. Horikawa and Kuo, (1966) identified entrained bubbles as a key factor in wave energy dissipation, especially in the initial stages of breaking. Führboter, (1970) observed a significant reduction in wave height and energy in the surf zone linked to the presence of air bubbles. Theoretical reviews of void fraction distributions during wave breaking were conducted by Thorpe, (1982). Hoque and Aoki, (2014) analyzed the impact of void fraction on plunging breaking waves, with their findings supported by experimental data.

Although various models have been developed to estimate wave height and wave setup in the surf zone, there remains a gap in models that simultaneously account for wave height and wave setup attenuation due to air bubbles. While there is a solid understanding of air entrainment in breaking waves, research on the role of void fraction in the surf zone is limited. Furthermore, most existing models focus on regular waves, with a notable lack of models addressing irregular waves and their hydrodynamics, particularly in relation to the attenuation effects of air bubbles. This research aims to fill this gap by developing an energy dissipation model for irregular waves that incorporates the influence of air bubbles and provides accurate estimates of RMS wave height and wave setup.

3.3 Theoretical Approaches

3.3.1 Energy Balance Equation (Governing Equation)

To determine how wave height changes across the shore, the one-dimensional energy conservation equation can be expressed as: (Battjes and Janssen, 1978; Thornton and Guza, 1983):

$$\frac{\partial E c_g}{\partial x} = -D, \tag{3.01}$$

where c_g stands for the group celerity, which is used for shallow water as: $c_g = c = \sqrt{gh}$, c is the wave celerity, g stands for the gravitational acceleration, h stands for water depth, E stands for the energy of the wave train and D is the amount of energy dissipation caused by wave breaking, which is zero outside the surf zone area. The study does not account for energy dissipation due to bottom friction, and all considerations are based on linear wave theory. For irregular waves, the wave energy can be described by the following equation:

$$E = \frac{1}{8}\rho g \int_0^\infty H^2 P(H) dH = \frac{1}{8}\rho g H_{rms}^2, \tag{3.02}$$

where ρ is the density of water, g stands for the gravitational acceleration, H is the individual wave height of a wave train, H_{rms} represents the RMS wave height of a wave train and $P(H)$ represents the PDF (probability density function) of the Rayleigh distribution.

3.3.1.1 Model formulation owing to air bubble

Energy dissipation due to wave breaking in an irregular wave train is highly complex. Therefore, Roelvink (1993) proposed that the rate of energy dissipation per unit area, D, for an irregular wave train can be expressed as the product of two components:

$$D = Q_b D_{air}, \tag{3.03}$$

where Q_b meant for the fraction of all breaking waves and D_{air} energy dissipation owing to the effect of air bubbles.

3.3.1.2 Probability of wave breaking

As waves approach shallow water, they break due to various mechanisms, including interactions with the wave and bottom slope, as well as effects from currents or wind. Determining the exact location and nature of wave breaking is challenging, contributing to the complexity of the phenomenon. In this regard, Thornton and Guza, (1983) suggested that the probability of wave heights at the point of breaking can be represented by weighting the Rayleigh distribution for all waves in a wave train. This approach allows for the calculation of energy dissipation in breaking waves using the following formulation:

$$P_{brk} = W(H)P(H), \tag{3.04}$$

where $W(H)$ is the weighting function which must be less than or equal to 1 to strengthen $P_{brk} \leq P(H)$ in agreement that P_{brk} be the subset of the probability distribution *P(H)* for all waves (breaking and non-breaking). Therefore, the fraction of the breaking waves (Q_b) can be composed as follows:

$$Q_b = \int_0^\infty P_{brk} dH, \tag{3.05}$$

where $Q_b \to 0$ as $h \to \infty$, and $Q_b \to 1$ as $h \to 0$ inside the surf region (where all the waves are broken).

Considering the contribution of Thronton and Guza's, (1983) weighting function Kuriyama, (1997), validated and suggested a modified weighting function which is written as follows:

$$W(H) = \left(\frac{H_{rms}}{\gamma h}\right)^2 \left[1 - e^{-\left(\frac{H}{\gamma h}\right)^2}\right] \leq 1, \tag{3.06}$$

where H_{rms} represents the RMS wave height of a wave train, h is the water depth and γ is the arbitary coefficient and its value is approximately 0.42 (Thronton and Guza 1983).

Merging Eqs. (3.04), (3.05), and (3.06) that gives:

$$Q_b = \int_0^\infty \left(\frac{H_{rms}}{\gamma h}\right)^2 \left[1 - e^{-\left(\frac{H}{\gamma h}\right)^2}\right] P(H) dH, \tag{3.07}$$

where $P(H)$ is the PDF of Rayleigh distribution.

3.3.1.3 Air bubble model (Hoque et al., 2019)

In shallow water, waves break and generate numerous air bubbles that contribute to the dispersion of wave energy (Fig. 3.01). Taking this into account, Hoque et al., (2019) proposed a model for regular wave breaking, which is formulated as follows:

$$D_{air} = \alpha \rho_w g \frac{y}{2} \frac{c_0}{(1-c_0)} w_r, \tag{3.08}$$

where y, α, c_0, ρ_w and w_r link to the penetration depth, a free parameter, void fraction, density of water, and air bubble's rising velocity.

3.3.1.4 Formulation of the new model for spilling wave breakers

To formulate a new model for irregular wave energy dissipation, Eqs. (3.03), (3.07), and (3.08) must be integrated, yielding:

$$D = \int_0^\infty \alpha \rho_w g \frac{y}{2} \frac{C_0}{(1-C_0)} w_r \left(\frac{H_{rms}}{\gamma h}\right)^2 \left[1 - e^{-\left(\frac{H}{\gamma h}\right)^2}\right] P(H) dH. \tag{3.09}$$

Linking to Fuhrboter, (1970) conditions, for spilling breaking waves, the penetration depth, y can be written as: $y \propto H(x) = k_1 * H(x)$, where k_1 stands for the similarity constant, H is the individual wave height and x is the horizontal distance towards the shoreline. Reworking Eq. (3.09) that gives:

$$D = \int_0^\infty \alpha \rho_w g \frac{k_1 H(x)}{2} \frac{C_0}{(1-C_0)} w_r \left(\frac{H_{rms}}{\gamma h}\right)^2 \left[1 - e^{-\left(\frac{H}{\gamma h}\right)^2}\right] \frac{2H}{H_{rms}^2} e^{-\left(\frac{H}{H_{rms}}\right)^2} dH. \tag{3.10}$$

Simplification (see detail in Appendix A), yields:

$$D = \frac{3\sqrt{\pi}}{8} \frac{\rho_w k_1 g c_0 \alpha w_r}{(1-c_0)\gamma^4} \frac{H_{rms}^5}{h^4}. \tag{3.11}$$

This is the new irregular wave energy dissipation model owing to the air bubbles effect for spilling breakers. The next section will address solving this equation under different bathymetric conditions.

3.3.1.4.1 Solution for plane sloping beach

For obtaining an analytical solution of Eq. (3.11), wave transmission in shallow water is considered, specifically on a constant plane sloping beach, where the water depth varies by way of $h = xtan\theta$, where θ stands for the slope of the beach. Now, recall the Eq. (3.01) with *E* and *D* illustrated by the Eqs. (3.02) and (3.11) as follows:

$$\frac{1}{8}\rho_w g \frac{d}{dx} H_{rms}^2 \sqrt{gh} = -\frac{3\sqrt{\pi}}{8} \frac{\rho_w k_1 g c_0 \alpha w_r}{(1-c_0)\gamma^4} \frac{H_{rms}^5}{h^4}. \tag{3.12}$$

Initiating $Y = H_{rms}^2\sqrt{h}$ and $h = xtan\theta$ into the Eq. (3.12), which yields

$$\frac{dY}{dh} = -A \frac{Y^{5/2}}{h^{\frac{21}{4}}}, \tag{3.13}$$

where $A = \frac{3\sqrt{\pi}}{tan\theta} \frac{k_1 c_0 \alpha w_r}{\sqrt{g}(1-c_0)\gamma^4}$ is the arbitrary constant.

Once integrated, Eq. (3.13) gives:

$$-Y^{-(3/2)} = \frac{1}{a} h^{-\frac{17}{4}} + const., \tag{3.14}$$

where $a = \frac{17}{6A}$.

The offshore boundary condition is defined where the shallow water theory is applicable as follows:

$$Y = Y_0 = H_0^2\sqrt{h_0}, \qquad \text{at} \qquad h_0 \leq \frac{L}{20}. \tag{3.15}$$

To find the value of integrating *const.*, employing the offshore boundary condition that yields:

$$Y = a^{2/3}\left(h^{-\frac{17}{4}} - aY_0^{-(3/2)} - h_0^{-\frac{17}{4}}\right)^{-(2/3)}. \tag{3.16}$$

After some simplifications, the following equation is found in terms of H_{rms}:

$$H_{rms} = a^{1/3} h^{7/6} \left\{ 1 - h^{\frac{17}{4}} \left(h_0^{-\frac{17}{4}} - \frac{a}{Y_0^{3/2}} \right) \right\}^{-(1/3)} . \tag{3.17}$$

If $h \to 0$, Eq. (3.17) becomes:

$$H_{rms} \cong a^{1/3} h^{7/6}. \tag{3.18}$$

This indicates that within the inner surf zone, the RMS wave height is related to the water depth, taking into account the effect of air bubbles. This finding aligns with the observations of Thornton and Guza, (1983).

3.3.1.4.2 Solution for irregular bathymetry

Obtaining an analytical solution for the above model is challenging, especially for irregular water depths. Therefore, emphasis is placed on the numerical scheme adopted to solve the model. In this context, the x-axis is oriented in the direction of the shore for analysis. The study area has been parted into grids, each one with a Δx space in the x-path (Fig. 3.02).

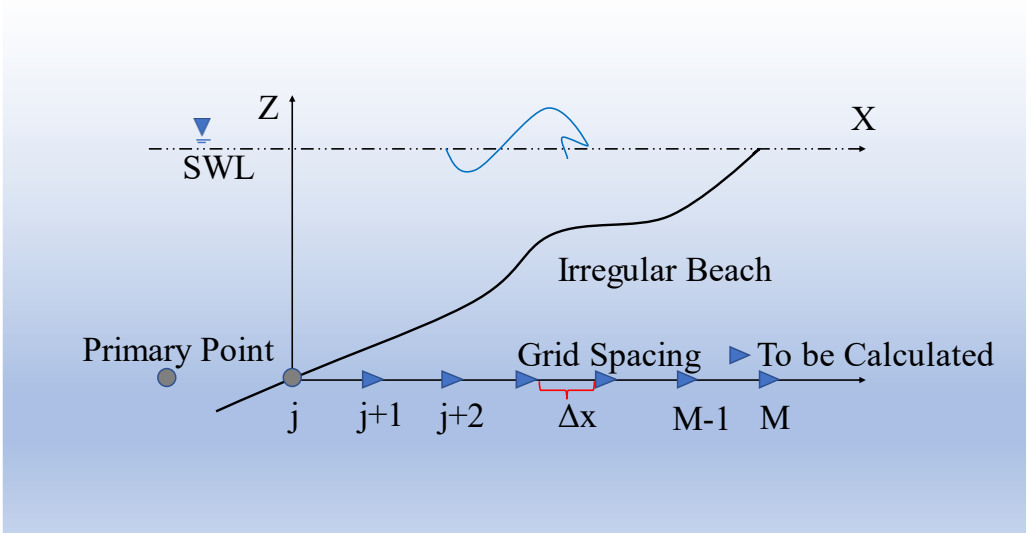

Figure 3.02: A sketch of the solving technique for the irregular beach.

Substituting the Eqs. (3.02) and (3.11) in Eq. (3.01) that yields:

$$\frac{d}{dx}(H_{rms}^2\sqrt{h}) = -A_1\frac{H_{rms}^5}{h^4}, \tag{3.19}$$

where $A_1 = \frac{3\sqrt{\pi}}{\sqrt{g}}\frac{k_1 c_0 \alpha w_r}{(1-c_0)\gamma^4}$ is the arbitrary constant.

The left-hand side of Eq. (3.19) is discretized using the forward finite difference scheme along the x-direction. For the right-hand side, a central difference scheme is applied to each parameter, resulting in:

$$\frac{(H_{rms}^2\sqrt{h})_{k+1} - (H_{rms}^2\sqrt{h})_k}{\Delta x} = -A_1\frac{(H_{rms}^5)_k}{h_k^4}. \tag{3.20}$$

Simplification, yields:

$$(H_{rms})_{k+1} = \sqrt{\frac{(H_{rms}^2\sqrt{h})_k - \frac{A_1\Delta x(H_{rms}^5)_k}{h_k^4}}{(\sqrt{h})_{k+1}}}. \tag{3.21}$$

In Eq. (3.21), since all parameters are known, calculating the improved RMS wave height is straightforward.

3.3.1.5 Formulation of the new model for plunging wave breakers

Corresponding to Fuhrboter, (1970) condition, for plunging breaking wave, *y* can be written as: $y \propto H_b = const$, where H_b is the individual breaking wave height and it can be written as follows (Thornton and Guza, 1983):

$$H_b = h\gamma, \tag{3.22}$$

where γ is the arbitrary constant.

Using Eq. (3.22) to rewrite Eq. (3.09), the following expression is obtained:

$$D = \int_0^\infty \alpha\rho_w g\frac{h\gamma}{2}\frac{C_0}{(1-C_0)}w_r\left(\frac{H_{rms}}{\gamma h}\right)^2\left[1 - e^{-\left(\frac{H}{\gamma h}\right)^2}\right]\frac{2H}{H_{rms}^2}e^{-\left(\frac{H}{H_{rms}}\right)^2}dH. \tag{3.23}$$

Upon simplification of Eq. (3.23), the following expression is derived (see detail in Appendix B):

$$D = \frac{1}{2}\frac{\rho_w g c_0 \alpha w_r}{(1-c_0)\gamma^3}\frac{H_{rms}^4}{h^3}. \tag{3.24}$$

This is the new irregular wave energy dissipation model for plunging breakers owing to the effect of air bubbles. In the subsequent section, the aim is to solve Eq. (3.24) by considering various bathymetric conditions.

3.3.1.5.1 Solution for plane sloping beach

For plunging breaking waves, to derive an analytical solution for Eq. (3.24), wave propagation in shallow water is specifically considered, typically on a uniform plane sloping shore, where the water depth differs as $h = xtan\theta$, where θ denotes the slope of the shore. Recall the Eq. (3.01) with *E* and *D* demonstrated by the Eqs. (3.02) along with (3.24) as follows:

$$\frac{d}{dx}(H_{rms}^2\sqrt{h}) = -\frac{4}{\sqrt{g}}\frac{c_0\alpha w_r}{(1-c_0)\gamma^3}\frac{H_{rms}^4}{h^3}. \tag{3.25}$$

Commencing $Y = H_{rms}^2\sqrt{h}$ and $h = xtan\theta$ into the Eq. (3.25), which generates:

$$\frac{dY}{dh} = -A_2\frac{Y^2}{h^4}, \tag{3.26}$$

where $A_2 = \frac{4}{tan\theta}\frac{c_0\alpha w_r}{\sqrt{g}(1-c_0)\gamma^3}$ is defined as the arbitrary constant.

Next, integrate, Eq. (3.26), which supplies:

$$-Y^{-1} = \frac{1}{b}h^{-3} + const., \tag{3.27}$$

where $b = \frac{3}{A_2}$.

Now, the offshore boundary must be specified where the shallow water approximation is satisfied as follows:

$$Y = Y_0 = H_0^2\sqrt{h_0}, \qquad \text{at } h_0 \leq \frac{L}{20}. \tag{3.28}$$

To obtain the value of integrating *const.*, applying the outer boundary condition which gives the complete solution of *Y* as follows:

$$Y = b(h^{-3} - bY_0^{-1} - h_0^{-3})^{-1}. \tag{3.29}$$

Now, simplifying the above equation and shifting back in terms of H_{rms}, which supplies:

$$H_{rms} = b^{1/2} h^{5/4} \left\{1 - h^3 \left(\frac{1}{h_0^3} - \frac{a}{Y_0}\right)\right\}^{-(1/2)}. \tag{3.30}$$

When the depth turns very shallow (asymptotic case), Eq. (3.30) becomes:

$$H_{rms} \cong b^{1/2} h^{5/4}, \tag{3.31}$$

which tells that in the inward surf region, the RMS wave height is stated in terms of the water depth combined with the air bubbles effect. This result is like the spilling breaker's outcome except for the constant.

3.3.1.5.2 Solution for irregular bathymetry

Finding an analytical solution for the above model becomes challenging when dealing with irregular beach profiles. Thus, the emphasis shifts towards utilizing numerical methods to solve the model. In this concern, the *x*-axis focuses on the direction of the shoreline. The research area is divided into grids, every grid put up with Δx spacing in the *x*-path (Fig. 3.02). Switching the Eqs. (3.02) and (3.24) in Eq. (3.01) and reorganizing the result returns:

$$\frac{d}{dx}(H_{rms}^2 \sqrt{h}) = -A_3 \frac{H_{rms}^4}{h^3}, \tag{3.32}$$

where $A_3 = \frac{4}{\sqrt{g}} \frac{c_0 \alpha w_r}{(1-c_0)\gamma^3}$ is defined as the arbitrary constant.

Now, the left side of Eq. (3.32) is discretized in the *x*-path by the forward finite difference scheme, with the central difference scheme used for every quantity resting on the later side, which takes the lead to as follows:

$$\frac{(H_{rms}^2 \sqrt{h})_{j+1} - (H_{rms}^2 \sqrt{h})_j}{\Delta x} = -A_3 \frac{(H_{rms}^4)_j}{h_j^3}. \tag{3.33}$$

After simplification, Eq. (3.33) might be written as follows:

$$(H_{rms})_{j+1} = \sqrt{\frac{\left(H_{rms}^2\sqrt{h}\right)_j - \frac{A_3\Delta x\left(H_{rms}^4\right)_j}{h_j^3}}{\left(\sqrt{h}\right)_{j+1}}}. \tag{3.34}$$

Now, every single parameter on the right-hand side of Eq. (3.34) is known. Therefore, the RMS wave height can be easily calculated using this equation.

3.3.2 Momentum Balance Equation

As waves shoal and break toward the shore, the momentum flux becomes concentrated and counteracts the effects on the water surface. This impact, which exceeds that of radiation stress, becomes more pronounced with decreasing water depth. To clearly demonstrate this effect, it is essential to observe the wave-induced setup and set-down of the average water level. Therefore, the gradient of the time- and depth-averaged cross-shore wave momentum flux is theoretically related to the cross-shore pressure gradient associated with the average wave setup (Longuet-Higgins and Stewart, 1964). This is written down as follows:

$$\frac{d\bar{\eta}}{dx} + \frac{1}{\rho_w g(h+\bar{\eta})}\frac{dS_{xx}}{dx} = 0, \tag{3.35}$$

where $\bar{\eta}$ is the wave set-up, ρ_w is the density of the water, g is the gravitational acceleration, h is the water depth and S_{xx} is the radiation stress along the x-axis.

However, Hoque et al., (2019, 2021) modified this equation considering the air bubbles effect which is written as follows:

$$\frac{d\bar{\eta}'}{dx} = -\frac{1}{\rho_w g M}\frac{dS_{xx}'}{dx} + \frac{N}{M}\frac{dy}{dx} - \frac{P}{M}\frac{dh}{dx}, \tag{3.36}$$

where $\bar{\eta}'$ is the wave set-up entrained by the air bubbles, $M = (h+\bar{\eta}) - c_0\bar{\eta} - \frac{c_0 y}{2}$,

$N = \frac{c_0\bar{\eta}}{2} + \frac{c_0 y}{3}$, $P = c_0\bar{\eta} + \frac{c_0 y}{2}$ and

$S_{xx}' = \frac{1}{8}\frac{\rho_w H^2\sigma^2}{sinh^2 kh}\left\{(y - 2c_0 y - c_0 h)\left(\frac{\Delta h}{y}\right) + 2h - c_0\frac{y}{2} - (1-c_0)\frac{sinh2kh}{2k} + \frac{c_0}{2k}\frac{(1-cosh2kh)}{2ky}\right\} + \rho_w c_0^2 w_r^2 y\left(\frac{4-3c_0}{12}\right) + E\frac{1-c_0}{2}$ is the radiation stress including the air bubbles effect.

Now, for irregular waves assume that the Rayleigh distribution (narrow-banded in frequency) is followed by wave heights (Longuet-Higgins, 1952), so that all individual waves have nearly the same group velocity and period. Therefore, the Eq. (3.36) can be written for spilling breaking wave ($y \propto H(x) = k_1 * H(x)$), as follows:

$$\frac{d\bar{\eta}}{dx} = -\frac{1}{\rho_w g L}\frac{dS_{xx}^{''}}{dx} + \frac{Q}{L}\frac{dy}{dx} - \frac{R}{L}\frac{dh}{dx}, \tag{3.37}$$

where $L = (h + \bar{\eta}) - c_0\bar{\eta} - \frac{k_1 c_0\sqrt{\pi}}{4}H_{rms}$, $Q = \frac{k_1 c_0\bar{\eta}}{2} + \frac{c_0\sqrt{\pi}}{6}H_{rms}$, $R = c_0\bar{\eta} + \frac{k_1 c_0\sqrt{\pi}}{4}H_{rms}$ and $S_{xx}^{''} = \frac{1}{8}\rho_w g H_{rms}^2\left\{\frac{3}{2} - \left(\frac{2c_0^2 - c_0}{2-2c_0}\right)\right\} + \frac{c_0^2 w_r^2 \rho_w k_1\sqrt{\pi}}{2}\left(\frac{4-3c_0}{12}\right)H_{rms}$ (Applying shallow water approximation).

For plunging breaking waves ($y \propto H_b = const$), the Eq. (3.37) is the same, but the parameters are like as:

$L = (h + \bar{\eta}) - c_0\bar{\eta} - \frac{c_0\gamma}{2}h$, $Q = \frac{c_0\bar{\eta}}{2} + \frac{c_0\gamma}{3}h$, $R = c_0\bar{\eta} + \frac{c_0\gamma}{2}h$ and

$S_{xx}^{''} = \frac{1}{8}\rho_w g H_{rms}^2\left\{\frac{3}{2} - \left(\frac{2c_0^2 - c_0}{2-2c_0}\right)\right\} + (4 - 3c_0)\frac{c_0^2 w_r^2 \rho_w \gamma}{12}h$ (Applying shallow water approximation).

3.3.2.1 Numerical Solution of the momentum balance equation

It has been seen that Eq. (3.37) is non-linear, so it is not easy to obtain a systematic solution. Therefore, the same methodology is applied in Eq. (3.37), and the result yields:

$$\bar{\eta}_{j+1} = \bar{\eta}_j - \frac{1}{\rho_w g L}\left(S_{xx(j+1)}^{''} - S_{xx(j)}^{''}\right) + \frac{Q}{L}(y_{j+1} - y_j) - \frac{R}{L}(h_{j+1} - h_j). \tag{3.38}$$

Now, Using the shallow water linear approximation ($kh \ll 1$) in radiation stress term and later Führboter, (1970) article regarding penetration depth, Eq. (3.38) reformulated as follows:

For spilling breaking waves ($y \propto H(x) = k_1 H(x)$):

$$\bar{\eta}_{j+1} = \bar{\eta}_j - \frac{3}{16L}\left(H^2_{rms(j+1)} - H^2_{rms(j)}\right) + \left(\frac{2c_0^2 - c_0}{8L(2-2c_0)}\right)\left(H^2_{rms(j+1)} - H^2_{rms(j)}\right) - (4 - 3c_0)\frac{c_0^2 w_r^2 k_1\sqrt{\pi}}{24gL}\left(H_{rms(j+1)} - H_{rms(j)}\right) + \frac{Qk_1}{L}\left(H_{rms(j+1)} - H_{rms(j)}\right) - \frac{R}{L}\left(h_{j+1} - h_j\right). \quad (3.39)$$

For plunging breaking wave ($\gamma \propto H_b = const.$):

$$\bar{\eta}_{j+1} = \bar{\eta}_j - \frac{3}{16L}\left(H^2_{rms(j+1)} - H^2_{rms(j)}\right) + \left(\frac{2c_0^2 - c_0}{8L(2-2c_0)}\right)\left(H^2_{rms(j+1)} - H^2_{rms(j)}\right) - (4 - 3c_0)\frac{c_0^2 w_r^2 \gamma}{24gL}\left(h_{j+1} - h_j\right) + \frac{Q\gamma}{L}\left(h_{j+1} - h_j\right) - \frac{R}{L}\left(h_{j+1} - h_j\right). \quad (3.40)$$

Now, all the parameters on the right side of both the Eqs. (3.39) and (3.40) are known. Hence, it is easy to compute the wave set-up from these equations.

3.4 Collected Data

Tables 2.2 and 2.3 in Chapter 2 provide a comprehensive summary of the collected datasets, offering concise descriptions of the data for wave height and set-up. The datasets are classified into three categories: small-scale, large-scale, and field data, covering a range of wave and bottom topography conditions. To validate the accuracy and effectiveness of the current model, the datasets were employed during the validation process.

3.5 Results And Validations

3.5.1 Boundary Conditions

To properly run the model for a specific situation, two boundary conditions must be defined: the seaward boundary and the coastline boundary. The required parameters at the seaward boundary include (1) the incident RMS wave height and water depth, (2) the beach profile, and (3) the wave period. Additionally, the incident set-down is needed for calculating wave set-up. To prevent infinite wave heights, previous calculations at the coastline have usually assumed a water depth close to zero.

3.5.2 Identification of Wave Breaking and Breaker Types

Considering an irregular wave propagating over a beach profile, as illustrated in Fig. 3.01, the wave energy and RMS wave height diminish as the waves approach the shoreline and begin to break. Thus, it is essential to determine the point where wave breaking starts. In this context, Thornton and Guza's (1983) recommendation is relevant, as follows:

$$H_{rms,b} = \gamma h, \tag{3.41}$$

where $H_{rms,b}$ is the RMS wave height at the breaking point, h is the water depth and γ is an arbitrary constant.

The breaker types are found in the Battjes, (1974) surf similarity parameter (ζ_b) that can be written as follows:

$$\left.\begin{array}{ll} \zeta_b < 0.4, & \text{for spilling breakers} \\ 0.4 \leq \zeta_b < 2.0, & \text{for plunging breakers} \\ \zeta_b \geq 2.0, & \text{for surging or collapsing breakers} \end{array}\right\} \tag{3.42}$$

where ζ_b were found from the following equation

$$\zeta_b = \frac{tan\alpha}{\sqrt{\frac{H_{rms,b}}{L_0}}}. \tag{3.43}$$

In Eq. (3.43), L_0 stands for deep-water wavelength and $tan\alpha$ is the beach slope.

3.5.3 Comparison of RMS Wave Height and Set-Up with Different Experimental Data and Models

Calculating RMS wave height and wave set-up begins with identifying the breaker types using the initial parameters along with Eqs. (3.42) and (3.43). For plane-sloping beaches, Eq. (3.18) is employed for spilling breakers, and Eq. (3.31) for plunging breakers after confirming the breaker types. In the case of irregular sloping beaches, Eq. (3.21) is used for spilling breakers, while Eq. (3.34) applies to plunging breakers. Finally, wave set-up for both spilling and plunging breakers is calculated

using equations (3.39) and (3.40), respectively. The void fraction was set between 0.14 - 0.16 for spilling breaking waves and 0.17 - 0.18 for plunging breaking waves in the computation that was suggested by some investigators (Hoque and Aoki, 2005; Huang et al., 2009). For the calculation, the grid size *(Δx)* was set to be equal length of the measured RMS wave height, except *Δx* is greater than *5m*. Also, to compute H_{rms} ad $\bar{\eta}$; α, and k_1 were set to 0.82 and 0.56, respectively, as recommended by Hossain et al., (2022).

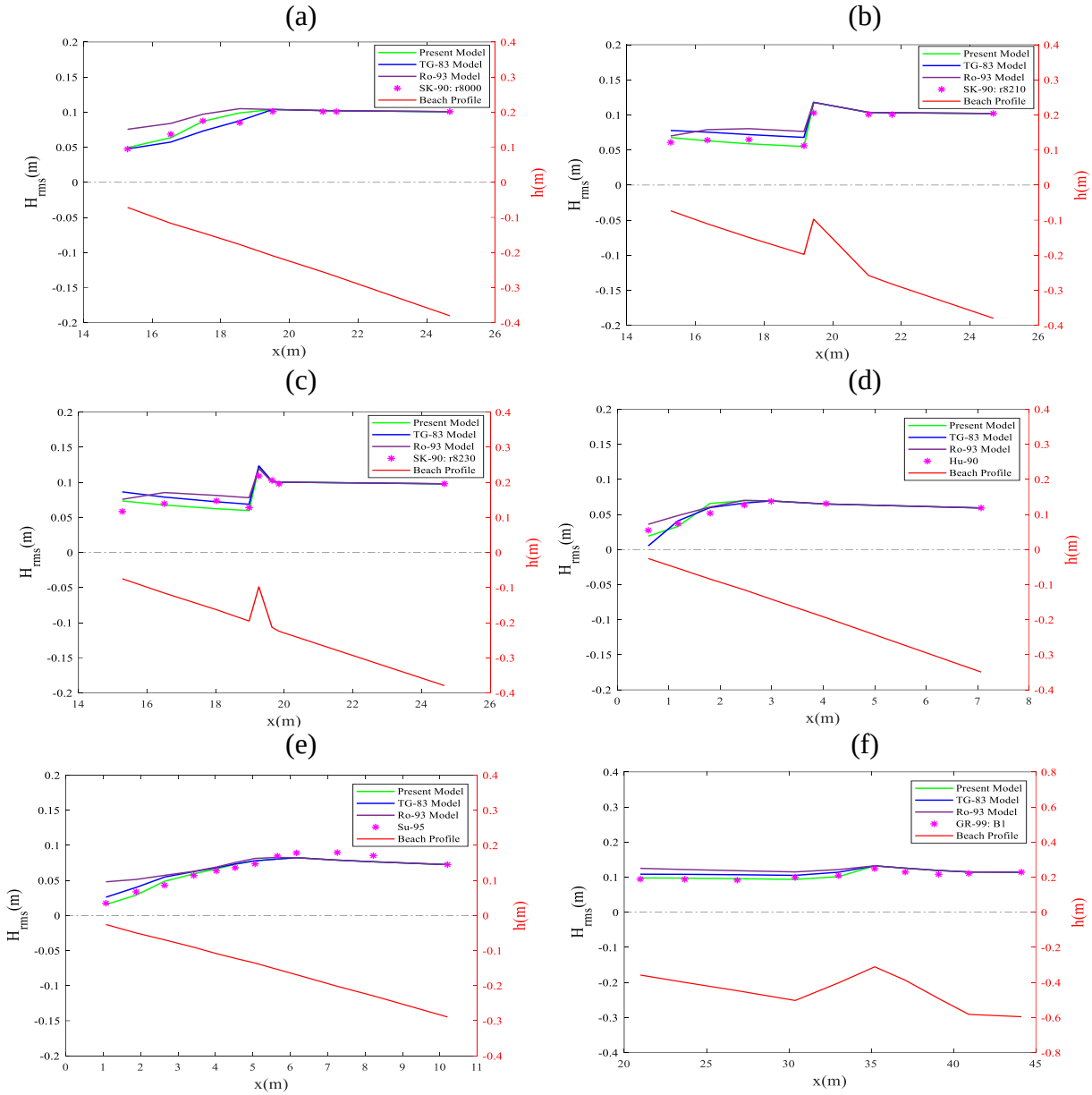

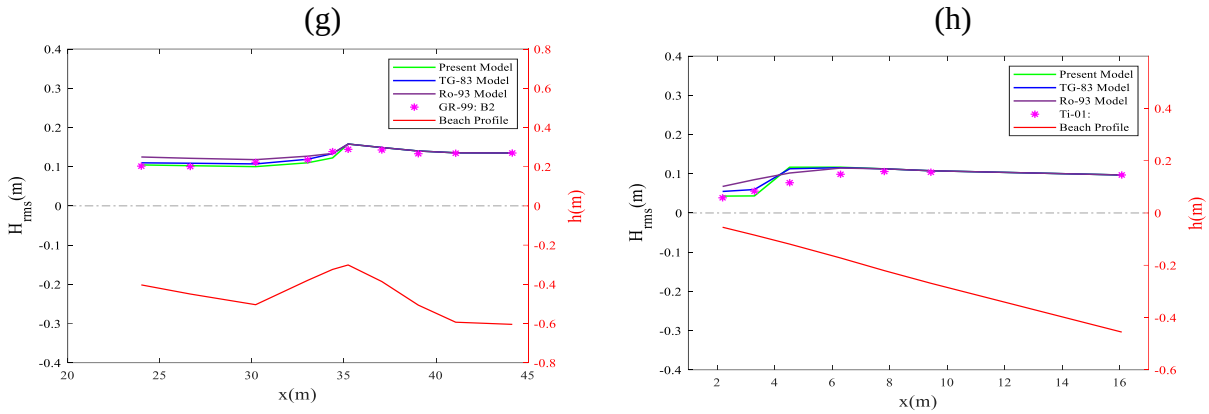

Figure 3.03: RMS wave height comparison of the present model with various small-scale experimental data sets ((a), (b), and (c) for SK-90; (d) for Hu-90; (e) for Su-95; (f), and (g) for GR-99; and (h) for Ti-01) and models (TG-83 and Ro-93), including different beaches.

Results from this model were evaluated against small-scale experimental data from various researchers and established models, specifically Ro-93 (Roelvink, 1993) and TG-83 (Thornton and Guza, 1983), as shown in Fig. 3.03. The findings indicated that the majority of the data and the established models (Ro-93 and TG-83) closely matched the current model's results. Notably, the model exhibited strong concordance with experimental data, particularly on plane-sloping beaches and on steep slopes near narrow-crested bars, aligning with the observations made by Smith and Kraus, (1990) and Grasmeijer and Rijn, (1999). However, the model was less effective in accurately predicting RMS wave heights in proximity to the shoreline.

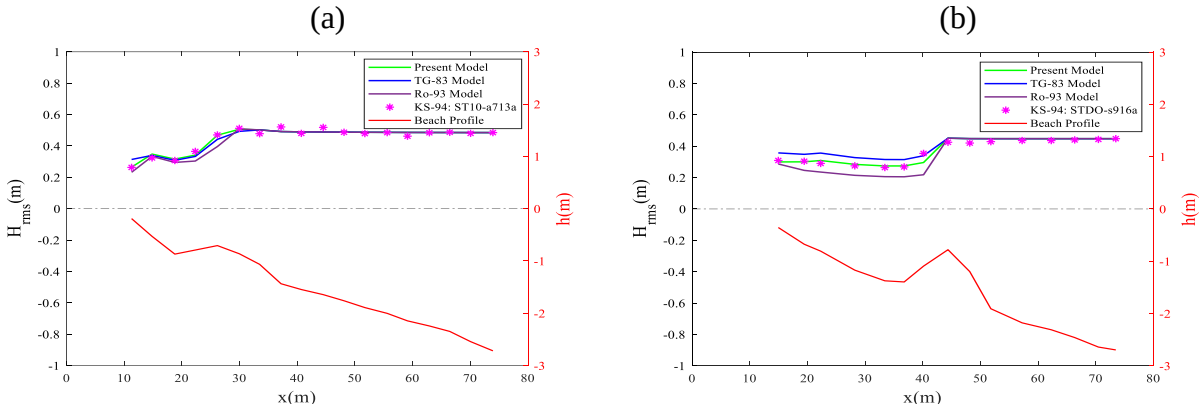

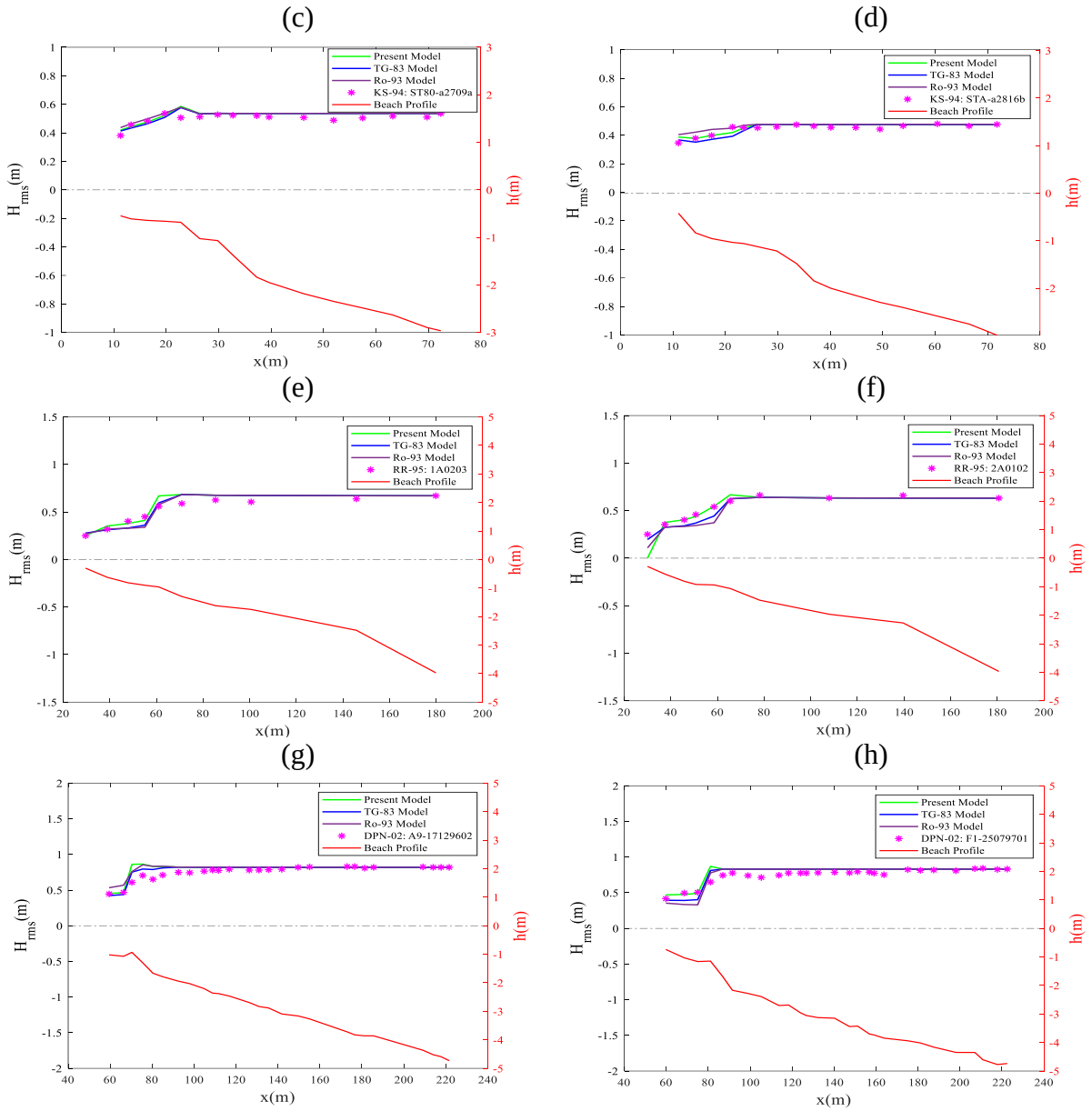

Figure 3.04: RMS wave height comparison of the present model with various large-scale experimental data ((a), (b), (c), and (d) for KS-94; (e), and (f) for RR-95; and (g), and (h) for DPN-02) and models (TG-83 and Ro-93), including different beaches.

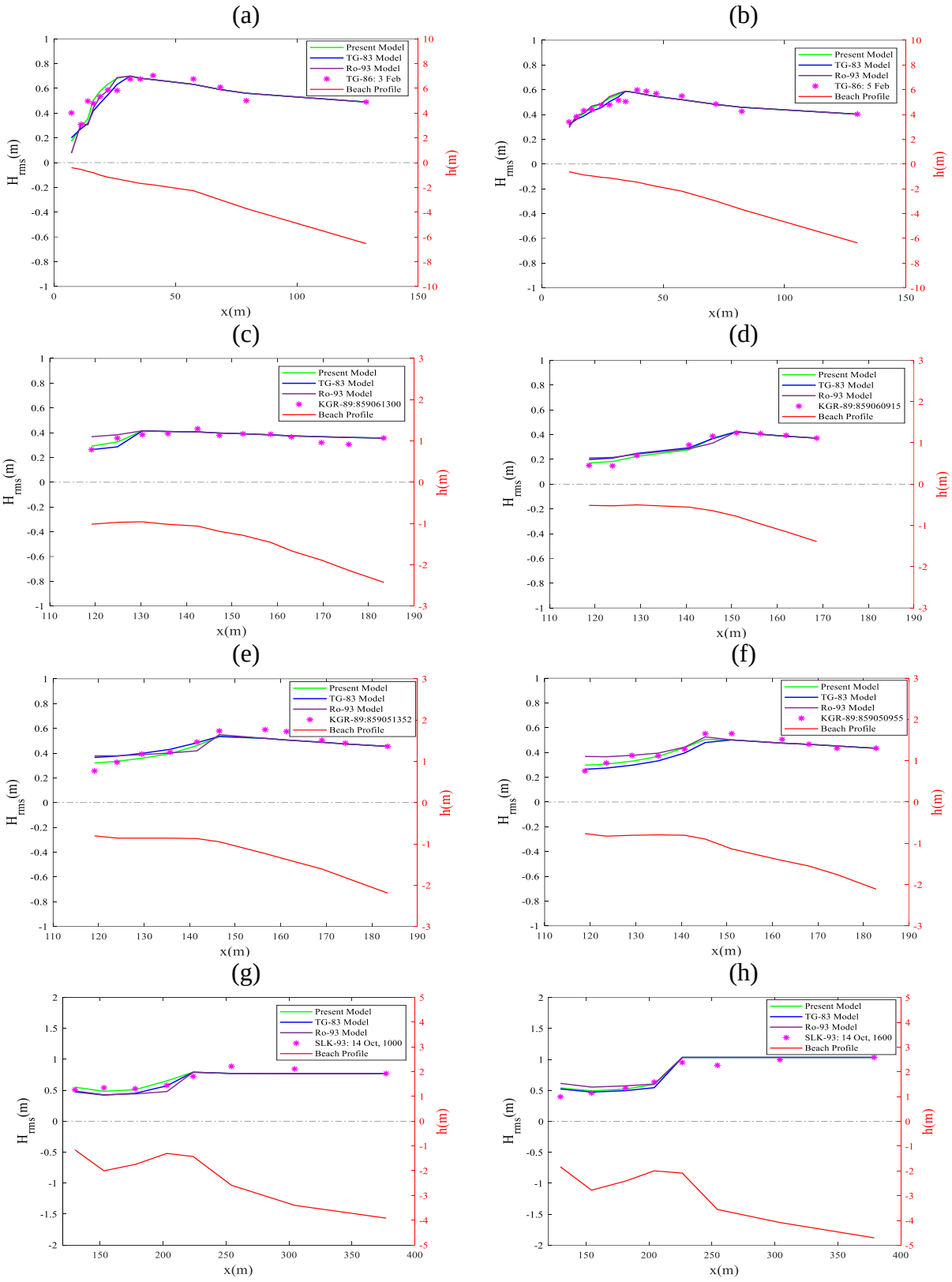

Figure 3.05: RMS wave height comparison of the present model with various Field data ((a), and (b) for TG-86; (c), (d), (e), and (f) for KGR-89; and (g), and (h) for SLK-93) and models (TG-83 and Ro-93), including different beaches.

The present model was compared with large-scale experimental data from various authors and models, such as Ro-93 and TG-83 (see Table 2.2 in Chapter 2), as depicted in Fig. 3.04. This analysis shows a strong agreement in calculating RMS wave heights. The model performed exceptionally well with the datasets from Kraus and Smith, (1994) and Roelvink and Reniers, (1995). Nonetheless, inconsistencies were observed in the breaking point when compared to the findings of Dette et al. (1998), which could be due to the data being collected during stormy wave environments.

Fig. 3.05, presents a comparison between the current model and field data sets collected from various sources, including models such as Ro-93 and TG-83 (refer to Table 2.2 in Chapter 2). The current model shows strong performance with the data from Smith et al. (1993) and Kraus et al. (1989). However, some variation is observed near the shoreline when analyzing the data from Thornton and Guza, (1986).

Lastly, Fig. 3.06 illustrates a comparison of wave set-ups, highlighting the overall performance of the current model in calculating these values. The model demonstrates strong agreement with the experimental data from Stive, (1985) and Battjes and Janssen, (1978).

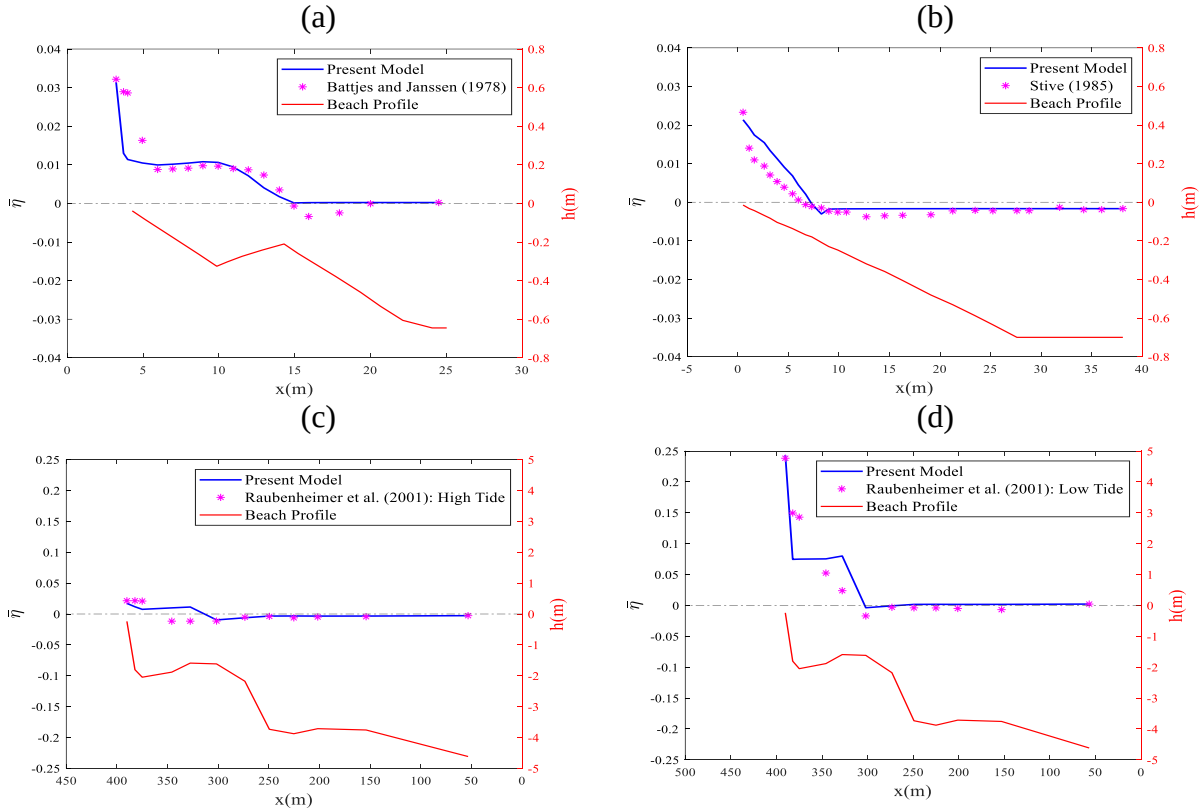

Figure 3.06: Wave set-up comparisons of the present model with a variety of experimental data ((a), for BJ-78; (b), for St-85; and (c), & (d) for RGS-01).

However, some discrepancies are noted at the onset of the breaking point, indicating areas for potential improvement in the model's accuracy. In the case of the experimental data from Raubenheimer et al. (2001), the model tends to overestimate results slightly. Nonetheless, the overall wave set-up results from the current model are comparable to those of Hoque et al. (2019). The following section will illustrate the overall performance of the model by presenting the normalized RMS error across all cases evaluated.

3.5.4 Error Analysis

This section quantifies the error using the normalized root mean square error (NRMSE), which serves as a general indicator of model performance. According to Jadhav and Chen, (2013), the NRMSE can be expressed as follows:

$$NRMSE = \sqrt{\frac{1}{n}\sum_{j=1}^{n}\left(\frac{(H_{rms})_{c,j}}{(H_{rms})_{o,j}} - 1\right)^2}, \tag{3.44}$$

where n stands for the total number of wave data points, $(H_{rms})_{c,j}$ is the computed RMS wave height, and $(H_{rms})_{o,j}$ denotes the observed RMS wave height, respectively.

The NRMSE values for the current model are summarized in Tables 3.1 and 3.2, which correspond to RMS wave height and wave set-up, respectively. For the prediction of H_{rms}, the average NRMSE for small-scale experimental data is 11.49%, slightly exceeding the 7.09% observed for large-scale experimental data. This difference indicates that the current model is influenced by a minor scale influence.

Table 3.1: A summary of NRMSE for the RMS wave height.

Data sources	NRMSE of Present model, TG-83, & Ro-93 (%)	Data Types	Avr. NRMSE of Present model, TG-83, & Ro-93 (scale %)	Avr. NRMSE of Present model, TG-83, & Ro-93 (%)
Ti-01	19.25, 20.72 & 21.93	SS	11.49, 12.09 & 13.24	9.49, 10.28, & 11.21
GR-99	5.53, 5.89 & 6.21	SS		
Su-95	12.84, 13.27 & 15.96	SS		
SK-90	11.02, 11.52 & 12.93	SS		
Hu-90	15.76, 16.41 & 16.86	SS		
DPN-02	5.96, 6.31 & 6.98	LS	7.09, 7.41 & 7.97	
RR-95	13.48, 13.73 & 14.91	LS		

KS-94	4.47, 4.79 & 4.99	LS		
SLK-93	12.86. 14.86 & 16.28	FE	9.90, 11.34 & 12.41	
KGR-89	8.58, 9.87 & 10.74	FE		
TG-86	9.61, 10.76 & 11.89	FE		

Increasing the number of data points from small-scale experiments could help reduce the error. In contrast, the model shows reasonable performance with an average NRMSE of 9.90% for field data. The present model achieves an average NRMSE of 9.49%, which is an improvement over the average NRMSEs of other models, such as Ro-93 and TG-83, which are 10.28% and 11.21%, respectively. Regarding wave set-up, the current model's NRMSE of 13.37% suggests that it slightly underestimates the values compared to H_{rms}.

Table 3.2: A summary of NRMSE for wave set-up.

Data Sources	NRMSE (%)	Data Type	Average NRMSE (%)
RGS-01	17.21	FE	13.37
St-85	9.26	SS	
BJ-78	9.82	SS	

Fig. 3.07, the model is judged to three key types of collected data sets and other established models for RMS wave height (Fig. 3.07(i)) and wave set-up (Fig. 3.07(ii)), which reveal that the whole model performance is very good for predicting RMS wave height and good for predicting wave set-up (Rattanapitikon, 2008).

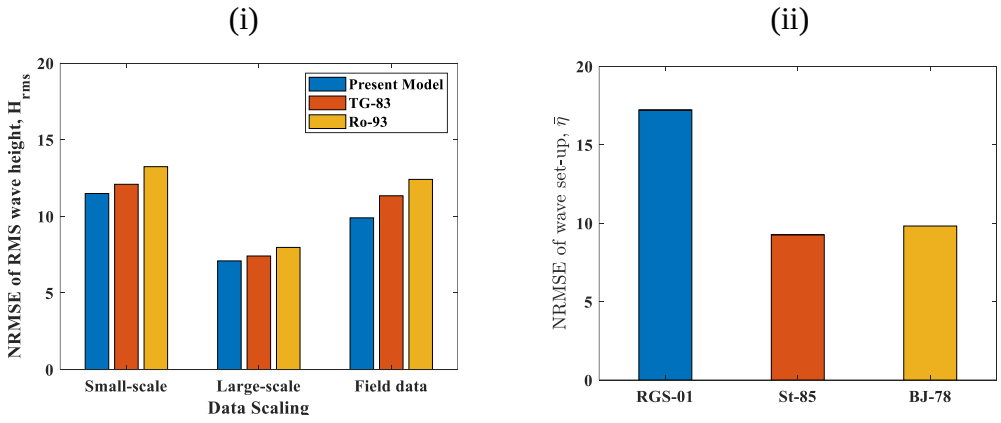

Figure 3.07: NRMSE variation of the present model with various experimental data sets and models: (i) RMS wave height, and (ii) Wave set-up.

3.6 Conclusions

This chapter presents a novel energy dissipation model for spilling and plunging breaking waves, which is utilized to calculate RMS wave height and wave set-up through the energy balance equation and momentum flux conservation law. The model builds upon the air bubbles model for regular breaking waves proposed by Hoque et al. (2019) and incorporates the concepts of breaking wave fractions introduced by Thornton and Guza, (1983). To identify breaking waves and classify breaker types, the modified Miche, (1944) breaking criterion and Battjes, (1974) surf similarity parameter are employed. The model's validity is demonstrated through various wave and bottom geography configurations, alongside small-scale, large-scale, and field experimental data from multiple authors and established models, including Ro-93 and TG-83. In most cases, the computed RMS wave heights closely matched experimental data, performing better than the Ro-93 and TG-83 models, although some discrepancies were noted near the shoreline. The model effectively computes wave set-up, with notable performance except near the breaking point. It was found that void fractions of 17% to 18% for plunging breakers and 14% to 16% for spilling breakers contribute to wave energy dissipation in irregular waves, aligning closely with the findings of Hoque and Aoki, (2005). The average NRMSE for calculating RMS wave height with this model is 9.49%, outperforming the TG-83 model at 10.28% and the Ro-93 model at 11.21%, indicating a strong correlation with experimental data. Additionally, the average NRMSE for wave set-up is 13.37%, suggesting that the model is effective for predicting wave set-up. Despite some inconsistencies near the coastline, the model demonstrates robust capabilities in simulating RMS wave height and set-up across a wide range of wave conditions and coastal profiles due to the effects of shoaling and wave breaking.

CHAPTER 4

Estimation of Air-Bubble-Induced Wave Height and Set-up using Representative Wave Approach

4.1 Abstract

This study has explored the potential of modeling wave height and set-up in the surf zone using the representative wave method influenced by air bubbles in irregular waves. Two existing wave-breaking models, incorporating air bubble effects, have been adapted and modified to develop new models for irregular wave-breaking. These models have been designed to calculate root mean square (RMS) wave height and wave set-up based on energy flux and momentum conservation laws. Model I has been solved analytically for plane-sloped beaches and numerically for irregularly sloped beaches, addressing spilling and plunging breakers separately. Model II has been solved numerically for both slope types and breaking conditions. The modified models have been calibrated and validated using extensive experimental data from large-scale, small-scale, and field experiments. Results have indicated that the modified models are highly accurate in computing wave heights and set-ups, with Model I outperforming Model II in terms of accuracy for RMS wave height and set-up calculations in irregular waves.

4.2 Introduction

Precise information on wave behavior in the surf zone is essential for many coastal engineering tasks, such as designing coastal structures and analyzing beach changes. In shallow water regions, waves break due to the bottom slope, causing many air bubbles to enter the water near the breaking point, as depicted in Fig. 4.01. This makes the interaction between air bubbles and the flow fields of broken waves more complex. Additionally, energy from this location is converted into turbulence and heat, reducing the wave height as waves approach the shore. Accurate measurements of sediment transport capacity, wave set-up, wave run-up, sound generation, and

overtopping are crucial for effective coastal management, necessitating a focus on the wave-breaking region.

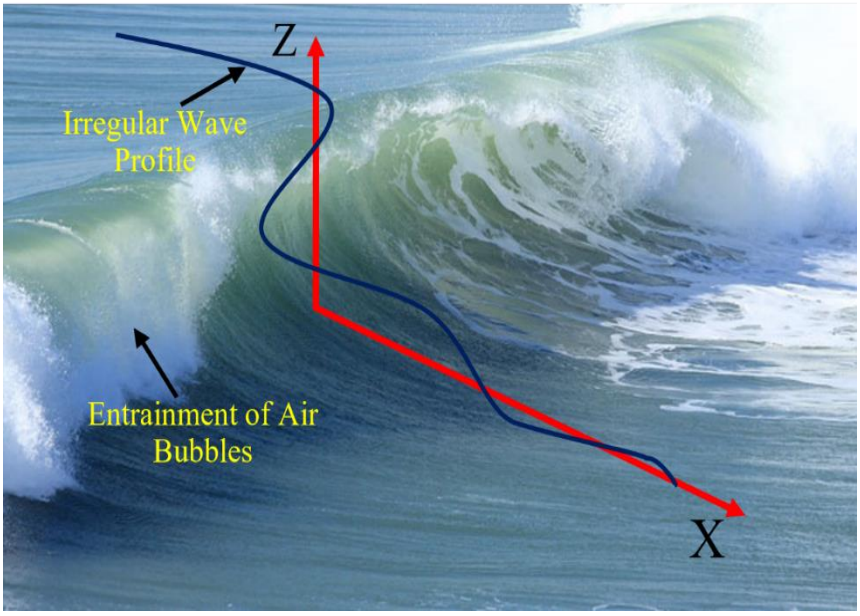

Figure 4.01: A picture of a real ocean wave with air bubbles

Recent research and experimentation have extensively focused on improving energy dissipation models. Given the complexity of wave breaking, researchers have developed models grounded in three main concepts: the bore model, the stable energy model, and the entrainment of air bubbles model to calculate wave energy.

Earlier, numerous scholars (Koga 1982; Lamarre and Melville 1991; Cox and Shin 2003; Mori, Suzuki, and Kakuno 2007; Hoque et al. 2021; Wu 1988; Blenkinsopp and Chaplin 2011; Hossain, Rahman, and Hoque 2022; Shi, Wüthrich, and Chanson 2023; Horikawa and Kuo 1966; Hoque 2002; Hoque and Aoki 2014; Hoque et al. 2019) have investigated the occurrence of air bubbles enhancing attuned in breaking waves and the various effects (containing gas interactions, the transfer of wave energy, the carriage of sediment, and the creation of sound) in the surf zone. Additionally, Hoque, (2002) developed an energy dissipation model that accounts for the influence of air bubbles, proposing that the void fraction changes rapidly and significantly with variations in water depth within the surf zone, following an exponential pattern. In a subsequent study, Hoque and Aoki, (2014) explored the effects of air bubbles on plunging breaking waves and introduced a model to calculate wave height and set-up in the surf zone. Similarly, Hoque et al. (2019) presented a model that incorporates the impact of air bubbles, based on the idea that the void fraction—the proportion of the water column

occupied by air bubbles—experiences significant and rapid changes with fluctuations in water depth, following a linear trend. Further investigations by Hoque et al. (2021) examined the roles of air bubbles, turbulence, and bottom friction, leading to the proposal of an energy dissipation model aimed at accurately calculating wave height and set-up.

While these models addressed the effects of air bubbles in the surf zone, they were primarily designed for regular breaking waves. It is well established that wave breaking in irregular waves is more complex than in regular waves, and distinct breakpoints for irregular waves are often not identified. Additionally, irregular waves distribute energy over a much broader area compared to regular waves. As a result, the interaction of irregular waves in shallow water, along with the entrainment of air, presents a significant and intriguing phenomenon. This raises the question: how can we develop an energy dissipation model for irregular breaking waves that take into account the effects of air bubbles?

In the quest to develop an energy dissipation model for wave breakers in irregular waves, researchers have identified four main approaches: representative, spectral, probabilistic, and parametric. Each of these methods provides a unique perspective on modeling the complex dynamics of wave breaking in irregular conditions and can contribute to a deeper understanding of wave behavior in the surf zone. Among the above-mentioned approaches, the representative wave method uses regular wave formulas to analyze irregular waves, utilizing specific representative wave parameters for this analysis (e.g., H_{rms}, $H_{s,}$ and H_{m0}). This approach offers advantages due to its simplicity and straightforwardness, as it does not necessitate any assumptions about the probability density function (PDF) of wave heights. Energy dissipation in irregular wave trains occurs over a much larger area compared to regular waves since the tallest waves in irregular trains often break at greater distances from the shore. This difference can lead to inaccuracies in surf zone predictions when using regular wave models (Rattanapitikon and Shibayama, 1998). However, recent research has demonstrated that the representative wave approach can effectively calculate the transformation of RMS wave height by integrating an appropriate coefficient into an energy dissipation model (Nuntakamol and Rattanapitikon, 2011; Rattanapitikon, 2008; Rattanapitikon et al., 2003).

While some models have been developed to assess wave height and set-up in shallow water using air entrainment phenomena, none have specifically addressed irregular waves through the representative wave approach. This study seeks to address this gap by creating a suitable energy dissipation model that accounts for the effects of air bubbles on wave breakers in irregular waves, allowing for accurate calculations of RMS wave height and set-up using this method.

4.3 Mathematical Formulation

The governing equation for this study is the energy balance equation, formulated for the average energy flux in a one-dimensional context within an irregular wave train, as follows (Rattanapitikon 2008):

$$\frac{\partial(\overline{Ec_{gp}})}{\partial x} = -\bar{D}, \tag{4.01}$$

where E is the energy, c_{gp} is the group velocity, $\overline{Ec_{gp}}$ is the average of Ec_{gp}, x is the horizontal distance toward the coastline and $\bar{D}$ represents the average energy dissipation of the wave train.

In general, the average energy flux of an irregular wave train can be represented within the framework of linear wave theory as follows (Rattanapitikon 2008):

$$\overline{Ec_{gp}} = \frac{\sum_{j=1}^{n}(E_j c_{gp,j})}{n} = \frac{\rho_w g}{8}\frac{\sum_{j=1}^{n} H_j^2 c_{gp,j}}{n}, \tag{4.02}$$

where ρ_w is the density of water, g is the gravitational acceleration, H_j is the j^{th} individual wave height, $c_{gp,j}$ remains j^{th} individual group velocity, and n is the total waves in the wave train.

For simplification, the analysis assumes wave heights follow a Rayleigh distribution, suggesting that the waves are narrow-band in frequency. This leads to each wave having a nearly identical period and group velocity. Consequently, Eq. (4.02) can be rewritten as follows:

$$\overline{Ec_{gp}} = \frac{\rho_w g c_{gp}}{8}\frac{\sum_{j=1}^{n} H_j^2}{n}. \tag{4.03}$$

It is well known that $\sqrt{\frac{\sum_{j=1}^{n} H_j^2}{n}} = H_{rms}$; thus, Eq. (4.03) can be converted into:

$$\overline{Ec_{gp}} = \frac{\rho_w g c_{gp}}{8} H_{rms}^2. \tag{4.04}$$

Now, Eq. (4.01) can be written as follows:

$$\frac{\rho_w g}{8} \frac{\partial \left(H_{rms}^2 c_{gp}\right)}{\partial x} = -\overline{D}. \tag{4.05}$$

By substituting the formula for energy dissipation $\overline{D}$ and solving from the seaward boundary to the coastline, the changes in RMS wave height can be determined using the conservation equation (Eq. (4.05)). The main challenge lies in calculating the value of $\overline{D}$ for breakers in irregular waves. To address this, two regular wave models of air bubbles are reviewed in the following section.

4.3.1 Review of Existing Regular Wave Air Bubble Models

4.3.1.1 Hoque et al., (2019) model

The model for energy dissipation relies on the idea that introducing air entrainment into a system raises the potential energy, ΔPE. This increase in potential energy demands that the flow provide an equivalent amount of work, which is then dissipated within the flow field. It is assumed in the model that the distribution of air bubbles varies linearly with water depth, mathematically $c(z) = c_0 \left(\frac{y+z}{y}\right)$, where *c(z)* is the fraction of the air volume per unit width, and *z*, *y*, c_0 resemble the vertical distance, penetration depth, and reference void fraction at $z = 0$, correspondingly (depicted in Fig. 4.02).

Applying this hypothesis, the model calculates the energy dissipation rate, D_{air} that can be written as follows:

$$D_{air} = \frac{\Delta PE}{t_r} \alpha, \tag{4.06}$$

where α represents a free parameter that incorporates factors such as turbulence dissipation, bottom friction, and other mechanisms that contribute to wave energy dissipation, $\Delta PE = \frac{g \rho_w c_0 y^2}{6}$ represents the potential energy, ρ_w is the density of water,

g represents the gravitational acceleration and t_r is the average air bubble releasing time, $t_r = \frac{h_G}{w_r}$. Here, w_r is the bubble rising velocity whose value is 0.25ms^{-1} (Chanson 1997) and h_G is the depth of centre of gravity of air bubbles distribution that can be expressd as: $h_G = -\frac{\int_{-y}^{\Delta h} zc(z)dz}{\int_{-y}^{\Delta h} c(z)dz}$, implies as follows:

$$h_G = \frac{y(1-c_0)}{3}, \tag{4.07}$$

where $\Delta h = \int_{-y}^{0} c(z)dz + \int_{0}^{\Delta h} c(z)dz = \frac{yc_0}{2(1-c_0)}$ is the air bubble-induced water level rise above the still water depth (see Fig. 4.02).

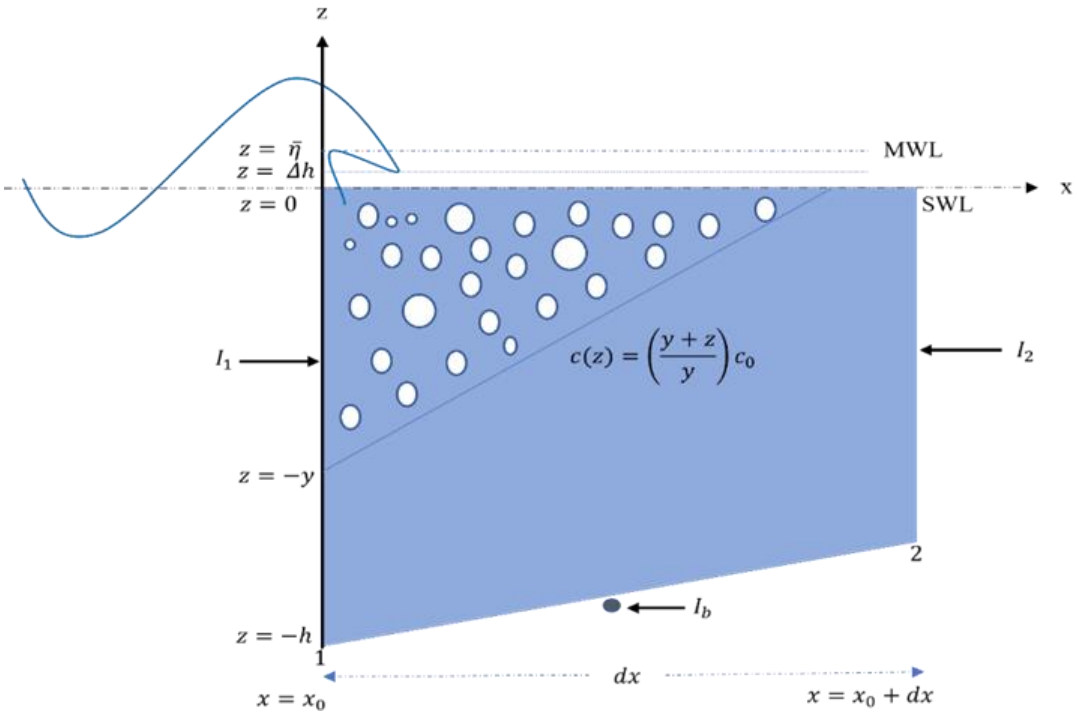

Figure 4.02: A visual representation of breaking wave propagation with entrainment of air bubbles for the Hoque et al., (2019) model.

Finally, upon adding the value of the above parameter, the following equation was obtained:

$$D_{air} = gw_r\alpha\rho_w \frac{yc_0}{2(1-c_0)}. \tag{4.08}$$

This is identified as the air bubble model.

4.3.1.2 Hoque, (2002) model

This model is also grounded in thermodynamic principles. It posits that the distribution of entrained air bubbles in water follows an exponential variation with respect to water depth, as expressed mathematically by the following equation:

$$c(z) = c_0 e^{k_0 z}, \tag{4.09}$$

where *c(z)* is the fraction of the air volume per unit width and k_0, z, c_0 resemble to the decay parameter exemplifying the vertical distribution of air bubbles, vertical distance positive upward direction, and reference void fraction at $z = 0$, correspondingly (depicted in Fig. 4.03).

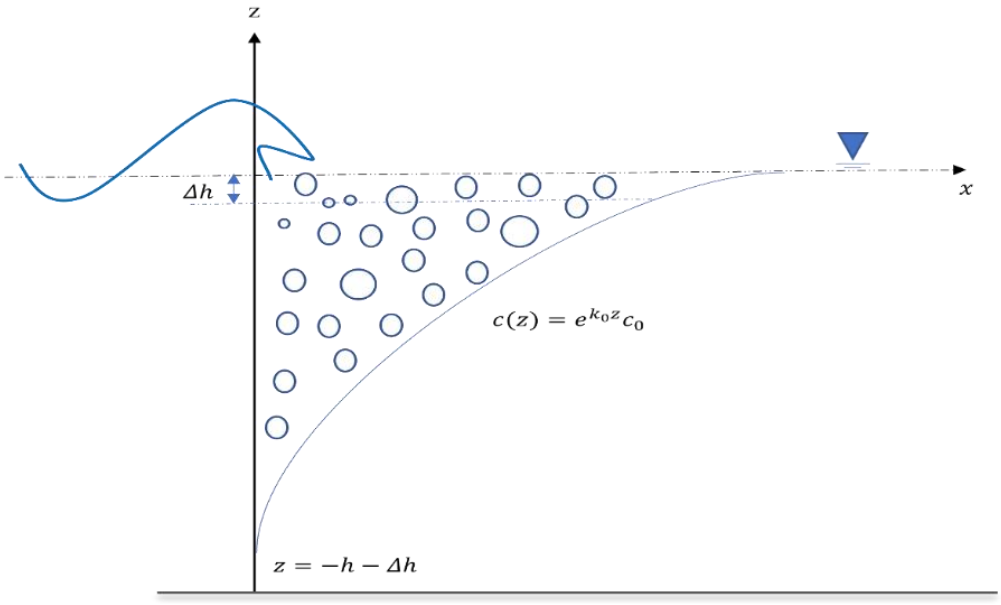

Figure 4.03: Definition sketch of breaking wave propagation with air bubble entrainment for the Hoque, (2002) model.

Given the above assumption, the increase in potential energy can be calculated as follows:

$$\Delta PE = V_a \rho_w g h_G, \tag{4.10}$$

where ρ_w, g, h_G describes in the previous section, and $V_a = \frac{c_0}{k_0} \frac{1-e^{-(k_0 h)}}{1-c_0 e^{-(k_0 h)}}$ is the volume per unit area of attuned air.

Since the entrained air bubbles, which rise due to buoyancy, quickly pass through the water's surface and are released into the air, the potential energy dissipation rate, D_{air}, is proportional to the rate at which the air bubbles rise, t_r. This relationship is expressed as:

$$D_{air} = \frac{\Delta PE}{t_r}\alpha = V_a w_r \alpha \rho_w g, \tag{4.11}$$

where $V_a, w_r, \alpha, \rho_w, g$ are now known parameters.

4.3.2 Modified Air-Bubble-Induced Models for Irregular Waves

This section details the application of the representative wave approach to adjust models for irregular waves. By using this method, the regular wave model is adapted for irregular waves through the representative wave height. Consequently, using this approach, the air bubble model for irregular waves can be formulated (based on Eqs. (4.05), (4.08), and (4.11)) as follows:

Model I

a) $\frac{1}{8}\rho_w g \frac{\partial(H_{rms}^2 c_{gp})}{\partial x} = -K_1 \rho_w g w_r \frac{c_0}{2(1-c_0)} H_{rms},$ (for spilling breakers) (4.12)

b) $\frac{1}{8}\rho_w g \frac{\partial(H_{rms}^2 c_{gp})}{\partial x} = -K_2 \rho_w g w_r \frac{c_0}{2(1-c_0)} \gamma h,$ (for plunging breakers) (4.13)

where K_1 and K_2 are the new unknown coefficients.

Führboter, (1970) conditions have been employed in the above equations, so that the depth of aeration, y can be expressed as $y \propto H(x)$ and, $y \propto H_b$, for spilling and plunging breaking waves, respectively. Here, $H_b = h\gamma$ is the individual breaking wave height(Thornton and Guza, 1983).

Model II

Given the same phenomenon, Hoque's model has been modified in the following manner:

$$\frac{1}{8}\rho_w g \frac{\partial(H_{rms}^2 c_{gp})}{\partial x} = -K_3 \rho_w g w_r \frac{c_0}{k_0} \frac{1-e^{-(k_0 h)}}{1-c_0 e^{-(k_0 h)}}, \tag{4.14}$$

where K_3 is the new undetermined coefficient.

4.3.3 Modified Models Solution for the Wave Height

Model I

This section presents the solution for Model I, which addresses spilling and plunging breakers, applied to two distinct bathymetries: a plane-sloping beach profile and an irregular beach profile.

4.3.3.1 Uniform plane sloping beach

For deriving the analytical solutions of the modified models, the study focuses on wave transmission in shallow water along a constant plane-sloping beach. Here, the water depth is expressed as $h = xtan\theta$, where θ is the slope of the beach.

Spilling breaking

Eq. (4.12) is reformulated for the case of spilling breakers condition as follows:

$$\frac{1}{8}\rho_w g \frac{d}{dx}(H_{rms}^2\sqrt{gh}) = -K_1\rho_w g w_r \frac{c_0}{2(1-c_0)} H_{rms}, \tag{4.15}$$

where $c_{gp} = \sqrt{gh}$.

Simplification yields:

$$\frac{d}{dx}(H_{rms}^2\sqrt{h}) = -AH_{rms}, \tag{4.16}$$

where $A = 4K_1 w_r \frac{c_0}{\sqrt{g}(1-c_0)}$.

Letting $Y = H_{rms}^2\sqrt{h}$ and $h = xtan\theta$ into Eq. (4.16), that yields:

$$\frac{dY}{dh} = \frac{A}{tan\theta}\frac{Y^{1/2}}{h^{1/4}}. \tag{4.17}$$

Integrating the above Eq. (4.17), it gives:

$$Y^{(1/2)} = ah^{(3/4)} + const., \tag{4.18}$$

where $a = \frac{2A}{3tan\theta}$.

To obtain the analytical solution, consider the shallow water boundary condition which can be composed as follows:

$$Y = Y_0 = H_0^2\sqrt{h_0}, \qquad \text{at} \qquad h_0 \leq \frac{L}{20}. \tag{4.19}$$

Therefore Eq. (4.18), yields:

$$Y = a^2\left(h^{\frac{3}{4}} - h_0^{\frac{3}{4}} + \frac{\sqrt{Y_0}}{a}\right)^2, \tag{4.20}$$

From the previously stated equation, the following equation is derived after simplifying it and working backward in terms of H_{rms}:

$$H_{rms} = a\sqrt{h}\left(1 - \left\{\frac{h_0}{h}\right\}^{\frac{3}{4}} + \frac{\sqrt{Y_0}}{ah^{\frac{3}{4}}}\right). \tag{4.21}$$

When the depth is very shallow, then Eq. (4.21) yields:

$$H_{rms} \cong a\sqrt{h}, \text{ as } h \to 0. \tag{4.22}$$

This implies that the RMS wave height is related to the water depth. This result aligns with the findings of Thornton and Guza (1983), which confirmed that the RMS wave height within the shore correlates with the water depth.

Plunging breaking

Similarly, Eq. (4.13) yields the following for plunging breakers:

$$\frac{1}{8}\rho_w g\frac{d}{dx}(H_{rms}^2\sqrt{gh}) = -K_2\rho_w g w_r \frac{c_0}{2(1-c_0)}\gamma h, \tag{4.23}$$

where $c_{gp} = \sqrt{gh}$.

Eq. (4.23) can be reorganized and transformed into:

$$\frac{d}{dx}(H_{rms}^2\sqrt{h}) = -Bh, \tag{4.24}$$

where $B = 4K_2 w_r \frac{c_0 \gamma}{\sqrt{g}(1-c_0)}$.

Supposing $Y = H_{rms}^2 \sqrt{h}$ and $h = x tan\theta$ into Eq. (4.24), which produces:

$$\frac{dY}{dh} = \frac{B}{tan\theta} h. \tag{4.25}$$

Integrating Eq. (4.25), which provides:

$$Y = bh^2 + const., \tag{4.26}$$

where $b = \frac{B}{2tan\theta}$.

Similarly, the following boundary condition can be applied:

$$Y = Y_0 = H_0^2 \sqrt{h_0}, \qquad \text{at} \qquad h_0 \leq \frac{L}{20}. \tag{4.27}$$

Therefore, Eq. (4.26) yields the following:

$$Y = bh^2 + Y_0 - bh_0^2. \tag{4.28}$$

Simplified in terms of H_{rms}, gives:

$$H_{rms} = \sqrt{b} h^{\frac{3}{4}} \left(1 - \left\{\frac{h_0}{h}\right\}^2 + \frac{Y_0}{bh^2}\right)^{\frac{1}{2}}. \tag{4.29}$$

For very shallow water, Eq. (4.29) provides:

$$H_{rms} \cong \sqrt{b} h^{\frac{3}{4}}, \qquad \text{as } h \to 0. \tag{4.30}$$

This indicates that the RMS wave height is related to the water depth, incorporating the effects of air bubbles within the inner surf zone. This conclusion is also consistent with Thornton and Guza's (1983) observations.

4.3.3.2 Irregular beach profile

Finding an analytical solution for irregular beach profiles is challenging for the models discussed. Therefore, a numerical approach, specifically the forward finite

difference scheme, is employed to find the solution of these models (see Fig. 3.02 in Chapter 3).

Model I (spilling breakers)

Applying a similar approach as outlined in Section 4.3.3.2 of Chapter 3 results in:

$$\frac{(H_{rms}^2\sqrt{h})_{i+1}-(H_{rms}^2\sqrt{h})_i}{\Delta x} = -AH_{rms,i}. \tag{4.31}$$

Eq. (4.31) can be simplified into:

$$(H_{rms})_{i+1} = \sqrt{\frac{(H_{rms}^2\sqrt{h})_i - A\Delta x H_{rms,i}}{(\sqrt{h})_{i+1}}}. \tag{4.32}$$

Model I (plunging breakers)

Similarly for Eq. (4.13), that yields:

$$\frac{(H_{rms}^2\sqrt{h})_{j+1}-(H_{rms}^2\sqrt{h})_j}{\Delta x} = -Bh_j. \tag{4.33}$$

Reshuffling Eq. (4.33), it supplies:

$$(H_{rms})_{j+1} = \sqrt{\frac{(H_{rms}^2\sqrt{h})_j - B\Delta x h_j}{(\sqrt{h})_{j+1}}}. \tag{4.34}$$

Model II (for both breakers)

Due to the presence of multiple nonlinear terms in Model II, finding an analytical solution for various beach profiles and breaker types (plane-sloping bathymetry and irregular-sloping bathymetry) proves to be highly challenging. Therefore, by applying the same approach to Eq. (4.14), the following equation is obtained:

$$\frac{(H_{rms}^2\sqrt{h})_{k+1}-(H_{rms}^2\sqrt{h})_k}{\Delta x} = -C\left\{\frac{1-e^{-(k_0h)_k}}{1-c_0e^{-(k_0h)_k}}\right\}, \tag{4.35}$$

where $C = 8K_3w_r\frac{c_0}{k_0\sqrt{g}}$.

After rearranging Eq. (4.35), it gives:

$$(H_{rms})_{k+1} = \sqrt{\frac{(H_{rms}^2\sqrt{h})_k - C\Delta x\left\{\frac{1-e^{-(k_0h)_k}}{1-c_0e^{-(k_0h)_k}}\right\}}{(\sqrt{h})_{k+1}}}. \quad (4.36)$$

Thus, with all variables on the right-hand sides of Eq. (4.32), Eq. (4.34), and Eq. (4.36) being known these equations can be utilized to compute the RMS wave height.

4.3.4 Review of Existing Air-Bubble-Induced Momentum Equations

4.3.4.1 Hoque et al., (2019) momentum equation

To analyze momentum conservation in a water column with a sloping bed and a free surface, it is important to balance the hydrostatic pressure forces with the radiation stress gradient. When incorporating the effects of air bubbles ($\bar{\eta}^{/}$), the forces acting on a plane at $x = x_0 + dx$ must be assessed. This assessment includes contributions from both hydrostatic pressure and radiation stress. The momentum flux Ix at the location of x = x0 considering the influence of air bubbles, is given by (see Fig. 4.02):

$$I_x = \int_{-h}^{-y} g\rho_w(\bar{\eta}^{/} - z)dz + \int_{-y}^{0} g\rho_w(\bar{\eta}^{/} - z)dz + \int_{0}^{\Delta h} g\rho_w(\bar{\eta}^{/} - z)dz + \int_{\Delta h}^{\bar{\eta}^{/}} g\rho_w(\bar{\eta}^{/} - z)dz + S_{xx}^{\acute{}}. \quad (4.37)$$

Simplification yields the following:

$$I_x = \left\{h^2 + 2h\bar{\eta}^{/} - \frac{c_0}{3}(y^2 + 3y\bar{\eta}^{/}) + (1 - c_0)\bar{\eta}^{/2}\right\}\frac{g\rho_w}{2} + S_{xx}^{\acute{}}, \quad (4.38)$$

where $S_{xx}^{\acute{}} = \frac{1}{8}\rho_w g H^2\left\{\frac{3}{2} - \left(\frac{2c_0^2 - c_0}{2-2c_0}\right)\right\} + yc_0^2 w_r^2 \rho_w\left(\frac{4-3c_0}{12}\right)$ represents the radiation stress caused by the air bubbles effect, and ρ_w, g, y, h are described in section 4.2.1.1.

Owing to the nonhorizontal nature of the bottom (depicted in Fig. 4.02), an external force is exerted as a result of bottom friction. This force includes a horizontal component, which can be characterized as follows:

$$I_b = \left\{(h + \bar{\eta}^{/})\frac{dh}{dx}dx - \left(\frac{yc_0}{2} + c_0\bar{\eta}^{/}\right)\frac{dh}{dx}dx\right\}g\rho_w. \quad (4.39)$$

When waves move closer to the shore and break, the momentum flux towards the shore decreases, which leads to compensating forces acting on the water column. A set of waves that hit the coast directly may be considered, with the assumption that they are perpendicular to the shoreline. Within a short distance *dx*, the balance of forces can be defined as follows:

$$I_1 = I_2 - I_b \text{ which implies } I_x = \left(I_x + \frac{dI_x}{dx}dx\right) - I_b. \tag{4.40}$$

Using Taylor series expansion, and calculate I at the centre, while I_b represents the reaction force of the bottom in the direction of x and utilising Eq. (4.38), (4.39), and (4.40), the following momentum equation is obtained:

$$\frac{d\bar{\eta}^{/}}{dx} = -\frac{1}{\rho_w g\left\{\left(h+\bar{\eta}^{/}\right)-c_0\bar{\eta}^{/}-\frac{c_0 y}{2}\right\}}\frac{dS_{xx}^{'}}{dx} + \frac{\left(\frac{c_0\bar{\eta}^{/}}{2}+\frac{c_0 y}{3}\right)}{\left\{\left(h+\bar{\eta}^{/}\right)-c_0\bar{\eta}^{/}-\frac{c_0 y}{2}\right\}}\frac{dy}{dx} - \frac{\left(c_0\bar{\eta}^{/}+\frac{c_0 y}{2}\right)}{\left\{\left(h+\bar{\eta}^{/}\right)-c_0\bar{\eta}^{/}-\frac{c_0 y}{2}\right\}}\frac{dh}{dx}. \tag{4.41}$$

To simplify the above equation, let $M = \left\{\left(h+\bar{\eta}^{/}\right) - c_0\bar{\eta}^{/} - \frac{c_0 y}{2}\right\}$, $N = \left(\frac{c_0\bar{\eta}^{/}}{2} + \frac{c_0 y}{3}\right)$ and $P = \left(c_0\bar{\eta}^{/} + \frac{c_0 y}{2}\right)$, that implies:

$$\frac{d\bar{\eta}^{/}}{dx} = -\frac{1}{\rho_w g M}\frac{dS_{xx}^{'}}{dx} + \frac{N}{M}\frac{dy}{dx} - \frac{P}{M}\frac{dh}{dx}. \tag{4.42}$$

This is the modified momentum equation owing to the effect of the air bubble.

4.3.4.2 Hoque, (2002) momentum equation

In this study, the author assumed that the increase in level results from flow bulking induced by air bubbles, which may improve the wave set-up in the surf zone. Therefore, it is important to note that the actual wave set-up, $\bar{\eta}^{/}$, should include the rise in the water level caused by entrained air bubbles. The expression for the actual wave set-up, $\bar{\eta}^{/}$, can be written as follows:

$$\bar{\eta}^{/} = \bar{\eta} + \Delta h, \tag{4.43}$$

where $\bar{\eta}^{/}$ is the wave set-up entrained by the air bubbles, Δh is the water level rise due to entrained air bubbles whose value can be written as $\Delta h = \int_{-h-\Delta h}^{0} c(z)dz$ which implies $\Delta h = \frac{c_0}{k_0}\frac{1-e^{-(k_0 h)}}{1-c_0 e^{-(k_0 h)}}$ and $\bar{\eta}$ is the elevation of the mean water level (see Fig.

4.03) that is derived from the modified momentum balance equation, which is written as follows:

$$\frac{d\bar{\eta}}{dx} = -\frac{1}{g\rho_w(h+\bar{\eta})}\frac{dS_{xx}^{''}}{dx}, \tag{4.44}$$

where $S_{xx}^{''}$ is the radiation stress entrained by the air bubbles effect, and the value of this is as follows:

$$\frac{2Ek}{sinh2kh}\int_{-h-\Delta h}^{0}(1-C_0e^{k_0z})\left[cosh^2k(h+z)-\left\{sinhk(h+z)+\frac{C_0}{(1-C_0e^{k_0z})(k^2-k_0^2)}\left[e^{k_0z}\left(kk_0coshk(h+z)-k_0^2sinhk(h+z)\right)-kk_0e^{k_0h}\right]\right\}\right]dz+\frac{\rho_w gH^2}{16}+\rho_w gh\Delta h,$$

where *k* represents the wave number that is derived from the dispersion relation of the linear wave theory.

4.3.5 Modified Air-Bubble-Induced Momentum Equation for Irregular Waves

This section focuses on modifying models for irregular waves using the representative wave approach. The approach involves directly utilising the regular wave model for irregular waves by incorporating the representative wave height (H_{rms}).

Model I

Before using the representative wave approach, it is necessary to classify wave breakers into different types. The classification of wave breakers is important because it can impact the characteristics of wave loads acting on structures in the surf zone. Therefore, understanding the different types of wave breakers is essential for developing models of wave loads on coastal structures. The two main types of wave breakers are spilling and plunging breakers, which are distinguished based on how they break.

Therefore, the Führboter, (1970) conditions have been employed, so that the penetration depth y is expressed as: $y \propto H(x) = c_1 * H(x)$ and, $y \propto H_b = h\gamma$, for spilling and plunging breaking waves, respectively.

Therefore, Eq. (4.41) is reformulated for the spilling breaking waves as follows:

$$\frac{d\bar{\eta}'}{dx} = -\frac{1}{\rho_w g\left\{\left(h+\bar{\eta}'\right)-c_0\bar{\eta}'-\frac{c_0c_1H}{2}\right\}}\frac{dS_{xx}'}{dx} + \frac{\left(\frac{c_0\bar{\eta}'}{2}+\frac{c_1c_0H}{3}\right)}{\left\{\left(h+\bar{\eta}'\right)-c_0\bar{\eta}'-\frac{c_0c_1H}{2}\right\}}\frac{d(c_1H)}{dx} - \frac{\left(c_0\bar{\eta}'+\frac{c_0c_1H}{2}\right)}{\left\{\left(h+\bar{\eta}'\right)-c_0\bar{\eta}'-\frac{c_0c_1H}{2}\right\}}\frac{dh}{dx}, \tag{4.45}$$

and plunging breaking waves as follows:

$$\frac{d\bar{\eta}'}{dx} = -\frac{1}{\rho_w g\left\{\left(h+\bar{\eta}'\right)-c_0\bar{\eta}'-\frac{c_0h\gamma}{2}\right\}}\frac{dS_{xx}'}{dx} + \frac{\left(\frac{c_0\bar{\eta}'}{2}+\frac{h\gamma c_0}{3}\right)}{\left\{\left(h+\bar{\eta}'\right)-c_0\bar{\eta}'-\frac{c_0h\gamma}{2}\right\}}\frac{d(h\gamma)}{dx} - \frac{\left(c_0\bar{\eta}'+\frac{c_0h\gamma}{2}\right)}{\left\{\left(h+\bar{\eta}'\right)-c_0\bar{\eta}'-\frac{c_0h\gamma}{2}\right\}}\frac{dh}{dx}. \tag{4.46}$$

Now, applying the 'representative wave approach' by incorporating the representative wave height (H_{rms}), Eqs. (4.45) and (4.46) can be rewritten as

$$\frac{d\bar{\eta}'}{dx} = -\frac{1}{\rho_w gL}\frac{dS_{xxs}'}{dx} + \frac{Q}{L}K_1\frac{dH_{rms}}{dx} - \frac{R}{L}\frac{dh}{dx}, \tag{4.47}$$

and

$$\frac{d\bar{\eta}'}{dx} = -\frac{1}{\rho_w g\acute{L}}\frac{dS_{xxp}'}{dx} + \frac{\acute{Q}}{\acute{L}}\gamma\frac{dh}{dx} - \frac{\acute{R}}{\acute{L}}\frac{dh}{dx}, \tag{4.48}$$

where $L = \left\{\left(h+\bar{\eta}'\right) - c_0\bar{\eta}' - \frac{K_1c_0H_{rms}}{2}\right\}$, $Q = \left(\frac{c_0\bar{\eta}'}{2} + \frac{K_1c_0}{3}H_{rms}\right)$, $R = \left(c_0\bar{\eta}' + \frac{K_1c_0}{2}H_{rms}\right)$, $S_{xxs}' = \frac{1}{8}K_1\rho_w gH_{rms}^2\left\{\frac{3}{2} - \left(\frac{2c_0^2-c_0}{2-2c_0}\right)\right\} + c_0^2w_r^2\rho_wK_1\left(\frac{4-3c_0}{12}\right)H_{rms}$ (spilling breakers);

and $\acute{L} = \left\{\left(h+\bar{\eta}'\right) - c_0\bar{\eta}' - \frac{c_0\gamma}{2}h\right\}, \acute{Q} = \left(\frac{c_0\bar{\eta}'}{2} + \frac{c_0\gamma}{3}h\right)$, $\acute{R} = \left(c_0\bar{\eta}' + \frac{c_0\gamma}{2}h\right)$, $S_{xxp}' = \frac{1}{8}K_1\rho_w gH_{rms}^2\left\{\frac{3}{2} - \left(\frac{2c_0^2-c_0}{2-2c_0}\right)\right\} + c_0^2w_r^2\rho_w\gamma\left(\frac{4-3c_0}{12}\right)h$ (plunging breakers).

Model II

Similarly, using the representative wave approach and incorporating the representative wave height (H_{rms}), the momentum balance equation can be expressed as:

$$\frac{d\bar{\eta}}{dx} = -\frac{1}{g\rho_w(h+\bar{\eta})}\frac{dS_{xx2}^{'}}{dx}, \tag{4.49}$$

where $S_{xx2}^{'} = \frac{2k}{8sinh2kh}\rho_w g H_{rms}^2 \int_{-h-\Delta h}^{0}(1 - C_0 e^{k_0 z})\left[cosh^2 k(h+z) - \left\{sinhk(h+z) + \frac{C_0}{(1-C_0 e^{k_0 z})(k^2-k_0^2)}\left[e^{k_0 z}\left(kk_0 coshk(h+z) - k_0^2 sinhk(h+z)\right) - kk_0 e^{k_0 h}\right]\right\}\right] dz + \frac{\rho_w g}{16} H_{rms}^2 + \rho_w g h \Delta h$.

The value of $\bar{\eta}$ obtained by solving Eq. (4.49) can be used to calculate the wave set-up for irregular waves via substitution in Eq. (4.43).

4.3.5.1 Modified models solution for wave set-up

It has been found that all of the equations for wave set-up are nonlinear, implying that obtaining a regular solution is impossible. As a result, need to emphasize the use of numerical schemes to solve these equations. Therefore, the same technique has been applied which was described in the previous section (section 4.2.3.2).

Model I (spilling breaker)

The schemes applied in Eq. (4.47) that yield the following equation:

$$\bar{\eta}'_{j+1} = \bar{\eta}_j - \frac{3}{16L}\left(H_{rms(j+1)}^2 - H_{rms(j)}^2\right) + \left(\frac{2c_0^2 - c_0}{8L(2-2c_0)}\right)\left(H_{rms(j+1)}^2 - H_{rms(j)}^2\right) - (4 - 3c_0)\frac{c_0^2 w_r^2 K_1}{12gL}\left(H_{rms(j+1)} - H_{rms(j)}\right) + \frac{QK_1}{L}\left(H_{rms(j+1)} - H_{rms(j)}\right) - \frac{R}{L}\left(h_{j+1} - h_j\right). \tag{4.50}$$

Eq. (4.50) represents the numerical solution of Eq. (4.47) for the spilling breakers.

Model I (plunging breakers)

Similarly, using the above-mentioned schemes in Eq. (4.48) provides:

$$\bar{\eta}'_{j+1} = \bar{\eta}_j - \frac{3}{16\acute{L}}\left(H_{rms(j+1)}^2 - H_{rms(j)}^2\right) + \left(\frac{2c_0^2 - c_0}{8\acute{L}(2-2c_0)}\right)\left(H_{rms(j+1)}^2 - H_{rms(j)}^2\right) - (4 - 3c_0)\frac{c_0^2 w_r^2 k_1 \gamma}{12g\acute{L}}\left(h_{j+1} - h_j\right) + \frac{\acute{Q}\gamma}{\acute{L}}\left(h_{j+1} - h_j\right) - \frac{\acute{R}}{\acute{L}}\left(h_{j+1} - h_j\right), \tag{4.51}$$

which is the numerical solution of Eq. (4.48) for plunging breakers.

All parameters on the right-hand side of Eqs. (4.50) and (4.51) are now known. As a result, calculating the wave set-up using these equations is simple.

Model II

The difference equation of Model II using the above numerical schemes can be written as (from Eq. (4.49)) follows:

$$\bar{\eta}_{i+1} = \bar{\eta}_i - \frac{1}{\rho_w g h_i}\left(S_{xx2,i+1}^{'} - S_{xx2,i}^{'}\right). \tag{4.52}$$

By substituting this value in Eq. (4.43), it is easy to calculate the $\bar{\eta}^{/}$.

4.4 Data Collection

To validate the modified models, it is essential to compare their results against experimental data. This analysis involves examining irregular wave height data gathered from various experiments, which span small-scale, large-scale, and field conditions, as well as diverse wave and bottom topography scenarios. Table 2.2 (in Chapter 2) summarizes the experimental data on RMS wave heights, while Table 2.3 (in Chapter 2) details the data on wave set-up. The collected experimental data are categorized into three groups based on the scale of the experiments: small-scale (SS), large-scale (LS), and field experiments (FE). These unbiased datasets, covering a broad spectrum of test conditions, were used to demonstrate the accuracy of the modified models.

4.5 Findings and Validations

4.5.1 Boundary Requirements

The modified models have two boundary requirements that must be successfully solved. These are the offshore boundary along with the onshore boundary. To apply the model correctly, the offshore boundary must have the following parameters: (i) incident $H_{rms,0}$ (RMS wave height) and the h_0 (water depth) (ii) bottom topography, and (iii) $\bar{T}$ (average wave period). The incident set-down was also required to compute the wave set-up, which is written as $\bar{\eta}$. The onshore boundary aligns with the experimental bathymetry data sets.

4.5.2 Classifying Wave Breakers

Consider an irregular wave travelling across the beach, as shown in Fig. 4.01. Once this wave starts to break, the wave's energy and height start to decrease as it approaches the shore. Thus, it is important to find the breaking point of the waves. In this regard, consider the suggestion made by Thornton and Guza, (1983), which can be expressed as follows:

$$H_{rms,b} = \gamma h, \tag{4.53}$$

where $H_{rms,b}$ represents the RMS wave height at the breaking point, h is the water depth, and γ is an arbitrary constant with a value of 0.42 (Thornton and Guza, 1982).

The different types of wave breakers are determined using the parameter of surf similarity, developed by Battjes, (1974), as described in Chapter 3 (section 3.4.2.).

4.5.3 Determination of c_0, y and k_0

Void fraction, c_0

To calculate the value of void fraction c_0, Hoque and Aoki, (2005) void fraction relation has been used for wave types with either spilling or plunging breaking. They discovered a relationship for calculating the void fraction, c_0, as a function of the breakpoint-to-shoreline distance, which is written as follows:

Spilling breaking waves

$$c_0 = \frac{(x-x_b)}{L_0} * 0.80 \quad \text{for} \quad 0.20 \geq \frac{(x-x_b)}{L_0} \geq 0, \tag{4.54}$$

$$c_0 = 0.238 - 0.39\frac{(x-x_b)}{L_0} \quad \text{for} \quad 0.20 \leq \frac{(x-x_b)}{L_0}, \tag{4.55}$$

Plunging breaking waves

$$c_0 = \frac{(x-x_b)}{L_0} * 1.285 \quad \text{for} \quad 0.14 \geq \frac{(x-x_b)}{L_0} \geq 0, \tag{4.56}$$

$$c_0 = 0.285 - 0.75\frac{(x-x_b)}{L_0} \quad \text{for} \quad 0.14 \leq \frac{(x-x_b)}{L_0}, \tag{4.57}$$

where x_b is the horizontal distance from the wave maker to the breakpoint towards the shoreline (see Fig. 4.02).

Depth of aeration, y

To determine the depth of aeration *y*, employed the relation proposed by Hoque et al., (2019) for breaking waves. They proposed a relationship that allows the calculation of the depth of aeration *y*, based on the breakpoint-to-shoreline distance. This relationship can be expressed as follows:

$$y = \frac{c_0 z}{c(z) - c_0}, \tag{4.58}$$

where *c(z)* is the fraction of the air volume per unit width and z, c_0 correspond to the vertical distance, and reference void fraction at $z = 0$, respectively (as shown in Fig. 4.02).

Decay parameter, k_0

The parameter k_0, which characterizes the void fraction distribution in the surf zone, was determined by Hoque and Aoki, (2005) through theoretical curve fitting based on experimental data from both spilling and plunging breaking waves by the following equation:

$$K = k_0 H, \tag{4.59}$$

where H is a local wave height and K is the new dimensionless parameter.

Their analysis led to the identification of the value K as 3.75 for spilling breakers and 4.00 for plunging breakers. In this study, these specific values are employed for the numerical calculations.

4.5.4 Determination of Unknown Coefficients K_1, K_2, and K_3

To determine three unknown coefficients in the modified models, the nonlinear regression analysis is employed, incorporating constraint values of c_0 to the test data (LS, SS, and FE). Determining the values of coefficients K_1 and K_2 for Model I, Eq. (4.12) and Eq. (4.13) were used for spilling and plunging breakers, respectively. However, for Model II, Eq. (4.14) was utilised to compute the coefficient K_3 for both

the different types of breakers. A comparison between the measured and predicted wave heights was made for LS experiments, SS experiments, and FE, as shown in Fig. 4.04. Table 4.1 lists the values of the unknown coefficients K_1, K_2, and K_3 with RMS wave height scaling error.

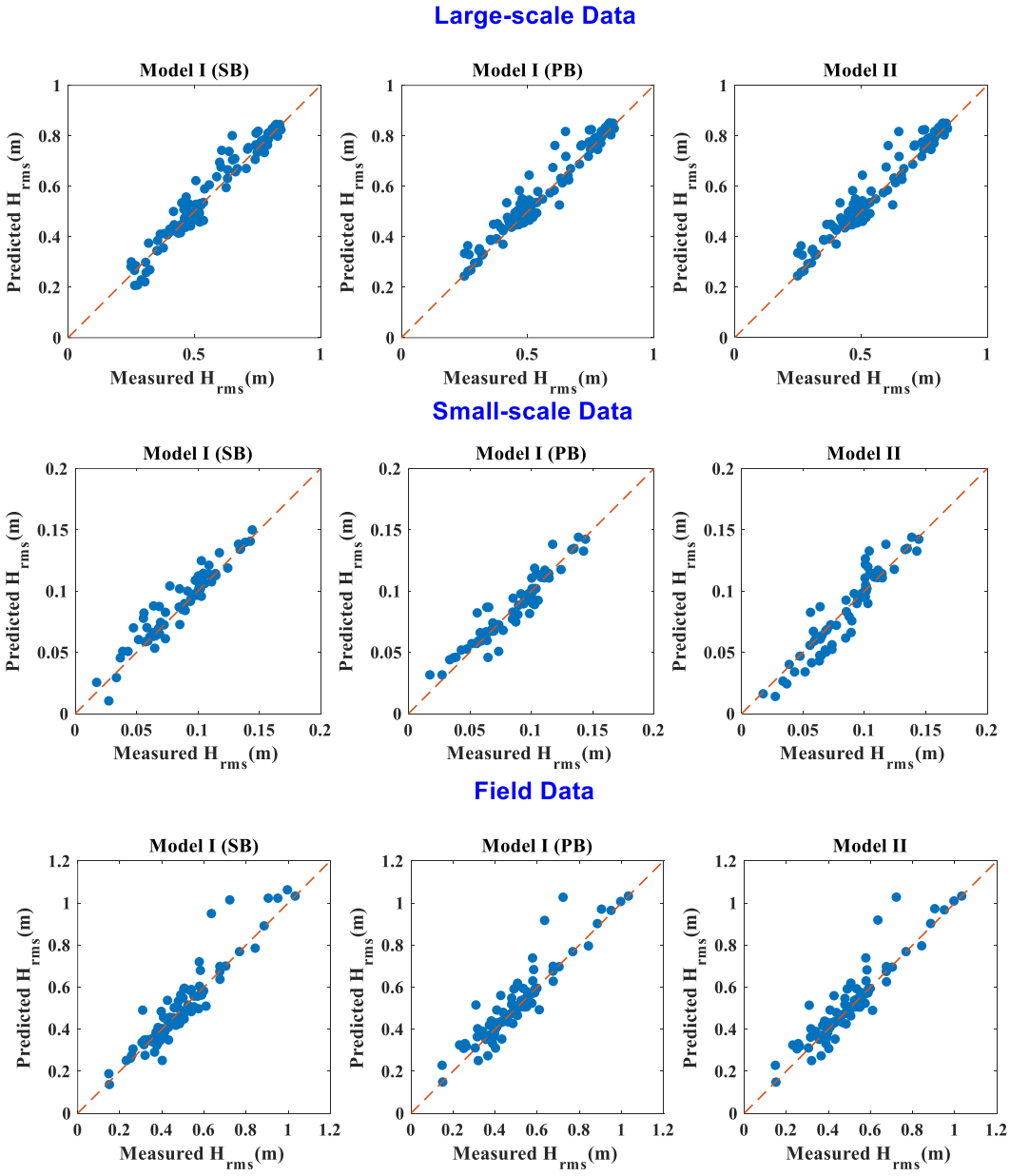

Figure 4.04: Comparison of predicted and measured (LS, SS, and FE data) RMS wave height, H_{rms} using Model I and (SB = Spilling Breaker and PB = Plunging Breaker) Model II.

4.4.5 Modified Models Vs. Experimental Data

To determine wave height and wave set-up, the first step is to classify the breaker types based on incident wave parameters and surf similarity criteria. For a plane-sloping beach, wave heights are calculated using Eq. (4.22) for spilling breakers and Eq. (4.30) for plunging breakers within Model I. For beaches with irregular slopes, the corresponding equations are Eqs. (4.32) and (4.34) for spilling and plunging breakers, respectively. In Model II, Eq. (4.36) is applicable for both breaker types and slopes. Following the calculation of RMS wave height, the wave set-up is computed using Eqs. (4.50) and (4.51) for spilling and plunging breakers in Models I and II. For scenarios involving both breaker types, Eqs. (4.52) and (4.43) are used. The void fraction, crucial for these calculations, is determined using Eqs. (4.54) and (4.55) for spilling breakers and Eqs. (4.56) and (4.57) for plunging breakers. The calculated void fraction (c_0) ranges from 13% to 15% for spilling breakers and 16% to 18% for plunging breakers, which is consistent with the values suggested by Blenkinsopp and Chaplin (2011), Huang et al. (2009), and Hoque and Aoki, (2005). The grid sizes (Δx) used in this study are based on the experimental measurements, with adjustments made to a maximum of 5 m when necessary. Specifically, a grid size of 0.2–1.5 m is used for small-scale (SS) experiments, and 2.1–5.0 m for large-scale (LS) and field experiments (FE) (Rattanapitikon, 2008). The coefficients (K_1, K_2, and K_3) used in the calculations for both models are detailed in Table 4.1.

Within Figs. 4.05 and 4.06, a comparative analysis was performed between the proposed modified models (Model I and II) and established regular wave models (Hoque et al. 2019; Hoque 2002) using a diverse range of experimental data sets, including large-scale (LS), small-scale (SS), and field experiments (FE). The comparison highlighted a substantial discrepancy, with errors exceeding 30% for the regular wave models when juxtaposed with the experimental data. This significant deviation underscores the inadequacy of the regular wave models in accurately representing irregular wave conditions. The results indicate that the regular wave models, which are primarily designed for scenarios with uniform wave characteristics, fail to capture the complexities and variations inherent in irregular wave patterns. Consequently, this discrepancy points to the necessity for more robust models that can account for the variability and intricacies of irregular waves.

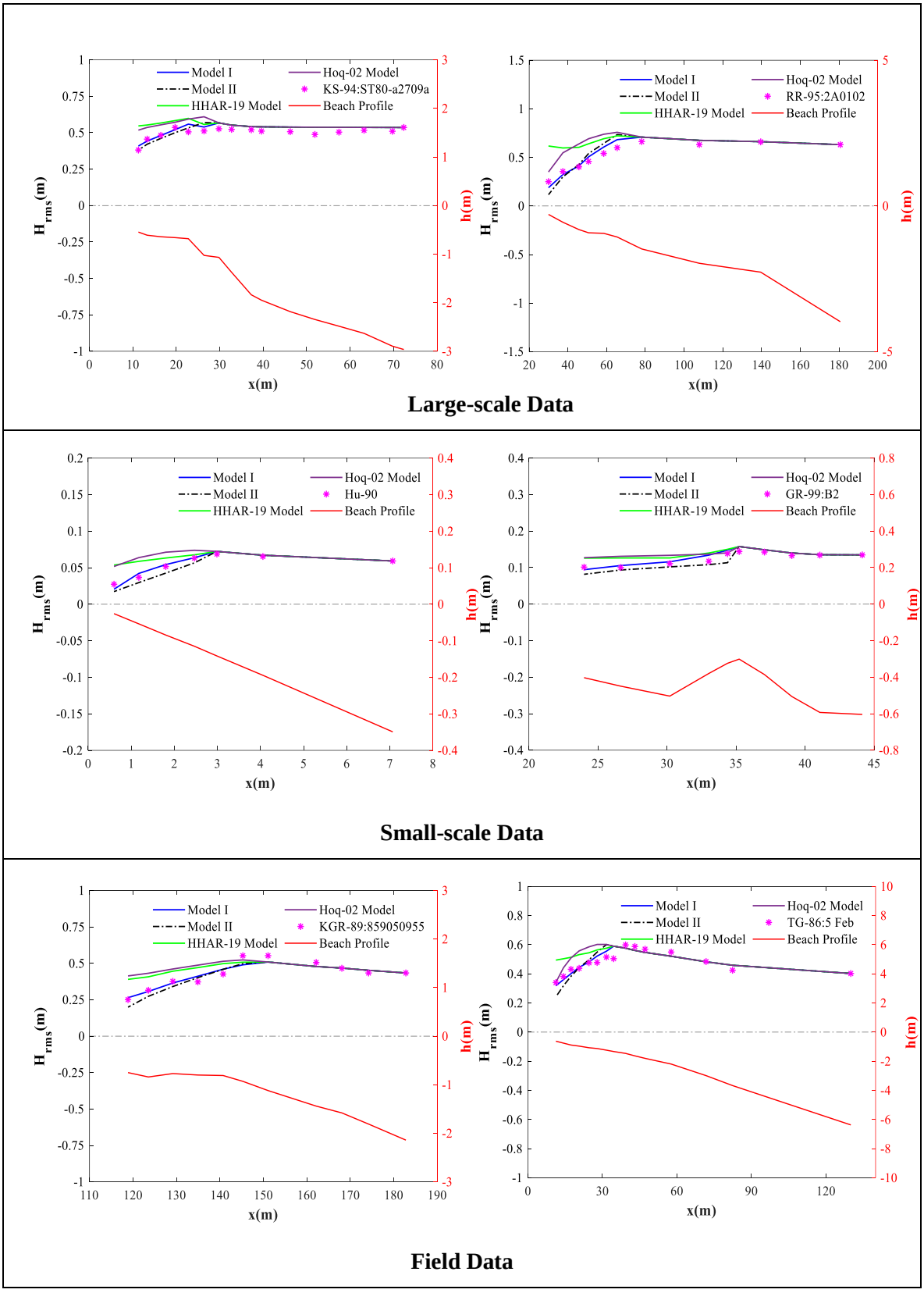

Figure 4.05: Comparison of regular and irregular energy dissipation model with various experimental data (LS, SS, and FE) and regular wave models (Hoque et al., 2019 as HHAR-19; Hoque 2002, as Hoq-02) including related beach profiles.

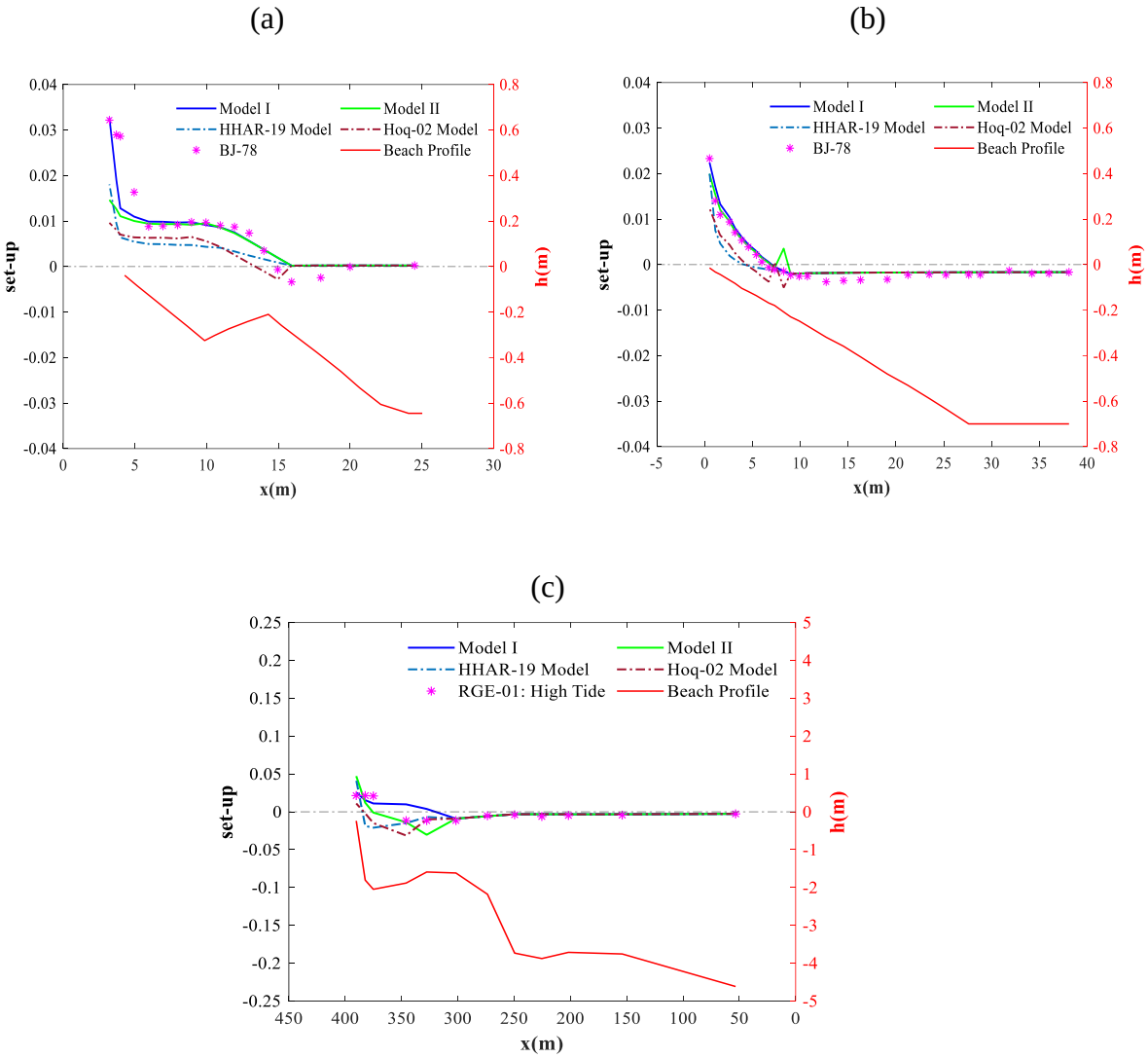

Figure 4.06: Variations of wave set-up for Models I and II based on various experimental data ((a): BJ-78, (b) St-85, and (c) RGE-01) and regular wave models (HHAR-19 and Hoq-02) including corresponding beach profiles.

The void fraction profile exhibits variability depending on the breaking points. First, identify the breaking point, followed by obtaining void fraction profile data for every gauge across all data cases. Analysis revealed that the maximum void fraction ranged from 13% to 19% across all cases. Subsequently, create a comparison in Fig. 4.07 using the maximum void fraction data from models I and II alongside experimental data (LS, SS, and FE). Specifically, the best matches between the void fraction of model I and experimental data were observed to be a maximum of 13%-15% and 16%-18% for spilling and plunging breaking waves, respectively, as well as 14%-16% and 17%-19% for model II.

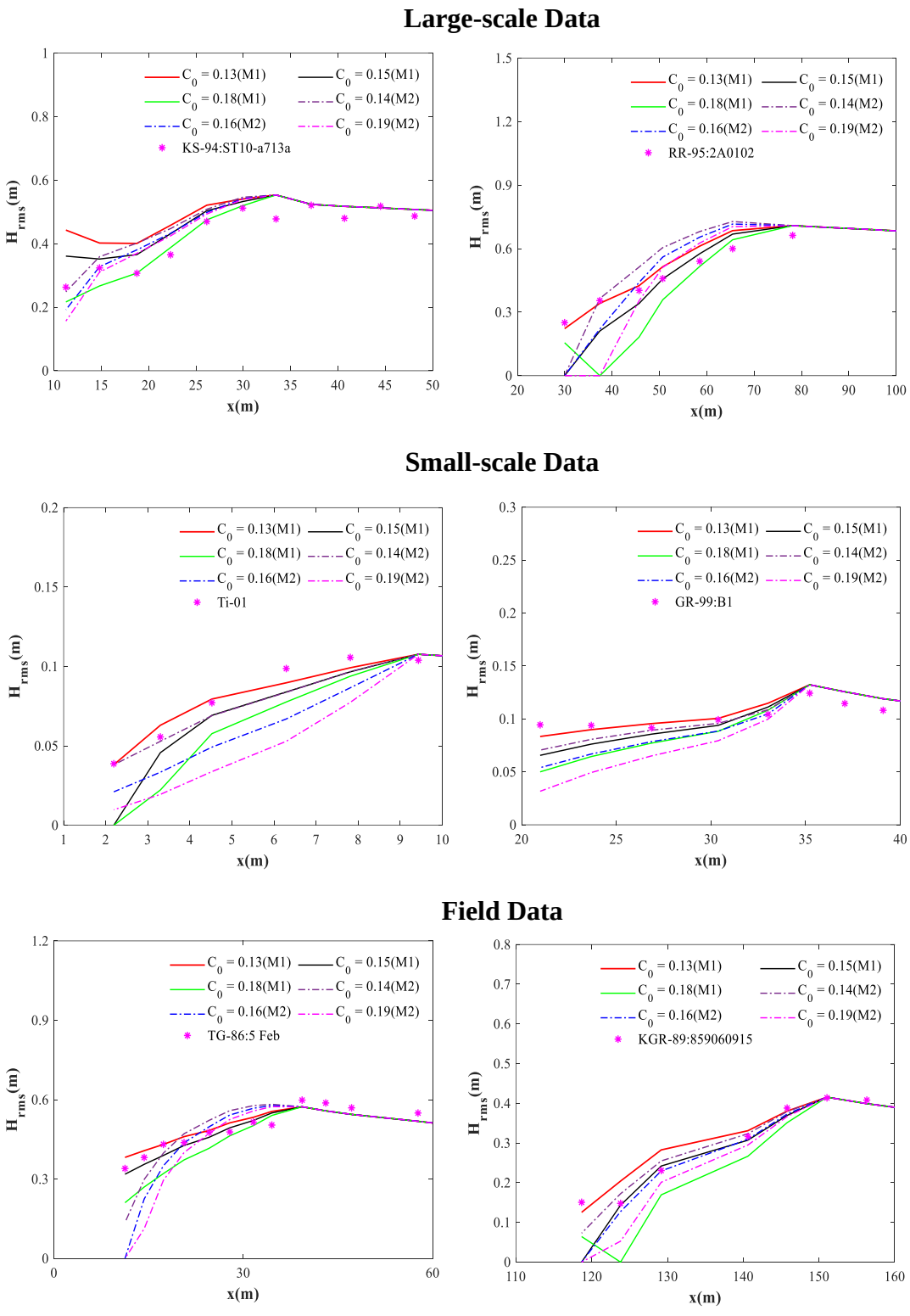

Figure 4.07: Variation of void fraction (Model I and II) with different experimental data (LS, SS, and FE).

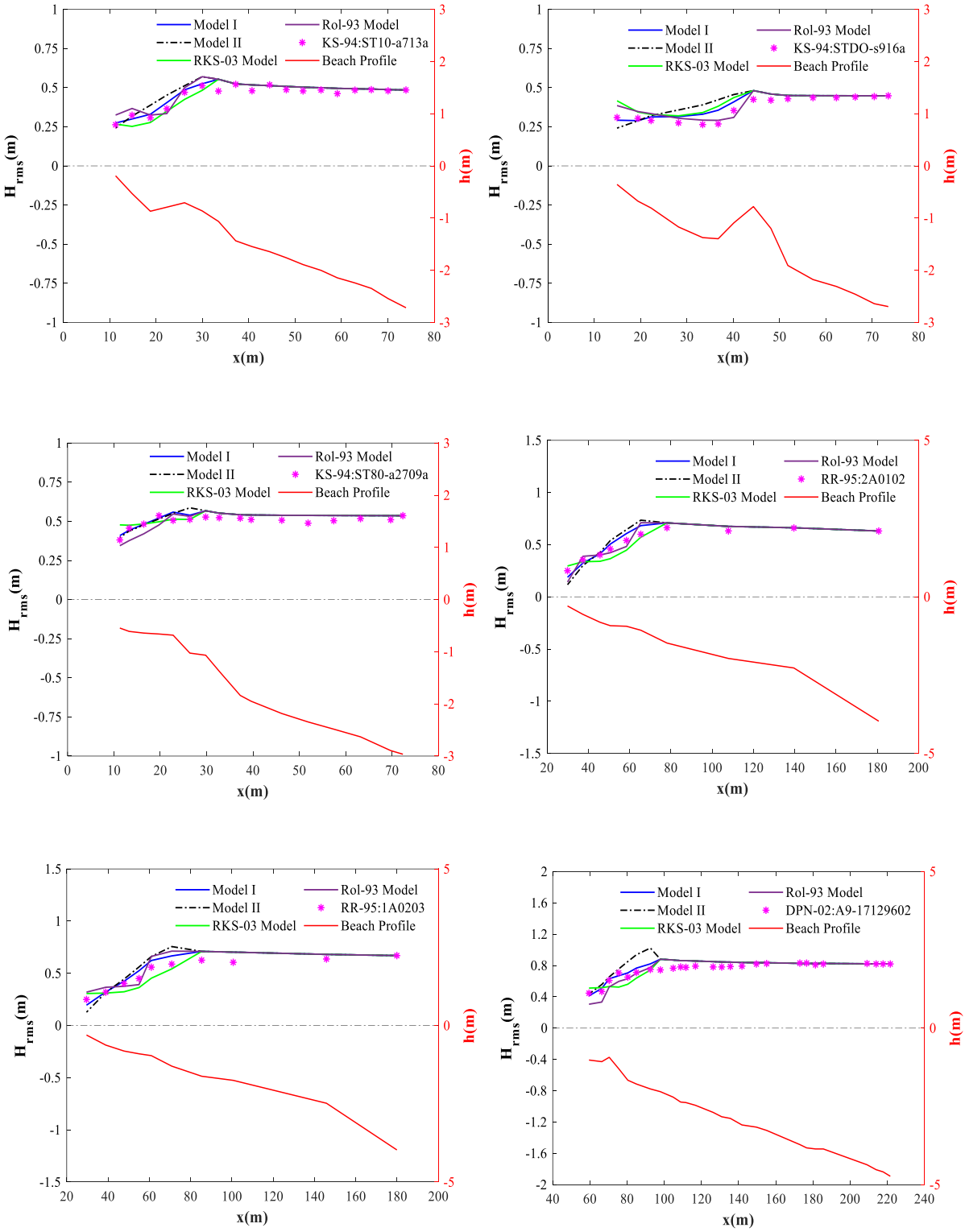

Figure 4.08: Comparison of the RMS wave height of Models I and II with data from LS experiments and different models (Rattanapitikon, Karunchintadit, and Shibayama, 2003 as RKS - 03; Roelvink, 1993 as Rol - 93) including various beach profiles.

Fig. 4.08 illustrates a comparison of the modified models (I and II) and LS datasets collected from several sources (see Table 2.2 in Chapter 2) and models (RKS-03 and Rol-93), which demonstrates an excellent match for computing the RMS wave height. In this particular instance, the execution of models (I and II) is excellent for the Kraus and McKee Smith, (1994) and Roelvink and Reniers, (1995) data series. However, there is some variation after wave breaking for the data collected by Dette et al., (2002). One possible reason for this is that the data were collected during storm-wave conditions. Because, stormy waves along with increased heights and winds, lead to notable air entrainment and turbulence, surpassing the capabilities of general wave energy dissipation models and resulting in prediction inaccuracies.

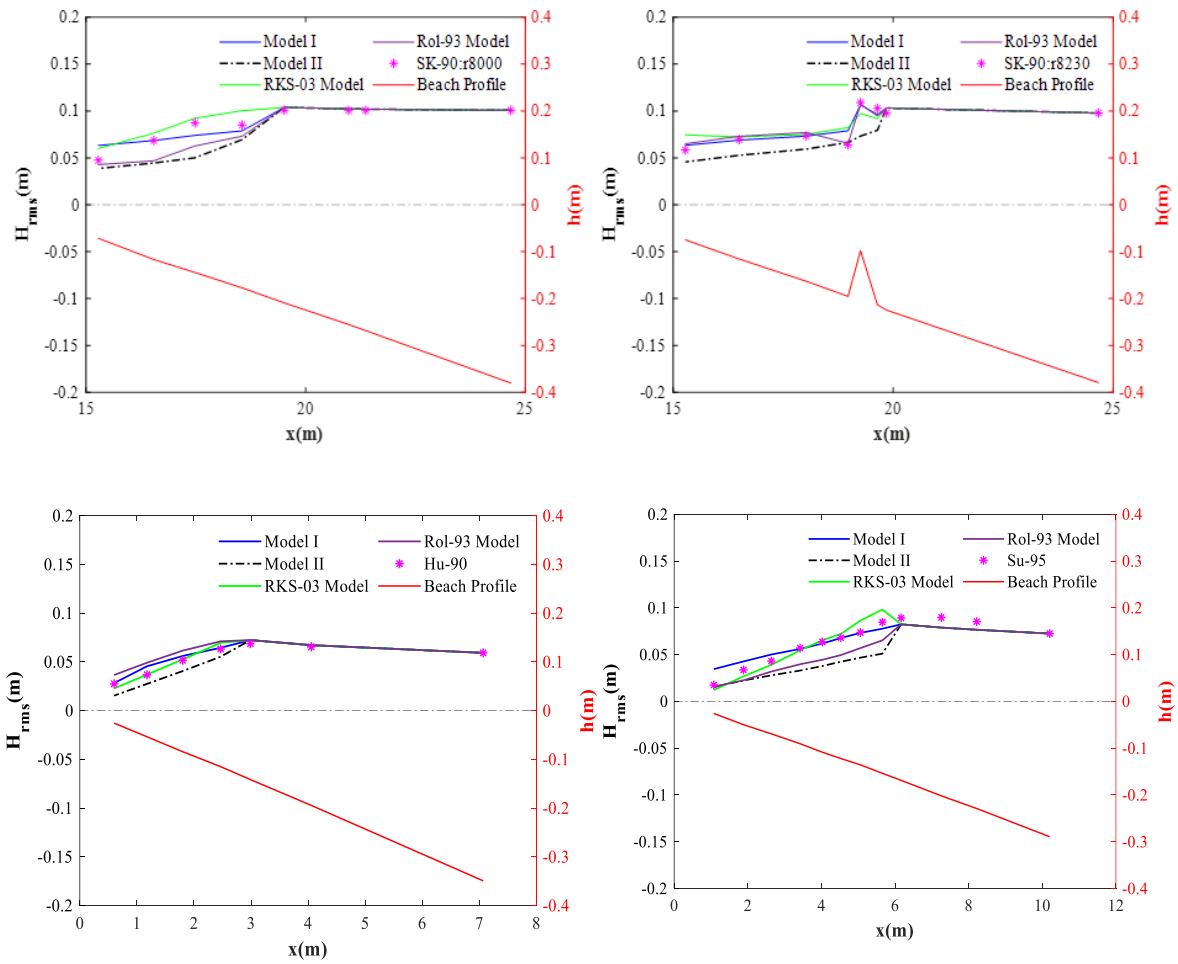

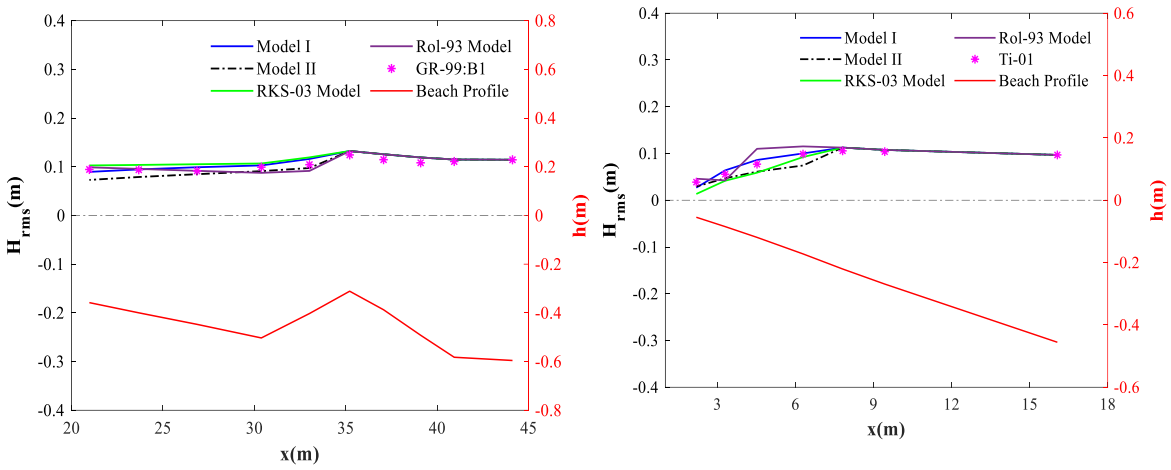

Figure 4.09: RMS wave height comparison of Models I and II with SS experimental data and different models (RKS – 03 and Rol - 93) including various beach profiles.

Furthermore, an observation was made regarding the performance of the modified models, particularly model I, which exhibited slightly superior performance compared to the Rol-93 and RKS-03.

The outcomes from the modified models (I and II) were assessed against small-scale (SS) datasets (see Table 2.2 in Chapter 2) provided by various researchers and compared with two established models, RKS–03 and Rol–93, as shown in Fig. 4.09. Model I closely matched nearly all the datasets, while Model II showed a minor increase in error, though not significant. Both models effectively represented the data, particularly for plane-sloping beaches, consistent with the findings of some researchers (Smith and Kraus 1990; Hurue 1990; Sultan 1995; Ting 2001). They also performed well in scenarios involving quick transitions, such as slopes adjacent to narrow bar crests, as noted by some researchers (Smith and Kraus 1990; Grasmeijer and Rijn 1999) Overall, the performance of all models, including Rol–93 and RKS–03, was similar across different conditions, with Model II being the exception.

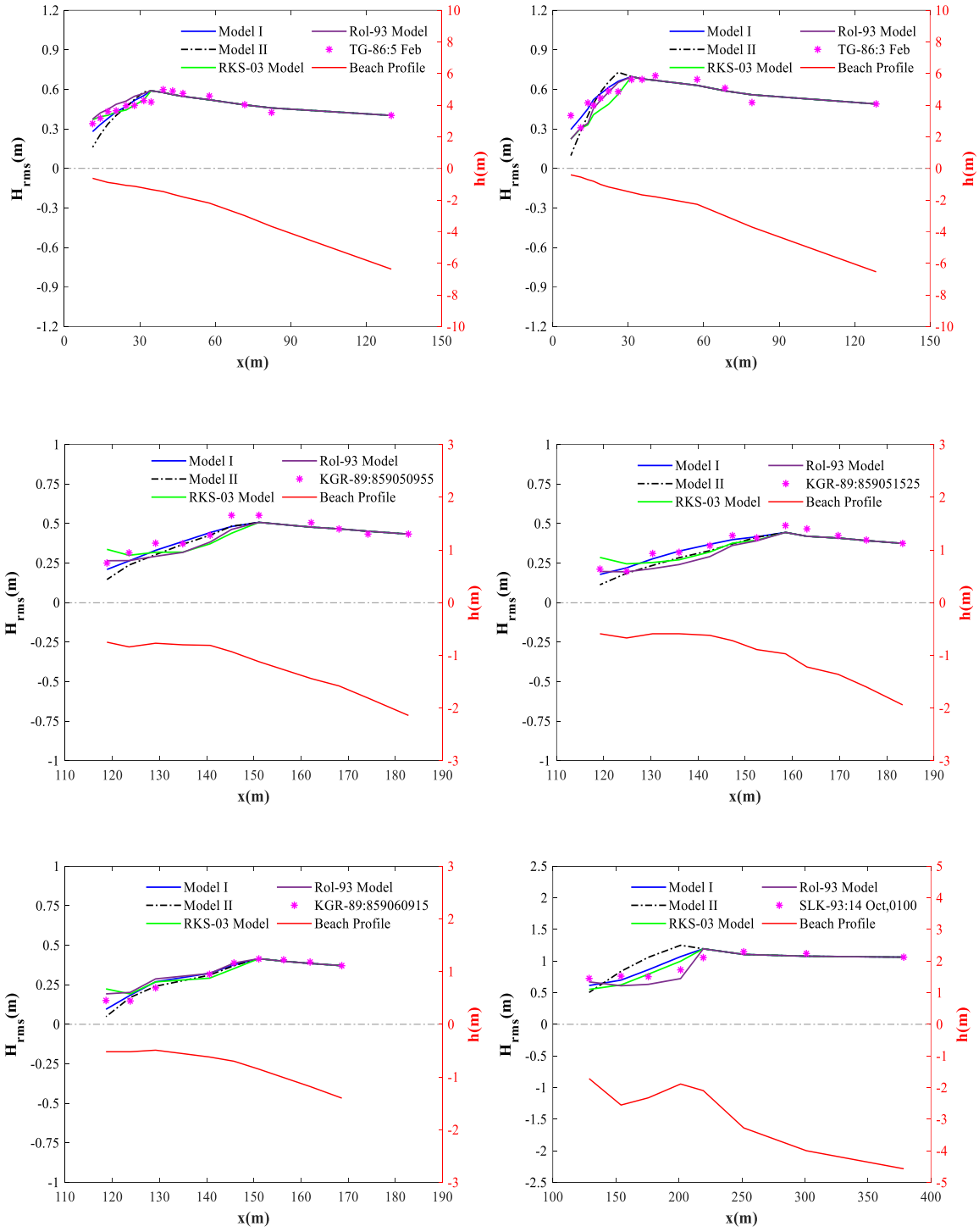

Figure 4.10: RMS wave heights of Models I and II compared with data from FE and different models (RKS - 03 and Rol - 93) including various beach profiles.

Another comparison of the modified models (I and II) with field experimental data, as detailed in Table 2.2 in Chapter 2 was conducted alongside evaluations against two established models, RKS–03 and Rol–93. The results of this comparison are shown in Fig. 4.10. The modified models (I and II) demonstrated strong performance with the

data from Thornton and Guza, (1986) and Kraus et al., (1989). But, discrepancies were observed near the wave-breaking point with data from McKee Smith et al., (1993), likely due to the presence of a mound at the breaking point. Notably, Model I outperformed both the Rol–93 and RKS–03 models in these scenarios. This indicates that Model I is highly effective in predicting RMS wave height across various beach profiles. On the other hand, Model II encountered difficulties in accurately calculating RMS wave height, particularly in areas with mounds on the beach and near the shoreline. Therefore, it is evident that the modified Model I efficiency is considerably satisfactory in terms of predicting the RMS wave height for any beach profile. However, Model II has certain limitations in calculating the RMS wave height, particularly the presence of mounds on the beach and near the shoreline.

Additionally, Fig. 4.11 presents a comparison of wave set-up calculations using different experimental data (refer to Table 2.3 in Chapter 2) and the established model DDD–85 (Dally, Dean, and Dalrymple, 1985). The modified models (I and II) performed exceptionally well against the data provided by Stive, (1985), highlighting their robustness in predicting wave set-up.

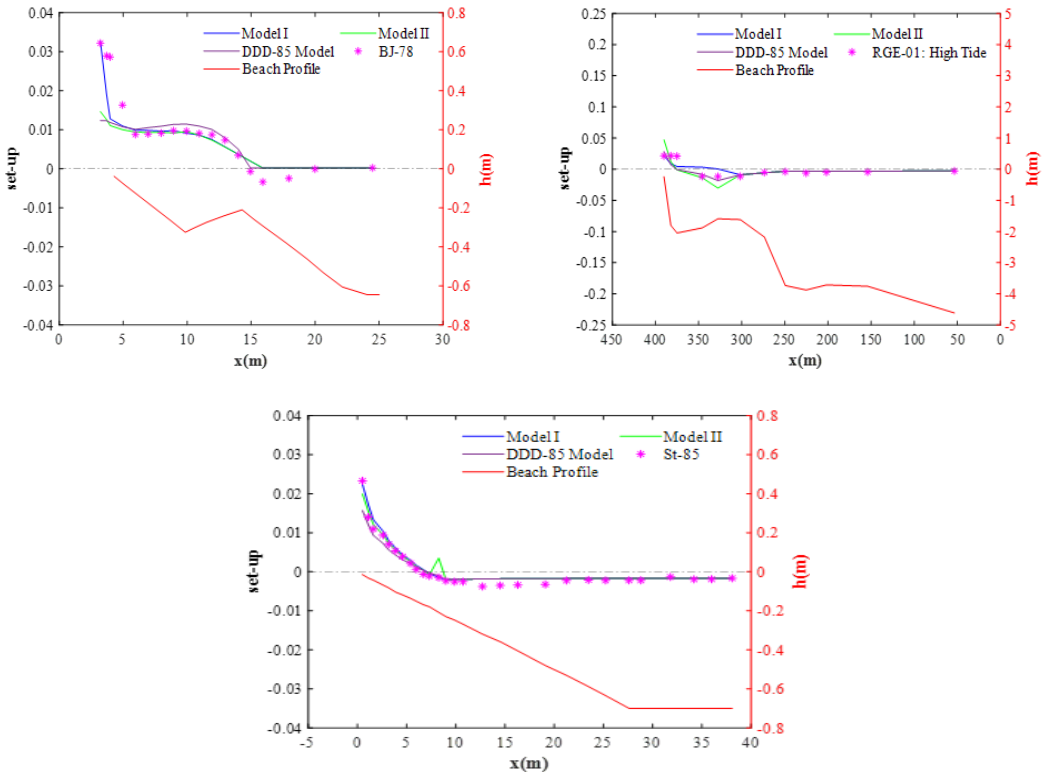

Figure 4.11: Variations of wave set-up for Models I and II based on various experimental data and DDD – 85 model.

Conversely, Model II shows some inaccuracies near the coastline when compared with the experimental data from Battjes and Janssen, (1978). Additionally, for the data provided by Raubenheimer et al. (2001), both modified models (I and II) tend to slightly overestimate the wave set-up. A comparison with the DDD–85 model reveals that the current models, especially Model I, perform marginally better. Overall, the results for wave set-up obtained from the modified models (I and II) are consistent with the findings from Hoque et al. (2019) and Hoque, (2002).

4.5.6 Error Analysis

In this section, the overall accuracy of the modified models (I and II) is displayed by exhibiting the NRMSE for each case (RMS wave height and set-up).

The NRMSE term is used to quantify the error. This term serves as an overall indicator of the model's performance. According to Jadhav and Chen, (2013), the NRMSE can be written as follows:

$$NRMSE = \sqrt{\frac{1}{n}\sum_{k=1}^{n}\left(\frac{(H_{rms})_{p,k}}{(H_{rms})_{m,k}} - 1\right)^2}, \tag{4.60}$$

where n is the total number of wave data points, $(H_{rms})_{p,k}$ is the predicted RMS wave height, and $(H_{rms})_{m,k}$ is the measured RMS wave height.

The NRMSE of the modified models (I and II) for the wave height and wave set-up are listed in Tables 4.1 and 4.2, respectively.

Table 4.1: Unknown coefficient determination with NRMSE.

Model Name	Coefficients Name	Coefficient Values	Error (%)			Avg. Error(%)
			SS	LS	FE	
Model I	K_1	0.34	11.33	5.6%	7.14	8.03
	K_2	0.36	11.71	5.83%	7.39	8.31
Model II	K_3	0.41	15.78	6.06%	8.26	10.03

For calculating H_{rms}, the modified Models I and II yielded an average NRMSE of 11.52% (with averages of 11.71% and 11.33% for the two models) and 15.78%, respectively, when compared to SS experimental data. This error rate is notably higher than that observed for LS data, which had an average NRMSE of 5.72% (averaging 5.6% and 5.83%) and 6.06%, respectively. This discrepancy suggests potential scaling issues with the models. However, the models performed reasonably well with FE data, showing an average NRMSE of 7.27% (averaging 7.14% and 7.39%) for Model I and 8.26% for Model II. Model I had an average NRMSE of 8.17%, which was lower than Model II's average NRMSE of 10.03%. For wave set-up calculations, the average NRMSE for the modified models was 9.38% for Model I and 11.15% for Model II, aligning closely with the performance of regular wave models.

Table 4.2: Overview of the NRMSE of $\bar{\eta}'$ in percentage (Models I and II).

Resources	NRMSE (Model I)	NRMSE (Model II)	Categories	Average NRMSE
RGS-01	11.89	8.68	FE	9.38 (Model I) 11.15 (Model II)
St-85	4.03	5.25	SS	
BJ-78	12.23	19.53	LS	

As noted by Rattanapitikon, (2008), the overall qualitative assessment of the modified Model I is very good for calculating both the RMS wave height and wave set-up. In contrast, Model II received a good qualitative ranking for these calculations.

4.6 Conclusions

This chapter utilized the representative wave approach to enhance two energy dissipation models tailored for spilling and plunging breaking waves. These modified models were employed to calculate the RMS wave heights and wave set-ups, based on principles of energy and momentum conservation. The conceptual framework for these models was primarily derived from the air bubble model of wave breakers established by Hoque et al. (2019) and Hoque, (2002). The breaking criterion for irregular waves by Thornton and Guza, (1983) and the surf similarity parameter by Battjes, (1974) were used to identify breaking waves and classify their types.

The validity of the modified models (I and II) was corroborated by a range of experimental data from small-scale, large-scale, and field experiments across different wave and bottom topography scenarios. The computed RMS wave heights closely matched the experimental data, though minor discrepancies were noted near mounds and coastlines. Similarly, the modified models performed well in predicting wave set-up, with some errors observed near the breaking points. The analysis revealed that air bubble contributions to wave energy dissipation were between 16% and 18% for plunging breakers, and 13% to 15% for spilling breakers. These values align closely with the experimental findings of Hoque and Aoki, (2005) and Huang et al. (2009). The average normalized root mean square error (NRMSE) for RMS wave height was 8.33% for Model I and 10.6% for Model II, demonstrating a high level of agreement with the experimental data. For wave set-up, the average NRMSE was 9.38% for Model I and 11.15% for Model II, indicating effective prediction capabilities. Model I showed slightly better accuracy compared to Model II. Despite some inconsistencies near the shoreline and mounds, the modified models (I and II) successfully simulated RMS wave height and set-up under various wave conditions and beach profiles. Their key strengths lie in their simplicity and ease of application, making them valuable tools for comparing with more complex models.

CHAPTER 5

Transformation of Spectral Significant Wave Height and Set-up Due to Entrained Air Bubbles in Breaking Waves

5.1 Abstract

Accurately assessing the transformation of wave height is crucial for coastal engineering and the design of coastal structures. To achieve this, a reliable energy dissipation model is necessary. This chapter introduced an optimized dissipation model that accounts for the impact of air bubbles to precisely determine changes in spectral significant wave height (H_{m0}) and wave set-up for irregular waves in the breaking phase. The approach adapted existing regular wave-breaking models—those incorporating air bubble effects—by creating new formulations suitable for irregular waves. These models utilize the probability distribution of broken waves to enhance precision. H_{m0} was derived using the energy balance equation, and wave set-up was calculated based on the momentum balance equation. The model's validity was tested across a range of scenarios, including small-scale and large-scale experiments as well as field data. Among the proposed models, Model-I (M-I) demonstrated particularly strong performance, showing lower error indices (P20), root-mean-square relative error (RMSRE), and Brier skill score (BSS) values for both H_{m0} and wave set-up calculations. Therefore, Model-I is recommended for accurate predictions of H_{m0} and wave set-up transformations.

5.2 Introduction

Understanding wave behavior in the surf zone is essential for addressing coastal engineering challenges, including the design of coastal structures and analysis of beach variations. As illustrated in Fig. 4.01 in Chapter 4, wave breaking occurs in shallow waters due to the bottom slope as waves approach the shoreline, leading to the entrainment of numerous air bubbles near the breaking point. This interaction introduces significant complexity into the dynamics of air bubbles and the flow fields of breaking waves (Chanson and Jaw-Fang 1997; Koga 1982; Deane and Stokes 2002). The energy dissipated in this process contributes to turbulence and heat flux, reducing

wave height as waves move shoreward (Paul et al. 2016). Irregular breaking waves, which are more complex than regular waves, distribute energy over a broader area (Rattanapitikon, Karunchintadit, and Shibayama 2003). The impact of air bubble entrainment during the wave-breaking process highlights the need to thoroughly examine wave-breaking dynamics to understand their effects on coastal structures, sediment transport, wave set-up, overtopping, run-up, and coastal management strategies.

Representative wave height is crucial for understanding coastal dynamics and designing coastal infrastructure. Key forms of representative wave heights include root-mean-square wave height (H_{rms}), highest one-tenth wave height ($H_{1/10}$), spectral significant wave height (H_{m0}), mean wave height (H_m), and maximum wave height (H_{max}). Among these, H_{m0} is most widely used in coastal engineering due to its prevalence in spectral analysis results and modern wave hindcasts. Although deep-water values for H_{m0} are commonly available, there is often a lack of data for shallow-water depths. To address this gap, models for transforming wave heights are necessary for accurate calculations in shallow-water regions.

Recent advancements in coastal engineering have increasingly utilized soft computing methods, like machine learning algorithms, to model significant wave heights and associated parameters. Various algorithms are now employed to forecast wave height by analyzing key input variables, including wind speed, wave period, and atmospheric pressure (Sadeghifar and Barati 2018; Sadeghifar et al. 2017; Mostafa et al. 2023; Ikram et al. 2023; Sadeghifar et al. 2022; Adnan et al. 2023; Sadeghifar and Barati 2018; Afzal et al. 2023; Duong et al. 2023; Chen et al. 2023). These algorithms leverage methods like regression, neural networks, and ensemble techniques, relying on extensive historical data to refine their predictions. By training on diverse datasets from multiple locations, these models are able to capture the intricate relationships between input factors and wave height, offering valuable insights for oceanographic study, weather prediction, and marine science & engineering. Nevertheless, the effectiveness of these models is heavily dependent on the availability of comprehensive experimental data, highlighting the necessity for robust observational datasets to guarantee accurate predictions.

Even though advanced machine learning methods have become popular for predicting significant wave heights, traditional techniques are still essential for accurately forecasting wave height and set-up. These conventional methods are grounded in established standards and methodologies, providing reliable standards for verifying new approaches. Although the improvements in machine learning, traditional methods offer a solid foundation for comparison and verification. This study focused on developing new empirical or semi-empirical mathematical formulas to address these needs. The models developed for shallow water wave height calculations primarily rely on three key concepts: air bubbles, stable energy, and bores. Le Mehaute, (1962), who pioneered the bore model, proposed that both broken waves and hydraulic jumps are equally effective in dissipating wave energy. Various models have since been developed to estimate average wave height in the surf zone (Alsina and Baldock, 2007; Apotsos et al., 2008; Battjes and Janssen, 1978; Thornton and Guza, 1983). The energy dissipation model introduced by Dally et al. (1985) was based on the principle of stable energy. Taking into consideration this concept Swift, (1993) and Rattanapitikon and Shibayama, (1998) improved their models. On the other hand, numerous studies have explored air bubble entrainment in breaking waves and its impact on the surf zone, addressing aspects such as gas exchange, representative wave height transformation, and sediment transport (Blenkinsopp and Chaplin, 2011; Deike et al., 2016; Hoque et al., 2021; Hossain et al., 2022; Koga, 1982; Leng and Chanson, 2019; Shi et al., 2023). Among them, Hossain and Araki (2022, 2023) recently recommended two models that incorporate the effects of air bubbles: one parametric modeling and the other representative wave modeling. Their findings indicated that the representative approach slightly outperformed the parametric model in predicting the root mean square (RMS) wave height following wave set-up.

However, these models typically focus on calculating the RMS wave height rather than the spectral significant wave height. Significant wave heights are crucial for understanding wave characteristics, energy distribution, and long-term wave climate variability, especially in shallow water environments. Despite this, many measurement instruments and results are reported in terms of significant wave heights. Additionally, wave set-up, which refers to the increase in water level due to waves, can cause significant damage to coastal areas and is an important factor in beach management. Unfortunately, there has been limited research on wave set-up.

Despite the development of various models using different approaches to evaluate wave height and surf zone dynamics, there is currently no model that can simultaneously calculate both spectral significant wave height and wave set-up accounting for air bubble entrainment in irregular waves. While previous research has examined air entrainment during wave breaking, there has been limited investigation into how air bubbles affect the transformation of spectral significant wave height and wave set-up in shallow water. This study aims to fill this gap. Typically, wave height is determined using energy conservation principles, while wave set-up is calculated based on momentum conservation laws. The following section discusses the governing equations derived from these principles.

5.3 Model Formulation

Predicting wave breaking, a complex process in the surf zone is particularly challenging. In this area, waves lose energy as they break, leading to a decrease in wave height and a rise in the water level as they approach the shore. This study utilized the energy flux law and momentum flux law as governing equations to forecast wave height reduction and the resulting wave set-up along the shoreline.

5.3.1 Energy Conservation Law

To represent the evolution of wave height in a dissipative surf zone, the study employs the energy balance equation for one-dimensional wave propagation which can be written as follows:

$$\frac{\partial E c_g}{\partial x} = -D. \tag{5.01}$$

Here E stays the wave energy; $c_g = \sqrt{gh}$ indicate the group celerity in shallow water areas; g stands for the gravitational acceleration; x is the horizontal distance to the shoreline; h is the water depth; and D denotes the energy dissipated as waves travel from the breaking point to the coastline. This study assumes that all parameters are derived from linear wave theory, with the neglect of energy dissipation caused by bottom friction.

The moments of a wave spectrum are crucial in spectral analysis because they provide a characterization of the spectrum and demonstrate how the spectral representation of

waves relates to significant wave height. The zero moments of the wave spectrum, referred to as m_0, signifies the total wave energy. This moment is determined by integrating the wave spectrum, $S(f)$, across the complete frequency range f. Corresponding to Goda, (2000), the zero moment can be expressed as follows:

$$m_0 = \frac{1}{t_N}\int_0^{t_N} \xi^2 dt = \int_0^{\infty} S(f) df, \tag{5.02}$$

Here t stands for the time, t_N represents the total time of a wave record, and ξ is the surface elevation.

The relationship among the zero moment, total energy density, and significant wave height, H_{m0}, of a wave train in linear wave theory can be expressed as follows:

$$E = \frac{2}{t_N}\int_0^{t_N} \frac{\rho_w g}{2} \xi^2 dt = \rho_w g\, m_0, \tag{5.03}$$

where ρ_w signifies the density of water.

But, H_{m0} expressed as follows:

$$H_{m0} = 4\sqrt{m0}. \tag{5.04}$$

therefore, Eq. (5.03) yields:

$$E = \frac{\rho_w g}{16} H_{m0}^2. \tag{5.05}$$

Consequently, Eq. (5.01) yields:

$$\frac{1}{16}\rho_w g \frac{\partial\left(H_{m0}^2 c_g\right)}{\partial x} = -D. \tag{5.06}$$

The examination of wave height variations as waves approach the shoreline can be conducted using the energy-conservation equation (Eq. (5.06)). To do this, the energy dissipation rate, D, needs to be substituted into Eq. (5.06), enabling the calculation of wave height along the coastline. The main challenge is to determine the rate of energy loss for waves that break in the surf zone. To calculate D, this study first reviewed two regular wave models that account for air bubble entrainment and then developed new models for irregular breaking waves in the subsequent section.

5.3.1.1 Existing Air Bubble Models for Regular Waves

5.3.1.1.1 Model by Hoque et al., (2019)

A brief overview of this model can be found in Section 4.3.1.1. This model is expressed as follows:

$$D_a = \frac{\Delta PE}{t_r}\alpha, \tag{5.07}$$

where all the parameters are described in the relevant section.

Ultimately, the values of these parameters provide the subsequent models:

$$D_a = g w_r \alpha \rho_w \frac{y c_0}{2(1-c_0)}. \tag{5.08}$$

5.3.1.1.2 Model by Hoque, (2002)

A comprehensive overview of this model, along with the related parameters, is provided in Section 4.3.1.2, and the model is written as follows:

$$D_a = \frac{\Delta PE}{t_r}\alpha = \Delta h w_r \alpha \rho_w g. \tag{5.09}$$

5.3.1.2 Proposed models

The energy dissipation process in an irregular wave train due to wave breaking is highly complex. In creating a new model, the principle outlined by Roelvink, (1993) has been followed. This principle suggests that the energy loss rate per unit area, D, in an irregular wave train is likely influenced by two distinct factors and can be stated as follows:

$$D = Q_{br} D_a. \tag{5.10}$$

Here Q_{br} signifies the fraction of breaking waves, and D_a is the energy lost due to the presence of air bubbles in regular wave scenarios.

As waves approach shallow-water regions, the breaking process becomes increasingly important, causing the wave height distribution to deviate from the Rayleigh distribution (Hossain, Rahman, and Hoque 2022; Wu et al. 2016; Mendez, Losada, and

Medina 2004; Jurjen A. Battjes and Groenendijk 2000). Thus, the following equation for Q_{br} suggested by Stringari and Power, (2019) constructed from the Weibull distribution is for this study:

$$Q_{br} = e^{-\left(\frac{H_b}{H_{rms}}\right)^{\kappa}}. \tag{5.11}$$

Here H_{rms} signifies the root-mean-square wave height, H_b is the individual wave height at the breaking point, and κ is the shape parameter.

According to Thornton and Guza, (1983), the average rate of energy loss can be approximated by multiplying the energy dissipated by a given broken wave of height H with the associated probability of wave breaking, as expressed in Eq. (5.10). Building on this principle, this study presents a model for irregular waves, designated as Model-I (M-I), as follows::

M-I:

$$D_{Ia} = Q_{br} D_a = \int_{\mathbf{0}}^{\infty} g w_r \alpha \rho_w \frac{c_0}{2(1-c_0)} Q_{br} y P(H) dH, \tag{5.12}$$

where D_{Ia} represents the energy dissipation rate owing to the influence of attuned air bubbles for an irregular wave train, Q_{br} found from Eq. (5.11), D_a come from Eq. (5.08), and $P(H) = \frac{\kappa}{H_{rms}}\left(\frac{H}{H_{rms}}\right)^{\kappa-1} e^{-\left(\frac{H}{H_{rms}}\right)^{\kappa}}$ is the PDF of the Weibull distribution. Other parameters such as $g, w_r, \alpha, \rho_w, c_0, and\ y$ described in the previous sections.

Now, according to Führboter, (1970), y is written as follows:

$$y \propto H(x) = d_1 * H(x) \qquad \text{for spilling breakers} \tag{5.13}$$

$$y \propto H_b = \gamma h \qquad \text{for plunging breakers} \tag{5.14}$$

where d_1 is an arbitrary constant, and $H_b = \gamma h$, γ =0.42 (Thornton and Guza 1982).

Applying Eq. (5.13) in Eq. (5.12) yields:

$$D_{IaS} = \frac{g w_r \alpha d_1 \rho_w c_0}{2(1-c_0)} \int_{\mathbf{0}}^{\infty} H e^{-\left(\frac{H_b}{H_{rms}}\right)^{\kappa}} \frac{\kappa}{H_{rms}}\left(\frac{H}{H_{rms}}\right)^{\kappa-1} e^{-\left(\frac{H}{H_{rms}}\right)^{\kappa}} dH, \tag{5.15}$$

where D_{IaS} is the energy dissipation rate due to attuned air bubbles in spilling breaking waves.

Simplification yields the following model for spiling breakers in terms of H_{m0} (see Appendix C):

$$D_{IaS} = K_1 \rho_w g \frac{C_0}{2\sqrt{2}(1-C_0)} w_r \Gamma \left(\frac{1}{\kappa}+1\right) H_{m0} e^{-\left(\frac{\sqrt{2}\gamma h}{H_{m0}}\right)^{\kappa}}. \tag{5.16}$$

In a similar way using Eq. (5.14) in Eq. (5.12) the following model is found for plunging breaking waves:

$$D_{IaP} = \frac{g w_r \alpha \rho_w c_0}{2(1-c_0)} \gamma \int_0^{\infty} h e^{-\left(\frac{H_b}{H_{rms}}\right)^{\kappa}} \frac{\kappa}{H_{rms}} \left(\frac{H}{H_{rms}}\right)^{\kappa-1} e^{-\left(\frac{H}{H_{rms}}\right)^{\kappa}} dH. \tag{5.17}$$

Here D_{IaP} is the energy dissipation rate owing to the air bubbles effect for plunging breaking waves.

Similarly, simplification yields the following model for plunging breakers in terms of H_{m0} (see Appendix D):

$$D_{IaP} = K_2 \rho_w g \frac{C_0 \gamma}{2(1-C_0)} w_r h e^{-\left(\frac{\sqrt{2}\gamma h}{H_{m0}}\right)^{\kappa}}. \tag{5.18}$$

M-II:

In a comparable fashion, based on the assumptions of Thornton and Guza, (1983), Model-II (M-II) can be constructed using Eq. (5.10) along with the regular wave model presented by Hoque, (2002), as outlined below::

$$D_{IIa} = Q_{br} D_a = \frac{c_0}{k_0} \alpha \rho_w g w_r \int_0^{\infty} \left(\frac{1-e^{-k_0 h}}{1-c_0 e^{-k_0 h}}\right) e^{-\left(\frac{H_b}{H_{rms}}\right)^{\kappa}} P(H)\, dH, \tag{5.19}$$

where D_{IIa} is the energy dissipation rate owing to the entrained air bubbles effect.

Simplification yields the following model in terms of H_{m0} (see Appendix C):

$$D_{IIa} = K_3 \rho_w g c_0 w_r \left(\frac{1-e^{-k_0 h}}{1-c_0 e^{-k_0 h}}\right) e^{-\left(\frac{\sqrt{2}\gamma h}{H_{m0}}\right)^{\kappa}}. \tag{5.20}$$

5.3.2 Momentum Conservation Law

The conservation of momentum is assumed to be applicable in the context of wave setup. Using this assumption, Longuet-Higgins and Stewart, (1964) formulated the following equation to determine wave setup:

$$\frac{d\bar{\eta}}{dx} = -\frac{1}{\rho_w g(h+\bar{\eta})}\frac{dS_{xx}}{dx}, \tag{5.21}$$

where $\bar{\eta}$ signifies the surface elevation, and S_{xx} represents the radiation stress.

5.3.2.1 Existing models for wave set-up

5.3.2.1.1 Model by Hoque et al., (2019)

The belief of momentum conservation law demonstrates the balance between the pressure force from the mean water surface slope and the radiation stress gradient. To analyze momentum equilibrium in a water region with an inclined bed and exposed surface, while accounting for air bubbles, Hoque et al. (2019) referenced Eq. (5.21) and proposed a revised momentum equation, which can be written as follows:

$$\frac{d\bar{\eta}^{/}}{dx} = -\frac{1}{\rho_w g\left\{(h+\bar{\eta}^{/})-c_0\bar{\eta}^{/}-\frac{c_0 y}{2}\right\}}\frac{dS_{xx}^{'}}{dx} + \frac{\left(\frac{c_0\bar{\eta}^{/}}{2}+\frac{c_0 y}{3}\right)}{\left\{(h+\bar{\eta}^{/})-c_0\bar{\eta}^{/}-\frac{c_0 y}{2}\right\}}\frac{dy}{dx} - \frac{\left(c_0\bar{\eta}^{/}+\frac{c_0 y}{2}\right)}{\left\{(h+\bar{\eta}^{/})-c_0\bar{\eta}^{/}-\frac{c_0 y}{2}\right\}}\frac{dh}{dx}, \tag{5.22}$$

where $(\bar{\eta}^{/})$ represents the wave set-up owing to the effect of the air bubble, and $S_{xx}^{'} = \frac{1}{8}\rho_w g H^2\left\{\frac{3}{2}-\left(\frac{2c_0^2-c_0}{2-2c_0}\right)\right\} + y c_0^2 w_r^2 \rho_w\left(\frac{4-3c_0}{12}\right)$ is the radiation stress owing to the air bubbles effect.

To make straightforward Eq. (5.22), let $M = \left\{\left(h+\bar{\eta}^{/}\right) - c_0\bar{\eta}^{/} - \frac{c_0 y}{2}\right\}$, $N = \left(\frac{c_0\bar{\eta}^{/}}{2} + \frac{c_0 y}{3}\right)$, and $P = \left(c_0\bar{\eta}^{/} + \frac{c_0 y}{2}\right)$, that yields Hoque et al., (2019):

$$\frac{d\bar{\eta}^{/}}{dx} = -\frac{1}{\rho_w g M}\frac{dS_{xx}^{'}}{dx} + \frac{N}{M}\frac{dy}{dx} - \frac{P}{M}\frac{dh}{dx}. \tag{5.23}$$

5.3.2.1.2 Model by Hoque, (2002)

The details of this model can be found in Section 4.3.4.2. The genuine wave set-up, $\bar{\eta}^{/}$, suggested by Hoque, (2002) is writtens as follows:

$$\bar{\eta}' = \bar{\eta} + \Delta h, \tag{5.24}$$

where the $\bar{\eta}$ is obtained from:

$$\frac{d\bar{\eta}}{dx} = -\frac{1}{g\rho_w(h+\bar{\eta})}\frac{dS''_{xx}}{dx}. \tag{5.25}$$

Here S''_{xx} is the radiation stress owing to the air bubbles effect and written as follows:

$$\frac{2Ek}{sinh2kh}\int_{-h-\Delta h}^{0}(1-C_0e^{k_0z})\left[cosh^2k(h+z)-\left\{sinhk(h+z)+\frac{C_0}{(1-C_0e^{k_0z})(k^2-k_0^2)}\left[e^{k_0z}\left(kk_0coshk(h+z)-k_0^2sinhk(h+z)\right)-kk_0e^{k_0h}\right]\right\}\right]dz+\frac{\rho_w gH^2}{16}+\rho_w gh\Delta h,$$

where k is the wavenumber.

5.3.2.2 Proposed models for wave set-up

In this section, two models for irregular waves are proposed, focusing on significant wave height.

M-I based on the model by Hoque et al., (2019)

Prior to modifying the model, it is important to identify the various types of wave breakers associated with wave breaking. This classification is critical since it can greatly influence the properties of wave-induced forces on structures located in the surf zone. Therefore, a thorough understanding of the different types of wave breakers is essential for developing these models. The two main types of wave breakers—spilling and plunging—are characterized by their specific breaking mechanisms. As a result, the assumptions made by Führboter, (1970) regarding the penetration depth y for both spilling and plunging breakers, outlined in Eqs. (5.13) and (5.14), are utilized in Eq. (5.22), leading to the following:

For spilling breakers:

$$\frac{d\bar{\eta}'}{dx} = -\frac{1}{\rho_w g\left\{(h+\bar{\eta}')-c_0\bar{\eta}'-\frac{c_0d_1H}{2}\right\}}\frac{dS'_{xx}}{dx}+\frac{\left(\frac{c_0\bar{\eta}'}{2}+\frac{d_1c_0H}{3}\right)}{\left\{(h+\bar{\eta}')-c_0\bar{\eta}'-\frac{c_0c_1H}{2}\right\}}\frac{d(d_1H)}{dx}-\frac{\left(c_0\bar{\eta}'+\frac{c_0d_1H}{2}\right)}{\left\{(h+\bar{\eta}')-c_0\bar{\eta}'-\frac{c_0d_1H}{2}\right\}}\frac{dh}{dx}. \tag{5.26}$$

For plunging breakers:

$$\frac{d\bar{\eta}'}{dx} = -\frac{1}{\rho_w g\left\{(h+\bar{\eta}')-c_0\bar{\eta}'-\frac{c_0 h\gamma}{2}\right\}}\frac{dS_{xx}'}{dx} + \frac{\left(\frac{c_0\bar{\eta}'}{2}+\frac{h\gamma c_0}{3}\right)}{\left\{(h+\bar{\eta}')-c_0\bar{\eta}'-\frac{c_0 h\gamma}{2}\right\}}\frac{d(h\gamma)}{dx} - \frac{\left(c_0\bar{\eta}'+\frac{c_0 h\gamma}{2}\right)}{\left\{(h+\bar{\eta}')-c_0\bar{\eta}'-\frac{c_0 h\gamma}{2}\right\}}\frac{dh}{dx}. \tag{5.27}$$

In terms of H_{m0} for both types of breakers:

M-I (set-up):

For spilling breakers,

$$\frac{d\bar{\eta}'}{dx} = -\frac{1}{\rho_w g L}\frac{dS_{xxs}'}{dx} + \frac{Q}{L}K_1\frac{dH_{m0}}{dx} - \frac{R}{L}\frac{dh}{dx}, \tag{5.28}$$

where $L = (h+\bar{\eta}) - c_0\bar{\eta} - \frac{c_0 K_1}{2\sqrt{2}}\Gamma\left(\frac{1}{\kappa}+1\right)H_{m0}$, $Q = \frac{c_0\bar{\eta}}{2} + \frac{c_0 K_1}{3\sqrt{2}}\Gamma\left(\frac{1}{\kappa}+1\right)H_{m0}$,

$R = c_0\bar{\eta} + \frac{c_0 K_1}{2\sqrt{2}}\Gamma\left(\frac{1}{\kappa}+1\right)H_{m0}$, and $S_{xxs}' = \frac{1}{16}\rho_w g\Gamma\left(\frac{2}{\kappa}+1\right)H_{m0}^2\left\{\frac{3}{2} - \left(\frac{2c_0^2-c_0}{2-2c_0}\right)\right\} + \frac{c_0^2 w_r^2\rho_w K_1}{\sqrt{2}}\left(\frac{4-3c_0}{12}\right)\Gamma\left(\frac{1}{\kappa}+1\right)H_{m0}$.

M-I (set-up):

For plunging breakers,

$$\frac{d\bar{\eta}'}{dx} = -\frac{1}{\rho_w g\acute{L}}\frac{dS_{xxp}'}{dx} + \frac{\acute{Q}}{\acute{L}}\gamma\frac{dh}{dx} - \frac{\acute{R}}{\acute{L}}\frac{dh}{dx}, \tag{5.29}$$

where $\acute{L} = (h+\bar{\eta}) - c_0\bar{\eta} - \frac{c_0\gamma}{2}h$, $\acute{Q} = \frac{c_0\bar{\eta}}{2} + \frac{c_0\gamma}{3}h$, $\acute{R} = c_0\bar{\eta} + \frac{c_0\gamma}{2}h$, and $S_{xxp}' = \frac{1}{16}\rho_w g\Gamma\left(\frac{2}{\kappa}+1\right)H_{m0}^2\left\{\frac{3}{2} - \left(\frac{2c_0^2-c_0}{2-2c_0}\right)\right\} + \frac{c_0^2 w_r^2\rho_w\gamma}{2}h\left(\frac{4-3c_0}{12}\right)$.

M-II:

In this context, the equation for wave setup is identical to that outlined in Eq. (5.24). However, the conservation of momentum equation (Eq. (5.25)) can be revised for both spilling and plunging breakers as follows:

$$\frac{d\bar{\eta}}{dx} = -\frac{1}{\rho_w g(h+\bar{\eta})}\frac{dS_{xx2}''}{dx}, \tag{5.30}$$

where $S''_{xx2} = \frac{2Ek}{sinh2kh}\int_{-h-\Delta h}^{0}(1 - C_0 e^{k_0 z})\left[cosh^2 k(h+z) - \left\{sinhk(h+z) + \frac{C_0}{(1-C_0 e^{k_0 z})(k^2-k_0^2)}\left[e^{k_0 z}\left(kk_0 coshk(h+z) - k_0^2 sinhk(h+z)\right) - kk_0 e^{k_0 h}\right]\right\}\right]dz + \frac{\rho_w g H_{m0}^2}{32}\Gamma\left(\frac{2}{\kappa}+1\right) + \rho_w g h \Delta h$.

5.3.3 Solutions for Proposed Models

Achieving analytical solutions for M-I and M-II in the contexts of wave height and setup is particularly challenging because of the numerous nonlinear terms involved. Therefore, a numerical method was employed to solve these models. The x-axis is considered to point toward the shoreline. The entire domain is discretised for systematic analysis and evaluation, and the spacing in the *x*-direction in the grid is equal to Δx. For the discretisation of the derivative terms, it has been used the forward finite difference (FFD) method, whereas, for the discretisation of all the other terms, the central value is used.

5.3.3.1 Solutions for significant wave height

M-I (spilling breaker):

Combining Eqs. (5.06) and Eq. (5.16) and reorganising the result yields:

$$\frac{1}{16}\rho_w g \frac{d\left(H_{m0}^2\sqrt{gh}\right)}{dx} = -\frac{K_1 w_r c_0 \rho_w g}{2\sqrt{2}(1-c_0)}\Gamma\left(\frac{1}{\kappa}+1\right)H_{m0}e^{-\left(\frac{\sqrt{2}\gamma h}{H_{m0}}\right)^{\kappa}}. \tag{5.31}$$

Applying the FFD scheme in Eq. (5.31), yields:

$$(H_{m0})_{i+1} = \sqrt{\frac{\left(H_{m0}^2\sqrt{h}\right)_i - A\Delta x H_{m0,i} e^{-\left(\frac{\sqrt{2}\gamma h_i}{H_{m0,i}}\right)^{\kappa}}}{(\sqrt{h})_{i+1}}}, \tag{5.32}$$

where $A = \frac{8K_1 c_0 w_r}{\sqrt{2g}(1-c_0)}\Gamma\left(\frac{1}{\kappa}+1\right)$.

M-I (plunging breaker):

Similarly, Eqs. (5.06) and (5.18) togetherly provide:

$$\frac{1}{16}\rho_w g\frac{d\left(H_{m0}^2\sqrt{gh}\right)}{dx} = -\frac{K_2 w_r c_0 \gamma \rho_w g}{2(1-c_0)} h e^{-\left(\frac{\sqrt{2}\gamma h}{H_{m0}}\right)^{\kappa}}. \quad (5.33)$$

Applying the FFD technique in Eq. (5.33), yields:

$$(H_{m0})_{j+1} = \sqrt{\frac{\left(H_{m0}^2\sqrt{h}\right)_j - B\Delta x h_j e^{-\left(\frac{\sqrt{2}\gamma h_j}{H_{m0,j}}\right)^{\kappa}}}{\left(\sqrt{h}\right)_{j+1}}}, \quad (5.34)$$

where $B = \frac{8K_2 c_0 w_r \gamma}{\sqrt{g}(1-c_0)}$.

M-II:

For M-II, combined Eqs. (5.06) and (5.20) that yield:

$$\frac{1}{16}\rho_w g\frac{d\left(H_{m0}^2\sqrt{gh}\right)}{dx} = -K_3 w_r c_0 \rho_w g\left(\frac{1-e^{-k_0 h}}{1-c_0 e^{-k_0 h}}\right) e^{-\left(\frac{\sqrt{2}\gamma h}{H_{m0}}\right)^{\kappa}}. \quad (5.35)$$

Similarly, By applying the FFD scheme in Eq. (5.35), provides:

$$(H_{m0})_{j+1} = \sqrt{\frac{\left(H_{m0}^2\sqrt{h}\right)_j - \mathrm{C}\Delta x h_j e^{-\left(\frac{\sqrt{2}\gamma h_j}{H_{m0,j}}\right)^{\kappa}}}{\left(\sqrt{h}\right)_{j+1}}}, \quad (5.36)$$

where $\mathrm{C} = \frac{8K_3 c_0 w_r}{\sqrt{g}(1-c_0)}$.

5.3.3.2 Solution for wave set-up

M-I (spilling breaker):

Eq. (5.28) is discretised by using the aforementioned scheme to obtain a solution for the wave set-up in the case of spilling breaking waves. This yields:

$$\acute{\eta}_{j+1} = \acute{\eta}_j - \frac{3}{32L}\Gamma\left(\frac{2}{\kappa}+1\right)\left(H_{m0(j+1)}^2 - H_{m0(j)}^2\right) + \Gamma\left(\frac{2}{\kappa}+1\right)\left(\frac{2c_0^2-c_0}{16L(2-2c_0)}\right)\left(H_{m0(j+1)}^2 - H_{m0(j)}^2\right) - (4-3c_0)\frac{c_0^2 w_r^2 K_1}{12\sqrt{2}gL}\Gamma\left(\frac{1}{\kappa}+1\right)\left(H_{m0(j+1)} - H_{m0(j)}\right) + \Gamma\left(\frac{1}{\kappa}+1\right)\frac{QK_1}{\sqrt{2}L}\left(H_{m0(j+1)} - H_{m0(j)}\right) - \frac{R}{L}\left(h_{j+1} - h_j\right), \quad (5.37)$$

where the other (L, Q, and R) parameters provide the central value.

M-I (plunging breaker)

Similarly, Eq. (5.38) can be obtained by discretising Eq. (5.29) by using the same numerical scheme.

$$\acute{\eta}_{j+1} = \acute{\eta}_j - \frac{3}{32L}\Gamma\left(\frac{2}{\kappa}+1\right)\left(H^2_{m0(i+1)} - H^2_{m0(i)}\right) + \left(\frac{2c_0^2 - c_0}{16L(2-2c_0)}\Gamma\left(\frac{2}{\kappa}+1\right)\right)\left(H^2_{m0(i+1)} - H^2_{m0(i)}\right) - (4-3c_0)\frac{c_0^2 w_r^2 \gamma}{12gL}(h_{i+1}-h_i) + \frac{Q\gamma}{L}(h_{i+1}-h_i) - \frac{R}{L}(h_{i+1}-h_i), \quad (5.38)$$

where other ($\acute{L}$, $\acute{Q}$ and $\acute{R}$) parameters supply the central value.

M-II

To solve M-II, Eq. (5.30) is discretised using the same scheme which yields:

$$\acute{\eta}_{j+1} = \acute{\eta}_j - \frac{1}{\rho_w g(h_i + \acute{\eta}_j)}\left(S''_{xx,i+1} - S''_{xx,i}\right). \quad (5.39)$$

The value of each parameter on the right-hand sides of Eqs. (5.32), (5.34), (5.36), (5.37), (5.38), and (5.39) are known. Hence, calculating the spectral significant wave height and wave set-up using these equations is straightforward.

5.4 Results and Validations

5.4.1 Data

Validating the developed models through comparison with experimental data is crucial. To this end, conducted experiments (as detailed in section 5.4.1.1.) and compiled experimental data from alternative sources (as elaborated in section 5.4.1.2.).

5.4.1.1 Experiment

To evaluate the accuracy of the developed model, the authors carried out experiments and collected data between November 2nd and 12th, 2023, at a wave flume situated in the S2 building of the Graduate School of Osaka University in Japan. The primary objective of the experiment was to explore the complexities of cross-shore hydrodynamics and the behavior of air bubbles in breaking waves. The setup featured a compact wave tank that measured 20 m in length, 0.7 m in width, and 1.0 m in-depth, along with a 5 m long sloping beach profile made of wood and steel, designed with a

slope ratio of 1/10. During the experiments, the beach remained unchanged. Both regular and irregular waves were generated, and the study comprised three main tests, each consisting of several cases, with two of the tests conducted under irregular wave conditions.

For the generation of irregular waves, the authors used the JONSWAP spectrum developed by Hasselmann et al. (1973), setting the spectral width parameter at 3.3. The experimental campaign included 24 cases, with incident significant wave heights ranging from 6.8 cm to 9.30 cm (see Table 5.1). The spectral peak periods varied between 1.72 s and 1.91 s. Of the 24 test scenarios, 8 cases employed JONSWAP spectra, another 8 used Modified Bretschneider spectra, and the remaining cases featured regular waves. Among the JONSWAP spectrum cases, 4 tests focused on plunging breakers, while the other 4 concentrated on spilling breakers. Data were gathered by measuring water surface elevation at 9 cross-shore locations using capacitance-type wave gauges (see Fig. 2.01 in Chapter 2).

To maintain consistency, each case underwent more than five pre-testing procedures prior to the final test. Each actual test lasted 5 minutes, with a sampling frequency of 100 Hz, generating 30,000 data points. Following each test, approximately 10 minutes were dedicated to preparation before moving on to the next test. The zero-up crossing method was utilized to isolate individual wave heights and periods. Afterward, formulas for irregular wave heights and periods were applied to calculate statistical wave heights and periods for each test at every gauge (Bosboom et al., 1984; Hughes, 1993). Each test scenario produced over 250 waves.

Table 5.1: Incident wave parameters for the experiment.

Cases	H_{m0} (m)	Tp (s)	h_0 (m)
Case I	0.093	1.91	0.30
Case II	0.085	1.72	0.30
Case III	0.068	1.85	0.30
Case IV	0.079	1.86	0.30

5.4.1.2 Collected experimental data

To improve the validation process, a comprehensive dataset on spectral significant wave height and wave setup was compiled from various sources, encompassing a wide range of cases. This collection includes experiments conducted at different scales, such as SS, LS, and FE, reflecting diverse wave conditions and bottom topographies. An overview of the varied experimental data for significant wave heights is presented in Table 2.2 of Chapter 2, while Table 2.3 in Chapter 2 details the gathered experimental data for wave set-up.

5.4.2 Classifying Wave Breakers

Consider a beach traversed by an irregular wave, as illustrated in Fig. 4.02 in Chapter 4. As the wave enters the breaking phase, both its energy and height gradually decrease as it approaches the shoreline. Therefore, it is essential to determine the exact locations where these waves begin to break. In this context, we can refer to the equation developed by Thornton and Guza, (1983), which can be concisely expressed as follows:

$$H_{m0,b} = \sqrt{2}\gamma h, \tag{5.40}$$

where $H_{m0,b}$ is the spectral significant wave height at the breaking point.
Utilized the surf similarity parameter (ξ_b), suggested by Battjes, (1974), to detect the wave breakers (see section 3.4.2. in Chapter 3), where ξ_b can be obtained using the following equation:

$$\xi_b = \frac{tan\alpha}{\sqrt{\frac{H_{m0,b}}{\sqrt{2}L_0}}}. \tag{5.41}$$

Here L_0 is the deep water wavelength, and α is the slope.

5.4.3 Determination of Void Fraction (c_0)

In their study, Hoque and Aoki, (2005) examined a substantial amount of experimental data to develop a relationship for calculating the void fraction (c_0). This relationship is defined as a function of the horizontal distance from the breakpoint to the shoreline (see Section 4.5.3 in Chapter 4)

5.4.4 Models Against Experimental Data

To accurately calculate both wave height and wave set-up, it is essential to satisfy the boundary conditions at both the seaward and coastline boundaries. The following parameters are needed for the seaward boundary to effectively apply the model: water depth, incident spectral significant wave height, bottom topography, and peak wave period. Additionally, an incident set-down is required for calculating the wave set-up. Once the boundary conditions are confirmed, the types of breakers are identified using the incident wave parameter values, the breaker index formula, and the surf similarity parameter. For Model I (M-I), the wave height of spilling breakers is calculated using Eq. (5.32), while Eq. (5.34) is applied for plunging breakers. Model II (M-II) uses Eq. (5.36) for both types of breakers. After determining the wave height, the wave set-up is calculated using Eqs. (5.37) and (5.38) for both spilling and plunging breakers in M-I. In contrast, Eq. (5.39) is used for M-II for both breaker types. In these calculations, the reference void fraction for spilling and plunging breakers is considered. The computed void fraction ranges from 12% to 15% for spilling breakers and from 16% to 18% for plunging breakers, aligning with values reported in the literature (Blenkinsopp and Chaplin 2011; Huang et al. 2009; Hoque and Aoki 2005; Hossain and Araki 2022). The mesh size used in the computations is the same as the measured wave height, except when it exceeds 5 m (Rattanapitikon 2008). The unspecified coefficients *K1*, *K2*, and *K3* were determined using the least-squares method, with the resulting values of 0.36, 0.39, and 0.47 applied in the calculations for both proposed models.

Significant wave height

Fig. 5.01 compares the proposed models (M-I and M-II) with the established models RS-10 (Rattanapitikon and Shibayama, 2010) and NLHO-17 (Nam et al., 2017) using a variety of experimental data scenarios (Authors, 2023).

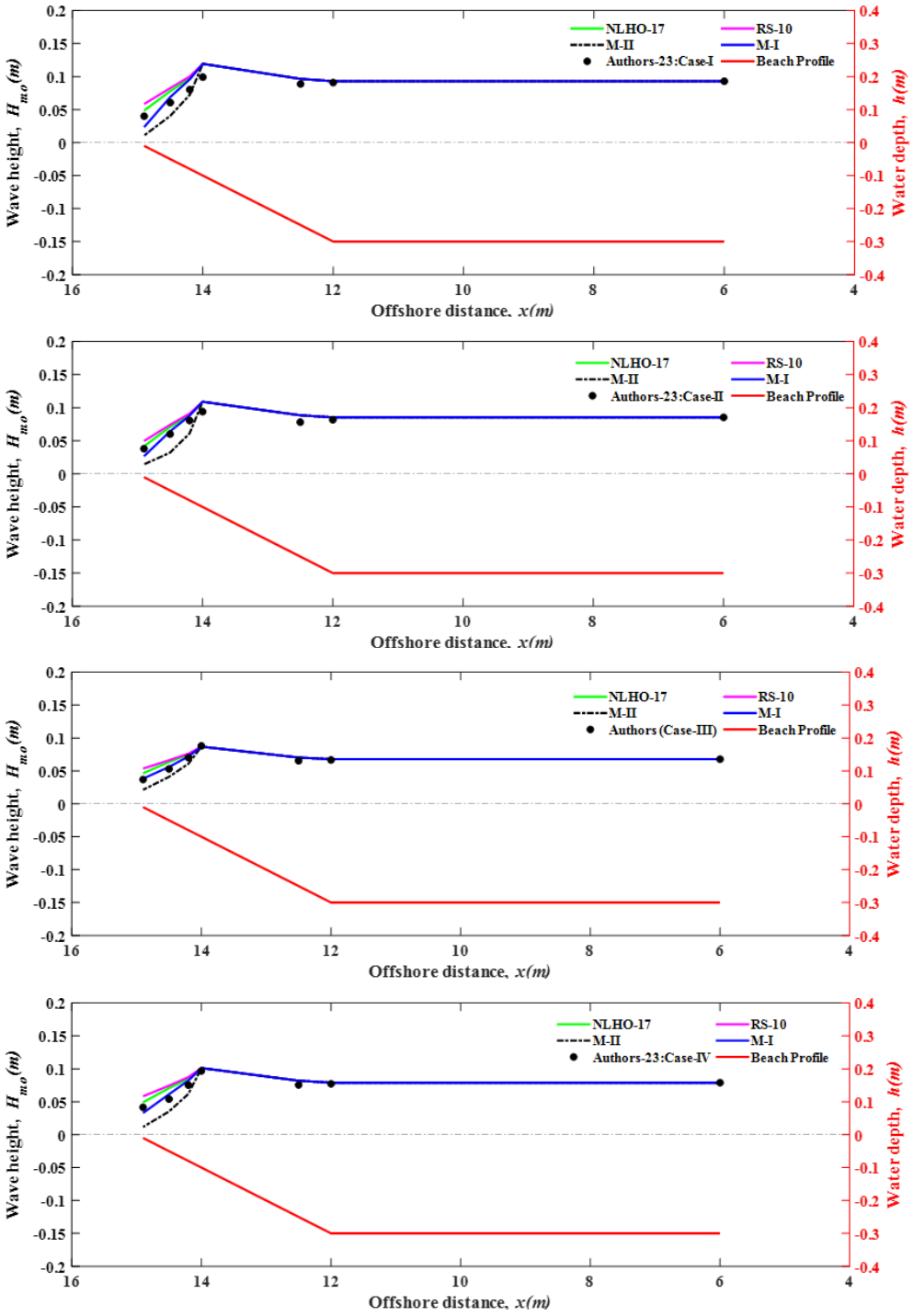

Figure 5.01: Comparison of the spectral significant wave heights of M-I, M-II, RS-10, and NLHO-17 with authors' experimental data.

M-I exhibited strong performance across a wide range of experimental cases, though some discrepancies were observed with M-II. Among the datasets evaluated, the developed models, especially M-I, showed excellent agreement with the existing RS-10 and NLHO-17 models.

The analysis of large-scale datasets, as shown in Fig. 5.02 and detailed in Table 2.2 of Chapter 2, reveals a strong correlation in wave height calculations across various models. M-I, NLHO-17, and RS-10 show significant consistency with the experimental data provided by Kraus and Smith, (1994) and Roelvink and Reniers, (1995). However, when examining the dataset from Dette et al. (2002), discrepancies in wave breaking are observed, especially for M-II. These deviations are likely due to the unique conditions of storm-wave data collection. Such findings are consistent with the observations made by Hossain and Araki, (2023).

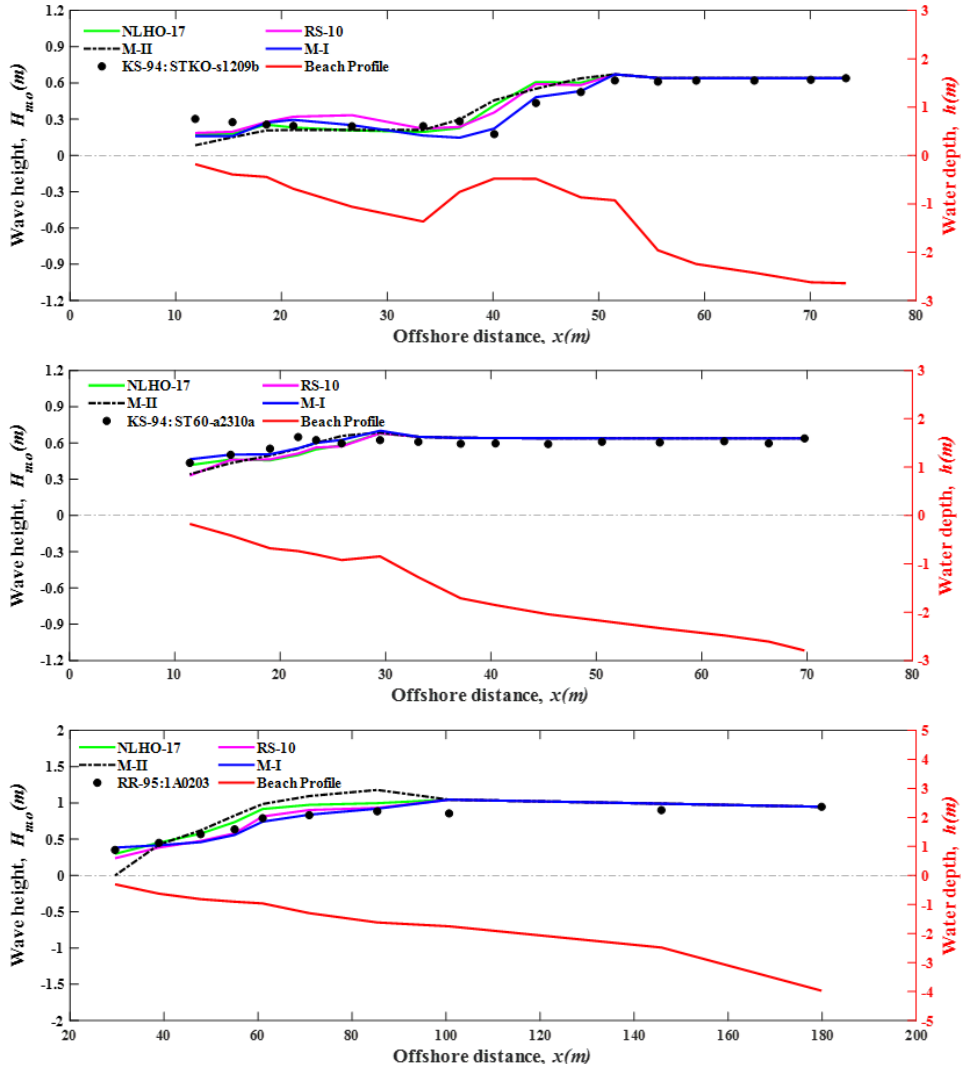

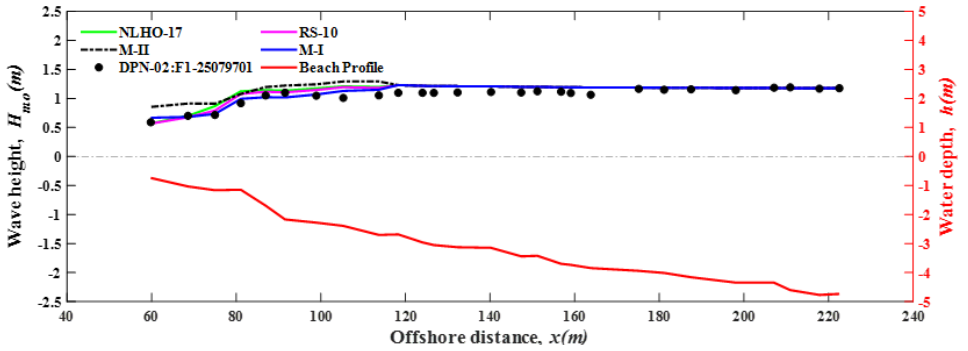

Figure 5.02: Comparison of the spectral significant wave height of M-I, M-II, RS-10, and NLHO-17 with large-scale experimental data.

The results of the proposed models were compared with RS-10 and NLHO-17 against small-scale data collected from multiple studies (refer to Table 2.2 in Chapter 2). As illustrated in Fig. 5.03, the results from M-I, NLHO-17, and RS-10 show a high level of agreement for almost all data points. M-II exhibited a minor error, but it was not statistically significant.

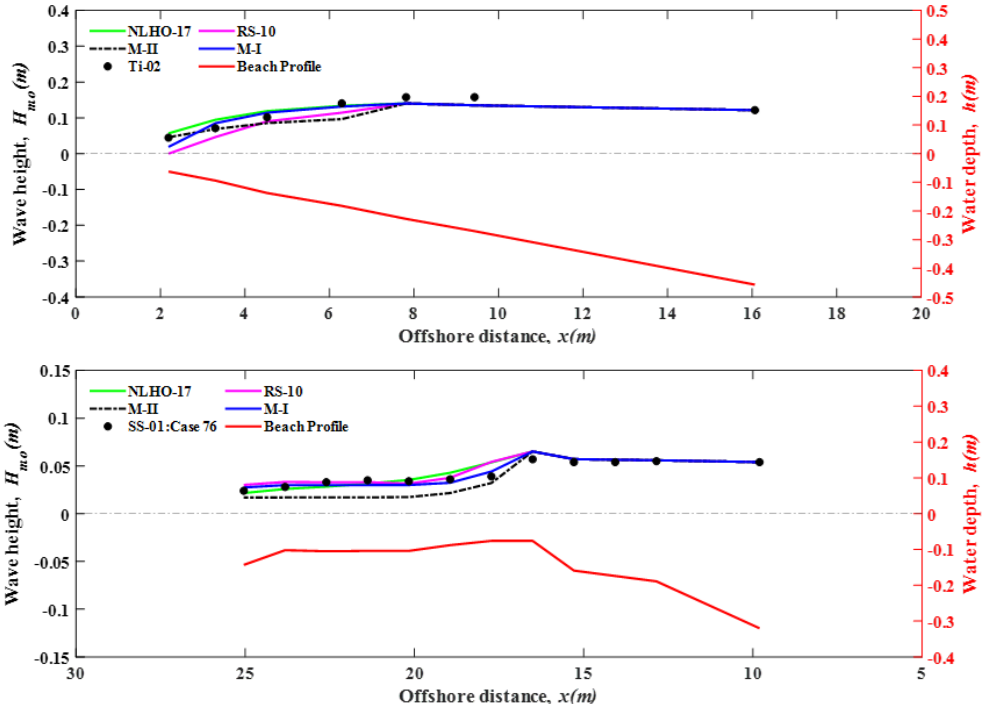

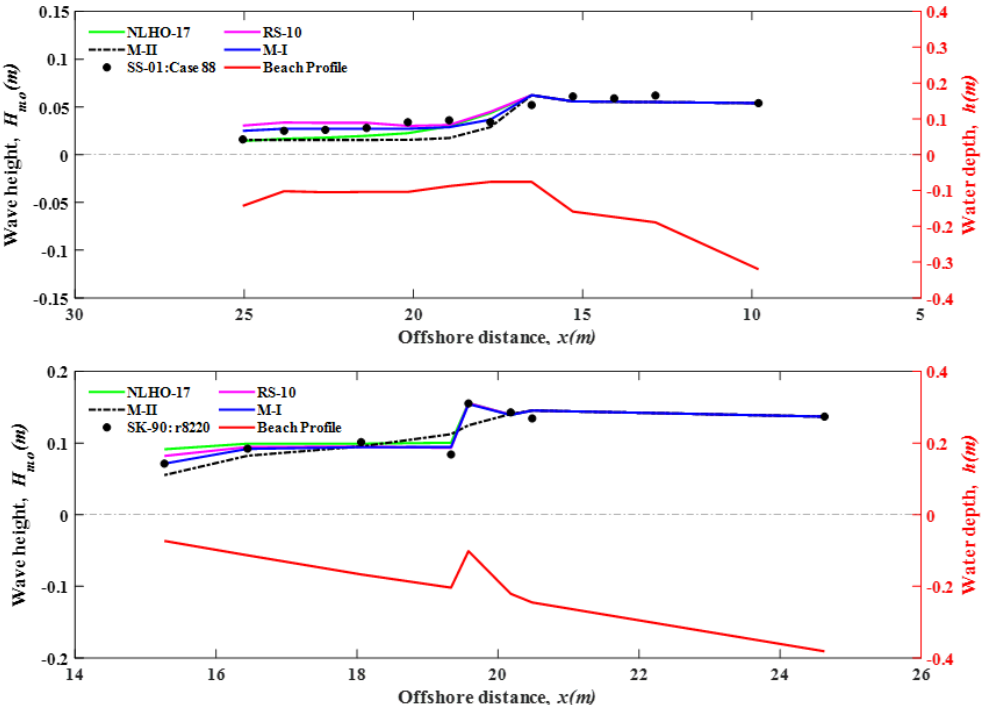

Figure 5.03: Comparison of the spectral significant wave height of M-I, M-II, RS-10, and NLHO-17 with small-scale experimental data.

The models showed good agreement with data from plane-sloping beaches (Ting 2002) and quick rise and fall slopes (Smith and Seabergh 2001; Smith and Kraus 1990), particularly in areas near bars with narrow crests. Nonetheless, M-II displayed slightly less accuracy in predicting wave heights close to the shoreline.

The evaluation of the proposed models, as well as RS-10 and NLHO-17, against experimental field data (refer to Table 2.2, Chapter 2) is shown in Fig. 5.04. The models demonstrated strong agreement with the datasets provided by Birkemeier et al. (1997) and Kraus et al. (1989). However, M-II exhibited a minor deviation near the wave-breaking point in the dataset from Smith et al. (1993). This discrepancy is attributed to the presence of a mound close to the breaking point.

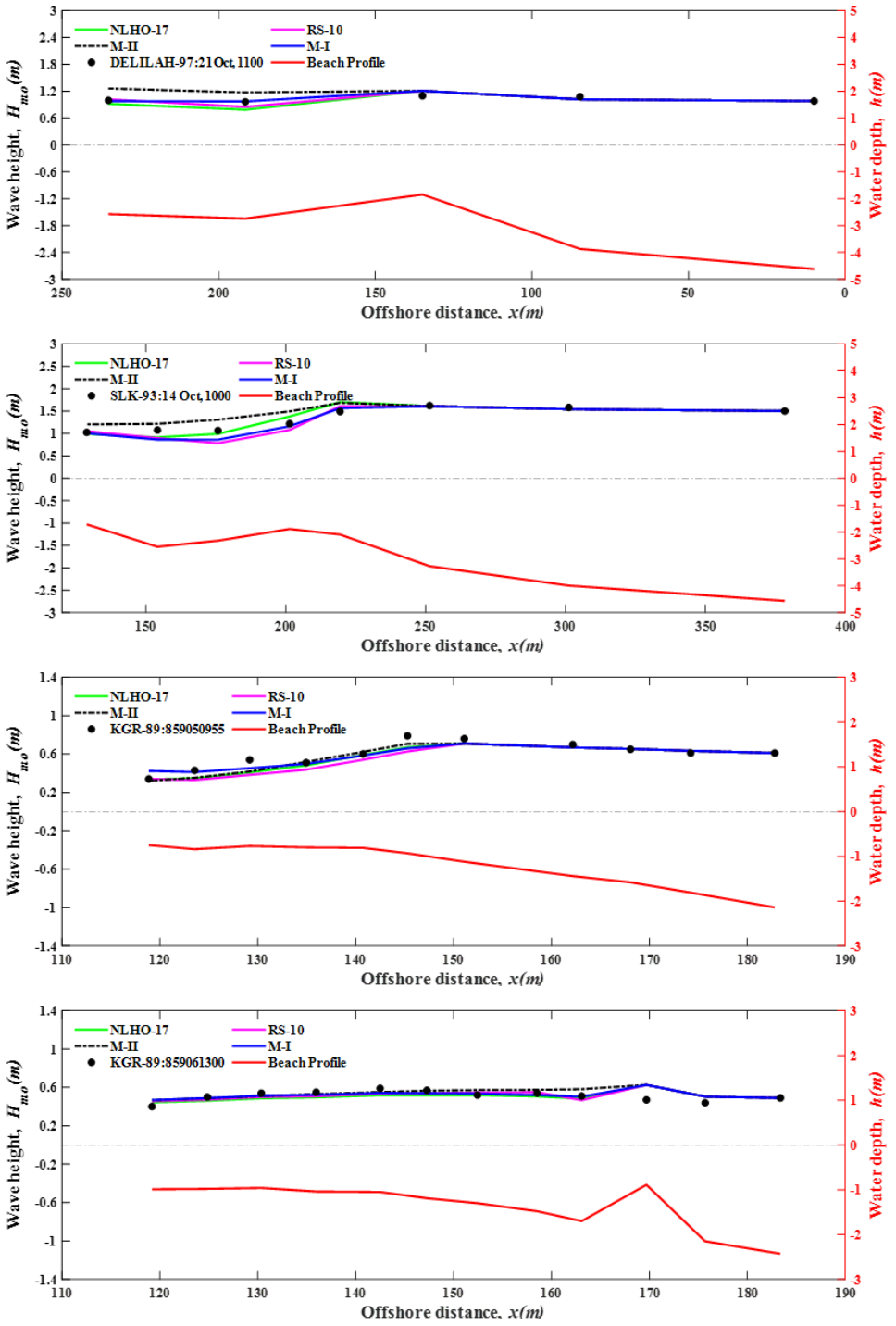

Figure 5.04: Comparison of the spectral significant wave height of M-I, M-II, RS-10, and NLHO-17 with field experimental data.

Fig. 5.05 compares M-I, M-II, and NLHO-17 concerning the RS-10 model, using different datasets (LS, SS, and FE). The results reveal that M-I steadily outperforms M-II in the comparison.

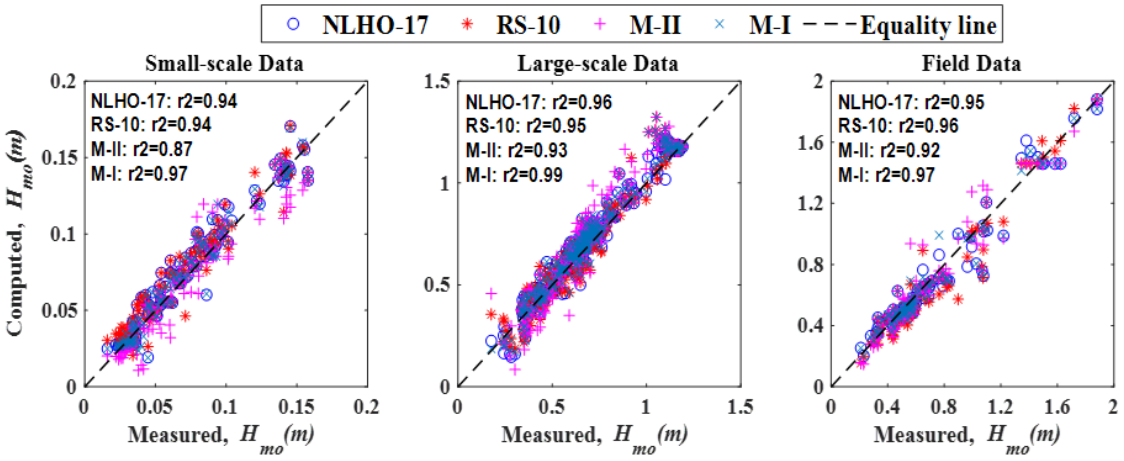

Figure 5.05: Variation of computed spectral significant wave heights of M-I, M-II, RS-10, and NLHO-17 with different measured data.

As a result, the M-I model demonstrates strong performance in predicting wave heights across diverse bathymetry. However, M-II has some limitations, particularly in accurately calculating wave heights in the presence of beach mounds immediately along the coastline.

Wave set-up

Fig. 5.06 illustrates a comparison of wave set-up calculations, highlighting the performance of the proposed models alongside NLHH-09 (Nam et al. 2009) and DDD-85 (Dally, Dean, and Dalrymple 1985). The results reveal that M-I, NLHH-09, and DDD-85 exhibit outstanding promise with the experimental datasets (Authors-23).

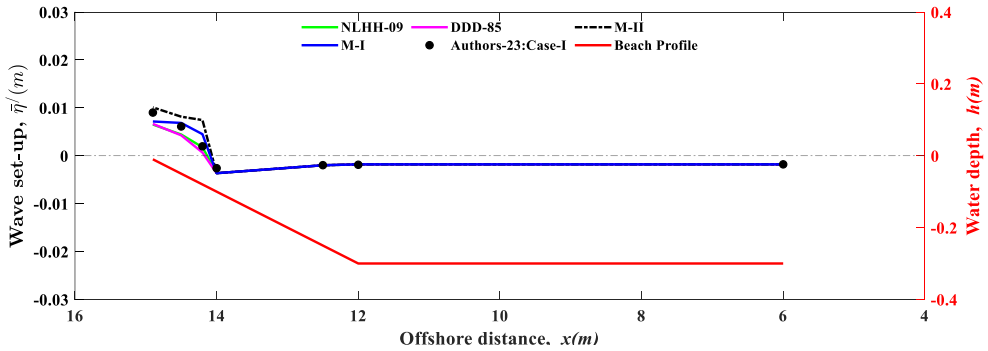

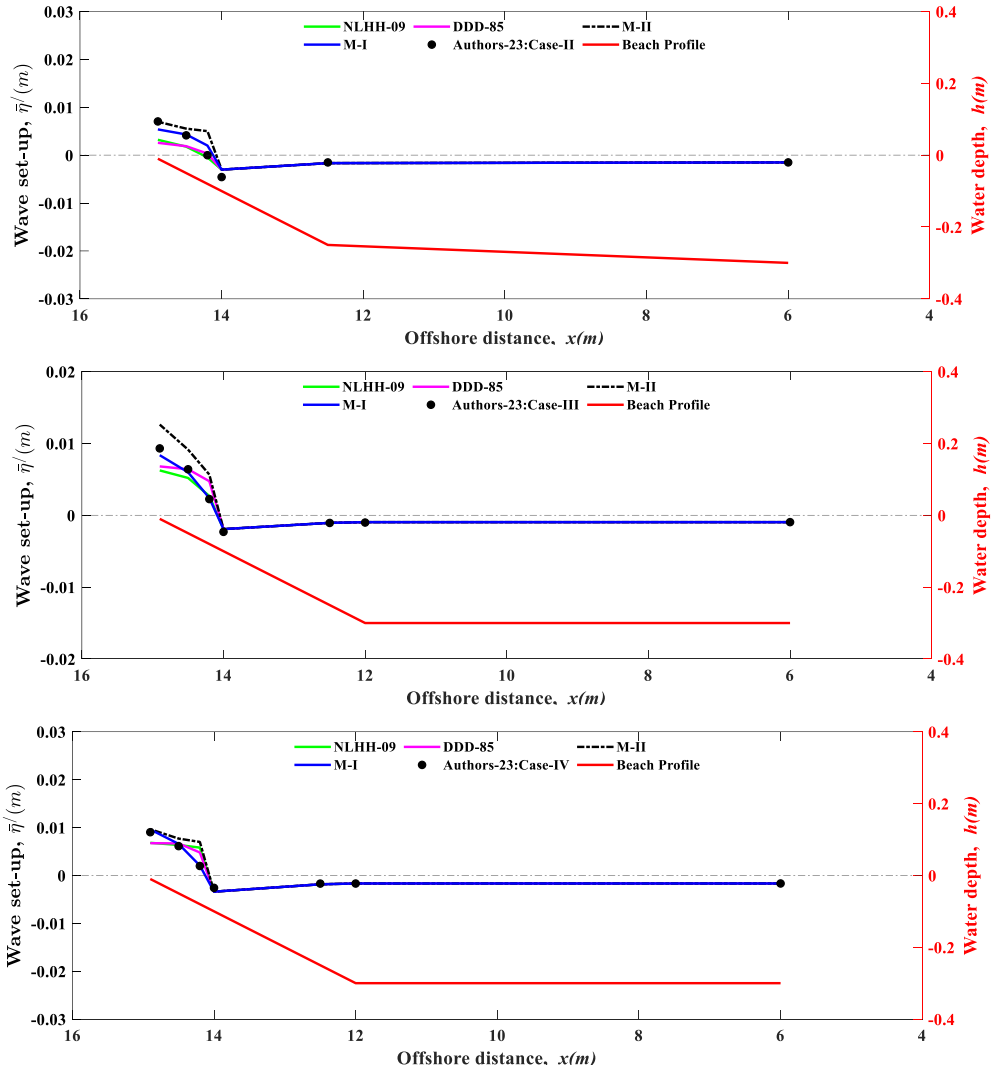

Figure 5.06: Wave set-up differences of M-I, M-II, DDD-85, and NLHH-09 with the authors' experimental data.

Additionally, another comparison, depicted in Fig. 5.07 and utilizing the datasets listed in Table 2.3 of Chapter 2, mirrors the results shown in Fig. 5.06. Nonetheless, in both comparisons, M-II displayed discrepancies after the breaking point and near the shoreline.

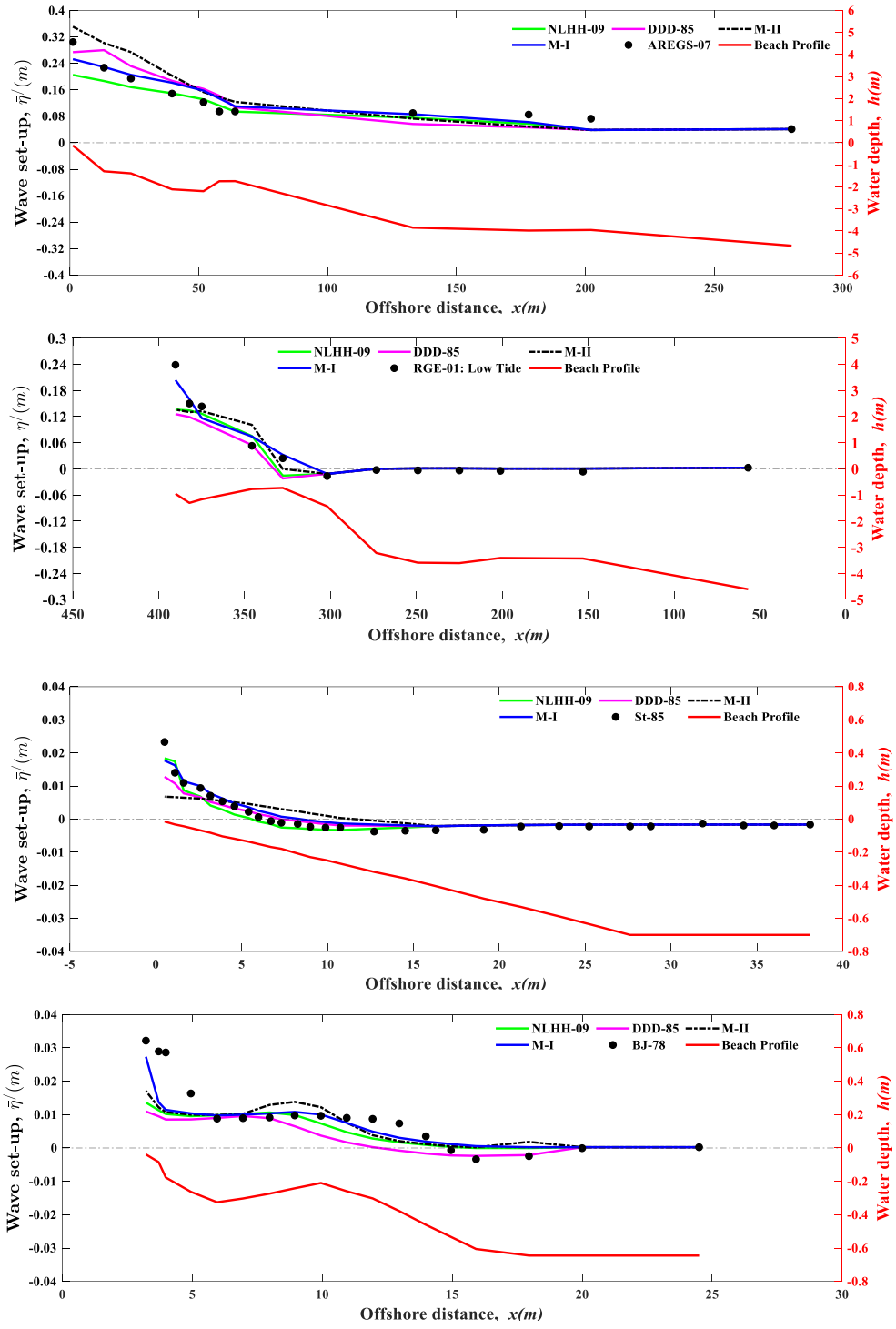

Figure 5.07: Wave set-up variations of M-I, M-II, DDD-85, and NLHH-09 with different experimental data.

The results for wave set-up from the proposed models were found to be in close agreement with the regular wave models proposed by Hoque et al., (2019) and Hoque, (2002), respectively.

Also, Fig. 5.08 presents a comparison between the proposed models and the NLHH-09 model, alongside the DDD-85 model, using various experimental datasets. This analysis underscores the performance of M-I and M-II, revealing that M-I demonstrates superior effectiveness compared to M-II.

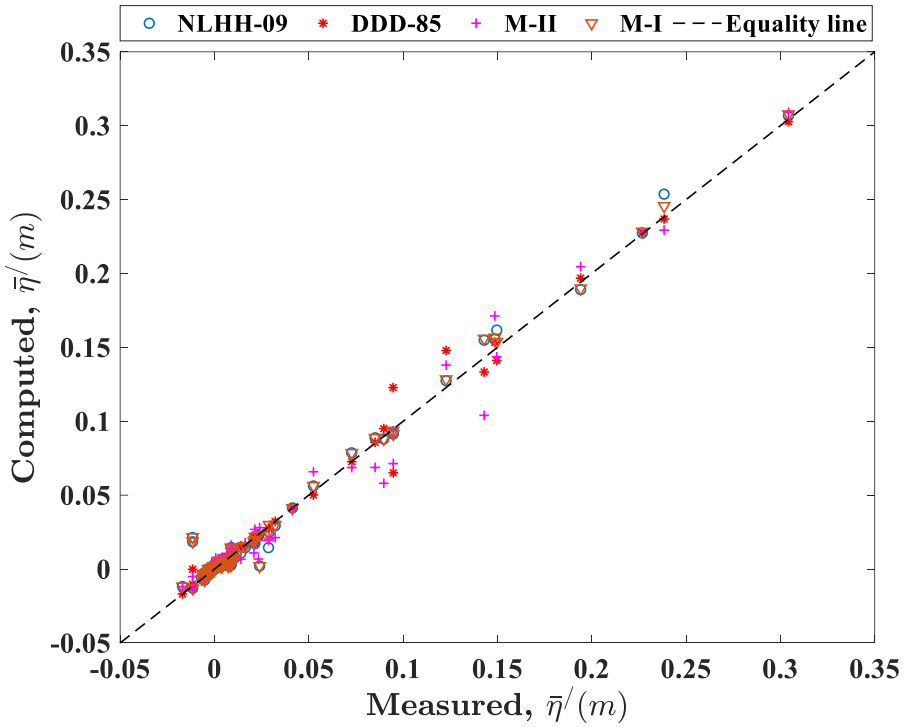

Figure 5.08: Variations of computed wave set-up of M-I, M-II, DDD-85, and NLHH-09 with different measured data.

5.4.5 Error Assessment

A thorough assessment was conducted to evaluate the performance of M-I and M-II in comparison to RS-10 and NLHO-17 for predicting spectral significant wave height, and to DDD-85 and NLHH-09 for estimating wave set-up. This evaluation utilized various experimental datasets detailed in Tables 2.2 and 2.3 of Chapter 2. The accuracy of the models was measured using several error metrics, including the root mean square relative error (RMSRE), the percentage error index (P20), and the Brier skill score (BSS).

RMSRE

The RMSRE is used to evaluate the accuracy of a model's predictions by comparing them to observed values. This metric is particularly useful for understanding the scale of errors across different ranges of values.

The calculation of RMSRE for wave height is given by:

$$RMSRE = \sqrt{\frac{\sum_{j=1}^{M}\left(H_{mo.cj}-H_{mo.mj}\right)^2}{\sum_{j=1}^{M}H_{mo,mj}^2}} * 100, \tag{5.42}$$

where $H_{mo.cj}$ is the computed significant wave height, $H_{mo.mj}$ is the measured significant wave height, and M is the number of data points.

Likewise, for the wave set-up:

$$RMSRE = \sqrt{\frac{\sum_{j=1}^{M}\left(\acute{\eta}_{cj}-\acute{\eta}_{mj}\right)^2}{\sum_{j=1}^{M}\acute{\eta}_{mj}^2}} * 100, \tag{5.43}$$

where $\acute{\eta}_{cj}$ is the computed wave set-up, $\acute{\eta}_{mj}$ indicates the measured wave set-up, and M is the number of data points.

Fig. 5.09 illustrates the RMSRE for H_{m0}, comparing the proposed models (M-I and M-II) with RS-10 and NLHO-17. For H_{m0}, the average RMSRE values for the proposed models are 6.17% for M-I (with sub-averages of 5.52% for LS, 6.90% for SS, and 6.14% for FE) and 10.09% for M-II (with sub-averages of 8.11% for LS, 11.53% for SS, and 10.64% for FE). In comparison, the RS-10 and NLHO-17 models show average RMSRE values of 7.82% and 7.43%, respectively, with RS-10 having sub-averages of 6.5% for LS, 8.33% for SS, and 8.62% for FE, and NLHO-17 having sub-averages of 6.12% for LS, 8.21% for SS, and 7.97% for FE.

The error analysis, as depicted in Fig. 5.10, reveals that M-I excels in predicting wave set-up with an average RMSRE of 7.91%. In comparison, M-II has a higher RMSRE of 12.42%, while NLHH-09 and DDD-85 show average RMSRE values of 8.76% and 9.85%, respectively. This analysis highlights M-I's superior performance in accurately forecasting wave set-up, outperforming the other models.

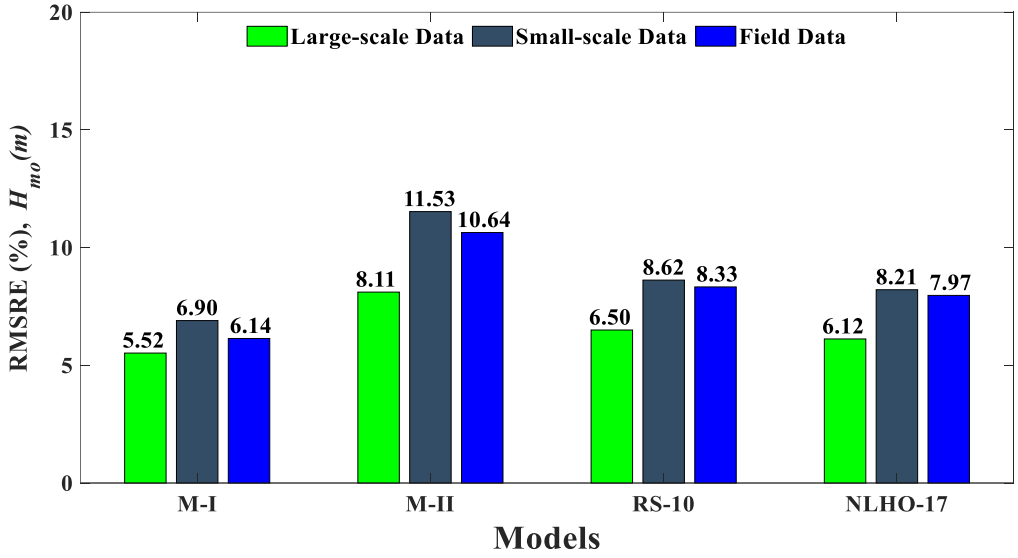

Figure 5.09: RMSRE values of M-I, M-II, RS-10, and NLHO-17 for spectral significant wave heights.

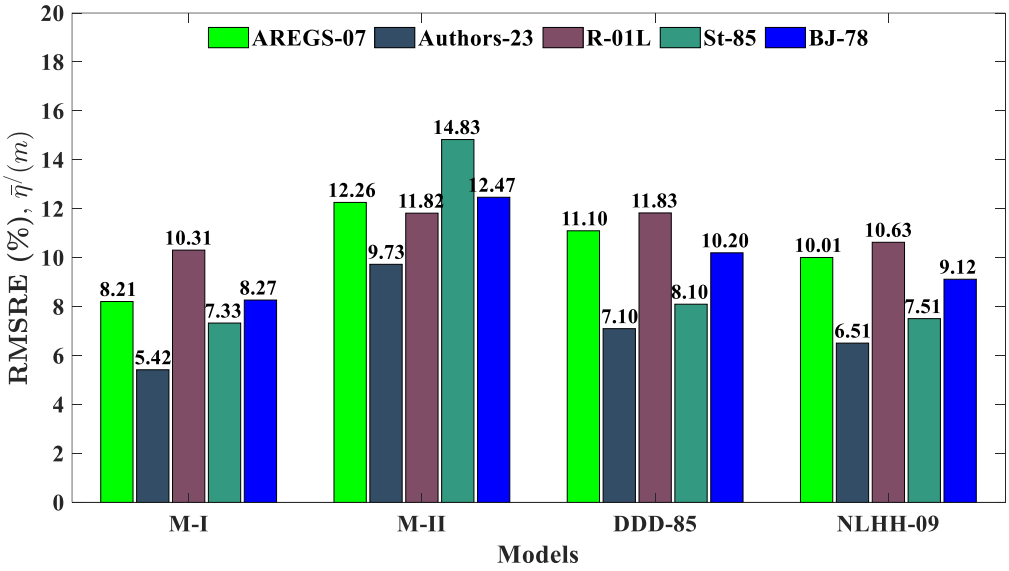

Figure 5.10: RMSRE values of M-I, M-II, DDD-85, and NLHH-09 for wave set-up.

Percentage Error

The P20 metric reflects the percentage of cases where the deviation between predicted and observed values is within 20%. As shown in Fig. 5.11 and summed up in Table 5.2, which outlines the performance of the models for predicting significant wave heights, the average P20 values are 3.01% for M-I, 10.21% for M-II, 3.38% for NLHO-17, and 3.67% for RS-10. This analysis reveals that M-II had a higher proportion of predictions falling outside the 20% margin, indicating its comparatively lower accuracy in forecasting significant wave heights.

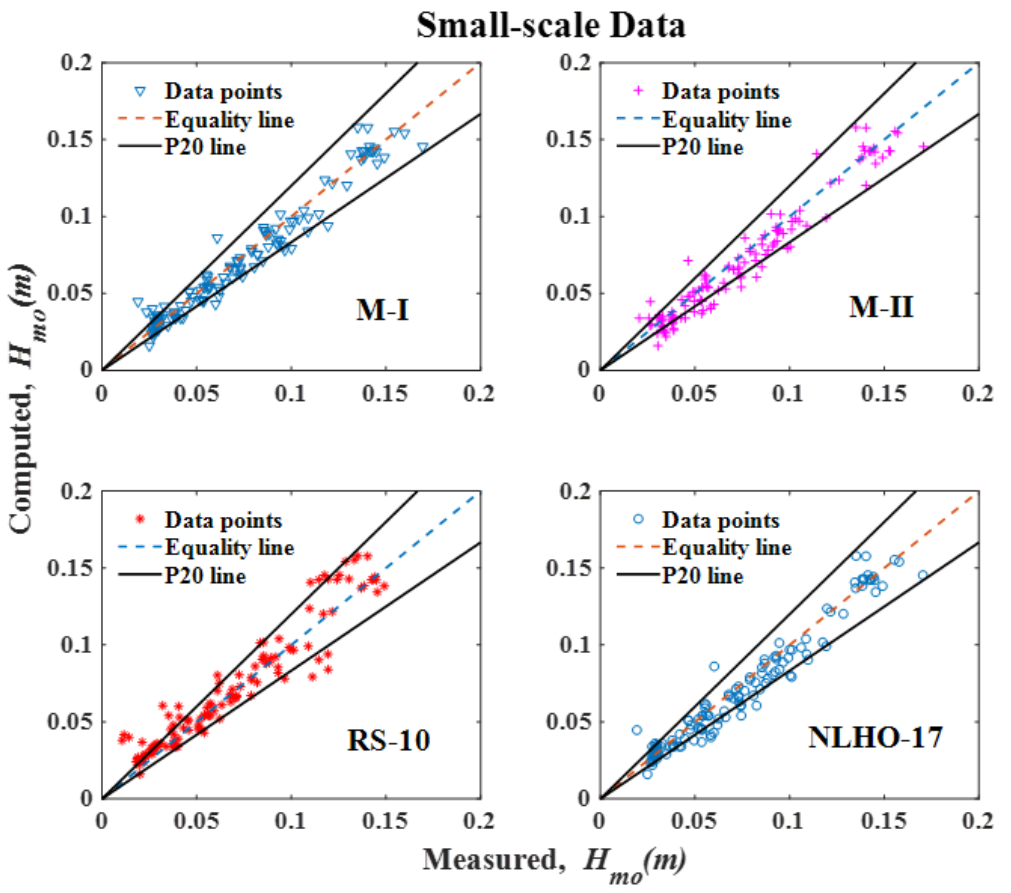
Small-scale Data
Data points
Equality line
P20 line
M-I
M-II
RS-10
NLHO-17
Computed, H_{mo} (m)
Measured, H_{mo} (m)
0
0.05
0.1
0.15
0.2

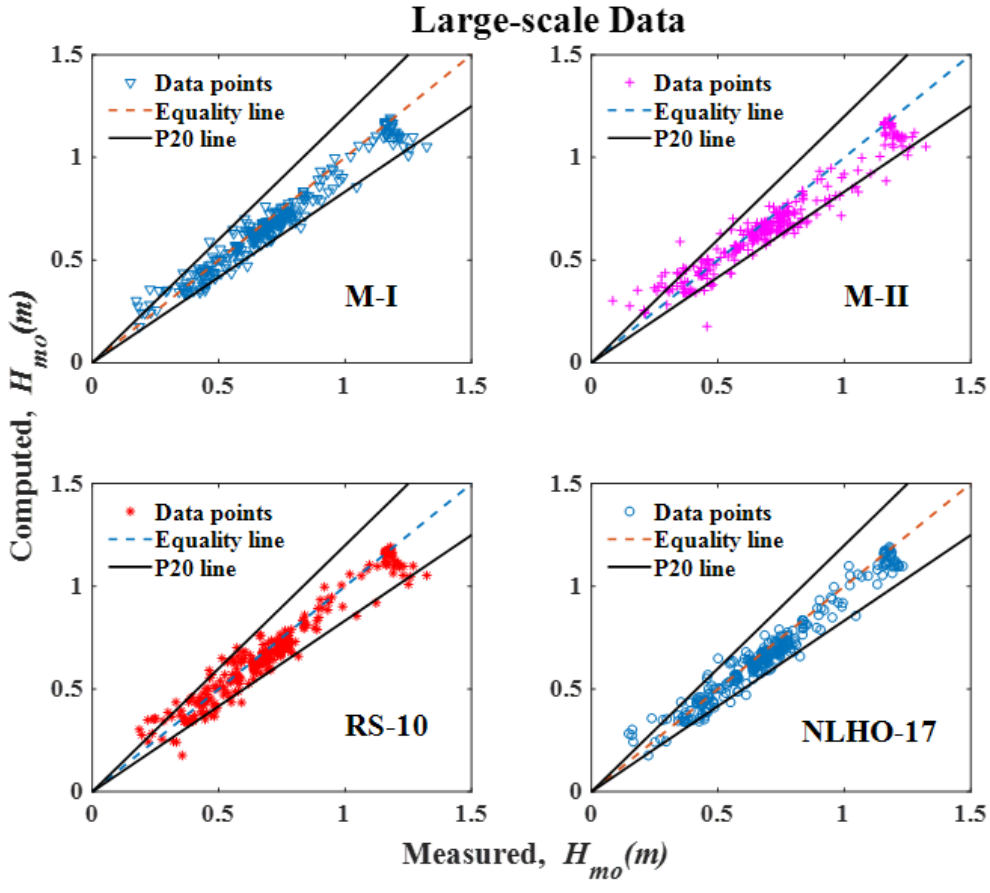
Large-scale Data
Data points
Equality line
P20 line
M-I
M-II
RS-10
NLHO-17
Computed, H_{mo} (m)
Measured, H_{mo} (m)
0
0.5
1
1.5

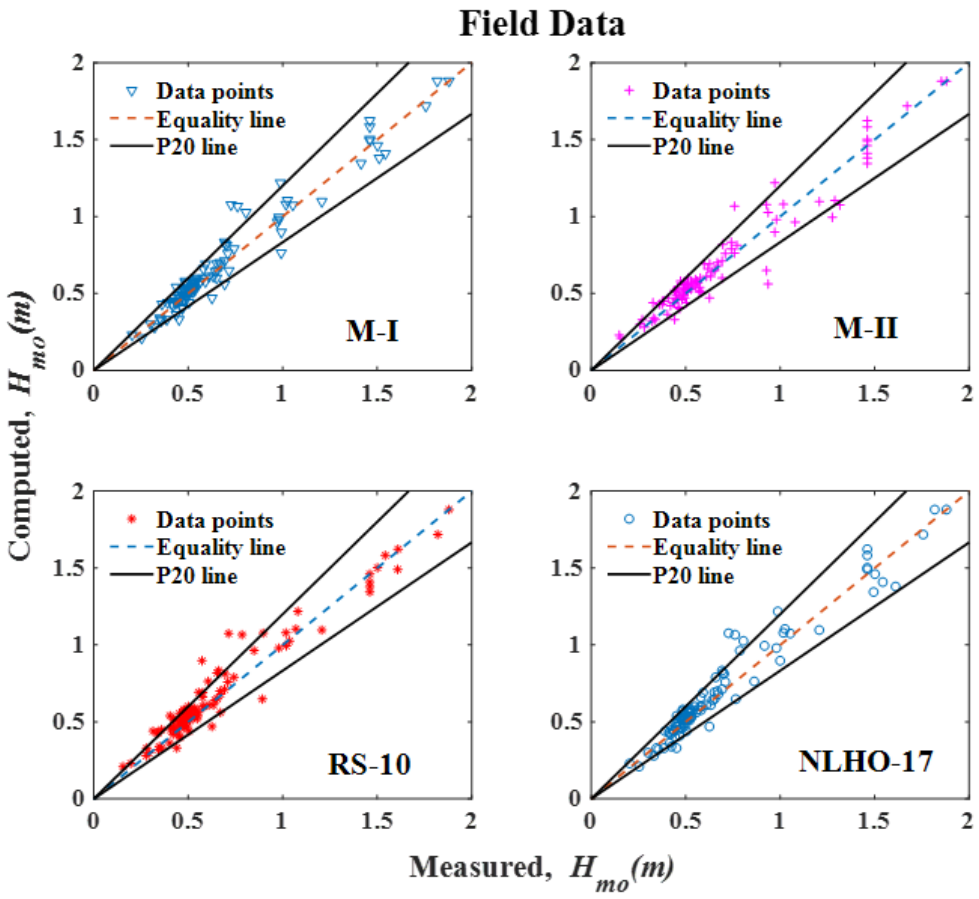

Figure 5.11: P20 Comparison of the spectral significant wave height of M-I, M-II, NLHO-17, and RS-10 with various experimental data (LS, SS, and FE).

Table 5.2: P20 error summary for spectral significant wave height.

Model Names	Error (%)			Average Error (%)
	LS	SS	FE	
M-I	2.07	3.59	3.11	3.01
M-II	7.78	14.09	8.86	10.21
RS-10	3.13	3.86	4.02	3.67
NLHO-17	2.91	3.71	3.53	3.38

Furthermore, in evaluating the wave set-up, Fig. 5.12 and Table 5.3 display the variations in P20 values for the different models (M-I, M-II, NLHH-09, and DDD-85). The average P20 values are 7.11% for M-I, 19.41% for M-II, 8.15% for NLHH-09, and 9.07% for DDD-85. These results also indicate that M-I stands out with superior accuracy in predicting wave set-up compared to the other models.

Table 5.3: P20 error summary for wave set-up.

Model Names	Average Error (%)
M-I	7.31
M-II	19.41
DDD-85	9.07
NLHH-09	8.15

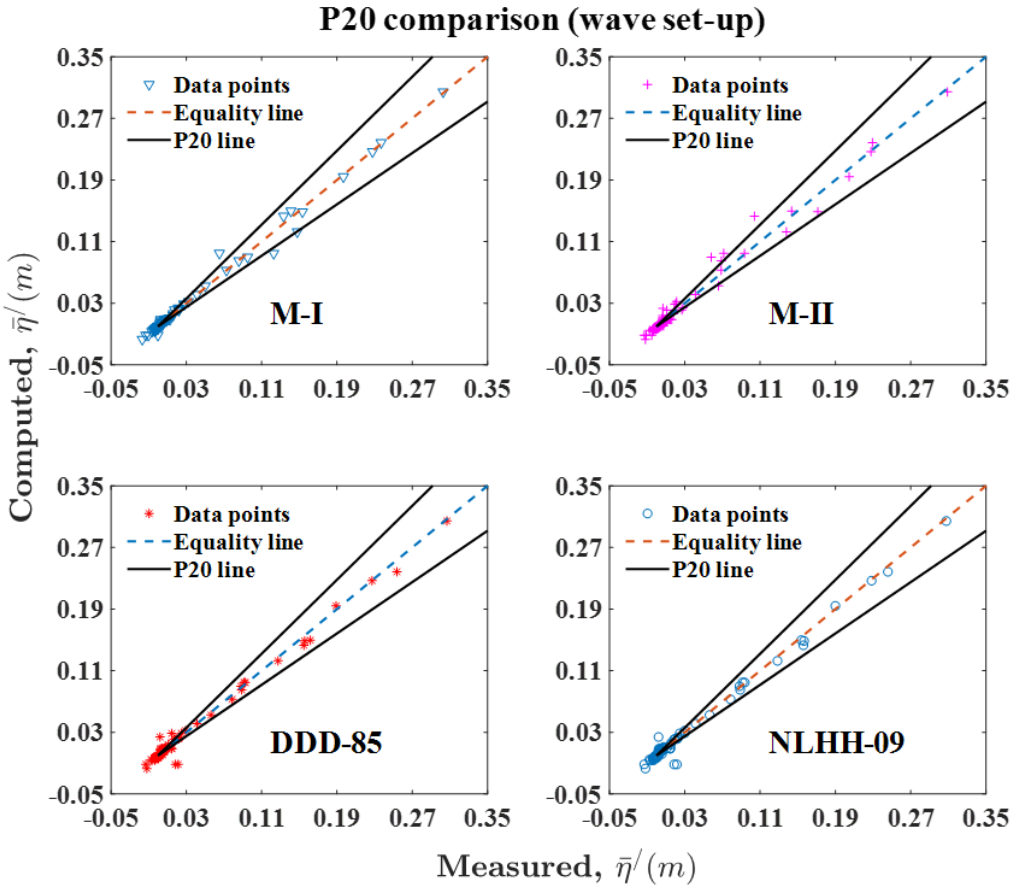

Figure 5.12: P20 differences of the wave set-up of M-I, M-II, NLHH-09, and DDD-85 with different experimental data.

BSS

The BSS measures how well the current model reduces relative error compared to previous models. It is expressed mathematically as follows:

$$BSS = \left\{1 - \frac{RMSRE(present\ model)}{RMSRE(previous\ model)}\right\}. \tag{5.44}$$

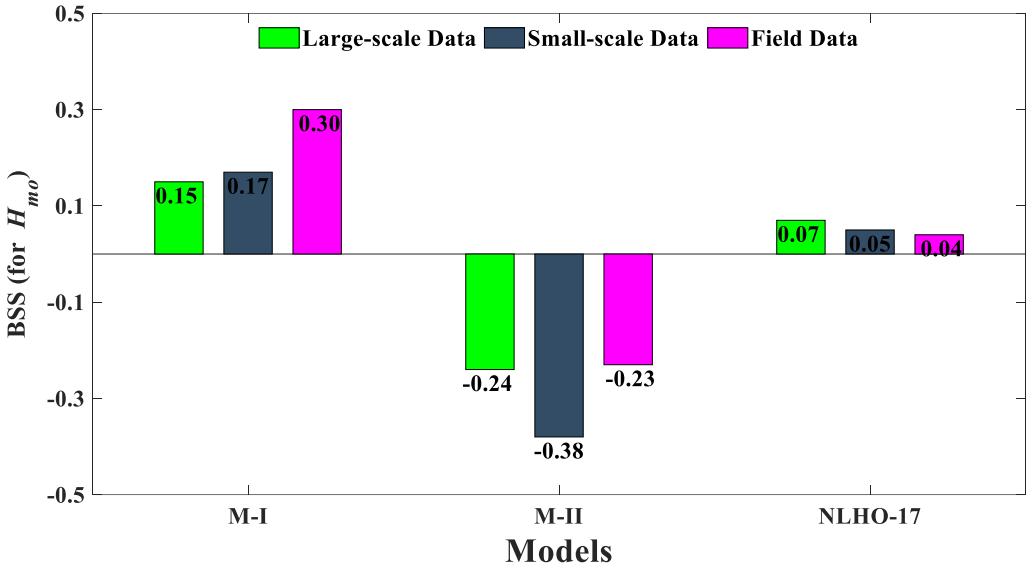

Figure 5.13: BSS comparison of M-I, M-II, and NLHO-17 concerning RS-10 for spectral significant wave height.

Fig. 5.13 illustrates the BSS values for models M-I, M-II, and NLHO-17, compared to RS-10 across LS, SS, and FE datasets for spectral significant wave height prediction. The positive BSS values for M-I highlight its superior performance relative to M-II, which shows negative BSS values, indicating its less effective performance.

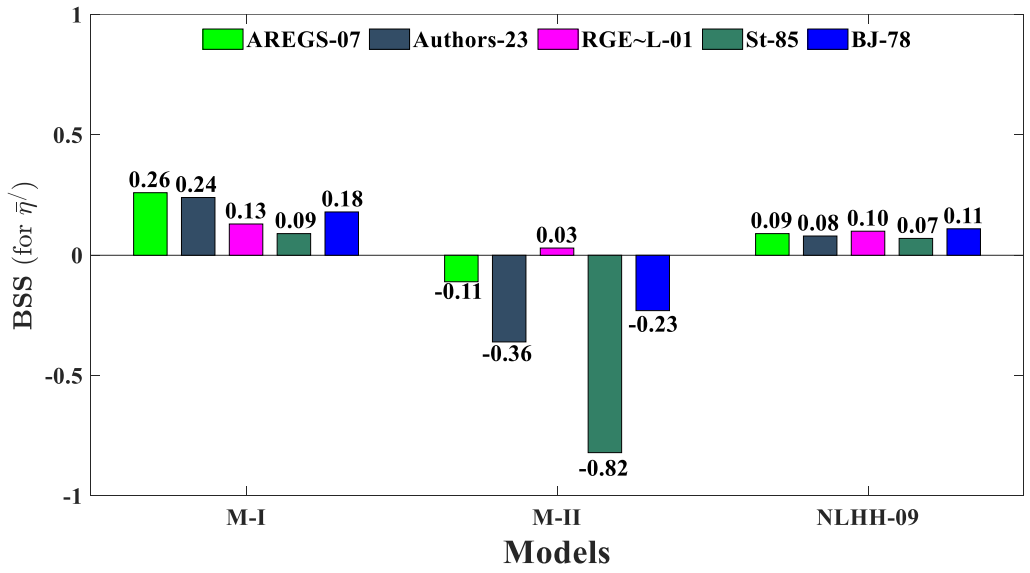

Figure 5.14: BSS comparison of M-I, M-II, and NLHH-09 with respect to DDD-85 for wave set-up.

In the context of wave set-up analysis, Figure 5.14 illustrates the Brier Skill Score (BSS) values for models M-I, M-II, and NLHH-09 compared to DDD-85. The

evaluation spans a range of datasets: AREGS-07, Authors-23, RGE~L-01, St-85, and BJ-78. Particularly, away from the instance of the RGE~H-01 data, M-I consistently shows positive BSS values, highlighting its effectiveness in accurately predicting wave set-up dynamics.

5.5 Conclusion

In this chapter, two energy-dissipation models were developed to study irregular waves undergoing both spilling and plunging breaking phenomena. The models, M-I and M-II, were based on the integration of air bubbles and the concept of the fraction of breaking waves, as suggested by Hoque, (2002) and Stingray et al. (2019), respectively. The foundational framework of these models was inspired by the air-bubble model for wave breakers under regular wave conditions proposed by Hoque et al. (2019) and Hoque, (2002). The breaking criterion established by Thornton and Guza, (1983) and the surf similarity parameter introduced by Battjes, (1974) were utilized to identify and categorize breaking waves. These models were then used to calculate spectral significant wave heights and wave set-ups by applying the principles of energy and momentum conservation laws. The validation of the adapted models was achieved through application across various wave conditions and seabed profiles, utilizing data from multiple experiments, including SS, LS, and FE by different researchers. The spectral significant wave height calculated by M-I showed excellent agreement with experimental data and existing models (NLHO-17 and RS-10), while M-II showed some discrepancies near mounds and the coastline. For wave set-up calculations, M-I performed exceptionally well across various experimental datasets and compared favorably with models like NLHH-09 and DDD-85, except near the breaking point. In contrast, M-II exhibited more inconsistencies near the breaking point and coastline compared to experimental data. The performance of the proposed models was assessed using error analysis with three error indices: RMSRE, P20, and BSS, to ensure an unbiased evaluation. When comparing the proposed models with established models (NLHO-17 and RS-10 for significant wave height; NLHH-09 and DDD-85 for set-up), the average P20 values for spectral significant wave height prediction were 3.01%, 10.21%, 3.38%, and 3.67% for M-I, M-II, NLHO-17, and RS-10, respectively. The RMSRE values were 6.17%, 10.09%, 7.82%, and 7.82%, respectively. For the BSS evaluation, M-I, M-II, and NLHO-17 were compared with RS-10 models, with M-I

showing all positive BSS values (LS, SS, and FE), whereas M-II had negative values, highlighting M-I's superiority. In terms of wave set-up, the average P20 values were 7.11%, 19.41%, 8.15%, and 9.07% for M-I, M-II, NLHH-09, and DDD-85, respectively. The RMSRE values were 7.91%, 12.42%, 8.76%, and 9.85% for these models. In the BSS assessment, M-I, M-II, and NLHH-09 were compared against DDD-85. Interestingly, M-I's BSS values were consistently positive, while M-II mostly had negative BSS values, except for the Authors-23 data, and the St-85 data were close to -1.00 (-0.82). This indicates the superior performance of M-I and unsatisfactory results for M-II in predicting wave set-up. Overall, despite some minor inconsistencies close to the shoreline, particularly for M-II, the models, especially M-I, demonstrated strong simulation capabilities for both spectral significant wave height and wave set-up across an extensive series of wave circumstances and coastal outlines.

CHAPTER 6

Wave Height Distribution for Plunging Breakers Induced by Air Bubbles

6.1 Abstract

This chapter examines how wave height distributions are influenced by plunging breaking waves and air bubbles in the surf zone. The wave height distributions that were formerly predicted by various models have been redeveloped to account for the effects of air bubbles. The most widely used wave height distributions were evaluated against laboratory observations conducted in a custom-built wave flume. The findings indicate a significant deviation from the Rayleigh distribution, with the proposed model showing a closer alignment with experimental data, especially for larger wave heights. The probability densities for larger waves are significantly reduced due to the presence of entrained air bubbles, resulting in measured wave heights that are lower than those predicted by the Rayleigh distribution. Moreover, the wave height parameters derived from the proposed model show good agreement with laboratory measurements when compared to the Rayleigh distribution. The theoretical analysis further demonstrates the dependency of the scale parameter on the decay coefficient, which matches well with the observed data and simplifies the proposed distribution to a one-parameter model. Error analysis confirms that the results from the proposed model perform well in comparison to existing models.

6.2 Introduction

In coastal and marine engineering, understanding wave height distribution is vital for several applications. It is crucial for tasks like evaluating wave loading on coastal infrastructure, estimating wave overtopping, and designing offshore structures and wind turbines. This knowledge ensures the reliability and effectiveness of engineering solutions in marine environments (Goda, 2010; Karmpadakis et al., 2022). The representative wave heights are typically obtained from a suitable distribution and integrated into design calculations. In some cases, wave heights—whether individual or representing the entire distribution—are estimated offshore and then modeled

towards the shoreline using numerical techniques. Accurate estimation of wave height distributions is essential, as inaccuracies can introduce uncertainty and errors into the design process. Although the Rayleigh probability density function (PDF) is often used for non-breaking waves, its accuracy diminishes in shallow waters where depth limitations and breaking waves occur. In these conditions, the actual wave height distribution can differ significantly from the Rayleigh model, necessitating alternative approaches for more accurate modeling(Battjes and Groenendijk, 2000; Dally, 1990; Hossain et al., 2022; Stringari and Power, 2019).

In recent years, coastal engineers have struggled to accurately model the distribution of wave heights in shallow water areas, especially in depth-limited breaking conditions along shallow foreshores and in the surf zone. When waves transport from deep water into the nearshore zone, they become steeper, eventually leading to breaking waves. This transition adds complexity to the modeling process. During the breaking process, air bubbles get entrained in the water, as shown in Fig. 6.01(a). This air entrainment transforms the wave energy into turbulence, resulting in a decrease in wave height as the waves approach the shoreline (Hoque et al., 2021, 2019). In shallow regions, four types of breakers are commonly observed, with plunging breakers being particularly significant. In a plunging breaker, the wave crest becomes unstable, collapses forward, and releases a large amount of energy, making it especially destructive. This type of breaking wave generates turbulent motion and high kinetic energy, which draws air into the water. As the wave crest falls, it forms air pockets within the water, enhancing turbulence and increasing energy dissipation. Consequently, some of the wave's kinetic energy is converted into turbulent kinetic energy, contributing to the overall dissipation of wave energy. Understanding this process is crucial, as it influences nearshore currents, sediment transport, and coastal morphology. The phenomenon of air bubble entrainment in plunging breaking waves has been extensively studied by numerous researchers (Chanson et al., 2002, 2006; Hoque and Aoki, 2008; Hossain and Araki, 2022, 2023). Research from the studies mentioned above has demonstrated that plunging breaking waves have higher levels of air entrainment, which results in greater energy dissipation. This leads to a more complex distribution of wave heights in the presence of plunging breaking waves.

Many studies have also examined the derivation of probability density functions and analytical distributions of wave heights, factoring in the impact of depth-induced wave

breaking in both deep and shallow water regions (Battjes and Janssen, 1978; Karmpadakis and Swan, 2022; Katsardi et al., 2013; Longuet-Higgins, 1952; Tayfun and Fedele, 2007; Thornton and Guza, 1983).

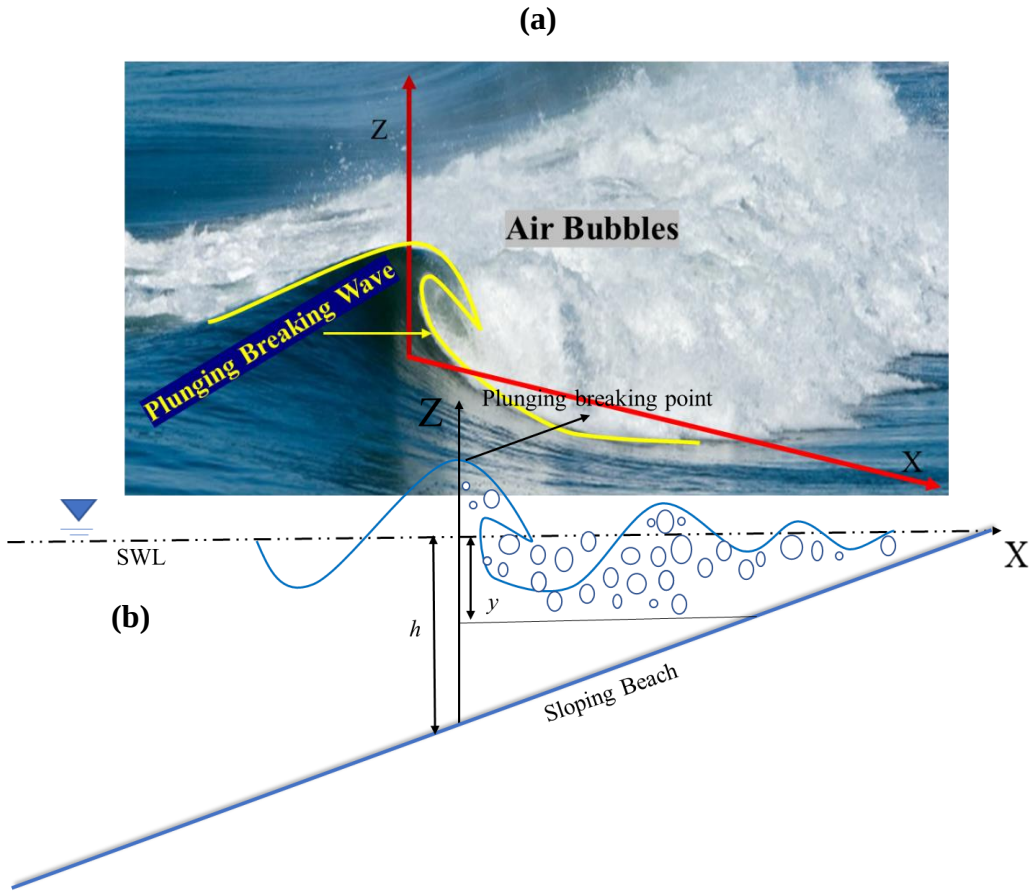

Figure 6.01:(a) An image depicting the ideal plunging breaking wave with air bubbles, and (b) A conceptual illustration outlining the propagation of plunging breaking waves over a uniform sloping seabed.

To determine the wave height distribution across the surf zone or a shallow foreshore, researchers have mainly focused on two approaches: (i) the point model (Battjes and Groenendijk, 2000; Klopman et al., 1989; Naess, 1985; Tayfun, 1991), and ii) the wave energy propagation model (WEPM) (Battjes and Janssen, 1978; Jadhav and Chen, 2013; Mendez et al., 2004; Thornton and Guza, 1983).

The point model, which uses a localized analysis that takes into account bathymetry and coastal morphology, offers site-specific predictions for individual wave heights based solely on local parameters. On the other hand, WEPM depends on the balance of

energy conservation for wave decay, which is determined by the specific energy dissipation model used.

An examination of various studies on wave height distributions in both deep and shallow water environments reveals a wide array of approaches to comprehending wave dynamics. It was found that, Thornton and Guza, (1983) successfully illustrated the applicability of a modified Rayleigh distribution for spilling breakers in the surf zone, utilizing the bore energy dissipation concept. In contrast, Hossain et al. (2022) proposed a novel distribution based on the dynamics of air bubbles for similar phenomena. The impact of vegetation on wave heights was specifically addressed by Jadav and Chen, (2013), who developed a probability density function that accounts for the attenuation effects caused by vegetation. Further research by Glukhovskiy et al. (1966), supported by Xiong et al. (2020), favored the Weibull distribution, which provided a better fit for shallow water conditions compared to the Rayleigh distribution. Mendez et al. (2004) formulated a probability density function for transformed waves in the surf zone, incorporating a bore energy dissipation model, which accurately represented wave height distribution on planar beaches. Meanwhile, Wu et al. (2016) introduced a two-part Weibull-generalized Pareto model for wave height in shallow water, parameterized using laboratory and field data to enhance understanding of coastal wave dynamics. Additionally, Katsardi et al. (2013) and Power et al. (2016) emphasized the intricate interactions between environmental factors and wave dynamics, highlighting the necessity for refined models capable of accurately predicting wave height distributions across various circumstances.

Research on probability density functions and wave height distributions in shallow water, especially regarding breaking waves, has garnered significant attention from scholars. However, there is still a lack of understanding regarding the modifications of wave height distributions, particularly in irregular waves affected by air bubble dynamics during plunging breaking events. This study seeks to fill this gap by developing a wave height distribution model specifically designed for random waves influenced by air bubble effects in plunging-breaking scenarios. The research highlights the essential requirement for precise wave height distribution models to guide the design of coastal structures and the management of oceanic controls.

6.3 Review of Existing Distribution for Shallow Water

This section delivers an in-depth examination of various wave height distributions that have been tailored for shallow water conditions, based on contributions from various investigators (Glukhovskiy, 1966; Battjes and Groenendijk, 2000; Mendez et al., 2004; Jadhav and Chen, 2013; Wu et al., 2016; Hossain et al., 2022). Developed under various assumptions, these distributions provide valuable insights into the PDF and cumulative distribution function (CDF), covering a range of models suitable for shallow water surroundings.

6.3.1 Glukhovskiy Distribution

Glukhovskiy, (1966) utilized a Weibull distribution to characterize the probability density function for wave height in shallow water, the PDF of this distribution can be written as follows:

$$P(H) = \frac{B\kappa}{H_m}\left(\frac{H}{H_m}\right)^{\kappa-1} exp\left[-B\left(\frac{H}{H_m}\right)^{\kappa}\right], \tag{6.01}$$

and CDF:

$$F_H = 1 - exp\left[-B\left(\frac{H}{H_m}\right)^{\kappa}\right] \tag{6.02}$$

where H is the local wave height, H_m represents the local significant wave height, κ denotes the shape parameter, and B represents the scale parameter. This distribution simplifies to the Rayleigh distribution when the shape parameter (κ) is set to 2, and the scale parameter (B) is set to 1.

Limitations: The empirical basis of this distribution limits its applicability, which may lead to inaccuracies in complex wave conditions, and it does not establish specific upper and lower bounds.

6.3.2 BG distribution

To model wave heights in shallow water, Battjes and Groenendijk, (2000) developed a bimodal Weibull-Weibull distribution. This distribution's parameters were derived from laboratory measurements, focusing on wave heights that exceed a

specified threshold, H_{tr}. The equations for the PDF and CDF of this distribution are as follows:

$$P(H) = \begin{cases} \frac{\kappa_1}{H_1}\left(\frac{H}{H_1}\right)^{\kappa_1 - 1} exp\left[-\left(\frac{H}{H_1}\right)^{\kappa_1}\right] \\ \frac{\kappa_2}{H_2}\left(\frac{H}{H_2}\right)^{\kappa_2 - 1} exp\left[-\left(\frac{H}{H_2}\right)^{\kappa_2}\right] \end{cases}, \quad \text{for} \begin{cases} H \le H_{tr} \\ H > H_{tr} \end{cases}, \tag{6.03}$$

and

$$F_H = \begin{cases} 1 - exp\left[-\left(\frac{H}{H_1}\right)^{\kappa_1}\right] \\ 1 - exp\left[-\left(\frac{H}{H_2}\right)^{\kappa_2}\right] \end{cases} \quad \text{for} \begin{cases} H \le H_{tr} \\ H > H_{tr} \end{cases}, \tag{6.04}$$

where $\kappa_1 = 2, \kappa_2 = 3.6$, H is the local wave height, and $H_{tr} = h(5.8\, tan\theta + 0.35)$, here $tan\theta$ is the bed slope. Nevertheless, it is essential to emphasize that the calibration of this model is derived solely from unidirectional laboratory measurements, without considering bathymetric changes in other directions. The normalization wave heights H_1 and H_2 are detailed in Table 2 of Battjes and Groenendijk (2000).

Limitation: One notable drawback of this distribution is that its probability density function displays a discontinuity at the transition wave height (Karmpadakis et al., 2020).

6.3.3 MLM distribution

Adopting an entirely different perspective, Mendez et al. (2004) formulated a distribution that examines the transformation of wave heights as they near the shoreline. They based their model on wave energy propagation, starting with an initial Rayleigh distribution in deep water, and subsequently deriving a unique wave height distribution for shallow water. This approach incorporates the effects of wave shoaling following Green's law and wave breaking, as outlined by Battjes and Janssen, (1978). The PDF and CDF for this distribution are presented below:

$$P(H) = \varphi^2(\kappa)\frac{2HH_{rms}}{(H_{rms} - \kappa H)^3} exp\left[-\left(\frac{H}{(H_{rms} - \kappa H)}\right)^2 \varphi^2(\kappa)\right], \tag{6.05}$$

and

$$F_H = 1 - exp\left[-\left(\frac{H}{(H_{rms}-\kappa H)}\right)^2 \varphi^2(\kappa)\right] \quad (6.06)$$

where, H is the local wave height, H_{rms} stands for the root-mean-square wave height, $\phi(\kappa) \approx (1-\kappa^{0.944})^{1.19}$, and $\kappa = \frac{H_{rms}}{H_{max}}$, here κ is computed from the subsequent equation:

$$\kappa = (26.2I_r^2 - 20.8I_r + 4.7)\left(\frac{H_{rms}}{h}\right)^{2.5} \text{for} \begin{cases} \left(\frac{H_{rms}}{h}\right) < 0.66 \\ 0.25 > I_r > 0.02 \end{cases}, \quad (6.07)$$

where

$$I_r = tan\theta \sqrt{\frac{g\bar{T}^2}{2\pi H_{rms}}}. \quad (6.08)$$

Here, $\bar{T}$ stands for the mean wave period, and θ represents the bed slope.

Limitations: Although the MLM distribution forms the foundation for WEPM-type wave height distributions, it has significant limitations. Notably, its shape parameter is constrained for Irrebian numbers below 0.3, and it lacks simple equations for calculating statistical parameters.

6.3.4 JC distribution

Adjustments to the Rayleigh distribution model have been made by Jadhav and Chen, (2013) to incorporate the effects of vegetation on waves as they move into shallow water areas. The proposed PDF and CDF are expressed as follows:

$$P(H) = \frac{2H}{\left(1-\frac{\alpha H}{H_{rms}}\right)^3}\left(\frac{\beta}{H_{rms}}\right)^2 exp\left[-\left(\frac{H}{\left(1-\frac{\alpha H}{H_{rms}}\right)H_{rms}}\right)^2 \beta^2\right], \text{where } 0 \le H < \frac{H_{rms}}{\alpha} \quad (6.09)$$

and the CDF:

$$F_H = 1 - exp\left[-\left(\frac{H}{\left(1-\frac{\alpha H}{H_{rms}}\right)H_{rms}}\right)^2 \beta^2\right]. \quad (6.10)$$

where H is the local wave height, H_{rms} represents the root-mean-square wave height, the shape parameter is α, and the scale parameter β, looks like the form of the Weibull

distribution. Here, $\alpha = C_1 H_{rms}$, and $\beta = 1 - C_2 H_{rms}$, C_1 and C_2 are the vegetational coefficients.

Limitations: This distribution has been customized for salt marsh vegetation, with the shape parameter being impacted by the Keulegan–Carpenter number. The model's accuracy heavily depends on the precise estimation of its derivations.

6.3.5 WRCEJ distribution

To derive this model, a transition wave height H_{tr}, was selected to separate the distribution into two distinct segments. Ensuring continuity of the probability density functions at H_{tr} and fitting each segment independently led to the following formulation for the PDF (Wu et al., 2016):

$$P(H) = \begin{cases} \frac{\kappa\mu}{\rho H_s}\left(\frac{H}{\rho H_s}\right)^{\kappa-1} exp\left[-\mu\left(\frac{H}{\rho H_s}\right)^{\kappa}\right] \\ \frac{1}{\sigma}\left\{1+\frac{\xi}{\sigma}(H-\rho H_s)\right\}^{-\frac{1}{\xi}-1} exp[-\mu] \end{cases}, \quad \text{for} \begin{cases} H \le H_{tr} \\ H > H_{tr}, \end{cases} \tag{6.11}$$

and CDF:

$$F_H = \begin{cases} 1 - exp\left[-\mu\left(\frac{H}{\rho H_s}\right)^{\kappa}\right] \\ 1 - exp[-\mu]\left\{1+\left[1+\frac{\xi}{\sigma}(H-\rho H_{tr})\right]\right\}^{-\frac{1}{\xi}}, \end{cases} \quad \text{for} \begin{cases} H \le H_{tr} \\ H > H_{tr}, \end{cases} \tag{6.12}$$

where H is the local wave height; H_s represents the significant wave height; μ, σ, and κ represent the scale and shape parameters of the Weibull component individually; and ξ signifies the shape parameter of the Generalized Pareto factor (see Wu et al., (2016)).

Limitations: In the generalized Pareto distribution, a negative shape parameter signifies an upper bound on the distribution, which is often used to characterize maximum wave height. However, applying this criterion to random waves in intermediate and shallow water depths can be problematic (Karmpadakis et al., 2020). Additionally, the presence of multiple scale parameters in the distribution complicates the process of accurately determining their values across a wide range of applications.

6.3.6 HRH distribution

In their study, Hossain et al. (2022) developed a model aimed at understanding wave height distributions while factoring in the influence of air bubbles during spilling breaking waves. This model is based on an initial Rayleigh distribution applicable to deep water, which is then modified to establish a specific wave height distribution for shallower waters. The formulation considers wave shoaling effects in accordance with Green's law and integrates the dynamics of wave breaking, including the interaction of air bubbles, as described by Hoque et al. (2019). The PDF and CDF for this wave height distribution are presented as follows:

$$P(H) = \frac{2(H-q)}{(H_{rms}-w)^2} exp\left[-\left(\frac{H-q}{H_{rms}-w}\right)^2\right], \qquad \text{where } q \leq H < \infty. \tag{6.13}$$

and the CDF:

$$F_H = 1 - exp\left[-\left(\frac{H-q}{H_{rms}-w}\right)^2\right], \qquad \text{where } q \leq H < \infty. \tag{6.14}$$

Here, H is the local wave height; H_{rms} represents the root-mean-square wave height; and q, w signify decay coefficients attributed to the effect of air bubbles, as described in Hossain et al., (2022).

Limitations: A key drawback of this distribution is its emphasis on spilling and breaking waves, which may limit its applicability in other wave conditions. Furthermore, it tends to perform better for smaller wave heights, making it less effective for accurately representing larger wave events.

The extensive literature review highlights a significant emphasis on wave height distribution within specific frameworks, including the effects of vegetation, energy dissipation, and traditional modeling approaches. However, there is a notable lack of research addressing the role of air bubbles in plunging breaking waves, particularly in shallow water environments. This gap is critical for several reasons. Firstly, accurately forecasting wave forces on coastal structures is essential for their design and durability against the added stresses caused by entrained air. Secondly, understanding how air bubbles affect wave energy dissipation and sediment transport is crucial for analyzing coastal erosion and deposition processes. Thirdly, recognizing this distribution is vital

for ensuring safety in navigation and coastal operations, as air bubbles influence water density and buoyancy. Finally, precise modeling of these interactions is necessary for environmental evaluations and for addressing the effects of climate change on coastal ecosystems. Consequently, this study seeks to fill this gap by developing a new distribution model for plunging breaking waves that incorporates the effects of air bubbles, enabling accurate predictions of wave height in shallow water settings.

6.4 Model Formulation Considering the Impact of Air Bubbles

6.4.1 Mathematical Background

This study introduces a wave height distribution model that incorporates the influence of air bubbles, building on the findings of Hoque et al. (2019). It emphasizes the crucial role air bubbles play in determining wave heights in shallow water. Unlike some existing models that overlook the impact of wave energy in shallower regions, this approach recognizes the significant effect of air bubbles on wave height distribution. The model begins by transitioning wave heights from deep water to shallow water using a Gaussian distribution that takes local conditions into account. As waves approach extremely shallow depths, they begin to break, leading to the entrainment of air bubbles and subsequent energy dissipation, as illustrated in Fig. 6.01(a). This approach treats random waves as individual regular waves, consistent with methodologies previously employed in research (Mendez et al., 2004; Jadhav and Chen, 2013). In the surf zone, waves lose energy due to air bubbles generated by breaking waves, which inspired Hoque et al. (2019) to develop a model for wave energy dissipation based on this process, expressed as follows:

$$D_a = \frac{y}{2}\frac{w_r \alpha \rho_w g c_0}{(1-c_0)}, \tag{6.15}$$

where D_a is the energy dissipation rate owing to the air bubble effect, y signifies the penetration depth, ρ_w stays the density of water, α remains an adjusting parameter and for plunging breakers, its value is 1.50 as recommended by Hoque et al., (2019), w_r is the rising bubbles' velocity, and c_0 is the reference void fraction.

Due to the intense and turbulent characteristics of the plunging wave-breaking process, which leads to the incorporation of a significant number of air bubbles, the Führboter,

(1970) condition can be utilized to adjust for y such as $y \propto H_b = \gamma h$, and Eq. (6.15) yields:

$$D_a = \frac{\gamma h}{2} \frac{w_r \alpha \rho_w g c_0}{(1-c_0)}, \tag{6.16}$$

where H_b, h and γ are denote the breaking wave height, still water depth, and an arbitrary constant, individually.

Merging the one-dimensional energy conservation equation with the aforementioned dissipation model, and utilizing the principles of linear water wave theory, leads to the formulation expressed as follows:

$$\frac{dE_f}{dx} = -D_a, \tag{6.17}$$

where E_f is given by Hoque et al., 2019 as follows:

$$E_f = \frac{1}{8} \rho_w g \left\{ H^2 \sqrt{h} + \frac{c_0}{2(1-c_0)} H^2 \sqrt{h} \right\}. \tag{6.18}$$

The seaward boundary is identified at the point where the waves break (as shown in Fig. 6.01(b)), and at this boundary, shallow water conditions are assumed. For shallow water waves propagating normally along a planar-sloping beach, Eqs. (6.17) and (6.18) can be rewritten as:

$$\frac{d(H^2\sqrt{h})}{dx} + A \frac{d(H^2\sqrt{h})}{dx} = -A_1 h, \tag{6.19}$$

where $A = \frac{c_0}{2(1-c_0)}$, and $A_1 = \frac{4\alpha w_r \gamma}{\sqrt{g}} \frac{c_0}{(1-c_0)}$ are the arbitrary constants.

For a uniform-sloping beach, $h = h_0 - mx$, where m is the slope, and h_0 indicates the still water depth at the toe of the slope.

Propositioning $Z = H^2\sqrt{h}$ in Eq. (6.19) that yields:

$$\frac{dZ}{dh} = \frac{A_1}{(1+A)m} h = A_2 h, \tag{6.20}$$

where $A_2 = \frac{A_1}{(1+A)m}$.

Simplification yields:

$$Z = A_3 h^2 + B, \tag{6.21}$$

where $A_3 = \frac{A_2}{2}$ and B is the integrating constant.

Transfering back using $Z = H^2\sqrt{h}$, generates:

$$H^2\sqrt{h} = A_3 h^2 + \mathbb{C}_1. \tag{6.22}$$

By applying the boundary conditions $H = H_0$ and $h = h_0$ at $x = x_0$, the constant of integration is figured out as follows:

$$\mathbb{C}_1 = H_0^2\sqrt{h_0} - A_3 h_0^2. \tag{6.23}$$

Ultimately, employing the expression for $\mathbb{C}_1$ as per Eq. (6.23), which gives:

$$H = (aH_0^2 + b)^{\frac{1}{2}}, \tag{6.24}$$

where the parameter $a = \left(\frac{h_0}{h}\right)^{1/2}$ corresponds to the shoaling coefficient as per Green's law and the other parameter $b = A_3\left(\frac{h^2 - h_0^2}{\sqrt{h}}\right)$ signifies the damping effect attributed to air bubbles.

6.4.2 PDF Derivation

In a region immediately before the breaking zone, the wave characteristics follow the Rayleigh PDF, assuming a narrow-banded Gaussian process as outlined by Dally, (1990), the expression for the incident wave height $P_0(H_0)$ is written as follows:

$$P_0(H_0) = \frac{2H_0}{H_{rms,0}^2} exp\left[-\left(\frac{H_0}{H_{rms,0}}\right)^2\right], \text{ where } \quad 0 \le H_0 < \infty. \tag{6.25}$$

Here, the expression $H_{rms,0}^2$ is derived from the integral of $\int_0^\infty H_0^2\, P_0(H_0) dH_0$ over the range from 0 to infinity, where $H_{rms,0}$ denotes the root-mean-square wave height at the seaward boundary.

Believing the validity of the transformation defined by Eq. (6.24) for each wave H_0, the assessed probability density function $P(H)$ at a specific point within the breaking zone can be computed through a standard transformation of variables, as follows:

$$P(H) = P_0(H_0)\left|\frac{\partial H_0}{\partial H}\right|. \tag{6.26}$$

To acquire the value of $\left|\frac{\partial H_0}{\partial H}\right|$, differentiating Eq. (6.24) with respect to H, result in:

$$\left|\frac{\partial H_0}{\partial H}\right| = \frac{H}{a}\frac{1}{\sqrt{\frac{H^2-b}{a}}}. \tag{6.27}$$

By combining Eqs. (6.25), (6.26), and (6.27), yields:

$$P(H) = \frac{2H}{aH_{rms,0}^2} exp\left[-\frac{H^2-b}{aH_{rms,0}^2}\right], \text{ where } \sqrt{b} \le H < \infty. \tag{6.28}$$

Conversion to local parameter, H_{rms}

Typically, the distribution of wave heights in random waves is predominantly influenced by local wave parameters, with a foundation in the incident wave parameters within the surf zone. In the case of narrow-banded waves experiencing damping due to air bubble effects, the root-mean-square wave height ($H_{rms,0}$) can be expressed with the local H_{rms} (as detailed in Hossain and Araki, (2023)). They introduced an energy dissipation model ($D_{a,p}$) for plunging breaking waves attributed to air bubble effects using the representative wave approach as follows:

$$D_{a,p} = \frac{\rho_w g c_0 \alpha w_r \gamma}{2(1-c_0)} h, \tag{6.29}$$

where all parameters are detailed in the preceding section.

Now, to derive the local H_{rms}, revisiting the energy balance equation using this energy dissipation model (Eq. (6.29)), this can be expressed as follows (following Thornton and Guza, (1983)):

$$\frac{d(Ec_g)}{dx} = -\frac{\rho_w g c_0 \alpha w_r \gamma}{2(1-c_0)} h, \tag{6.30}$$

where $E = \frac{1}{8}\rho g \int_0^\infty H^2 P(H) dH = \frac{1}{8}\rho_w g H_{rms}^2$ and $c_g = \sqrt{gh}$, is the wave celerity, g remains for the gravitational acceleration.

Now, by substituting these values in the above and performing simplifications, yields:

$$\frac{d(H_{rms}^2\sqrt{h})}{dx} = -\frac{4c_0\alpha w_r\gamma}{\sqrt{g}(1-c_0)}h. \tag{6.31}$$

Letting, $Y = H_{rms}^2\sqrt{h}$, and employing $h = h_0 - mx$ in Eq. (6.31), which provides:

$$\frac{dY}{dh} = \frac{4c_0\alpha w_r\gamma}{m\sqrt{g}(1-c_0)}h. \tag{6.32}$$

Integrating and reverting to its original form, yields:

$$H_{rms}^2\sqrt{h} = Bh^2 + \mathbb{C}_2, \tag{6.33}$$

where $\mathbb{C}_2$ is the integrating constant and $B = \frac{2c_0\alpha w_r\gamma}{m\sqrt{g}(1-c_0)}$.

By applying the boundary conditions $H_{rms} = H_{rms,0}$ and $h = h_0$ at $x = x_0$, the value of $\mathbb{C}_2$ is obtained and then Eq. (6.33) becomes:

$$H_{rms}^2\sqrt{h} = B(h^2 - h_0^2) + H_{rms,0}^2\sqrt{h_0}. \tag{6.34}$$

After some simplification, Eq. (6.34) provides the following:

$$H_{rms,0} = \sqrt{\frac{H_{rms}^2 - c}{a}}, \tag{6.35}$$

where $a = \left(\frac{h_0}{h}\right)^{1/2}$ and $c = B\frac{(h^2-h_0^2)}{\sqrt{h}}$.

To enhance the transformed probability density function $P(H)$ considering air bubble effects, substitute Eq. (6.35) into Eq. (6.28) and express the new PDF, $P(H)$ as follows:

$$P(H) = \frac{2H}{(H_{rms}^2 - c)} exp\left[-\left(\frac{H^2-b}{H_{rms}^2-c}\right)\right], \qquad \text{where } \sqrt{b} \le H < \infty. \tag{6.36}$$

After integrating Eq. (6.36), the corresponding CDF, (F_H) is found as follows:

$$F_H = 1 - exp\left[-\left(\frac{H^2-b}{H_{rms}^2-c}\right)\right], \qquad \text{where } \sqrt{b} \le H < \infty. \tag{6.37}$$

Finally, Eqs. (6.36) and (6.37) represent the new PDF and CDF of plunging breaking waves attributed to air bubble effects, respectively.

In the absence of air bubble effects ($c_0 = 0$) in deep water, Eqs. (6.36) and (6.37) correspond to the Rayleigh distribution model.

To present Eq. (6.36) in a more simplified form, by introducing $\kappa = \frac{b}{H_{rms}^2}$, $\Phi = 1 - \frac{c}{H_{rms}^2}$ are local dimensionless parameters and $\Psi = \frac{H}{H_{rms}}$ as the non-dimensional wave height in Eq. (6.36) and performing subsequent algebraic operations, it transforms into a local dimensionless PDF, $P(\Psi)$ as follows:

$$P(\Psi) = \frac{2\Psi}{\Phi} exp\left[-\frac{(\Psi^2-\kappa)}{\Phi}\right], \qquad \text{where} \qquad \frac{\sqrt{\kappa}}{H_{rms}} \leq \Psi < \infty. \tag{6.38}$$

By integrating the above dimensionless PDF, the CDF has been derived as follows:

$$F_\Psi = 1 - exp\left[-\frac{(\Psi^2-\kappa)}{\Phi}\right], \qquad \text{where} \qquad \frac{\sqrt{\kappa}}{H_{rms}} \leq \Psi < \infty. \tag{6.39}$$

Finally, Eqs. (6.38) and (6.39) characterize the updated PDF and CDF of plunging breaking waves, considering the effects of air bubbles, presented in a dimensionless form.

6.4.3 Derivation of Characteristic Wave Height

By considering the impact of air bubble effects, statistical parameters for wave height can be established. In this context, revisit and present the mathematical representation of the average wave height of the highest qN waves taking the limits from $H = \widehat{H}_q$ to ∞, gives:

$$\overline{H}_q = \frac{\int_{\widehat{H}_q}^{\infty} HP(H)dH}{\int_{\widehat{H}_q}^{\infty} P(H)dH} = \frac{\int_{\widehat{H}_q}^{\infty} \frac{2H^2}{(H_{rms}^2-c)} exp\left[-\left(\frac{H^2-b}{H_{rms}^2-c}\right)\right]dH}{\int_{\widehat{H}_q}^{\infty} \frac{2H}{(H_{rms}^2-c)} exp\left[-\left(\frac{H^2-b}{H_{rms}^2-c}\right)\right]dH}, \tag{6.40}$$

where the probability that the wave height is greater than or equal to a given threshold $\widehat{H}_q$ and is surpassed by the qN waves is given by $\widehat{H}_q = \sqrt{(H_{rms}^2 - c)}\sqrt{ln\frac{1}{q}}$ (see details in Longuet-Higgins, 1952).

Upon integrating Eq. (6.40) the result yields the simplified form for the average wave height of the highest qN waves as follows:

$$\bar{H}_q = \left\{\sqrt{ln\left(\frac{1}{q}\right)} + \frac{\sqrt{\pi}}{2q} erfc\left(\sqrt{ln\left(\frac{1}{q}\right)}\right)\right\}\left\{\sqrt{(H_{rms}^2 - c)}\right\}, \tag{6.41}$$

where $erfc\left(\sqrt{ln\left(\frac{1}{q}\right)}\right)$ represents the complementary error function.

Now, utilizing Eq. (6.41), it is easy to deduce the statistical parameters of wave height, such as H_1, $H_{1/3}$, and $H_{1/10}$ in the following manner:

$$H_1 = H_{avr} = \left\{\sqrt{ln(1)} + \frac{\sqrt{\pi}}{2} erfc\left(\sqrt{ln(1)}\right)\right\}\left\{\sqrt{(H_{rms}^2 - c)}\right\} = 0.886 * \left\{\sqrt{(H_{rms}^2 - c)}\right\}, \tag{6.42}$$

$$H_{\frac{1}{3}} = \left\{\sqrt{ln(3)} + \frac{\sqrt{\pi}}{\frac{2}{3}} erfc\left(\sqrt{ln(3)}\right)\right\}\left\{\sqrt{(H_{rms}^2 - c)}\right\} = 1.416 * \left\{\sqrt{(H_{rms}^2 - c)}\right\}, \tag{6.43}$$

and

$$H_{\frac{1}{10}} = \left\{\sqrt{ln(10)} + \frac{\sqrt{\pi}}{\frac{2}{10}} erfc\left(\sqrt{ln(10)}\right)\right\}\left\{\sqrt{(H_{rms}^2 - c)}\right\} = 1.80 * \left\{\sqrt{(H_{rms}^2 - c)}\right\}. \tag{6.44}$$

It is evident that as q decreases in Eq. (6.41), there is a notable alteration in the statistical wave height parameters.

6.5 Findings and Validation

6.5.1 Experiment

To verify the accuracy of the developed model, the authors conducted experiments. Detailed descriptions of these experiments are provided in Chapter 2, with a concise explanation included in the experiment section of Chapter 5. The case used in this chapter is presented in the following table.

Table 1: Incident wave parameter variations across plunging breaking cases.

Cases	Wave Height, H_s (m)	Wave Period, T_s (s)	Water depth, h_0 (m)
Case I	0.093	1.35	0.30
Case II	0.085	1.31	0.30
Case III	0.079	1.48	0.30
Case IV	0.068	1.44	0.30

6.5.2 Identification of Breaking and Plunging Breakers

Examining a random wave train progressing toward the beach, depicted in Fig. 6.01(a), as the wave initiates breaking, its energy and height diminish approaches the shore. Identifying the breaking point becomes crucial. In this context, consider the recommendation proposed by Thornton and Guza, (1983), which can be articulated as follows:

$$H_{rms,b} = \gamma h, \tag{6.45}$$

Here, $H_{rms,b}$ denotes the RMS wave height at the breaking point, h represents the water depth, and γ is an arbitrary constant with a specified value of 0.42 as suggested by (Thornton and Guza, 1982).

The classification of various types of wave breakers relies on the surf similarity parameter ξ_b (see details in Chapter 3, section 3.4.2), formulated by Battjes, (1974), as determined by the following equation:

$$\xi_b = \frac{m}{\sqrt{\frac{H_{rms,b}}{L_0}}}, \tag{6.46}$$

In this context, L_0, defined as $\frac{g\bar{T}^2}{2\pi}$, which represents the wavelength in deep water, while m characterizes the slope of the beach and $\bar{T}$ is the average period.

6.5.3 Determination of c_0, κ, and Φ

Void Fraction (c_0)

In computing the void fraction, utilized the void fraction relation presented by Hoque and Aoki, (2005) specific to plunging breaking waves. They identified a formula

for determining the void fraction as a function of the breakpoint-to-shoreline distance, which is expressed as follows:

$$\text{If} \quad 0 \le \left(\frac{x-x_{brk}}{L_0}\right) \le 0.14 \quad \text{then} \quad c_0 = \left(\frac{x-x_{brk}}{L_0}\right) * 1.285. \tag{6.47}$$

$$\text{If} \quad \left(\frac{x-x_{brk}}{L_0}\right) > 0.14 \quad \text{then} \quad c_0 = 0.285 - 0.75\left(\frac{x-x_{brk}}{L_0}\right). \tag{6.48}$$

In this context, x is the horizontal distance from the wave maker to the shoreline, x_{brk} denotes the horizontal distance from the wave maker to the breakpoint in the direction of the shoreline, as depicted in Fig. 1(b), and L_0 is the incident wavelength.

Decay coefficient $(\boldsymbol{\kappa})$

The suggested PDF is contingent upon a Decay coefficient κ. This coefficient encompasses details about local wave properties (H_{rms}) and the historical aspects of propagation (h, h_0, m, c_0, α, w_r and $\bar{T}$). Since κ serves as an indicator of saturation, it is anticipated that this coefficient can be formulated as a function of certain coefficients linked to the degree of saturation and the characteristics of the breaking process. Following this concept, κ was calculated from the straightforward relationship as follows:

$$\kappa = \frac{b}{H_{rms}^2}. \tag{6.49}$$

Scale parameter $(\boldsymbol{\Phi})$

Since both the scale and decay coefficients are defined concerning H_{rms}, the inclusion of this common factor can be omitted. This results in the formulation of the following relationship, specifically expressing the scale parameter in terms of the decay coefficient:

$$\Phi = 1 - \frac{c}{b}\kappa, \quad \text{which implies} \quad \Phi = 1 - \frac{(2-c_0)}{2(1-c_0)}\kappa. \tag{6.50}$$

In Eq. (6.50), it is evident that the scale parameter is directly influenced by both the decay coefficient and the reference void fraction.

6.5.4 Interpretation and Discussion

6.5.4.1 Void fractions vs decay coefficient and scale parameter

After performing the verification of plunging-breaking occurrences ($\xi_b = 0.87, \xi_b = 0.85, \xi_b = 1.00, \xi_b = 1.02$ for all cases I, II, III and IV, correspondingly), the void fraction entrainment was calculated for each scenario using Eqs. (6.47) and (6.48). The distribution of the void fraction along the horizontal distance for all experimental cases is illustrated in Fig. 6.02. In these cases, the highest void fraction recorded was approximately 16%, which is consistent with findings from other studies (Blenkinsopp and Chaplin, 2011; Hoque and Aoki, 2005; Hossain and Araki, 2023; Huang et al., 2009). Moreover, it has been observed that the void fraction increases with longer wave periods relative to wave heights. This trend results from the extended interaction time between longer wave periods and the water surface, which promotes greater air entrapment within the water column. Additionally, the slower oscillation associated with longer waves allows for the inclusion of larger volumes of air into the water, unlike smaller wave periods.

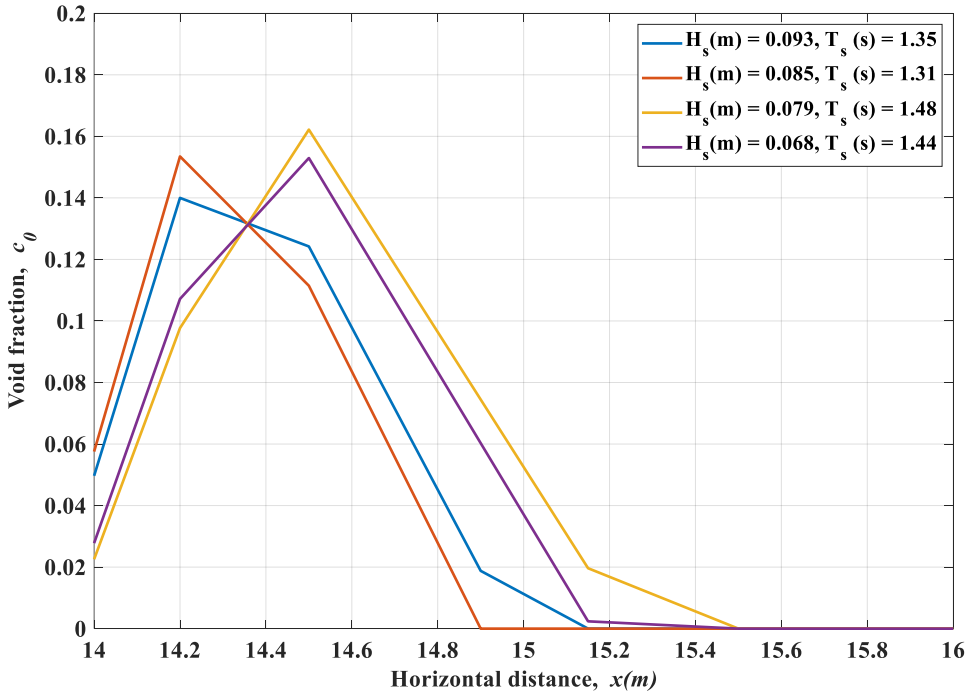

Figure 6.02: Variations in void fraction across horizontal distance.

The analysis of the decay coefficient (κ), which is dependent on parameters such as b and H_{rms} (see Eq. (6.49)), where b involves numerous components (h, h_0, m, c_0, α, w_r and $\bar{T}$), showed an interesting correlation with respect to the parameter c_0, considered substantial in this analysis. The analysis focused on the decay coefficient in relation to the void fraction, as shown in Fig. 6.03. The results revealed a positive relationship between the decay coefficient and the void fraction, peaking at around 0.16. This observation implies that the decay coefficient is contingent upon the void fraction. Consequently, a hypothesis is proposed that suggests a direct proportionality between the decay coefficient and the void fraction..

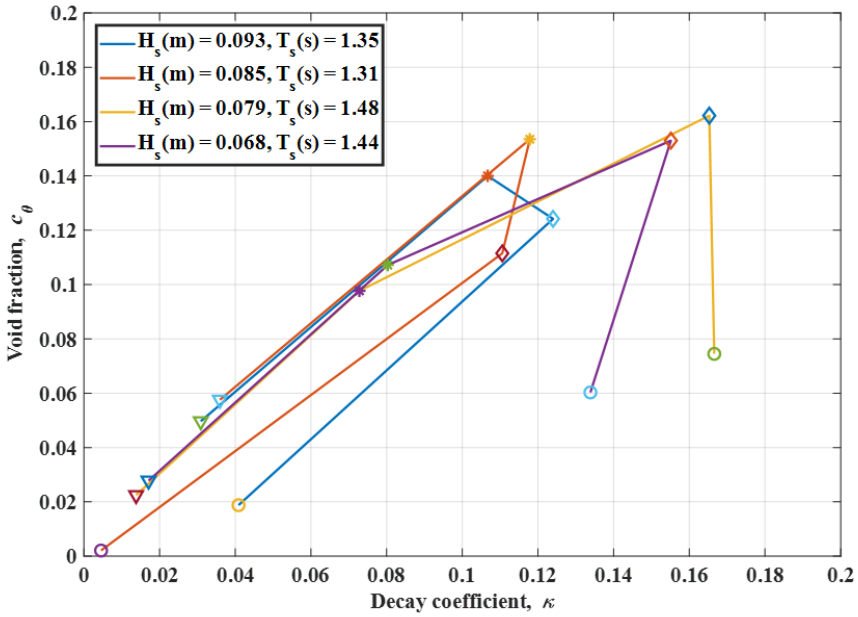

Figure 6.03: Variations of decay coefficient with void fractions (triangle, WG-6; asterisk, WG-5; diamond, WG4; and circle, WG-3).

Also, an analogous investigation explored the relationship between the scale parameter and two crucial factors: void fraction and decay coefficient (see Eq. (6.50)). The results, illustrated in Fig. 6.04 (a) and 6.04 (b), revealed noteworthy patterns. First, a negative correlation was found between the scale parameter and the void fraction, as shown in Fig. 6.04(a). In contrast, an inverse linear relationship emerged when analyzing the scale parameter in relation to the decay coefficient, depicted in Fig. 6.04(b). These observations suggest a hypothesis that the scale parameter is inversely related to the

void fraction while also displaying an inverse linear relationship with the decay coefficient.

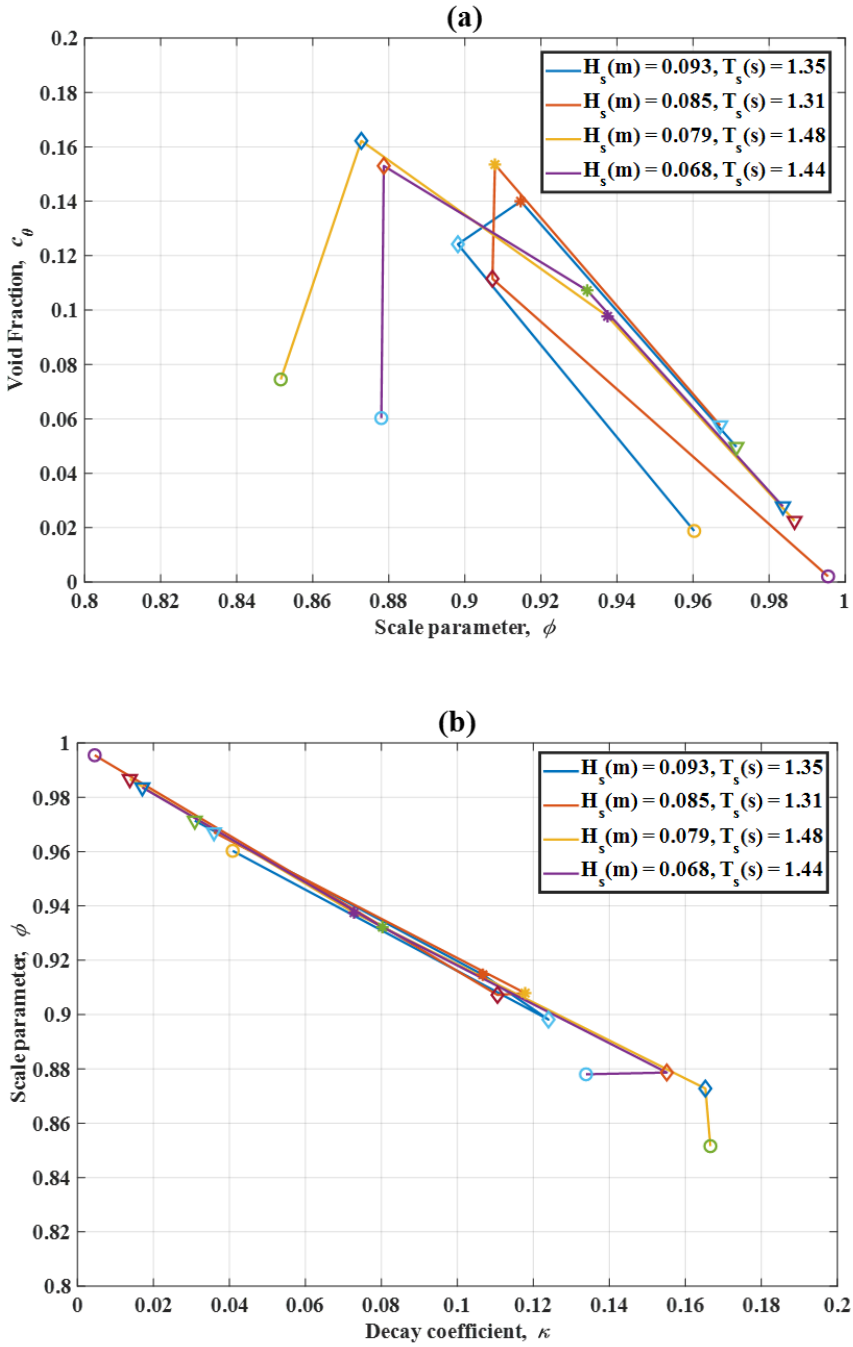

Figure 6.04: (a) Variations in the scale parameter with void fractions, and (b) Contrasts in the scale parameter with decay coefficients (Triangle, WG-6; Asterisk, WG-5; Diamond, WG4; and Circle, WG-3).

These findings provide valuable insights into how void fraction behaves under different wave conditions, enhancing our understanding of wave dynamics, particularly in the context of plunging breaking waves.

6.5.4.2 Statistical wave heights

This section focuses on validating the statistical wave height obtained from the proposed distribution against those derived from the Rayleigh distribution, utilizing experimental data. The parameters for the proposed distribution were calculated using Eqs. (6.42), (6.43), and (6.44). The results, illustrated in Figs. 6.05(a to d), demonstrates that the parameters from the proposed distribution align closely with the experimental observations, in contrast to the discrepancies noted with the Rayleigh distribution.

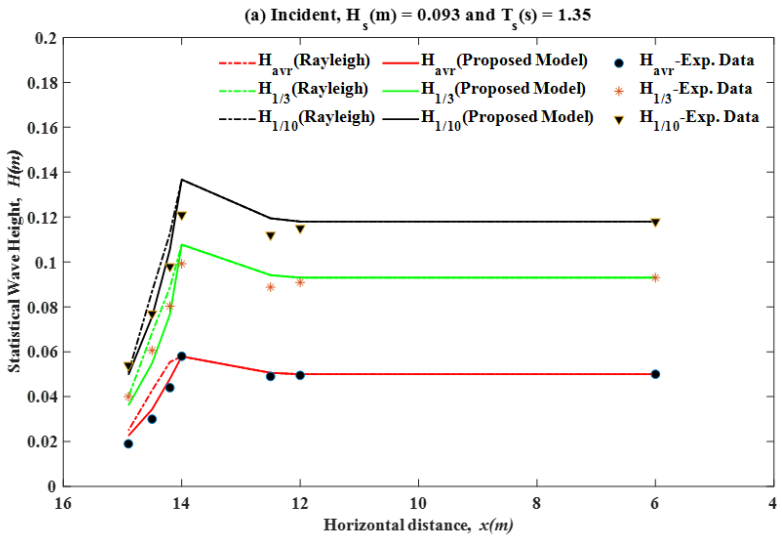

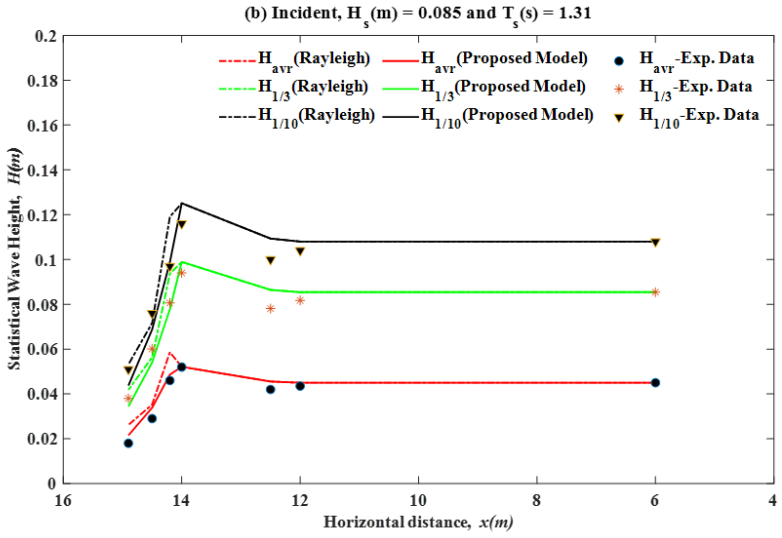

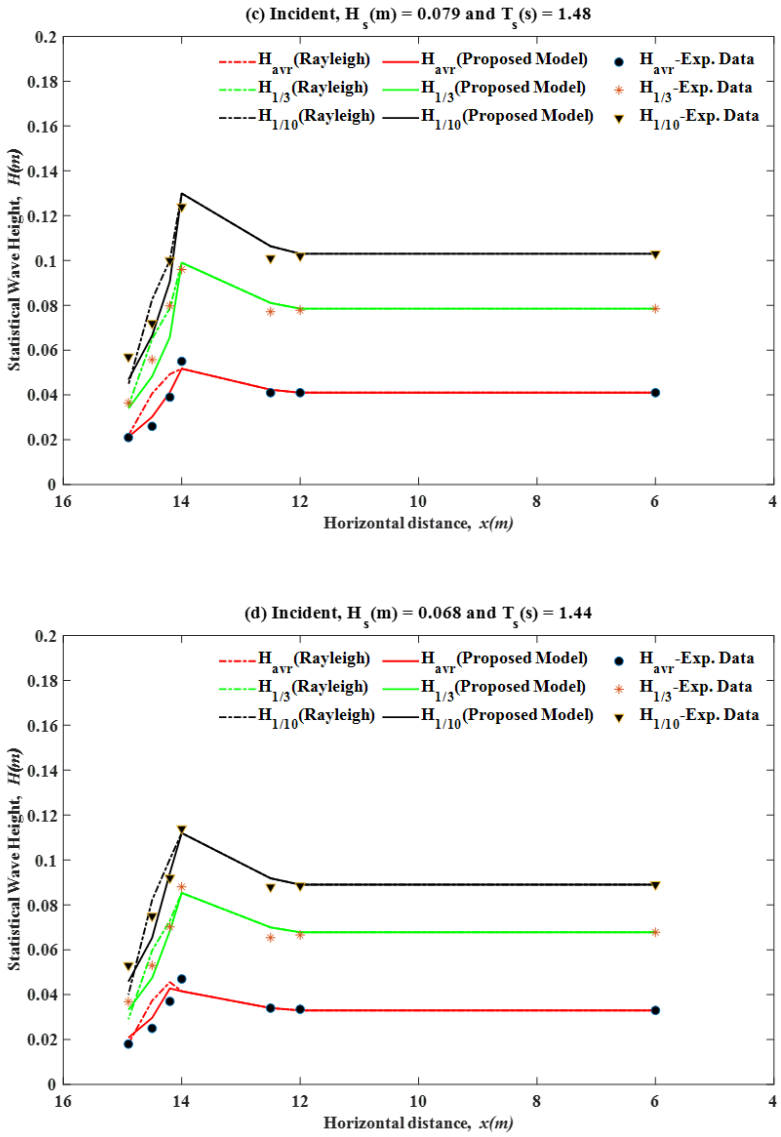

Figure 6.05: Changes in statistical wave heights ($H_{1/3}$, H_{avr}, and $H_{1/10}$) across horizontal distances for various incident wave heights and periods.

Additional information about the specific errors associated with the proposed and Rayleigh distributions is provided in the section focused on error assessment.

6.5.4.3 PDF and CDF comparison with experimental data and other model

This analysis evaluates the performance of the proposed PDF and CDF in comparison to established models such as JC-13, MLM-04, and the Rayleigh distributions across various experimental datasets. The relevant equations used include Eqs. (6.38) and (6.39) for the proposed models, Eqs. (6.09) and (6.10) for JC-13, and Eqs. (6.05) and (6.06) for MLM-04, along with standard expressions for PDF, and CDF

for the Rayleigh distribution. Visual comparisons of the predicted versus observed wave height distributions at four different gauges from four-wave records are illustrated in Fig. 6.06 and Figs. F1-F3 (found in Appendix F). The results indicate a high level of accuracy in capturing the observed deviations in wave height distribution when compared to the JC-13, MLM-04, and Rayleigh distributions, as seen in PDF and CDF estimates.

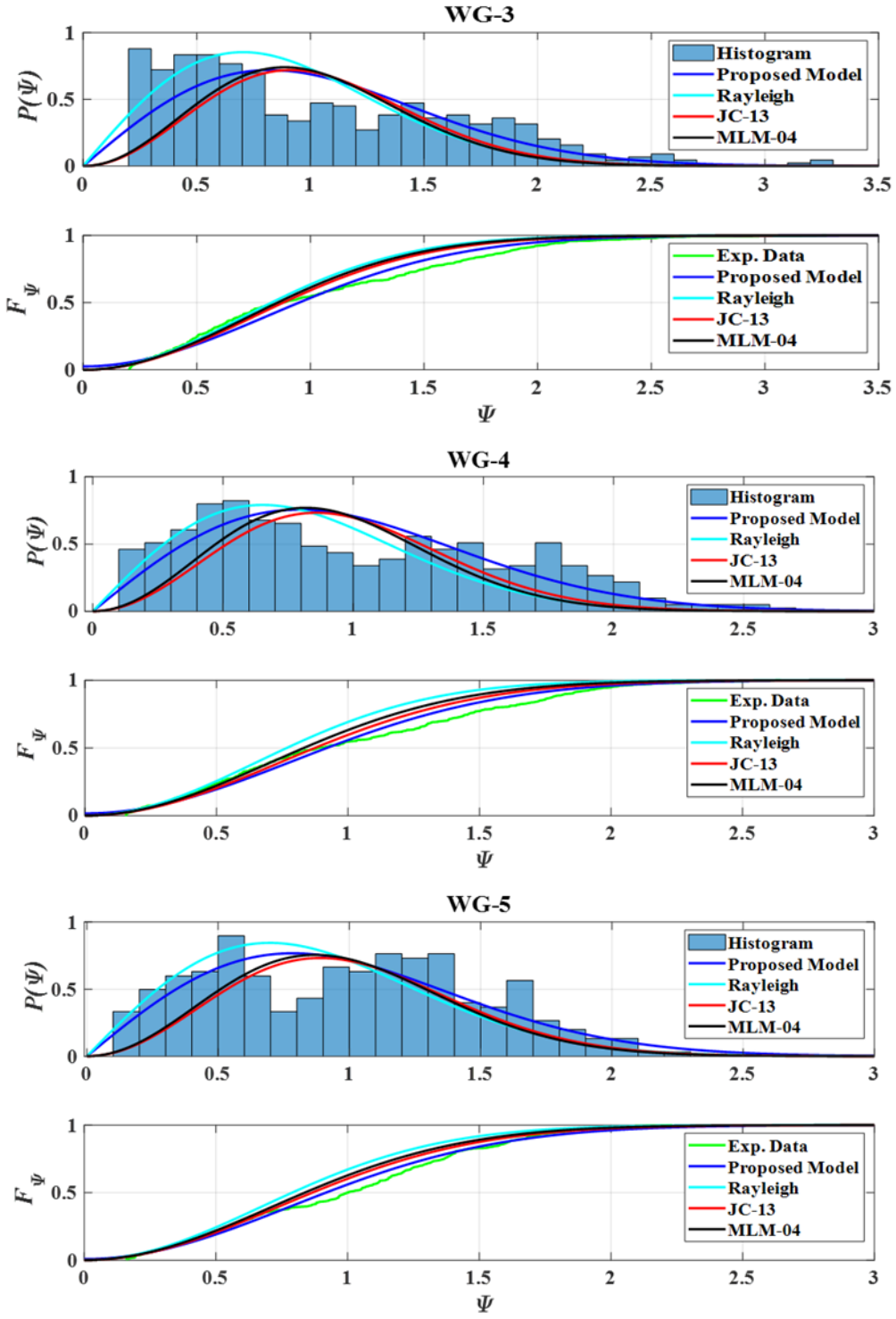

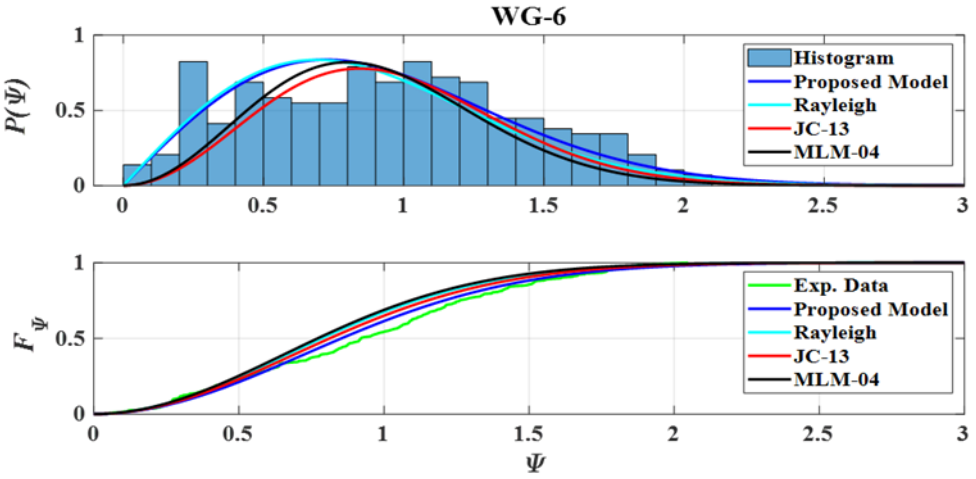

Figure 6.06: Comparison of the $P(\Psi)$, and F_{Ψ} concerning Ψ for the proposed model and other models (Rayleigh, MLM-04, and JC-13) for the incident, T_s = 1.35s, and H_s = 0.093m.

Again, the proposed model's effectiveness largely hinges on the relationship between the scale parameter and the decay coefficient, which together function as a unified parameter due to their interdependence. Notably, the model approaches the Rayleigh distribution when the decay coefficient nears zero. However, the investigation highlights significant limitations in the Rayleigh distribution's accuracy for predicting wave heights in the surf zones of natural beaches. This raises questions about its applicability, particularly in shallow water areas that are characterized by complex dynamics. In such regions, factors like wave breaking, turbulence, and air bubble entrainment have a considerable impact on wave height distributions, leading to deviations from the assumptions of the Rayleigh distribution (Battjes and Groenendijk, 2000; Power et al., 2016). Overall, both theoretical analysis and experimental comparisons suggest that the Rayleigh distribution may not be suitable for shallow water scenarios. However, it can still provide a reasonable approximation in cases involving very small wave heights, where the frequency components are closely aligned.

6.5.4.4 Exceedance of probability variations

Grasping the probability of exceedance is crucial for model development, as it provides essential insights into the likelihood of experiencing extreme events within a specific system or environment. This understanding enables researchers and engineers to evaluate and manage the risks linked to various extreme occurrences, including

floods, tsunamis, and storms. In this section, a detailed comparison of the probability of exceedance is conducted using several models, including JC-13, MLM-04, and Rayleigh. Figs. 6.07 and G1-G3 (found in Appendix G) illustrate the visual comparisons between predicted and observed wave height distributions at four different gauges across four-wave records. The proposed model demonstrates superior performance in capturing the observed deviations in wave height distribution compared to the JC-13, MLM-04, and Rayleigh distributions, particularly in its ability to predict the probability of exceedance accurately.

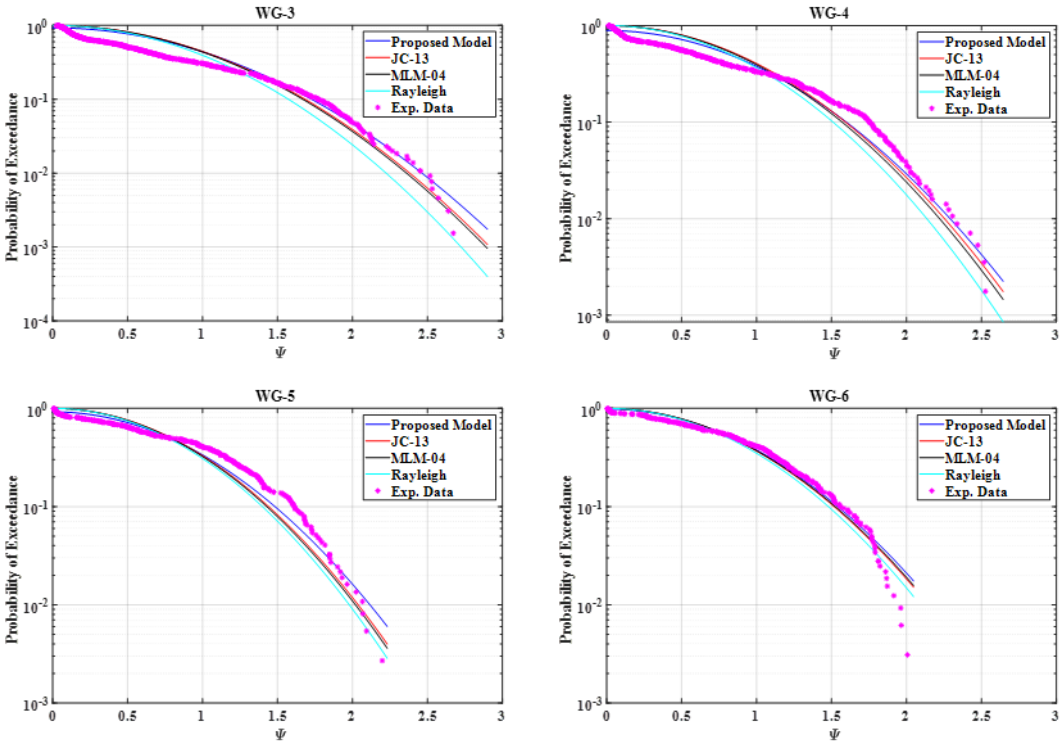

Figure 6.07: Variation of the exceedance of probability with respect to Ψ for the proposed model and other models (Rayleigh, MLM-04, and JC-13) for the specified incident wave conditions: T_s = 1.35s, and H_s = 0.093m.

Nonetheless, this study identifies considerable shortcomings in the Rayleigh distribution's capability to accurately forecast wave height in the surf zone of natural beaches. These inconsistencies raise doubts about the appropriateness of using the Rayleigh distribution in shallow water contexts. The findings highlight the critical need for specialized models that accurately reflect the distinct characteristics of various environments, thereby enhancing the precision and effectiveness of risk assessment and management approaches.

6.5.4.5 Error assessment

This section presents a thorough evaluation of the proposed models' accuracy when compared to the Rayleigh model, utilizing experimental data for analysis. The focus is on the statistical wave parameters derived from the proposed distribution. While straightforward equations were developed for these parameters, the JC-13 and MLM-04 models took a different approach, opting for numerical integration instead. The evaluation encompasses several experimental datasets, detailed in Table 6.1.

To assess accuracy, two error metrics are applied: the RMSRE and the percentage error indices (P20 and P10). The RMSRE serves as a valuable metric for measuring the precision of a model's predictions, taking into account the relative differences between the predicted and actual values. This approach is particularly effective for evaluating errors across different scales. The method for calculating RMSRE for wave height is specified as follows:

$$RMSRE = \sqrt{\frac{\sum_{i=1}^{N}\left(H_{St.,c,i}-H_{St.,m,i}\right)^2}{\sum_{i=1}^{N}H_{St.,m,i}^2}} * 100, \tag{6.51}$$

where $H_{St.,c,i}$ is the computed statistical wave height, $H_{St.,m,i}$ is the measured statistical wave height, and N signifies the total number of data points.

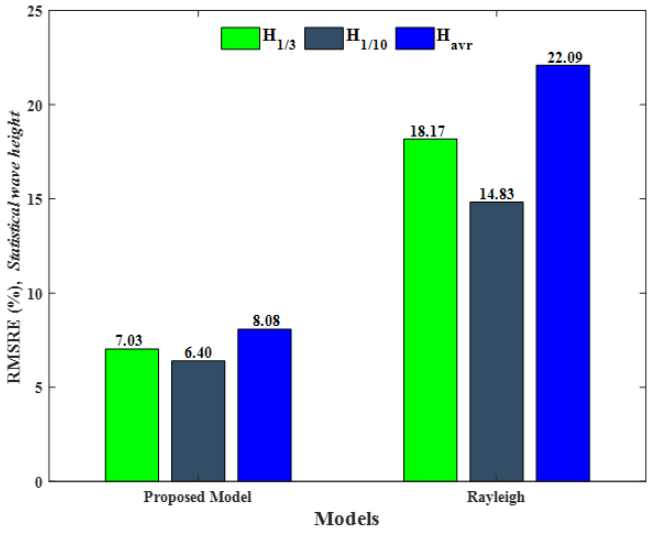

Figure 6.08: Comparison of RMSRE of different statistical wave heights concerning experimental data for the proposed and Rayleigh models.

The values of RMSRE shown in Fig. 6.08 provide a comparison between the wave height predictions of the proposed model and those produced by the Rayleigh model. The average RMSRE values for the proposed models are found to be 6.40% for $H_{1/3}$, 7.03% for $H_{1/10}$, and 8.08% for H_{avr}, respectively. Conversely, the Rayleigh model displays considerably higher RMSRE values of 14.83% for $H_{1/3}$, 18.17% for $H_{1/10}$, and 22.09% for H_{avr}, correspondingly. These observations imply that the Rayleigh distribution may not effectively predict representative wave heights in shallow water environments.

Table 6.2: Error summary for statistical wave height (%).

Statistical Wave Height	**RMSRE**		**P20**		**P10**	
	Proposed Model	Rayleigh	Proposed Model	Rayleigh	Proposed Model	Rayleigh
$H_{1/3}$	6.40	14.83	2.86	08.57	5.71	22.86
$H_{1/10}$	7.03	18.17	2.86	14.29	11.42	29.57
H_{avr}	8.08	22.09	5.71	28.58	17.14	37.14

In Fig. 6.09, the differences in P20 and P10 values between the proposed model and the Rayleigh model are illustrated, with Table 6.2 summarizing the statistical wave height calculations. The proposed model demonstrates P20 values of 2.86%, 2.86%, and 5.71% for $H_{1/3}$, $H_{1/10}$, and H_{avr}, correspondingly. Conversely, the Rayleigh model shows significantly higher P20 values, at 8.57%, 14.29%, and 28.58% $H_{1/3}$, $H_{1/10}$, and H_{avr}, correspondingly.

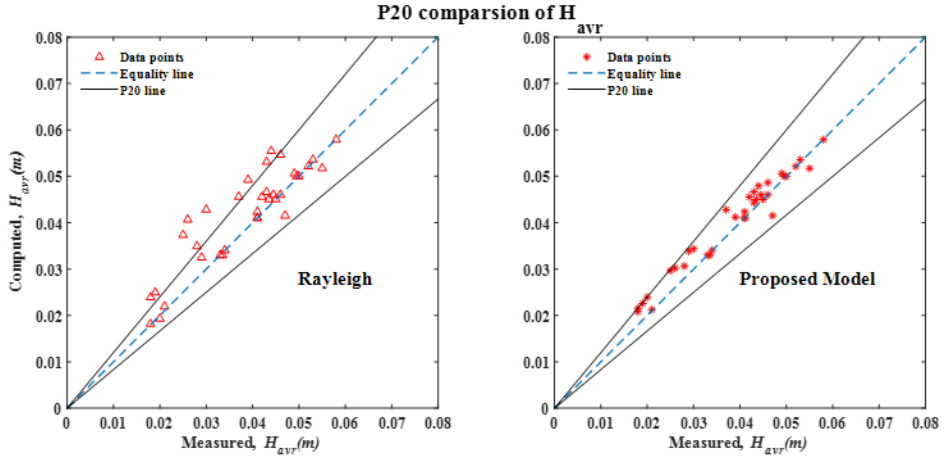

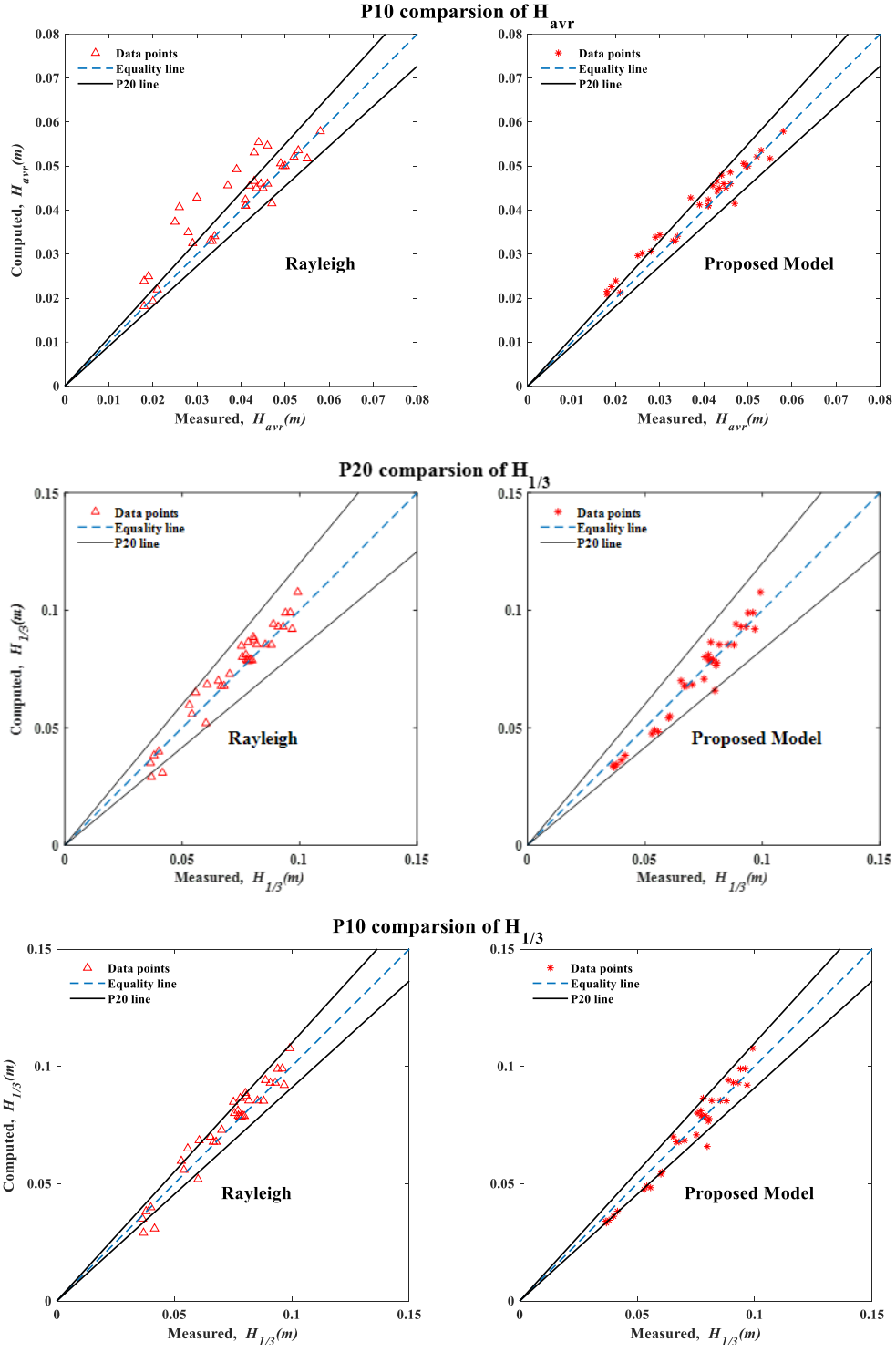
P10 comparsion of H avr
Data points
Equality line
P20 line
Rayleigh
Proposed Model
Computed, H avr (m)
Measured, H avr (m)
P20 comparsion of H 1/3
Computed, H 1/3 (m)
Measured, H 1/3 (m)
P10 comparsion of H 1/3

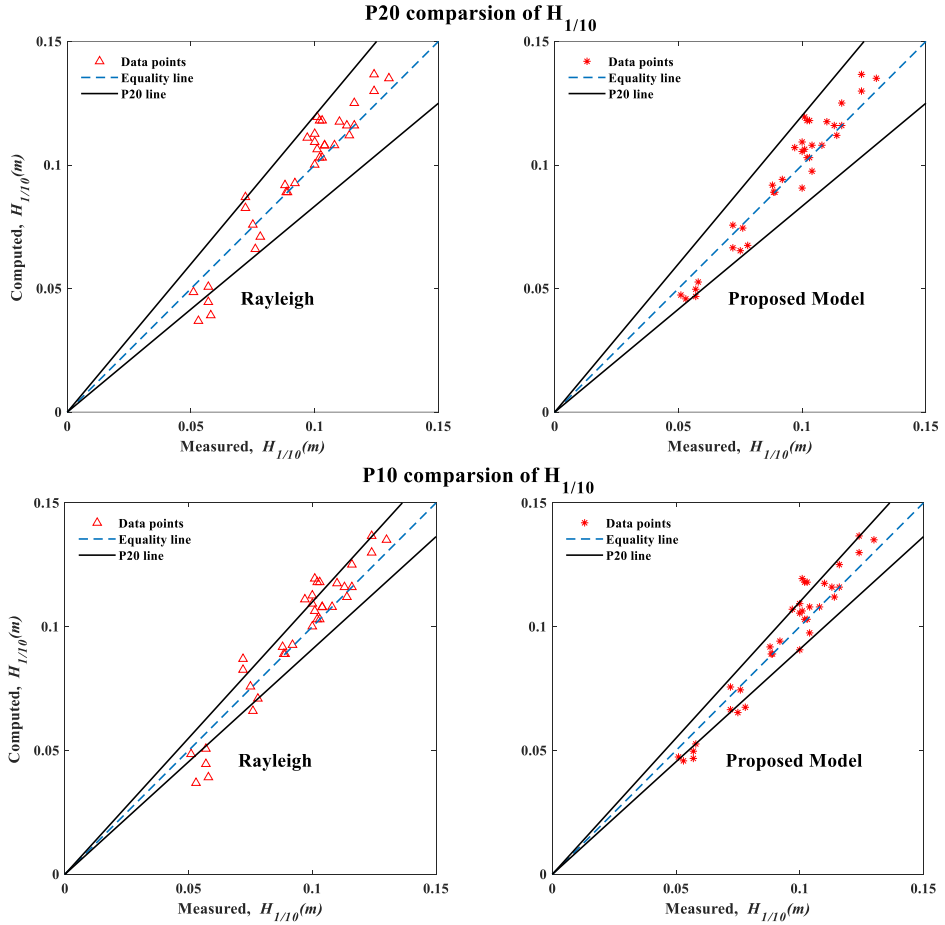

Figure 6.09: P20 and P10 comparison of different statistical wave heights concerning experimental data for the proposed model and Rayleigh model.

In addition, the proposed model exhibits P10 values of 5.71%, 11.42%, and 17.14% for $H_{1/3}$, $H_{1/10}$, and H_{avr}, individually. In comparison, the Rayleigh model reports significantly higher P10 values of 22.86%, 29.57%, and 37.14% for the same wave height parameters. These findings further emphasize the limitations of the Rayleigh model in effectively predicting statistical wave heights in shallow water environments.

6.6 Conclusions

This chapter investigated various wave height distributions, emphasizing statistical wave heights and variations in probability exceedance. It began by assessing the effectiveness of the Rayleigh PDF in describing wave height distributions just outside the breaking zone, while also introducing the role of air bubble-induced energy dissipation in plunging breaking waves within the surf zone.

Through algebraic manipulation, the proposed model was refined to depend solely on local wave characteristics, resulting in a streamlined point model characterized by a single function. Both theoretical and empirical findings revealed a strong correlation between the scale parameter of the distribution and the decay coefficient, simplifying the proposed distribution to a one-parameter model. Validation through experimental data confirmed the model's effectiveness, as indicated by various error metrics (RMSRE, P10, and P20) compared to the Rayleigh distribution, thereby demonstrating its accuracy in predicting representative wave heights. Notably, the transformed PDF was able to accurately replicate observed wave height histograms in laboratory environments within the breaking zone, surpassing the performance of models such as JC-13 and MLM-04. Furthermore, the model adeptly captured the complexities of wave height distribution changes under depth-limited breaking conditions, particularly for low probabilities of exceedance. These results underscored the theoretical framework's ability to represent wave height distribution transformations over shallow foreshores. Additionally, the dynamics governing these transformations were closely tied to the decay coefficient and scale parameter in the surf zone. In conclusion, the proposed model offers a robust and practical approach for characterizing wave height distributions in dynamic coastal settings, making it an essential tool for researchers and practitioners involved in coastal engineering, hazard calculation, and coastal management.

CHAPTER 7

General Conclusions

7.1 General

This chapter delves into the outcomes of the research detailed in this thesis, offering both an overview and an in-depth discussion. Later in the chapter, a concise summary and key findings from the study are provided. Furthermore, the chapter addresses the limitations of the research and offers suggestions for future directions. By providing a comprehensive analysis, this chapter contributes to a deeper understanding of the research outcomes and their implications for future research endeavors.

7.2 Summary

Irregular breaking waves with an air bubble effect are integral to the dynamics of shallow water waves, playing a crucial role in dissipating wave energy, which is vital for coastal protection and erosion control. As waves approach shallow water, their interaction with the seabed intensifies, leading to heightened turbulence and energy dissipation. The formation of air bubbles within breaking waves is pivotal in this process, facilitating the conversion of wave energy into turbulent kinetic energy. This mechanism effectively reduces wave height and intensity, thus mitigating the impact of waves on coastal structures and shorelines. Furthermore, irregular breaking waves with air bubble effects influence sediment transport dynamics, ecosystem processes, and wave-induced forces in shallow water environments. Understanding and accurately modeling these phenomena are imperative for effective coastal management, resilient infrastructure design, and the preservation of coastal ecosystems.

Given the importance of air bubbles in dissipating irregular wave energy, this study aimed to develop a comprehensive energy dissipation model to accurately calculate wave height and set-up in breaking waves. After an extensive literature review, this research objective was specified to develop the energy dissipation model using four approaches: parametric, representative, spectral, and probabilistic, to analyze the kinematics of irregular waves with air bubble effects in both spilling and plunging breaking conditions. In shallow water, wave breaking is induced by the sloping bottom,

and the entrainment of a significant amount of air bubbles in the breaking process is crucial for energy dissipation. However, quantifying the air entrainment itself is challenging, despite wave breaking being the dominant mechanism. With a focus on unsteady bubble entrainment, this study first explored steady bubbles in irregular waves and associated energy dissipation phenomena. Therefore, the subsequent section succinctly summarizes the key outcomes derived from this study.

7.3 Conclusion and Key Findings

The conclusions and major findings drawn from this thesis are outlined chapter by chapter, providing a comprehensive overview of this study's outcomes.

Chapter 2

In this chapter, a series of experiments was conducted to validate the developed models. Data on regular and irregular wave heights and set-ups were collected during the breaking phase. The entrainment of air bubbles into breaking waves and subsequent wave energy dissipation was also examined. Additionally, to maintain objectivity and mitigate bias, a significant amount of data was collected from external sources.

Major Outcomes:

- A new set of wave heights and set-up data were collected from the experiment.
- Explored the process of air bubble entrainment into breaking waves.

Chapter 3

In this chapter, the parametric approach concept was used to develop a new energy dissipation model for spilling and plunging breaking waves and utilized to calculate RMS wave height and wave set-up. The model was based on the air bubble model of regular breaking waves proposed by Hoque et al., (2019) and the fraction of breaking wave concepts proposed by Thornton and Guza, (1983). The modified Miche's, (1944) breaking criterion and Battjes, (1974) surf similarity parameter were employed to identify breaking waves and breaker types. The validity of the model was supported by various experimental data conducted by various authors and established models (Ro-93 and TG-83). In many cases, the computed RMS wave height excellently matched the experimental data and outperformed the Ro-93 and TG-83 models. The model

performed well in computing wave set-up except near the breaking zone. It was found that void fractions of 17% to 18% (plunging breaking) and 14% to 16% (spilling breaking) were responsible for wave energy dissipation for irregular waves, which closely resembled the results of Houqe and Aoki, (2005).

Major Outcomes:

- A novel energy dissipation model was introduced to account for the influence of air bubbles on irregular breaking waves, outlined as follows:

$$D = \frac{3\sqrt{\pi}}{8}\frac{\rho_w k_1 g c_0 \alpha w_r}{(1-c_0)\gamma^4}\frac{H_{rms}^5}{h^4}, \quad \text{for spilling breaking waves.} \quad (7.01)$$

$$D = \frac{1}{2}\frac{\rho_w g c_0 \alpha w_r}{(1-c_0)\gamma^3}\frac{H_{rms}^4}{h^3}, \quad \text{for plunging breaking waves.} \quad (7.02)$$

- A co-relationship was discovered between RMS wave height and water depth, considering the air bubble effect for plane-sloping bathymetry, which was expressed as:

- $H_{rms} \cong a^{1/3}h^{7/6}$, for spilling breaking waves. (7.03)
- $H_{rms} \cong b^{1/2}h^{5/4}$, for plunging breaking waves. (7.04)
- To calculate wave set-up, using the above model the momentum balance equation was modified (see Eqs. 3.36 and 3.37).

Weaknesses:

- A limitation of this model is its origin in the Rayleigh distribution, which is questionable for calculating breaking wave energy dissipation. Therefore, it is crucial to accurately determine unknown parameters such as k_1 and α to enhance the model's accuracy for practical application.

Chapter 4

In this chapter, the representative wave approach was employed to develop two energy dissipation models for spilling and plunging breaking waves. These models were then utilized to compute RMS wave heights alongside wave set-ups, applying energy conservation and momentum conservation principles. Drawing from the air bubble model proposed by Hoque et al., (2019) and Hoque, (2002) for regular waves,

this served as the foundational framework for both models (I and II). To identify breaking waves and their respective categories, the breaking criterion for irregular waves established by Thornton and Guza, (1983), along with the surf similarity parameter developed by Battjes, (1974) were applied. The computed RMS wave height and set-up exhibited excellent agreement with experimental data and established models (Ro-93 and RKS-03 for wave height and DDD-85 and RGE-01 for wave set-up), albeit with a few discrepancies near mounds and coastlines. The analysis revealed that air bubbles ranging from 16% to 18% for plunging breaking waves and 13% to 15% for spilling breaking waves (using Models I and II) were responsible for wave energy dissipation in irregular waves. These findings closely mirrored the experimental results reported by Hoque and Aoki, (2005) and Huang et al., (2009).

Major Outcomes:

- Two new energy dissipation models were introduced to accommodate the influence of air bubbles on irregular breaking waves, as detailed below:

$$D = K_1 \rho_w g w_r \frac{c_0}{2(1-c_0)} H_{rms}, \quad \text{for spilling breakers} \quad \left.\right\} \textbf{M-I.} \qquad (7.05)$$

$$D = K_2 \rho_w g w_r \frac{c_0}{2(1-c_0)} \gamma h, \quad \text{for plunging breakers} \quad \left.\right\} \qquad (7.06)$$

$$D = K_3 \rho_w g w_r \frac{c_0}{k_0} \frac{1-e^{-(k_0 h)}}{1-c_0 e^{-(k_0 h)}}, \quad \text{for both types of breakers} \quad \left.\right\} \textbf{M-II.} \qquad (7.07)$$

- A direct relationship emerged between the RMS wave height and water depth for plane-sloping bathymetry in M-I, as expressed:

- $H_{rms} \cong a\sqrt{h}$, for spilling breakers. (7.08)

- $H_{rms} \cong \sqrt{b} h^{\frac{3}{4}}$, for plunging breakers. (7.09)

- For calculating wave set-up, using the above models the momentum balance equation was modified (see Eqs. 4.47, 4.48, and 4.49).

Weaknesses:

- Since these models rely on applying regular wave models to irregular waves by using representative wave heights multiplied by unknown coefficients, the

accurate determination of these coefficients is essential for the model's continued development and accuracy.

Chapter 5

In this chapter, two energy dissipation models were developed using a spectral approach to address irregular waves undergoing both spilling and plunging breaking phenomena. These models, denoted as M-I and M-II, were built upon the incorporation of air bubbles and the application of the fraction of breaking waves concept, as proposed by Hoque, (2002) and Stingray et al., (2019), respectively. The conceptual basis for these models was inspired by the air bubble model introduced by Hoque et al., (2019) and Hoque, (2002) for wave breakers under regular wave conditions. To identify breaking waves and categorize them, the previous process is applied. Subsequently, these models were utilized to compute both spectral significant wave heights and wave set-ups, employing the principles of energy and momentum conservation laws. The computed spectral significant wave heights and set-ups exhibited excellent agreement with both experimental data and previous models (NLHO-17 & RS-10 for wave height and NLHH-09 & DDD-85 for set-up), particularly in the case of M-I. However, slight differences near the mound and coastline were observed in M-II.

Major Outcomes:

- Two novel energy dissipation models were introduced to address the impact of air bubbles on irregular breaking waves, as expressed below:

$$D = K_1 \rho_w g \frac{C_0}{2\sqrt{2}(1-C_0)} w_r \Gamma\left(\frac{1}{\kappa}+1\right) H_{m0} e^{-\left(\frac{\sqrt{2}\gamma h}{H_{m0}}\right)^{\kappa}}, \text{ for spilling breakers} \quad \text{(7.10)}$$

$$D = K_2 \rho_w g \frac{C_0 \gamma}{2(1-C_0)} w_r h e^{-\left(\frac{\sqrt{2}\gamma h}{H_{m0}}\right)^{\kappa}}, \text{ for plunging breakers} \quad \text{(7.11)}$$

M-I.

$$D = K_3 \rho_w g c_0 w_r \left(\frac{1-e^{-k_0 h}}{1-c_0 e^{-k_0 h}}\right) e^{-\left(\frac{\sqrt{2}\gamma h}{H_{m0}}\right)^{\kappa}}, \text{ for both breaking types} \quad \text{(7.12)}$$

M-II.

- For calculating wave set-up, using the above models the momentum balance equation was modified (see Eqs. 5.28, 5.29, and 5.30).

Weaknesses:

- ❖ A disadvantage of these models is that they involve several parameters, making it challenging to handle them, especially when calculating wave setup.

Chapter 6

This study highlights the probabilistic approach, especially wave height distributions in the surf zone, was the primary focus, with particular attention given to plunging breaking waves and the effects of air bubbles. A new wave height distribution was proposed. Previous wave height distribution models were re-evaluated in light of air bubble effects, and laboratory observations in a custom-built wave flume were used for validation. The results indicated significant deviations from the Rayleigh distribution, with this proposed model demonstrating closer agreement with experimental data, particularly for larger wave heights. Entrained air bubbles notably reduced the probability densities of larger wave heights, resulting in measured wave heights below the predictions of the Rayleigh distribution. Additionally, the wave height parameters derived from the proposed model showed good agreement with laboratory data compared to the Rayleigh distribution. Theoretical analysis revealed the scale parameter's dependence on the decay coefficient, which aligned well with measurements and allowed for simplification of the proposed distribution to a one-parameter model.

Major Outcomes:

- ❖ A novel wave height distribution was proposed for plunging breakers owing to the effect of air bubbles, as expressed below:

$$P(\Psi) = \frac{2\Psi}{\Phi} exp\left[-\frac{(\Psi^2-\kappa)}{\Phi}\right], \qquad \textbf{[PDF].} \qquad (7.13)$$

$$F_\Psi = 1 - exp\left[-\frac{(\Psi^2-\kappa)}{\Phi}\right], \qquad \textbf{[CDF].} \qquad (7.14)$$

- ❖ The statistical wave height parameters were derived from this proposed distribution, expressed as follows:

$$H_1 = H_{avr} = 0.886 * \left\{\sqrt{(H_{rms}^2 - c)}\right\}. \qquad (7.15)$$

$$H_{\frac{1}{3}} = 1.416 * \left\{\sqrt{(H_{rms}^2 - c)}\right\}. \quad (7.16)$$

$$H_{\frac{1}{10}} = 1.80 * \left\{\sqrt{(H_{rms}^2 - c)}\right\}. \quad (7.17)$$

- Energy dissipated by the air bubbles was found 16%(max.) for the plunging breaker.

Weaknesses:

- This PDF was developed specifically for plunging breaking waves, which makes the model potentially unsuitable for other types of breaking waves.

7.4 General Limitations and Recommendations for Future Work

Limitations

Although this research made a significant contribution to energy dissipation modeling in the surf zone by addressing the complexity of breaking waves and the dynamics of air bubbles within them, some limitations were identified regarding the future study of air bubble dynamics in irregular breaking waves expressed as follows:

- **Assumptions:** In further studies, it is essential to properly consider how air bubbles entrain into the water, particularly in terms of bubble distribution within breaking waves. This aspect is crucial for enhancing the accuracy and comprehensiveness of air bubble energy dissipation models, as they often rely on simplified assumptions that may not fully capture the intricacies of the phenomenon.

- **Complex air bubble dynamics:** The role of the air bubble effect in breaking waves is substantial and intricately complex. Achieving higher accuracy in the energy dissipation model necessitates careful consideration of air bubble size and water quality. These factors should be taken into account when updating the models in future endeavors.

Recommendations

- A comprehensive error analysis (refer to Fig. 7.01) indicates that in the study of irregular wave energy dissipation models, the representative wave approach is

viable and can be used as a reference model. Its simplicity and direct application of regular wave principles to irregular waves make it a favorable choice for ensuring accurate analysis.

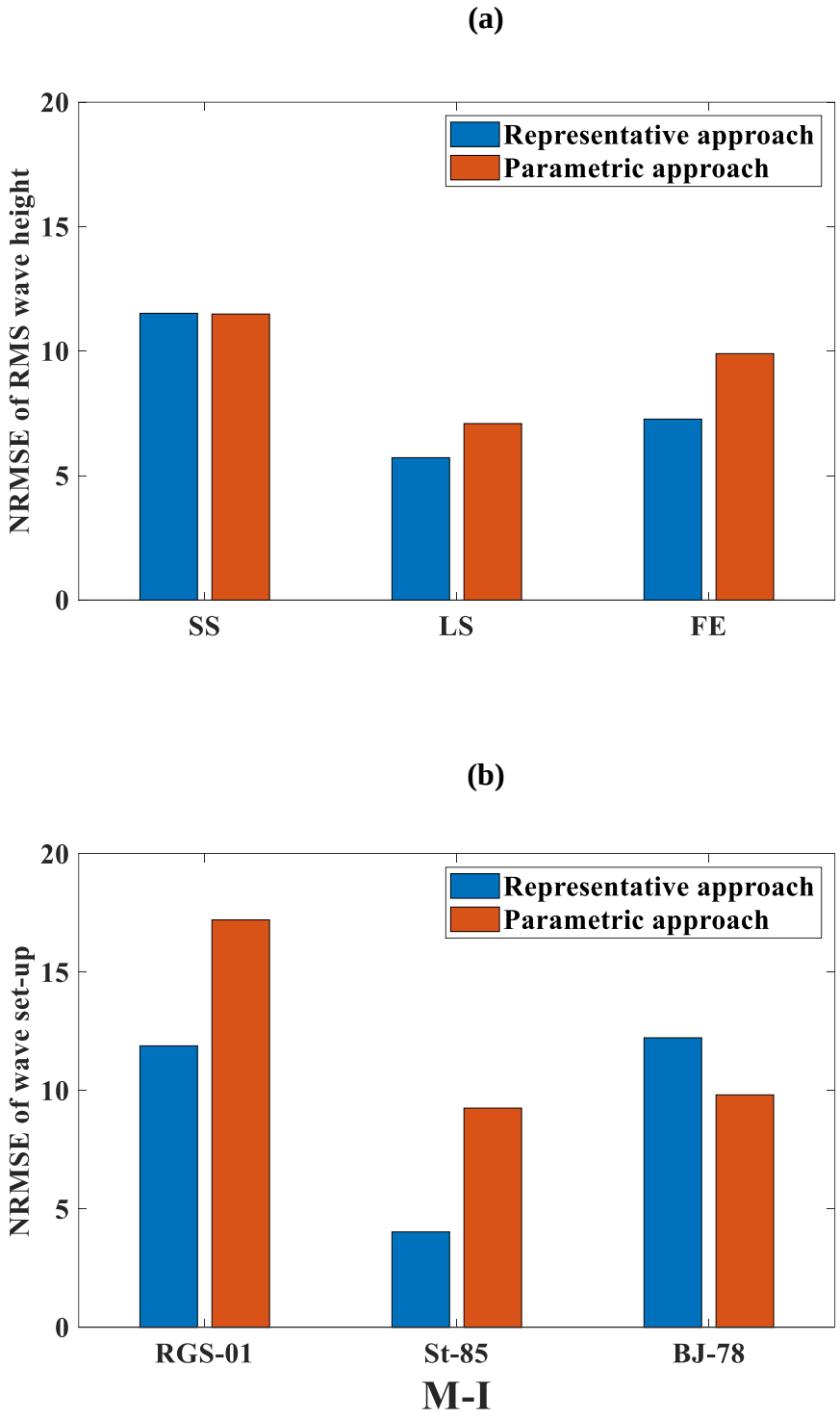

Figure 7.01: Comparison of NRMSE of representative approach and parametric approach with respect to M-I, (a) Wave height, and (b) Wave set-up.

- The M-I model excels in computing spectral significant wave height and set-up in shallow water, as evidenced by multiple error analyses comparing it to experimental data. Its accuracy renders it suitable for future studies and can offer valuable insights and applications in wave height and set-up calculations.

- In the context of shallow water wave height distribution, especially on plunging breaking waves, this study introduced a simple and user-friendly wave height distribution. This distribution holds promise as a valuable resource for future studies and can provide important insights for further research endeavors.

- This study generates a dataset comprising wave height and set-up data for breaking irregular waves, supplemented by analysis of additional data gathered from various sources. These datasets can prove valuable for verifying the energy dissipation model in future studies.

References

Adnan, R.M., Sadeghifar, T., Alizamir, M., Azad, M.T., Makarynskyy, O., Kisi, O., Barati, R., Ahmed, K.O., 2023. Short-term probabilistic prediction of significant wave height using bayesian model averaging: Case study of chabahar port, Iran. Ocean Eng. 272, 113887. https://doi.org/10.1016/j.oceaneng.2023.113887

Afzal, M.S., Kumar, L., Chugh, V., Kumar, Y., Zuhair, M., 2023. Prediction of significant wave height using machine learning and its application to extreme wave analysis. J. Earth Syst. Sci. 132. https://doi.org/10.1007/s12040-023-02058-5

Alam, E., 2023. Factors of cyclone disaster deaths in coastal Bangladesh. Heliyon 9, e18417. https://doi.org/10.1016/j.heliyon.2023.e18417

Alsina, J.M., Baldock, T.E., 2007. Improved representation of breaking wave energy dissipation in parametric wave transformation models. Coast. Eng. 54, 765–769. https://doi.org/10.1016/j.coastaleng.2007.05.005

Apotsos, A., Raubenheimer, B., Elgar, S., Guza, R.T., 2008. Testing and calibrating parametric wave transformation models on natural beaches. Coast. Eng. 55, 224–235. https://doi.org/10.1016/j.coastaleng.2007.10.002

Baldock, T.E., Holmes, P., Bunker, S., Van Weert, P., 1998. Cross-shore hydrodynamics within an unsaturated surf zone. Coast. Eng. 34, 173–196. https://doi.org/10.1016/S0378-3839(98)00017-9

Battjes, J.A., 1974. Surf similarity, in: Proc. 14th ASCE Coastal Engng. Conf. (Copenhagen, Denmark). https://doi.org/10.1061/9780872621138.029

Battjes, J.A., Groenendijk, H.W., 2000. Wave height distributions on shallow foreshores. Coast. Eng. 40. https://doi.org/10.1016/S0378-3839(00)00007-7

Battjes, J.A., Janssen, J.P.F.M., 1978. Energy loss and set-up due to breaking of random waves., in: Proceedings of the Coastal Engineering Conference. ASCE, pp. 569–587. https://doi.org/10.9753/icce.v16.32

Blenkinsopp, C.E., Chaplin, J.R., 2011. Void fraction measurements and scale effects in breaking waves in freshwater and seawater. Coast. Eng. 58. https://doi.org/10.1016/j.coastaleng.2010.12.006

Blenkinsopp, C.E., Chaplin, J.R., 2007. Void fraction measurements in breaking waves. Proc. R. Soc. A Math. Phys. Eng. Sci. 463. https://doi.org/10.1098/rspa.2007.1901

Bosboom, J. and Stive, M.J., 2021. Coastal dynamics, TU Delft Open. https://doi.org/10.5074/T.2021.001

Bouws, E., Gunther, H., Rosenthal, W., Vincent, C.L., 1985. Similarity of the wind wave spectrum in finite depth water 1. Spectral form. J. Geophys. Res. 90. https://doi.org/10.1029/JC090iC01p00975

Bretschneider, C.L., 1968. Significant waves and wave spectrum. Ocean Ind. (February), 40–46.

Bruun, P., 1954. Coastal erosion and development of beach profiles. Memo. No. 44, US Army Beach Eros. Board, US Army Corps Eng.

Chanson, H., 1997. Air bubble entrainment in free-surface turbulent shear flows. Acad. Press. London, U.K. 348.

Chanson, H., Jaw-Fang, L., 1997. Plunging jet characteristics of plunging breakers. Coast. Eng. 31. https://doi.org/10.1016/S0378-3839(96)00056-7

Chanson, H., Aoki, S., Hoque, A., 2006. Bubble entrainment and dispersion in plunging jet flows: Freshwater vs. seawater. J. Coast. Res. 22, 664–677. https://doi.org/10.2112/03-0112.1

Chanson, H., Aoki, S., Maruyama, M., 2002. Unsteady air bubble entrainment and detrainment at a plunging breaker: Dominant time scales and similarity of water level variations. Coast. Eng. 46, 139–157. https://doi.org/10.1016/S0378-3839(02)00069-8

Chen, Y., Zhang, D., Li, X., Peng, Y., Wu, C., Pu, H., Zhou, D., Cao, Y., Zhang, J., 2023. Significant wave height prediction through artificial intelligent mode

decomposition for wave energy management. Energy AI 14, 100257. https://doi.org/10.1016/j.egyai.2023.100257

Cox, D.T., Shin, S., 2003. Laboratory Measurements of Void Fraction and Turbulence in the Bore Region of Surf Zone Waves. J. Eng. Mech. 129. https://doi.org/10.1061/(asce)0733-9399(2003)129:10(1197)

Dally, W.R., 1990. Random breaking waves: A closed-form solution for planar beaches. Coast. Eng. 14. https://doi.org/10.1016/0378-3839(90)90026-S

Dally, W.R., Dean, R.G., Dalrymple, R.A., 1985. Wave height variation across beaches of arbitrary profile. J. Geophys. Res. 90. https://doi.org/10.1029/jc090ic06p11917

Deane, G.B., Stokes, M.D., 2002. Scale dependence of bubble creation mechanisms in breaking waves. Nature 418, 839–844. https://doi.org/10.1038/nature00967

Deigaard, R., Justesen, P., Fredsøe, J., 1991. Modelling of undertow by a one-equation turbulence model. Coast. Eng. 15, 431–458. https://doi.org/10.1016/0378-3839(91)90022-9

Deike, L., Melville, W.K., Popinet, S., 2016. Air entrainment and bubble statistics in breaking waves. J. Fluid Mech. 801, 91–129. https://doi.org/10.1017/jfm.2016.372

Dette, H.H., Larson, M., Murphy, J., Newe, J., Peters, K., Reniers, A., Steetzel, H., 2002. Application of prototype flume tests for beach nourishment assessment. Coast. Eng. 47. https://doi.org/10.1016/S0378-3839(02)00124-2

Duong, N.T., Tran, K.Q., Luu, L.X., Tran, L.H., 2023. Prediction of breaking wave height by using artificial neural network-based approach. Ocean Model. 182, 102177. https://doi.org/10.1016/j.ocemod.2023.102177

Führboter, A., 1970. Air Entrainment and Energy Dissipation in Breakers. Coastal Engineering, pp. 391–398. https://doi.org/10.1061/9780872620285.024

Goda, Y., 2010. Reanalysis of regular and random breaking wave statistics. Coast. Eng. J. 52, 71–106. https://doi.org/10.1142/S0578563410002129

Goda, Y., 2000. Random Seas and Design of Maritime Structures., World Scientific Publishing Co. Pte. Ltd., Singapore.

Grasmeijer, B.T., Rijn, L.C., 1999. Transport of Fine Sands by Currents and Waves. III: Breaking Waves over Barred Profile with Ripples. J. Waterw. Port, Coastal, Ocean Eng. 125. https://doi.org/10.1061/(asce)0733-950x(1999)125:2(71)

Grassa, J.M., 1990. Directional random waves propagation on beaches. Proc. Coast. Eng. Conf. 1, 798–811. https://doi.org/10.1061/9780872627765.063

Hasselmann, K., Barnett, T.P., Bouws, E., Carlson, H., Cartwright, D.E., Eake, K., Euring, J.A., Gicnapp, A., Hasselmann, D.E., Kruseman, P., Meerburg, A., Mullen, P., Olbers, D.J., Richren, K., Sell, W., Walden, H., 1973. Measurements of wind-wave growth and swell decay during the joint North Sea wave project (JONSWAP).

Hedges, T.S., 2003. Wave Breaking and Reflection. Univ. Liverpool. Dep. Civ. Eng. 1–3.

Hoque, A., 2002. Air Bubble Entrainment by Breaking Waves and Associated Energy Dissipation. PhD Thesis, Archit. Civ. Eng. TUT, Japan 1–164.

Hoque, A., Aoki, S., 2014. Wave-Energy Dissipation and Wave Setup Caused by Entrained Air Bubbles in Plunging Wave Breaking. J. Waterw. Port, Coastal, Ocean Eng. 140. https://doi.org/10.1061/(asce)ww.1943-5460.0000252

Hoque, A., Aoki, S., 2008. Air entrainment and associated energy dissipation in steady and unsteady plunging jets at free surface. Appl. Ocean Res. 30. https://doi.org/10.1016/j.apor.2008.03.004

Hoque, A., Aoki, S.I., 2005. Distributions of void fraction under breaking waves in the surf zone. Ocean Eng. 32. https://doi.org/10.1016/j.oceaneng.2004.11.013

Hoque, A., Hossain, N., Ali, S., Rahman, M., 2019. Wave breaking and bubble formation associate energy dissipation and wave setup. Ocean Dyn. 69. https://doi.org/10.1007/s10236-019-01279-x

Hoque, A., Rahman, Motiur, Rahman, Masudar, Hossain, N., Chandra Paul, G., 2021. Theoretical study of spilling wave attenuation by air bubbles, turbulence, and bottom friction. Estuar. Coast. Shelf Sci. 262, 107606. https://doi.org/10.1016/j.ecss.2021.107606

Horikawa, K., Kuo, C.-T., 1966. A study on wave transformation inside surf zone. Coast. Eng. Proc. 1. https://doi.org/10.9753/icce.v10.14

Hossain, M.N., Araki, S., 2023. Estimation of air-bubble-induced wave height and set-up using representative wave approach. Coast. Eng. J. 65, 495–513. https://doi.org/10.1080/21664250.2023.2246282

Hossain, M.N., Araki, S., 2022. Energy dissipation model for irregular breaking waves owing to air bubbles. Ocean Eng. 266, 112985. https://doi.org/10.1016/J.OCEANENG.2022.112985

Hossain, M.N., Rahman, M., Hoque, A., 2022. Statistical distribution of wave heights attenuation by entrained air bubbles in the surf zone. Ocean Eng. 250, 110911. https://doi.org/10.1016/j.oceaneng.2022.110911

Huang, Z.C., Hsiao, S.C., Hwung, H.H., Chang, K.A., 2009. Turbulence and energy dissipations of surf-zone spilling breakers. Coast. Eng. 56. https://doi.org/10.1016/j.coastaleng.2009.02.003

Hughes, S. A., 1993. Physical Models and Laboratory Techniques in Coastal Engineering, World Scientific. https://doi.org/10.1142/2154

Hurue, M., 1990. Two-dimensional distribution of undertow due to irregular waves. Undergraduate Thesis, Department of Civil Engineering, Yokohama National University.

Hweng Hwung, H., Min Chyan, J., 1993. Energy dissipation and air bubbles mixing inside surf zone, in: Proceedings of the Coastal Engineering Conference. https://doi.org/10.1061/9780872629332.023

Ikram, R.M.A.., Cao, X.., Sadeghifar, T.., Kuriqi, A.., Kisi, O.., Shahid, S., 2023. Improving Significant Wave Height Prediction Using a Neuro-Fuzzy Approach and Marine Predators Algorithm.pdf. J. Mar. Sci. Eng. 11, 1163.

Isobe, M. (1987). A Parabolic Equation Model for Transformation of Irregular Waves Due to Refraction, Diffraction and Breaking. Coastal Engineering in Japan, 30(1), 33–47. https://doi.org/10.1080/05785634.1987.11924463

Izumiya, T., & Horikawa, K. (1987). On the Transformation of Directional Random Waves Under Combined Refraction and Diffraction. Coastal Engineering in Japan, 30(1), 49–65. https://doi.org/10.1080/05785634.1987.11924464

Jadhav, R.S., Chen, Q., 2013. Probability distribution of wave heights attenuated by salt marsh vegetation during tropical cyclone. Coast. Eng. 82. https://doi.org/10.1016/j.coastaleng.2013.08.006

Jane M. Smith and William C. Seabergh, 2001. Wave Breaking on a Current at an Idealized Inlet with an Ebb Shoal. Coast. Inlets Res. Program-US Army Corps Eng. Waterw. Exp. Stn. Technical.

Karmpadakis, I., Swan, C., 2022. A new crest height distribution for nonlinear and breaking waves in varying water depths. Ocean Eng. 266, 112972. https://doi.org/10.1016/j.oceaneng.2022.112972

Karmpadakis, I., Swan, C., Christou, M., 2022. A new wave height distribution for intermediate and shallow water depths. Coast. Eng. 175, 104130. https://doi.org/10.1016/j.coastaleng.2022.104130

Karmpadakis, I., Swan, C., Christou, M., 2020. Assessment of wave height distributions using an extensive field database. Coast. Eng. 157, 103630. https://doi.org/10.1016/j.coastaleng.2019.103630

Katsardi, V., de Lutio, L., Swan, C., 2013. An experimental study of large waves in intermediate and shallow water depths. Part I: Wave height and crest height statistics. Coast. Eng. 73, 43–57. https://doi.org/10.1016/j.coastaleng.2012.09.007

Klopman, G., Stive, M.J.F., Box, P.O., Emmeloord, A.D., 1989. Wave and current kinematics and loading, Delft hydraulics.

Koga, M., 1982. Bubble entrainment in breaking wind waves. Tellus 34. https://doi.org/10.3402/tellusa.v34i5.10833

Kraus, N.C., Gingerich, K.J., Rosati, J.D., 1989. Duck85 surf zone sand transport experiment, Technical Report CERC (US Army Engineer Waterways Experiment Station Coastal Engineering Research Center).

Kraus, N.C., McKee Smith, J., 1994. SUPERTANK laboratory data collection project; volume I: main text. Tech. Rep. - US Army Coast. Eng. Res. Cent. 94–3.

Kuriyama, Y., 1997. Models of wave height and fraction of breaking waves on a barred beach, in: Proceedings of the Coastal Engineering Conference. https://doi.org/10.1061/9780784402429.020

Le Mehaute, B., 1962. On Non-Saturated Breakers and the Wave Run-Up. Coast. Eng. Proc. 1, 6. https://doi.org/10.9753/icce.v8.6

Lamarre, E., Melville, W.K., 1991. Air entrainment and dissipation in breaking waves. Nature 351. https://doi.org/10.1038/351469a0

Leng, X., Chanson, H., 2019. Air-water interaction and characteristics in breaking bores. Int. J. Multiph. Flow 120, 103101. https://doi.org/10.1016/j.ijmultiphaseflow.2019.103101

Longuet-Higgins, M.S., Stewart, R. W., 1964. Radiation stresses in water waves; a physical discussion, with applications. Deep. Res. Oceanogr. Abstr. 11. https://doi.org/10.1016/0011-7471(64)90001-4

Longuet-Higgins, M.S., 1952. On the Statistical Distribution of the Heights of Sea Waves. J. Mar. Res. 11.

Larson, B.M., 1995. Model for decay of random waves in surf zone. J. Waterw. Port, Coastal, Ocean Eng 121, 1–12. https://doi.org/10.1061/(ASCE)0733-950X(1995)121:1(1)

McKee Smith, J., Larson, M., Kraus, N.C., 1993. Longshore current on a barred beach: field measurements and calculation. J. Geophys. Res. 98. https://doi.org/10.1029/93jc02116

Mendez, F.J., Losada, I.J., Medina, R., 2004. Transformation model of wave height distribution on planar beaches. Coast. Eng. 50. https://doi.org/10.1016/j.coastaleng.2003.09.005

Miche, A., 1944. Mouvements ondulatoires de la mer en profondeur croissante ou décroissante. Première partie. Mouvements ondulatoires périodiques et cylindriques en profondeur constante. Ann. des Ponts Chaussées 114.

Mitsuyasu, H., 1970. On the Growth of the Spectrum of Wind-Generated Waves. Coast. Eng. Japan 13. https://doi.org/10.1080/05785634.1970.11924105

Mori, N., Suzuki, T., Kakuno, S., 2007. Experimental study of air bubbles and turbulence characteristics in the surf zone. J. Geophys. Res. Ocean. 112. https://doi.org/10.1029/2006JC003647

Mostafa, R.R., Kisi, O., Adnan, R.M., Sadeghifar, T., Kuriqi, A., 2023. Modeling Potential Evapotranspiration by Improved Machine Learning Methods Using Limited Climatic Data. Water (Switzerland) 15. https://doi.org/10.3390/w15030486

Naess, A., 1985. On the distribution of crest to trough wave heights. Ocean Eng. 12, 221–234. https://doi.org/10.1016/0029-8018(85)90014-9

Nam, P.T., Larson, M., Hanson, H., Hoan, L.X., 2009. A numerical model of nearshore waves, currents, and sediment transport. Coast. Eng. 56, 1084–1096. https://doi.org/10.1016/j.coastaleng.2009.06.007

Nam, P.T., Larson, M., Hanson, H., Oumeraci, H., 2017. Model of nearshore random wave transformation: validation against laboratory and field data. Ocean Eng. 135, 183–193. https://doi.org/10.1016/j.oceaneng.2017.02.023

Nuntakamol, P., Rattanapitikon, W., 2011. Transformation of mean and highest one-tenth wave heights using representative wave approach. Kasetsart J. - Nat. Sci. 45, 1171–1181.

Panchang, V.G., Wei, G., Pearce, B.R., Briggs, M.J., 1990. Numerical Simulation of Irregular Wave Propagation over Shoal. J. Waterw. Port, Coastal, Ocean Eng. 116, 324–340. https://doi.org/10.1061/(asce)0733-950x(1990)116:3(324)

Paul, G.C., Ismail, A.I.M., Rahman, A., Karim, M.F., Hoque, A., 2016. Development of Tide–Surge Interaction Model for the Coastal Region of Bangladesh. Estuaries and Coasts 39, 1582–1599. https://doi.org/10.1007/s12237-016-0110-4

Power, H.E., Nielsen, P., Hughes, M.G., Aagaard, T., Baldock, T.E., 2016. Wave height distributions in the surf zone on natural beaches. J. Coast. Res. 1, 917–921. https://doi.org/10.2112/SI75-184.1

Rattanapitikon, W., 2008. Verification of significant wave representation method. Ocean Eng. 35, 1259–1270. https://doi.org/10.1016/j.oceaneng.2008.03.008

Rattanapitikon, W., Karunchintadit, R., Shibayama, T., 2003. Irregular wave height transformation using representative wave approach. Coast. Eng. J. 45, 489–510. https://doi.org/10.1142/S0578563403000865

Rattanapitikon, W., Shibayama, T., 2010. Energy dissipation model for computing transformation of spectral significant wave height. Coast. Eng. J. 52, 305–330. https://doi.org/10.1142/S0578563410002191

Rattanapitikon, W., Shibayama, T., 1998. Energy dissipation model for regular and irregular breaking waves. Coast. Eng. J. 40. https://doi.org/10.1142/S0578563498000194

Raubenheimer, B., Guza, R.T., Elgar, S., 2001. Field observations of wave-driven setdown and setup. J. Geophys. Res. Ocean. 106. https://doi.org/10.1029/2000jc000572

Roelvink, J.A., 1993. Dissipation in random wave groups incident on a beach. Coast. Eng. 19. https://doi.org/10.1016/0378-3839(93)90021-Y

Roelvink, J.A., Reniers, A., 1995. LIP 11D Delta Flume experiments: a dataset for profile model validation, WL/Delft Hydraulics.

Sadeghifar, T., Barati, R., 2018. Application of Adaptive Neuro-Fuzzy Inference System to Estimate Alongshore Sediment Transport Rate (A Real Case Study: Southern Shorelines of Caspian Sea). J. Soft Comput. Civ. Eng. 2, 72–85. https://doi.org/10.22115/SCCE.2018.135975.1074

Sadeghifar, T., Barati, R., 2018. Prediction of Longshore Sediment Transport Rate using Soft Computing Techniques and Comparison with Semi-Empirical Formulas. Prog. River Eng. Hydraul. Struct. 2, 151–174.

Sadeghifar, T., Lama, G.F.C., Sihag, P., Bayram, A., Kisi, O., 2022. Wave height predictions in complex sea flows through soft-computing models: Case study of Persian Gulf. Ocean Eng. 245, 110467. https://doi.org/10.1016/j.oceaneng.2021.110467

Sadeghifar, T., Nouri Motlagh, M., Torabi Azad, M., Mohammad Mahdizadeh, M., 2017. Coastal Wave Height Prediction using Recurrent Neural Networks (RNNs) in the South Caspian Sea. Mar. Geod. 40, 454–465. https://doi.org/10.1080/01490419.2017.1359220

Shi, R., Wüthrich, D., Chanson, H., 2023. Air–water properties of unsteady breaking bore part 2: Void fraction and bubble statistics. Int. J. Multiph. Flow 159, 104337. https://doi.org/10.1016/j.ijmultiphaseflow.2022.104337

Smith, E.R., Kraus, N.C., 1990. Laboratory study on macro-features of wave breaking over bars and artificial reefs. Tech. Rep. - US Army Coast. Eng. Res. Cent. 90–12.

Stive, M.J.F., 1985. A scale comparison of waves breaking on a beach. Coast. Eng. 9. https://doi.org/10.1016/0378-3839(85)90003-1

Stringari, C.E., Power, H.E., 2019. The Fraction of Broken Waves in Natural Surf Zones. J. Geophys. Res. Ocean. 124, 9114–9140. https://doi.org/10.1029/2019JC015213

Sultan, N.J., 1995. Irregular wave kinematics in the surf zone. PhD Diss. Texas A M Univ. Coll. Station. Texas, USA.

Swift, R.H., 1993. A simplified model for wave height and set-up in the surf zone. Coast. Eng. 19. https://doi.org/10.1016/0378-3839(93)90028-7

Tayfun, B.M.A., 1991. Distribution of large wave heights 116, 686–707.

Tayfun, M.A., Fedele, F., 2007. Wave-height distributions and nonlinear effects. Ocean Eng. 34, 1631–1649. https://doi.org/10.1016/j.oceaneng.2006.11.006

Thornton, E.B., Guza, R.T., 1986. Surf zone longshore currents and random waves: Field data and models. J. Phys. Oceanogr. 16. https://doi.org/10.1175/1520-0485(1986)016<1165:SZLCAR>2.0.CO;2

Thornton, E.B., Guza, R.T., 1983. Transformation of wave height distribution. J. Geophys. Res. 88, 5925–5938. https://doi.org/10.1029/JC088iC10p05925

Thornton, E.B., Guza, R.T., 1982. Energy saturation and phase speeds measured on the natural beach. J. Geophys. Res. 87, 9499–9508. https://doi.org/10.1029/JC087iC12p09499

Thorpe S, 1982. On the clouds of bubbles formed by breaking wind-waves in deep water, and their role in air-sea gas transfer. Philos. Trans. R. Soc. London. Ser. A, Math. Phys. Sci. 304. https://doi.org/10.1098/rsta.1982.0011

Ting, F.C.K., 2002. Laboratory study of wave and turbulence characteristics in narrow-band irregular breaking waves. Coast. Eng. 46, 291–313. https://doi.org/10.1016/S0378-3839(02)00092-3

Ting, F.C.K., 2001. Laboratory study of wave and turbulence velocities in a broad-banded irregular wave surf zone. Coast. Eng. 43. https://doi.org/10.1016/S0378-3839(01)00013-8

William A. Birkemeier, Cinde Donoghue, C.E.L., Kent K. Hathaway, C.F.B., 1997. 1990 DELILAH Nearshore Experiment.

Wu, J., 1988. Bubbles in the near-surface ocean: A general description. J. Geophys. Res. 93. https://doi.org/10.1029/jc093ic01p00587

Wu, Y., Randell, D., Christou, M., Ewans, K., Jonathan, P., 2016. On the distribution of wave height in shallow water. Coast. Eng. 111. https://doi.org/10.1016/j.coastaleng.2016.01.015

Xiong, J., You, Z.J., Li, J., Gao, S., Wang, Q., Wang, Y.P., 2020. Variations of wave parameter statistics as influenced by water depth in coastal and inner shelf areas. Coast. Eng. 159, 103714. https://doi.org/10.1016/j.coastaleng.2020.103714

Appendices

Appendix A

Derivation of the model for spilling breakers:

For obtaining an analytical solution for Eq. (3.10), integration is required as follows:

$$D = \alpha\rho_w g \frac{k_1}{2}\frac{C_0}{(1-C_0)} w_r \int_0^{\infty} H(x)\left(\frac{H_{rms}}{\gamma h}\right)^2 \left[1 - e^{-\left(\frac{H}{\gamma h}\right)^2}\right] \frac{2H}{H_{rms}^2} e^{-\left(\frac{H}{H_{rms}}\right)^2} d(H). \quad \text{(A1)}$$

Now, let $\left(\frac{H}{H_{rms}}\right)^2 = z$ which implies $H = H_{rms}^2\sqrt{z}$ and $dz = \frac{2H}{H_{rms}^2}dH$.

Incorporate the above parameters in Eq. (A1) and adjust the limit, it provides:

$$D = \alpha\rho_w g \frac{k_1}{2}\frac{C_0}{(1-C_0)} w_r \frac{H_{rms}^3}{(\gamma h)^2} \int_0^{\infty} \sqrt{z}\left(1 - e^{-z\frac{H_{rms}^2}{(\gamma h)^2}}\right) e^{-z} dz. \quad \text{(A2)}$$

Now, integrating Eq. (A2) concerning *z* and use limit, which gives:

$$D = \alpha\rho_w g \frac{k_1}{2}\frac{C_0}{(1-C_0)} w_r \frac{H_{rms}^3}{(\gamma h)^2}\frac{\sqrt{\pi}}{2}\left\{1 - \left(1 + \left(\frac{H_{rms}}{\gamma h}\right)^2\right)^{-3/2}\right\}. \quad \text{(A3)}$$

Expanding the last part of the above equation and neglecting the higher power of $\left(\frac{H_{rms}}{\gamma h}\right)^2$, yields:

$$D = \alpha\rho_w g \frac{k_1}{2}\frac{C_0}{(1-C_0)} w_r \frac{H_{rms}^3}{(\gamma h)^2}\frac{\sqrt{\pi}}{2}\frac{3}{2\gamma^2}\left(\frac{H_{rms}}{\gamma h}\right)^2. \quad \text{(A4)}$$

Therefore, after reshuffling Eq. (A4), that yields:

$$D = \alpha\rho_w g \frac{k_1}{2}\frac{C_0}{(1-C_0)} w_r \frac{H_{rms}^5}{(\gamma h)^4}\frac{3\sqrt{\pi}}{4}. \quad \text{(A5)}$$

Eq. (A5) is the new dissipation model for spilling breaking irregular waves attenuation by the air bubbles effect.

Appendix B

Derivation of the model for plunging breakers:

To get an analytical solution for Eq. (3.24), need to integrate it in the following way:

$$D = \frac{1}{2}\alpha\rho_w g \frac{C_0}{(1-C_0)} w_r \int_0^{\infty} H_b \left(\frac{H_{rms}}{\gamma h}\right)^2 \left[1 - e^{-\left(\frac{H}{\gamma h}\right)^2}\right] \frac{2H}{H_{rms}^2} e^{-\left(\frac{H}{H_{rms}}\right)^2} d(H). \quad \text{(B1)}$$

At once, allow $\left(\frac{H}{H_{rms}}\right)^2 = z$ which implies $H = H_{rms}^2\sqrt{z}$ and $dz = \frac{2H}{H_{rms}^2} dH$.

Include the overhead parameters in Eq. (B1) and change the limit, it gives:

$$D = \frac{1}{2}\alpha\rho_w g \frac{C_0}{(1-C_0)} w_r \frac{H_{rms}^2}{(\gamma h)^2} \int_0^{\infty} \left(1 - e^{-z\frac{H_{rms}^2}{(\gamma h)^2}}\right) e^{-z} dz. \quad \text{(B2)}$$

Now, integrating Eq. (B2) concerning *z* and use limit, which delivers:

$$D = \frac{1}{2}\alpha\rho_w g \frac{C_0}{(1-C_0)} w_r \frac{H_{rms}^2}{(\gamma h)^2} \left\{1 - \left(1 + \left(\frac{H_{rms}}{\gamma h}\right)^2\right)^{-1}\right\}. \quad \text{(B3)}$$

Expanding the last part of the overhead equation and ignoring the greater power of $\left(\frac{H_{rms}}{\gamma h}\right)^2$, yields:

$$D = \frac{1}{2}\alpha\rho_w g \frac{C_0}{(1-C_0)} w_r \frac{H_{rms}^2}{(\gamma h)^2} \left(\frac{H_{rms}}{\gamma h}\right)^2. \quad \text{(B4)}$$

Hence, after reshuffling Eq. (B4), generates:

$$D = \frac{1}{2}\alpha\rho_w g \frac{C_0}{(1-C_0)} w_r \frac{H_{rms}^4}{(\gamma h)^4}. \quad \text{(B5)}$$

Eq. (B5) represents the new energy dissipation model for plunging breaking irregular waves attenuation by the air bubbles effect.

Appendix C

M-I (spilling breaking waves) derivation:

For spilling breaking waves, the new energy dissipation model for irregular waves could be written after applying Führboter, (1970) condition as follows:

$$D_{IaS} = \frac{g w_r \alpha \rho_w c_0 d_1}{2(1-c_0)} \int_{\mathbf{0}}^{\infty} H e^{-\left(\frac{H_b}{H_{rms}}\right)^{\kappa}} \frac{\kappa}{H_{rms}} \left(\frac{H}{H_{rms}}\right)^{\kappa-1} e^{-\left(\frac{H}{H_{rms}}\right)^{\kappa}} dH, \quad \text{(C1)}$$

To find an analytical solution of Eq. (C1), need to integrate it. So, assume $\left(\frac{H}{H_{rms}}\right)^{\kappa} = r$ which implies $H = r^{\frac{1}{\kappa}} H_{rms}$ and $dr = \frac{\kappa H^{\kappa-1}}{H_{rms}^{\kappa}} dH$.

Adjust the limit after incorporating the overhead parameters into Eq. (C1), it gives:

$$D_{IaS} = \frac{K_1 g w_r \rho_w c_0}{2(1-c_0)} \int_0^{\infty} r^{\frac{1}{\kappa}} H_{rms} e^{-\left(\frac{H_b}{H_{rms}}\right)^{\kappa}} e^{-r} dr, \quad \text{(C2)}$$

where $K_1 = \alpha d_1$ is the new arbitrary constant.

Now, integrating Eq. (C2) within the limit it supplies:

$$D_{IaS} = \frac{K_1 g w_r \rho_w c_0}{2(1-c_0)} H_{rms} \Gamma\left(\frac{1}{\kappa}+1\right) e^{-\left(\frac{H_b}{H_{rms}}\right)^{\kappa}}. \quad \text{(C3)}$$

Again, to adopt the above model in terms of significant wave height (H_{m0}) using $H_{m0} = \sqrt{2} H_{rms}$ which implies $H_{rms} = \frac{H_{m0}}{\sqrt{2}}$.

Therefore, after using the above transformation and $H_b = \gamma h$ in Eq. (C3), yields:

$$D_{IaS} = K_1 \rho_w g \frac{c_0}{2\sqrt{2}(1-c_0)} w_r \Gamma\left(\frac{1}{\kappa}+1\right) H_{m0} e^{-\left(\frac{\sqrt{2}\gamma h}{H_{m0}}\right)^{\kappa}}, \quad \text{(C4)}$$

which is the new dissipation model for irregular spilling breaking waves attenuated by the effect of air bubbles.

Appendix D

M-I (plunging breaking waves) derivation:

The new energy dissipation model for irregular waves can be written for plunging breaking waves using Führboter, (1970) condition as follows:

$$D_{IaP} = \frac{g w_r \alpha \rho_w c_0}{2(1-c_0)} \gamma \int_0^{\infty} h e^{-\left(\frac{H_b}{H_{rms}}\right)^{\kappa}} \frac{\kappa}{H_{rms}} \left(\frac{H}{H_{rms}}\right)^{\kappa-1} e^{-\left(\frac{H}{H_{rms}}\right)^{\kappa}} dH. \quad \text{(D1)}$$

To find an analytical solution of Eq. (D1), letting $\left(\frac{H}{H_{rms}}\right)^{\kappa} = r$ which gives $H = r^{\frac{1}{\kappa}} H_{rms}$ along with $dr = \frac{\kappa H^{\kappa-1}}{H_{rms}^{\kappa}} dH$.

Change the limit so that, once the above considerations have been incorporated into Eq. (D1), it gives:

$$D_{IaP} = \frac{K_2 g w_r \rho_w c_0}{2(1-c_0)} \gamma \int_0^{\infty} h e^{-\left(\frac{H_b}{H_{rms}}\right)^{\kappa}} e^{-r} dr, \quad \text{(D2)}$$

where $K_2 = \alpha$ represents the new arbitrary constant.

Now, by integrating Eq. (D2) into its limit, it provides:

$$D_{IaP} = \frac{K_2 g w_r \rho_w c_0}{2(1-c_0)} \gamma h e^{-\left(\frac{H_b}{H_{rms}}\right)^{\kappa}}. \quad \text{(D3)}$$

Again, to adopt the above model in terms of significant wave height (H_{m0}), using the relation, $H_{m0} = \sqrt{2} H_{rms}$ which implies $H_{rms} = \frac{H_{m0}}{\sqrt{2}}$.

Therefore, by applying the transformation described above and substituting $H_b = \gamma h$ into Eq. (D3), which provides:

$$D_{IaP} = K_2 \rho_w g \frac{c_0 \gamma}{2(1-c_0)} w_r h e^{-\left(\frac{\sqrt{2}\gamma h}{H_{m0}}\right)^{\kappa}}. \quad \text{(D4)}$$

This is the new air bubble-attenuated irregular plunging breaking wave dissipation model.

Appendix E

M-II derivation:

Following the assumption made by Thornton and Guza, (1983), M-II can write using Eq. (5.10) and Hoque, (2002) regular wave model as follows:

$$D_{IIa} = \frac{c_0}{k_0}\alpha\rho_w g w_r \int_0^{\infty}\left(\frac{1-e^{-k_0 h}}{1-c_0 e^{-k_0 h}}\right) e^{-\left(\frac{H_b}{H_{rms}}\right)^{\kappa}} P(H)\, dH, \tag{E1}$$

To get an analytical solution of M-II, integrate Eq. (E1), letting $\left(\frac{H}{H_{rms}}\right)^{\kappa} = r$ which gives $H = r^{\frac{1}{\kappa}} H_{rms}$ along with $dr = \frac{\kappa H^{\kappa-1}}{H_{rms}^{\kappa}} dH$.

Modify the limit such that Eq. (E1) yields after the aforementioned factors have been taken into account as follows:

$$D_{IIa} = K_3 g w_r \rho_w c_0 \int_0^{\infty}\left(\frac{1-e^{-k_0 h}}{1-c_0 e^{-k_0 h}}\right) e^{-\left(\frac{H_b}{H_{rms}}\right)^{\kappa}} e^{-r} dr, \tag{E2}$$

where $K_2 = \frac{\alpha}{k_0}$ is the new arbitrary constant.

Now, by integrating Eq. (E2) into its limit, it supplies:

$$D_{IIa} = K_3 g w_r \rho_w c_0 \left(\frac{1-e^{-k_0 h}}{1-c_0 e^{-k_0 h}}\right) e^{-\left(\frac{H_b}{H_{rms}}\right)^{\kappa}}. \tag{E3}$$

Similarly, using $H_{m0} = \sqrt{2} H_{rms}$ which means $H_{rms} = \frac{H_{m0}}{\sqrt{2}}$.

Finally, by using the transformation described above and substituting $H_b = \gamma h$ into Eq. (E3), yields:

$$D_{IIa} = K_3 \rho_w g C_0 w_r \left(\frac{1-e^{-k_0 h}}{1-c_0 e^{-k_0 h}}\right) e^{-\left(\frac{\sqrt{2}\gamma h}{H_{m0}}\right)^{\kappa}}, \tag{E4}$$

which is the new air bubble-attenuated irregular breaking wave energy dissipation model that comes from Hoque's, (2002) regular wave model.

Appendix F

PDF and CDF comparison:

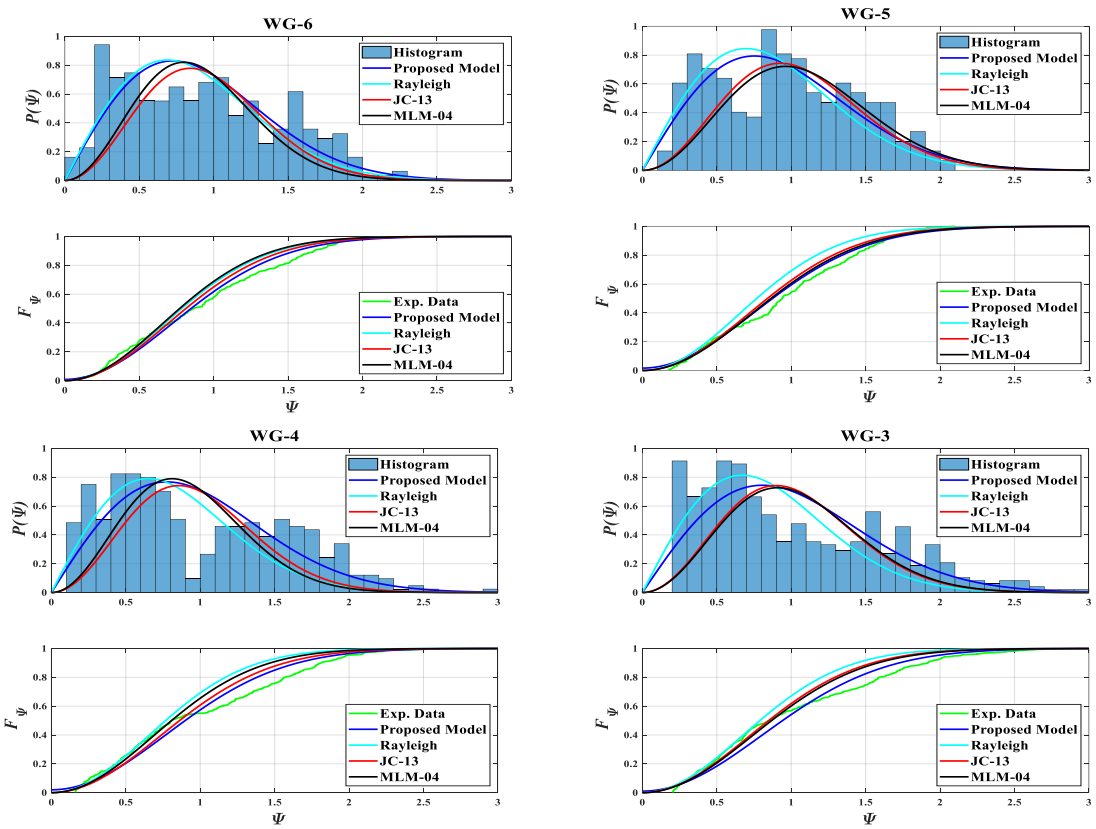

Figure F1: Comparison of the $P(\Psi)$, and F_{Ψ} concerning Ψ for the proposed model and other models (Rayleigh, MLM-04, and JC-13) for the incident, T_s = 1.31s, and H_s = 0.085m.

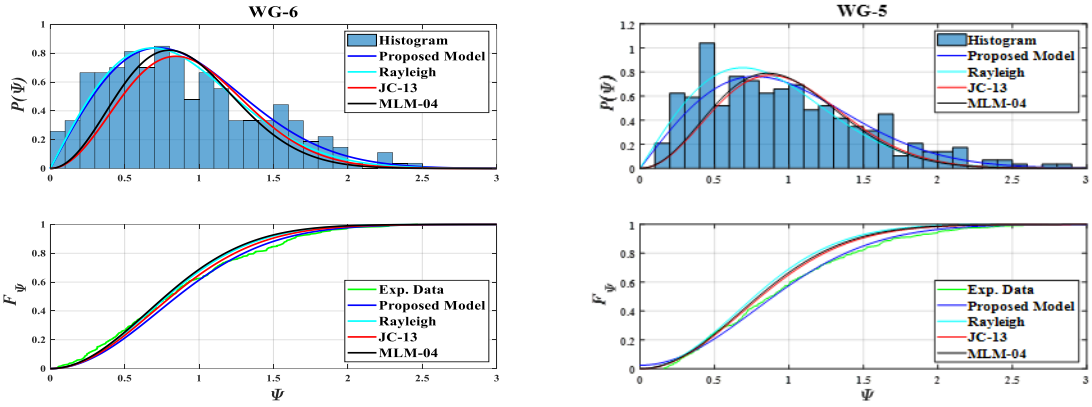

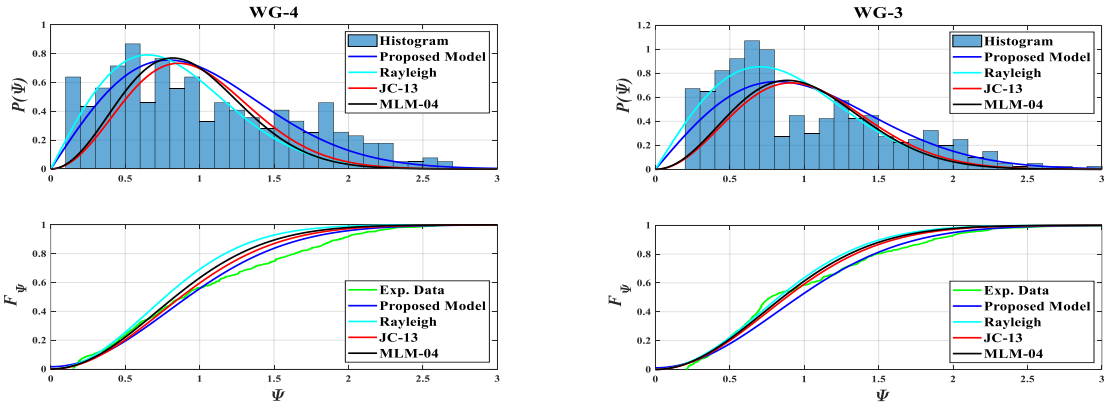

Figure F2: Comparison of the $P(\Psi)$, and F_{Ψ} with respect to Ψ for the proposed model and other models (Rayleigh, MLM-04, and JC-13) for the incident, T_s = 1.44s, and H_s = 0.068m.

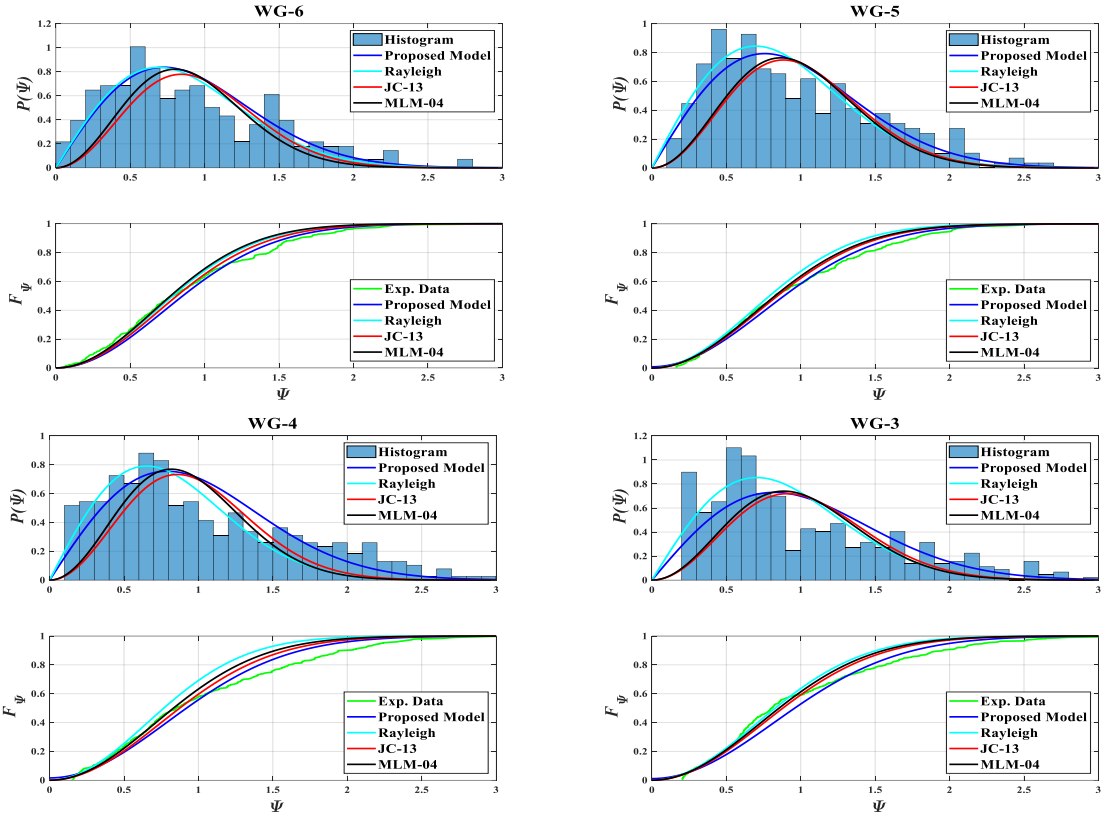

Figure F3: Comparison of the $P(\Psi)$, and F_{Ψ}, with respect to Ψ for the proposed model and other models (Rayleigh, MLM-04, and JC-13) for the incident, T_s = 1.48s, and H_s = 0.079m.

Appendix G

Probability of exceedance comparison:

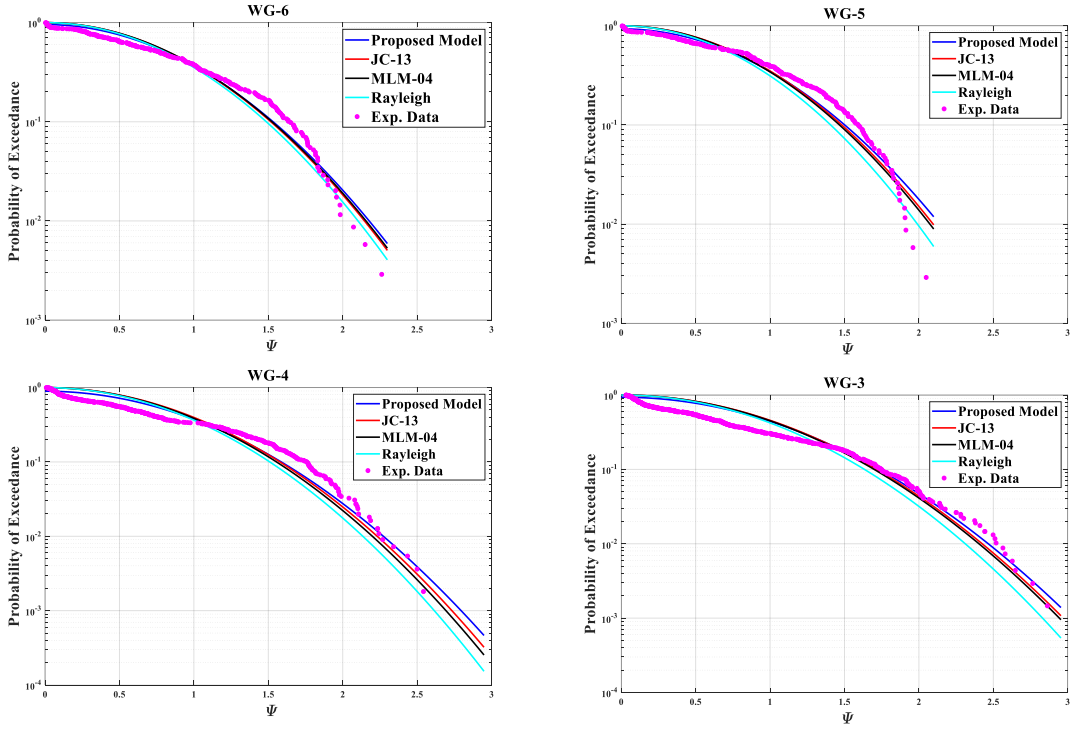

Figure G1: Variation of the exceedance of probability with respect to Ψ for the proposed model and other models (Rayleigh, MLM-04, and JC-13) for the specified incident wave conditions: T_s = 1.31s, and H_s = 0.085m.

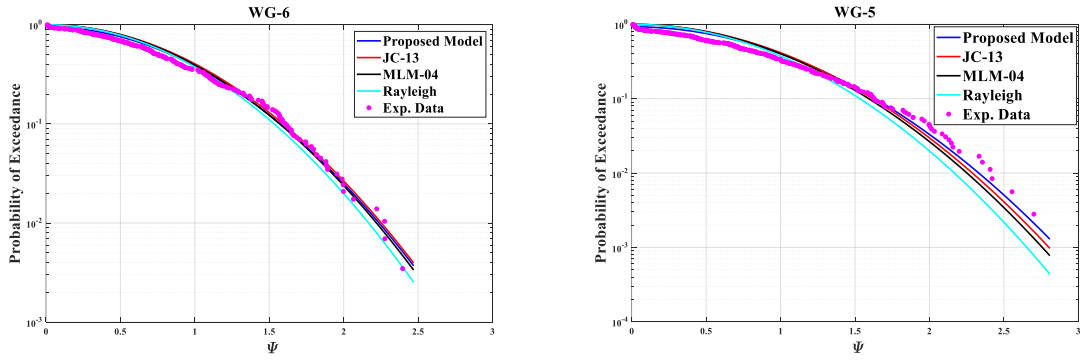

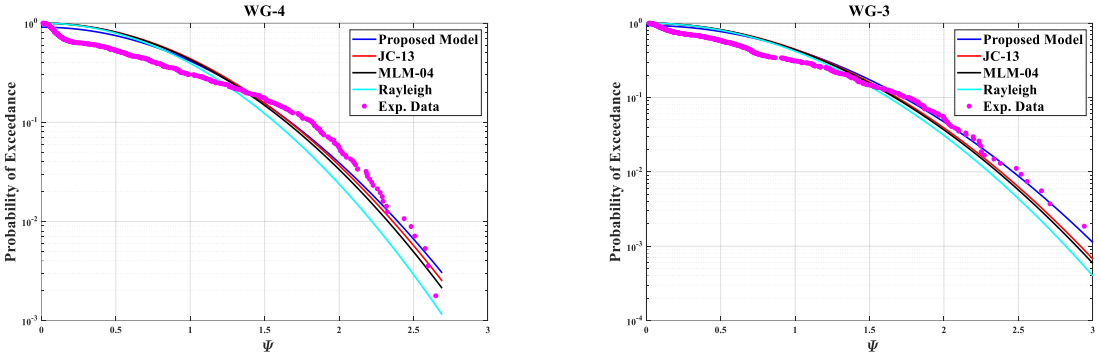

Figure G2: Variation of the exceedance of probability with respect to Ψ for the proposed model and other models (Rayleigh, MLM-04, and JC-13) for the specified incident wave conditions: T_s =1.48s, and H_s = 0.079m.

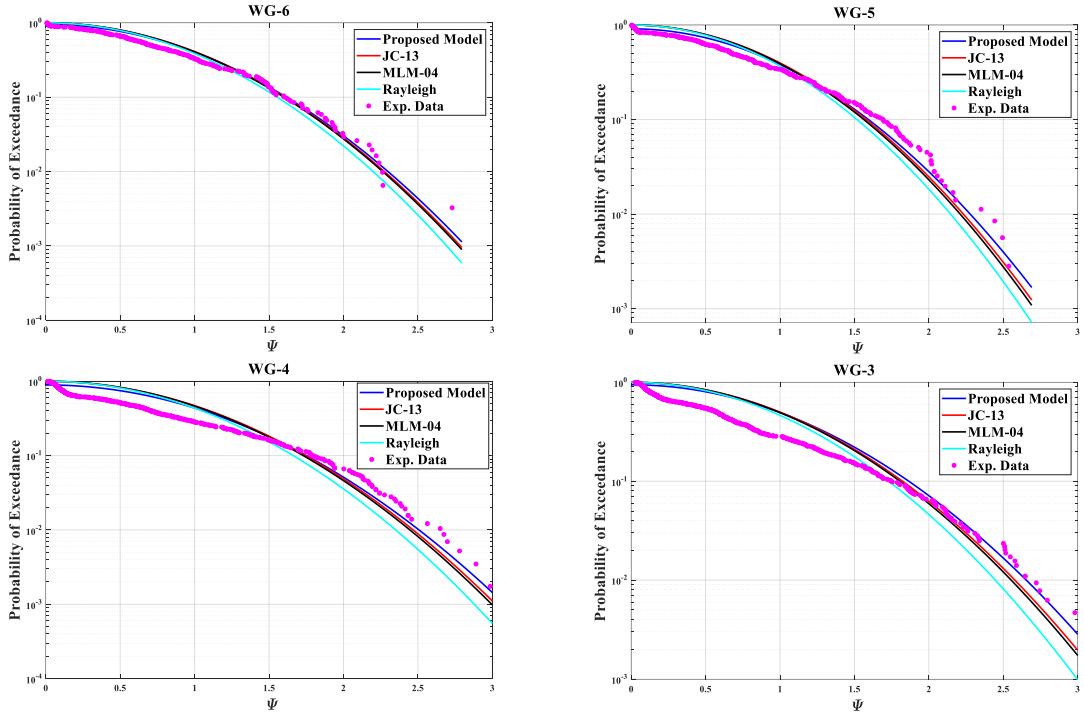

Figure G3: Variation of the exceedance of probability concerning Ψ for the proposed model and other models (Rayleigh, MLM-04, and JC-13) for the specified incident wave conditions: T_s = 1.44s, and H_s = 0.068m.